

Mathematical Models in Biology

By

BARBARA CATHRINE MAZZAG

B.A. (University of California, Santa Cruz), 1995

M.S. (University of California, Davis), 2000

DISSERTATION

Submitted in partial satisfaction of the requirements for the degree of

DOCTOR OF PHILOSOPHY

in

APPLIED MATHEMATICS

in the

OFFICE OF GRADUATE STUDIES

of the

UNIVERSITY OF CALIFORNIA

DAVIS

Approved:

Committee in Charge

2002

Contents

1	Introduction	1
2	Aerotaxis	4
2.1	Introduction	4
2.2	Background	6
2.2.1	Conventional chemotaxis	6
2.2.2	Aerotaxis	9
2.2.3	Aerotaxis experiments with <i>Azospirillum brasilense</i>	12
2.2.4	Mathematical models for conventional chemotaxis	16
2.3	Model	27
2.3.1	Mathematical model for aerotaxis	27
2.3.2	Expression for the turning frequencies	29
2.3.3	Non-dimensionalization and scaling	32
2.4	Results	36
2.4.1	Numerical simulations	36
2.4.2	Numerical results	36
2.4.3	Analytical results	41
2.5	Conclusions	57
3	Growth cone guidance	58

3.1	Introduction	58
3.2	Background	61
3.2.1	Biological background	61
3.2.2	Theoretical models of gradient sensing	69
3.3	Mathematical models and results	86
3.3.1	cAMP-adenylate cyclase switch	86
3.3.2	Adaptation and diffusion model	98
3.4	Conclusions and further direction	118
4	Endothelial cell deformation	120
4.1	Introduction	120
4.2	Mathematical Model	125
4.2.1	Kelvin bodies in series	125
4.2.2	Kelvin bodies in parallel	127
4.2.3	Model networks	137
4.2.4	Parameter values	138
4.3	Results	141
4.3.1	Parameter sensitivity analysis	141
4.3.2	Network simulations	163
4.4	Discussion	166
	Appendix	169
	A Receptor model	169
	B Analytical calculations	174
B.1	Asymptotic approximation	174
B.2	Steady state solution	177
B.3	Analytical solution and approximation	182

B.4 Calcium switch	188
C Sample Matlab code	191
Bibliography	195

List of Figures

2.1	Turning frequencies	7
2.2	Signal transduction pathway.	8
2.3	Aer and Tsr receptors.	10
2.4	Azospirillum brasilense.	12
2.5	Temporal assays.	13
2.6	Band formation.	15
2.7	Monte-Carlo simulation.	24
2.8	Derivation of the advection equation.	28
2.9	Turning rates.	30
2.10	PMF vs. oxygen.	31
2.11	Aerotactic band formation 1.	37
2.12	Aerotactic band formation 2.	37
2.13	Aerotactic band formation 3.	38
2.14	Aerotactic band formation 4.	38
2.15	Aerotactic band formation 5.	39
2.16	Numerical experiments with \tilde{L}_{max} and \tilde{L}_{min}	40
2.17	Steady state distribution of oxygen and bacteria.	42
2.18	Spatial assays for different oxygen concentrations.	47
2.19	Special steady state distribution of oxygen and bacteria 1.	48
2.20	Quasi steady state solution.	53

3.1	Part of the signal transduction pathway in growth cones.	64
3.2	Perfect adaptation according to Levchenko and Iglesias.	75
3.3	Amplification according to Levchenko and Iglesias.	77
3.4	Signal transduction in Levchenko and Iglesias.	78
3.5	Time evolution of Ca and AC.	92
3.6	Nullclines.	93
3.7	Bifurcation of AC	94
3.8	Bifurcation of Ca.	95
3.9	Steady states of Ca and AC.	97
3.10	Signal transduction pathway in one compartment.	99
3.11	Time evolution of the active substance.	102
3.12	Explanation of the two compartment model.	106
3.13	Time evolution of A in a ligand increment.	108
3.14	Time evolution of A from gradient to spatially uniform ligand. . . .	109
3.15	Steady state of the system in a gradient.	110
3.16	Temporal dynamics of A in a ligand increment, reaction-diffusion equation.	112
3.17	Temporal dynamics of A in a linear gradient, reaction-diffusion equation.	113
3.18	Temporal dynamics in a nonlinear gradient, reaction-diffusion system.	114
3.19	Signal amplification based on Goldbeter and Koshland.	116
4.1	Diagram to illustrate one viscoelastic Kelvin body.	126
4.2	n Kelvin bodies in series.	127
4.3	Two Kelvin bodies in parallel.	128
4.4	n Kelvin bodies in parallel.	132
4.5	Network I: model of an endothelial cell.	138
4.6	Network II: model of an endothelial cell.	138
4.7	Dependence of deformation on μ_{O_2} . Steady flow.	142

4.8	Dependence of deformation on μ_{02} . Oscillatory flow.	143
4.9	Dependence of peak deformation on μ_{02} . Oscillatory flow.	144
4.10	Dependence of steady state deformation on μ_{02}	144
4.11	Dependence of deformation on μ_{12} . Steady flow.	145
4.12	Dependence of peak deformation on μ_{12} . Oscillatory flow.	146
4.13	Dependence of steady state deformation on μ_{12}	146
4.14	Dependence of deformation on η_{12} . Steady flow.	148
4.15	Dependence of peak deformation on η_{12} . Oscillatory flow.	149
4.16	Dependence of steady state deformation on η_{12}	149
4.17	Dependence of force splitting on μ_{02} . Steady flow.	150
4.18	Dependence of force splitting on μ_{02} . Oscillatory flow.	151
4.19	Dependence of peak force splitting on μ_{02} . Oscillatory flow.	152
4.20	Dependence of steady state force splitting on μ_{02}	152
4.21	Dependence of force splitting on μ_{12} . Steady flow.	153
4.22	Dependence of peak force splitting on μ_{12} . Oscillatory flow.	154
4.23	Dependence of steady state force splitting on μ_{12}	154
4.24	Dependence of force splitting coefficient on η_{12} . Steady flow.	155
4.25	Dependence of peak force splitting on η_{12} . Oscillatory flow.	156
4.26	Dependence of steady state force splitting on η_{12}	156
4.27	Peak steady state deformation as a function of frequency of oscillations.	157
4.28	Peak steady state deformation as function of frequency and η_{12}	158
4.29	Dependence of peak steady state force splitting on the frequency. . .	159
4.30	Deformation with all parameters changed. Steady flow.	160
4.31	Deformation with all parameters changed. Oscillatory flow.	161
4.32	Force splitting with all parameters changed. Steady flow.	162
4.33	Force splitting with all parameters changed. Oscillatory flow.	163
4.34	Deformation of network I.	164

4.35	Deformation of network II.	165
A.1	Tar receptor.	169
A.2	Piston model of a receptor.	170
A.3	Fast and slow states of a receptor.	172
B.1	Calcium switch	189
B.2	Numerical results with the calcium switch.	190

List of Tables

2.1	Temporal assay.	14
2.2	Characteristic scales.	34
2.3	Non-dimensional parameter values.	34
3.1	Parameter values for the calcium-adenylate cyclase switch model . . .	91
4.1	Parameter values for the endothelial cell models	139

ACKNOWLEDGMENTS

My most grateful thanks go to my advisor, Prof. Alex Mogilner for all of his help and understanding. I feel extremely fortunate for the opportunity to work with him and learn from him. He has introduced me to mathematical biology, has encouraged me to participate in conferences and an internship, and in general has shown me how exciting and lively work in this area can be. I would like to thank him for providing me with a lot of practical help in research, for sharing his insights and intuition with me, and for the financial and emotional support he has given me. This dissertation is based on collaborations with him but, naturally, the errors in this work are mine alone. This document would not exist without his help.

Prof. Goodhill has generously provided a place for me while I was spending a six-month-long internship in his laboratory. I cannot thank him enough for teaching me to use many valuable research tools, for stimulating discussions, for a lot of personal help while I was at Georgetown, and for his continued interest and detailed comments on our collaborative project. Some day I hope to live up to his excellence in writing. Prof. Barakat also has given me many very useful comments and criticisms on our joint work as well as on my Masters' thesis. I also appreciate the excellent background he has given me on fluid dynamics in his course.

I would like to thank Prof. Angela Cheer and Prof. Albert Fannjiang for reading this work and for providing me with their comments and suggestions.

I am also very grateful to my personal system's administrator and support team, Tyler Evans. Writing this dissertation would have been much easier without having to follow him to Eureka, but it would have been impossible to complete it without him.

Abstract

Aerotaxis is the particular form of chemotaxis in which oxygen plays the role of both the attractant and the repellent. Aerotaxis occurs without methylation adaptation, and it leads to fast and complete aggregation toward the most favorable oxygen concentration. Biochemical pathways of aerotaxis remain largely elusive, however, aerotactic pattern formation is well documented. This allows mathematical modeling to test plausible hypotheses about the biochemical mechanisms. Our model demonstrates that assuming fast, non-methylation adaptation produces theoretical results that are consistent with experimental observations. We obtain analytical estimates for parameter values that are difficult to obtain experimentally.

Chemotaxis in growth cones differs from gradient sensing in other animal cells, because growth cones can change their attractive or repulsive response to the same chemical gradient based on their internal calcium or cAMP levels. We create two models describing different aspects of growth cone guidance. One model describes the internal switch that determines the direction of movement. However, this model allows chemotaxis under certain conditions only, so a second model is created to propose a mechanism that allows growth cone guidance in any environment.

Endothelial cells go through extensive morphological changes when exposed to shear stress due to blood flow. These morphological changes are thought to be at least partially the result of mechanical signals, such as deformations, transmitted to the cell structures. Our model describes an endothelial cell as a network of viscoelastic Kelvin bodies with experimentally obtained parameters. Qualitative predictions of the model agree with experiments.

Chapter 1

Introduction

Biology has gone through an extraordinary change in the past century, partially due to increasingly advanced methods of being able to collect data, and partially because of the sophistication in the quantitative analysis of this data. These changes are particularly striking in molecular and cellular biology, where incredibly complex interactions are revealed to be at the basis of all cell functions such as sensing, movement or reproduction. It is precisely the complexity of experimental observations that necessitates a more accurate and in-depth analysis. The need for a quantitative understanding of biological phenomena has lead to different modeling approaches. Many times highly advanced numerical simulations are created, and some research is aimed at highly realistic computer models of entire signal transduction pathways, or even entire cells. A very different, but equally valid approach, is to simplify possibly very complicated interactions to a smaller set of key components which lends itself easier to analytical models.

This dissertation is concerned with models of the latter type, namely, with arriving at biologically meaningful results from mathematical models based on a simplification of experimental observations. The hope of such models is that if they do indeed capture the key principles of the underlying the phenomenon, then a quantitative understand-

ing of these principles leads to new information which has not been uncovered by the experiments. In successful models the mathematical analysis leads to insights which are unattainable (or very difficult to attain) experimentally.

The first two chapters of this work are centered around a common theme: gradient sensing. Chapter 2 discusses a model of pattern formation due to bacteria searching for optimal oxygen concentrations. This work is based on experiments conducted by Zhulin et al. [78] on pattern formation of such bacteria. Our mathematical model presented in this chapter confirms that the experiments are produced by a novel form of gradient sensing, and in addition, it offers some experimentally testable predictions. Chapter 3 presents two models of how signal transduction events lead to the orientation of a neuron toward the appropriate target. This is an inherently difficult problem because of the limitations on experimental data available. In this dissertation two mathematical models of neuronal gradient sensing are developed, each aiming at understanding a different aspect of this question. Their advantages and disadvantages are discussed in detail in this chapter, and it is concluded that further work is necessary in this area. This chapter of my dissertation is a collaboration with Prof. Geoffrey J. Goodhill from the Neuroscience Department of Georgetown University Medical Center who introduced me to the biological background of growth cone guidance.

The third main topic of this work, presented in Chapter 4, also describes sensing on the cellular level, but in this case the signal is not biochemical, but mechanical. The mathematical model describes morphological changes in the cells lining the blood vessels when they are exposed to different types of shear stresses (induced by different types of flow over the cell surface). The predictions of the model agree qualitatively with the experiments, however, improvements of the model described in this chapter are necessary in order to make quantitative predictions. This work was done in collaboration with John S. Tamaresis from the Graduate Group in Applied Mathe-

matics and Prof. Abdul Barakat from the Mechanical and Aeronautical Engineering Department of the University of California, Davis.

Each chapter contains the biological terminology and data relevant to the topic, as well as a discussion and conclusion of the mathematical model presented. The three projects are quite distinct both biologically and mathematically, therefore separate conclusions appeared to be most appropriate.

Chapter 2

Aerotaxis

2.1 Introduction

The study of cell motility is a broad subject with numerous applications ranging from understanding how nerve cells find their place in the developing brain to understanding wound healing. Of all different forms of motile cell behavior, bacterial chemotaxis is the best understood. Bacterial aerotaxis differs from conventional chemotaxis in a number of interesting ways that were highlighted by experiments conducted at the Loma Linda Medical School by Zhulin et al. [78].

Some differences between conventional chemotaxis and aerotaxis are already known, but the biochemical signal transduction pathways involved in aerotaxis are not. The purpose of this work is to demonstrate that the unusual patterns found in Zhulin's aerotaxis experiments are consistent with a novel form of taxis without slow adaptation. The main result is a mathematical model based on fast adaptation that characterizes aerotactic behavior and uses experimentally obtained parameters. Analytical and numerical results of the model are compared to experimental data.

The biological background is introduced in Section 2.2 which explains the terms chemotaxis and aerotaxis in detail and describes the differences between the two.

Current knowledge of the biochemical pathways involved in chemotaxis is also explained.

A detailed description of the Zhulin aerotaxis experiments and explanation of the observed pattern follows, as well as questions that arise from these experiments. We conclude with descriptions of various chemotaxis models and their limitations when applied to aerotaxis experiments. In particular, we introduce the Keller-Segel model, and discuss the modeling assumptions. This is followed by a summary of Grünbaum's work on approximating a general class of equations describing random walk behaviors. We used his analysis to show why most conventional chemotaxis models cannot be applied to the Zhulin aerotaxis experiments. Some other mathematical models are discussed briefly (Tranquillo [75], Barkai & Leibler [4]), and we argue that no existing models in the literature provide an appropriate framework for aerotaxis.

Section 2.3 contains our mathematical model of aerotaxis. The terms of the simple advection-reaction equations are explained, and the main question is the determination of the turning rates (reaction terms). A phenomenological justification is given for the choice of the particular terms. Appendix A provides the biological reasoning behind choosing such form for the turning frequencies and provides a simple mathematical model for a receptor which could produce such turning rates. Section 2.3 also explains how non-dimensionalization and scaling were obtained for the model.

Section 2.4 contains the results, both analytic and numerical. We show the numerical simulations of the aerotactic band formation. The interpretation of numerical results emphasizes how the model matches and predicts the band formation. Analytical solutions are given for the steady state of the system. Various parameter values which are experimentally not easily measurable are estimated.

In Section 2.5 we summarize our findings and talk about potential future projects related to this topic.

2.2 Background

2.2.1 Conventional chemotaxis

Bacterial chemotaxis is a term used for motility in the direction of higher nutrient concentrations (such as sugars and amino acids) and away from repellents. In a neutral environment (i.e. one with uniform chemical concentrations) bacteria swim smoothly in a given direction for a period of time, then go through a period of abrupt changes of direction, called tumbling. The sequence of 'runs' and 'tumbles' results in a random walk. This random walk becomes biased when attractant (or repellent) is added (or removed). Additional attractants suppress the frequency with which tumbling occurs; therefore, the straight runs lengthen in the direction of the highest attractant concentration. This allows bacteria to move up the gradient. Removing repellents has the same effect. On the other hand, adding repellents or removing attractants both increase the frequency of tumbling and facilitate the movement of bacteria down the gradient [12]. Figure 2.1 shows how turning frequencies change in response to attractants or repellents. Keeping attractant (and repellent) concentrations constant results in adaptation of turning rates.

The swimming mechanism of cells can vary greatly, resulting in different types of swimming not discussed in this thesis. However, the underlying principle of a biased random walk is prevalent in all forms of bacterial motility.

Chemotactic movement is necessary for bacterial cells because concentration gradients are detected by temporal comparison. This means that rather than being able to measure concentrations at the different ends of the cell, bacteria must move through their environment to be able to detect concentration changes. In order to have a temporal sensing mechanism, it is crucial that cells retain some information about the previous environment; in other words, it is necessary for the cell to have some sort of memory.

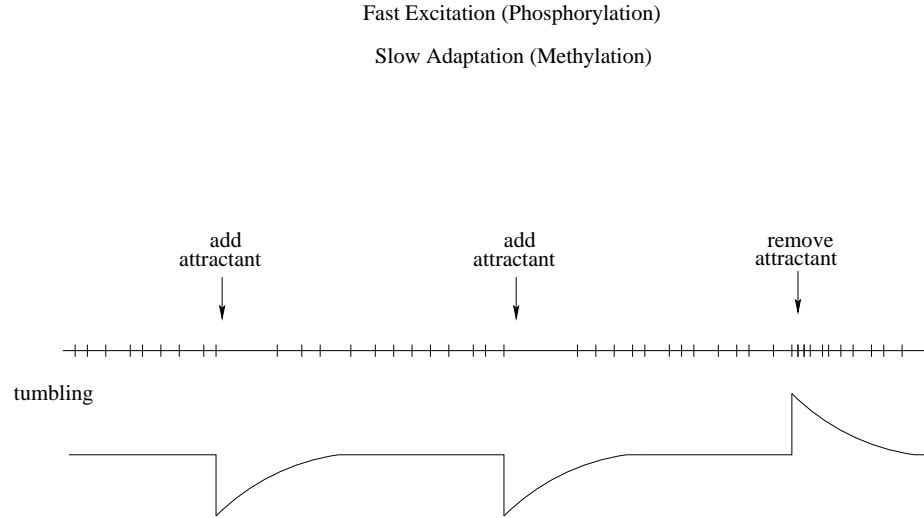


Figure 2.1: Changes in turning frequencies as a response to attractants and repellents. Fast excitation and slow adaptation are demonstrated. (Figure based on Bray, [12])

The mechanism for temporal sensing is also dependent on adaptation to the current level of attractants and nutrients. This allows cells to remain sensitive to concentration changes in a wide range of chemical environments. Adaptation and memory are related concepts, since memory is a consequence of a slow adaptation mechanism which allows cells to retain information about the previous environment for a period of time. During adaptation, the cell remains in a chemical state determined by the attractant (repellent) concentration before, and this time lag between the current and the past states serves as the memory of the cell. Any model of conventional chemotaxis must address the issues of sensitivity and memory.

The signal transduction pathways in bacteria such as *Escherichia coli* have been widely studied [4]. There are two important chemical reactions, phosphorylation and methylation, which are responsible for controlling the tumbling frequency, and which act on very different time scales. Phosphorylation is a very fast reaction (on the order of milliseconds [12]) that causes a fast response (on the order of 0.1 sec) to changes in the attractant or repellent concentration, while methylation acts on the same time

scale as a single run (1-3 sec), and it is responsible for the adaptation to current chemical concentrations.

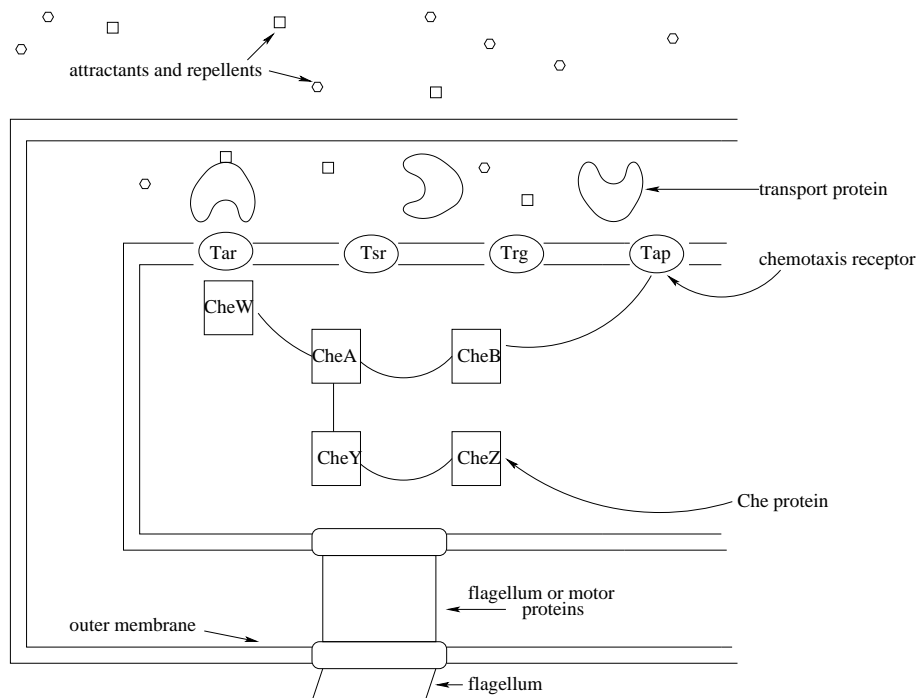


Figure 2.2: Signal transduction pathway in bacteria. (Figure based on Bray, [12].)

A simple model of the signal transduction pathway shown in Figure 2.2 involves a number of proteins, CheA, CheW, CheY, etc. The signaling works as follows: ligands (attractants and repellents) bind to transmembrane chemoreceptors of the bacteria. The cytosolic sides of the receptors are attached to kinases CheA and CheW. CheA phosphorylates both itself and CheY, which is a protein that acts as a messenger inside the cell. The role of CheY is to increase the tumbling frequency by reacting with the motor. CheY eventually dephosphorylates with the help of CheZ. Attractant binding slows down CheY phosphorylation, which in turn leads to suppressed tumbling and longer runs in the direction of attractants. Methylation, on the other hand, speeds up CheY phosphorylation which leads to an eventual return to the base tumbling rates, i.e. adaptation. Methylation occurs through a pair of enzymes, CheR and CheB,

which add and remove methyl groups. As the rate of methylation of the receptors slowly increases, the tumbling frequency increases as well, and the cell returns to the original turning rates. There is also a coupling between the phosphorylation and methylation pathways, and it is the phosphorylation of CheB by CheA. This results in an increase in the demethylation activity of CheB, so this also contributes to the suppression of tumbling rates [4].

2.2.2 Aerotaxis

Aerotaxis is a specific type of taxis (directed movement) in which both the attractant and the repellent are particular concentrations of oxygen. Very low and very high concentrations both act as repellents whereas some intermediate concentrations attract bacteria. The particular range of desirable concentration depends on the species. Aerotaxis was first discovered in 1676 by van Leeuwenhoek who noticed aggregation of cells underneath the surface of a solution. Later, in 1881, Englemann observed that bacteria aggregate at the edges of coverglass and around the air bubbles trapped underneath [71]. Initially, aerotaxis was considered a chemotactic response to oxygen, but further studies, summarized in Taylor's 1983 paper [71], reveal several aspects in which aerotaxis and conventional chemotaxis differ drastically.

First of all, we list these differences between conventional chemotaxis and aerotaxis, then explain their meaning and significance below. One of the most notable differences is that aerotaxis is metabolism-dependent. This means that while bacteria do consume the oxygen, chemotactic bacteria can be attracted to nutrients which they are unable to metabolize [1]. There is also quite a bit of evidence [59, 73, 78], that aerotaxis is an example of so called "energy taxis" in which cells monitor their internal energy balance and react to optimize it. (In contrast, chemotaxis is based on monitoring and optimizing the nutrient availability in the external environment.) We discuss the notion of energy taxis further below. The third factor distinguishing aero-

taxis and chemotaxis is the signal transduction pathway. This includes differences in the receptors utilized, as well as the fact that aerotactic movement does not have a methylation-dependent adaptation [71]. The precise mechanism of adaptation in aerotactic bacteria is currently unknown.

In order to explain energy taxis, we must introduce some new terms. Proton motive force refers to the electrochemical potential difference across the membrane [71], and it is produced by linking electron transport due to respiration to translocation of protons [71]. The coupling between the proton motive force and the electron transport system is tight, and currently it is not known which of the two acts as a signal for the cell's behavior [59]. However, it is believed [59, 73] that aerotactic bacteria respond to internal changes in the proton motive force or the electron transport system and not directly to the extracellular oxygen levels. This is supported by a series of experiments [71, 73] in which other signals that changed electron transport also resulted in behavioral responses. For example, Taylor and Zhulin [73] cite cases in which metabolized substrates elicit tactic response, as do chemicals which are able to donate electrons to or accept electrons from the electron transport system.

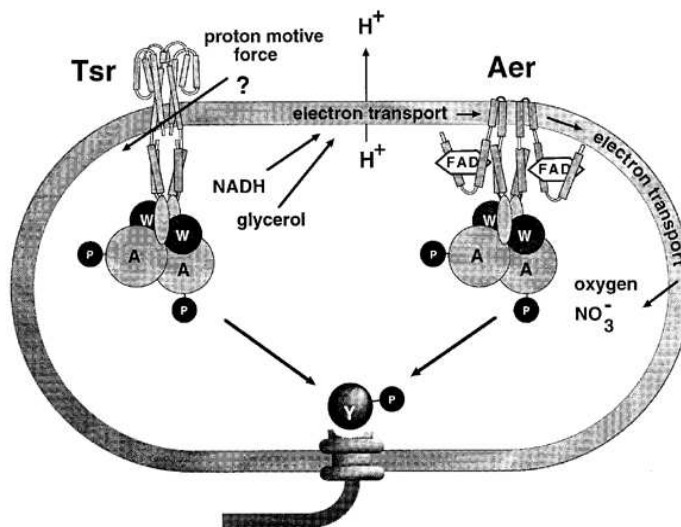


Figure 2.3: Aer and Tsr receptors. (Figure from Taylor and Zhulin, [73])

There are two receptors that have been proven to act as signal transducers [59]. The two receptors, Aer and Tsr are shown in Figure 2.3. Aer is a novel receptor which plays no role in conventional chemotaxis. Rebbapragada et al. [59] demonstrate that when mutants with a deactivated aer gene are exposed to an oxygen gradient, they find optimal oxygen concentrations much slower and less efficiently than wild type (non-mutant) bacteria. Meanwhile, the same mutants still exhibit normal chemotaxis indicating that the signal transduction pathways for chemotaxis and aerotaxis differ. When expression of Aer is restored, the aerotactic behavior returns.

Tsr, the other aerotaxis receptor, also works as a receptor for conventional chemotaxis, sensing external environments as well as monitoring internal pH. The aer tsr double mutants were not capable of aerotactic sensing; however, upon restoring one or both of the Tsr and Aer receptors, aerotactic response returns [59]. The signal transduction pathway of aerotaxis is not well understood, although it is believed to converge with the phosphorylation pathway of conventional chemotaxis [60]. CheA, CheW and CheY are part of the signal transduction pathway for aerotaxis [60], but there is evidence that adaptation is methylation-independent [71]), and it is much faster than the adaptation response in conventional chemotaxis [71].

Aerotaxis is thought to be beneficial, because finding the appropriate concentrations of oxygen is essential for the metabolism of some species and can, in fact, be a more immediate need than finding the appropriate nutrient levels [71]. According to Taylor and Zhulin [73], the aerotactic response might prevent bacteria from getting trapped in anaerobic, growth-limiting environments. In their hypothesis, bacteria living in conditions which support growth would mostly rely on their chemotactic behavior and would use aerotaxis when the maintenance of optimal internal energy levels becomes impossible. The mechanism for aerotaxis is expected to operate on simpler principles than that of chemotaxis, since it is "designed" to find a well-defined range of a single chemical, oxygen. On the other hand, chemotaxis allows bacteria to choose between

different types of nutrients of possibly different concentrations and quality, as well as allowing adaptation to a wide range of concentrations [59, 73, 78].

2.2.3 Aerotaxis experiments with *Azospirillum brasilense*

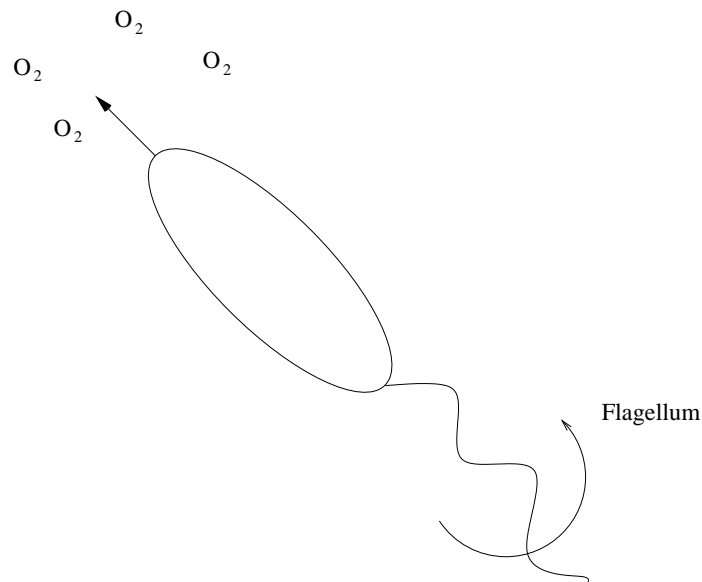


Figure 2.4: Schematic figure of *Azospirillum brasilense*. One flagellum is attached to the ellipsoidal body.

Azospirillum brasilense is a 1-2 μm nitrogen-fixing plant-associated bacterium [78] with an ellipsoidal body to which one flagellum is attached. (See Figure 2.4 for a schematic diagram of *A. brasilense*.) Counterclockwise rotation of the flagellum produces forward motion, while clockwise rotation reverses the direction. The essentially one dimensional movement of *A. brasilense* makes it a simple organism to model. It is generally accepted that its positive aerotaxis (attraction) is a response to changes in the proton motive force, and in Zhulin's hypothesis [78] this is also the signal for negative aerotaxis.

A. brasilense is aerobic, but it prefers very low concentrations of dissolved oxygen. Zhulin's experiments demonstrated by spatial and temporal assays that oxygen indeed

acts both as repellent and attractant, and Zhulin has provided evidence [78] that both are linked to monitoring the proton motive force inside the cell. As before, one can reason that aerotaxis provides an additional advantage for *A. brasilense* by guiding it to an optimal range of oxygen concentration. Nitrogen fixing can be accomplished only in environments where the oxygen concentration is below 1 percent [78], and in these environments *A. brasilense* remains capable of maintaining aerobic metabolism [78].

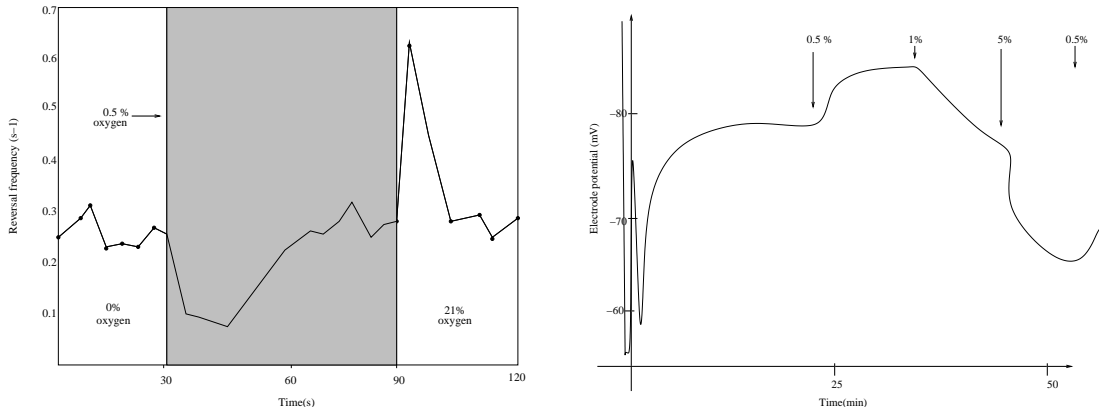


Figure 2.5: The graph on the left shows the turning frequency as a function of time. Significant changes occur as the oxygen concentration jumps to 0.5 percent from no oxygen, and as the oxygen concentration jumps to 21 percent. The figure on the right shows the proton motive force as a function of time. (Figure based on Zhulin,[78])

In the temporal assays for aerotaxis, a small droplet of bacterial suspension was spread on a slide [78] then exposed to different oxygen concentrations. Figure 2.5 illustrates the results of these experiments. It shows that the bacterial turning frequency remained constant at approximately 0.28 s^{-1} for most changes in oxygen concentration. There were two instances where significant changes were observed in the turning frequency. The reversal frequency dropped to 0.09 s^{-1} when cells were ventilated with 0.5 percent oxygen after being equilibrated to nitrogen (no oxygen). The other noticeable change occurred when cells adapted to 0.5 percent oxygen were exposed to

5 percent oxygen. In this case, the reversal frequency jumped to 0.49 s^{-1} . Table 2.1 summarizes the results of these experiments.

Change in oxygen concentration (percentage)	Reversal frequency (s^{-1})
21 to 100	0.32 ± 0.04
0 to 21	0.27 ± 0.04
100 to 21	0.24 ± 0.06
21 to 0	0.22 ± 0.05
0 to 0.5	0.09 ± 0.03
0.5 to 5	0.49 ± 0.09

Table 2.1: Turning frequencies as the oxygen concentration changes. (Table from Zhulin, [78])

These findings indicate that cells are attracted to 0.5 percent oxygen concentration, since both increases and decreases in the oxygen concentration caused negative aerotactic response. Zhulin also calculated the proton motive force for various oxygen concentrations and found that the highest values of proton motive force corresponded to the 0.3-0.5 percent oxygen concentration range.

In the spatial assay for aerotaxis, a flat 50 by 2 by 0.1 mm capillary tube was filled with a solution containing *A. brasilense* distributed uniformly, with no dissolved oxygen in the solution. At the open end of the capillary, the oxygen concentration was maintained at various fixed levels, and this induced a band formation inside the capillary within 50 seconds to 3 minutes, depending on the oxygen concentration. The oxygen diffused into the capillary and was consumed at a certain rate by the bacteria. The bacteria aggregated to the favorable oxygen concentration, and the region where their density was high was seen as the band inside the capillary. If the oxygen concentration was 100 percent, the band moved further away from the meniscus. If nitrogen replaced oxygen, then the band moved closer to the open end, and eventually disappeared. If air was introduced again, then the band reappeared. An unusual feature of these spatial assays was the steepness of the gradients produced.

Oxygen concentrations change from 20 percent to zero oxygen in about 1.6 mm.

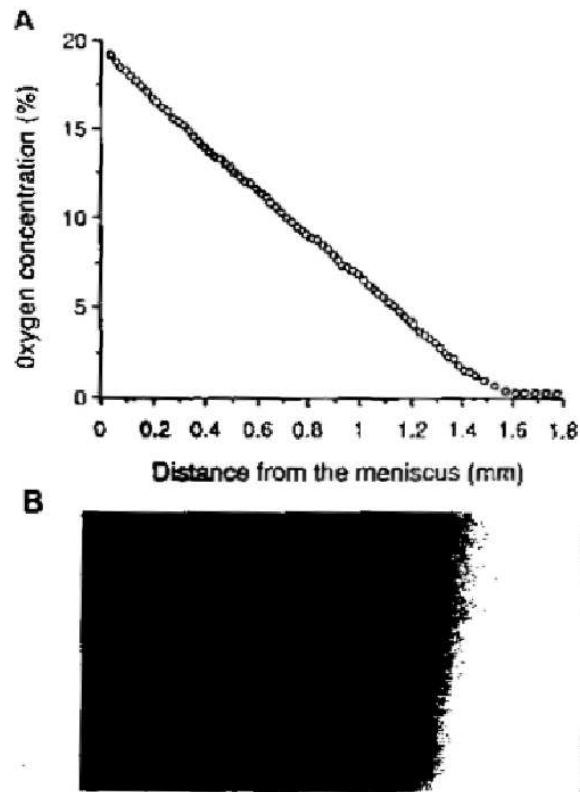


Figure 2.6: Figure A shows the oxygen concentration as a function of space. Figure B shows the aerotactic band on the same scale. The band forms about 1.6 mm from the meniscus where the oxygen concentration is 0.3-0.5 percent. (Figure based on Zhulin, [78])

In the spatial assay, the swimming speed of bacteria was observed. Inside the band, the cells swam with an average speed of $49 \frac{\mu\text{m}}{\text{s}}$ whereas outside the band the average speed was $14 - 22 \frac{\mu\text{m}}{\text{s}}$, depending on the oxygen concentration. The cells swimming in either direction would swim straight through the band then reverse direction immediately once they passed the band. The bacteria did not reverse their direction of swimming while inside the band [78]. The bacterial density inside the band was nearly a hundred times that in front of the band (between the band and the meniscus). The bacterial density behind the band remained approximately constant. Figure 2.6

shows the bacterial band which evolves in the spatial assay, and, on the same scale, the oxygen concentration corresponding to the various bacterial densities.

Our mathematical model will have to answer the following questions that arise based on the experiments: Can we create a model which leads to the evolution an aerotactic band with similar characteristics? We would like to test whether a model based on the simple turning rules which are suggested by the experiments would be able to produce the observed pattern. In particular, the hope is that of the model would demonstrate that the measurable quantities, such as the bacterial density inside the band and outside the band, the width of the band, and its distance from the meniscus, can be explained by assuming our simple turning rule.

Some deeper questions to pose beyond this model would be: What kind of signal transduction mechanism do aerotactic bacteria have? In particular, what sort of receptors make it possible for oxygen to act both as an attractant and a repellent? What sort of properties of this signal transduction mechanism allow the cells to react to such steep concentration gradients? How can the turning frequency of the cells change so abruptly at the boundaries of the aerotactic band? What is the underlying mechanism that allows the turning frequency to respond immediately? These questions are likely to be answered by further experiments.

2.2.4 Mathematical models for conventional chemotaxis

This section provides a brief overview of the mathematical tools used to describe conventional chemotaxis and briefly discusses why these existing models cannot be employed to study aerotaxis.

The first mathematical models for bacterial chemotaxis were created in the early 1970's by Keller and Segel [38, 63]. In their work [38], they show how local gradient detection by individual cells produces fluctuations in their path, and how the average over many cells corresponds to a macroscopic flux. They derive the macroscopic flux

equations based on individual bacteria. Although in this paper they make incorrect assumptions about the way bacteria are able to detect gradients (namely, they assume that bacteria can compare concentrations at their head and tail), they arrive at a very useful expression for the macroscopic flux:

$$J(x) = -\mu\left(\frac{db}{dx}\right) + \chi b \frac{dL}{dx}$$

In this equation $\mu(L)$ is the "diffusion", or motility coefficient, and $\chi(L)$ is the chemotactic coefficient. $b(x, t)$ is the bacterial density, and $L(x, t)$ is the concentration of the ligands. The rate of change of the bacterial density $b(x, t)$ can be given by

$$\frac{\partial b}{\partial t} = -\nabla J$$

with the appropriate boundary condition. In one dimension, this becomes the well known Keller-Segel chemotaxis equation:

$$\frac{\partial b}{\partial t} = -\frac{\partial}{\partial x}\left(-\mu\frac{\partial b}{\partial x} + \chi b \frac{\partial L}{\partial x}\right) \quad (2.1)$$

Again, boundary conditions must be imposed. It is clear in the equation (2.1) that the first term on the right-hand side is diffusion due to random motility, and the second term is due to chemotactic flux. Usually it is also assumed that the spatial gradient of the concentration is also small, and therefore $\frac{\partial L}{\partial x}$ can be approximated by a constant, and absorbed in χ , the chemotactic coefficient.

In a later paper [63], Segel derives the same chemotactic equation (2.1) based on changes in receptor configuration as a result of attractant (or repellent) binding. In this model, there is no need to use the incorrect hypothesis that bacteria are able to compare concentrations at different parts of their body. Instead, this model is developed by writing down a separate equation for left- and right-moving bacteria in different receptor configurations.

In order to arrive at (2.1) from this system of equations, Segel must use the assumption that spatial gradients are small. Almost the same analysis is summarized

more lucidly by Grünbaum; therefore, in order to understand where the assumption of small spatial gradients is needed, it is appropriate to look at Grünbaum's article "Advection-diffusion equations for internal state-mediated random walks" [23].

Grünbaum gives a simple argument regarding the validity of parabolic advection-diffusion approximations to hyperbolic advection equations. He starts with a system of one-dimensional advection equations describing left- and right-moving individuals, similar to the Segel system in [63].

$$\begin{aligned}\frac{\partial b^+}{\partial t} + v \frac{\partial b^+}{\partial x} &= \sigma^- b^- - \sigma^+ b^+ \\ \frac{\partial b^-}{\partial t} - v \frac{\partial b^-}{\partial x} &= \sigma^+ b^+ - \sigma^- b^-\end{aligned}\tag{2.2}$$

Boundary conditions are omitted again for the time being. The turning rates are denoted by σ^+ , σ^- and velocity by v . The velocity is chosen to be positive for the left-moving bacteria, and negative for the right-moving bacteria. Total bacterial density is given by $b(x, t) = b^+(x, t) + b^-(x, t)$; in other words, the total bacterial density is the sum of the right- and left-moving terms. Grünbaum also defines the density flux, $J(x, t)$ as $J(x, t) = v(b^+(x, t) - b^-(x, t))$, and introduces two new variables, $\sigma_0 = \frac{1}{2}(\sigma^+ + \sigma^-)$ and $\Delta\sigma = \frac{1}{2}(\sigma^+ - \sigma^-)$. By taking the sum and difference of the two equations in (2.2) and making the appropriate substitutions, he arrives at the following two equations:

$$\frac{\partial b}{\partial t} = -\frac{\partial J}{\partial x}\tag{2.3}$$

$$\frac{1}{2\sigma_0} \frac{\partial J}{\partial t} + J = \frac{1}{2\sigma_0} \left(-v^2 \frac{\partial b}{\partial x} + 2\Delta\sigma v b \right)\tag{2.4}$$

In equation (2.4), the objective is to estimate the term J_t using the conservation equation (2.3).

Grünbaum does this the following way. Assume that spatial derivatives are small, then a small J_x implies that b_t is small, or the bacterial density varies on a slow time scale. The solution to (2.4) is the linear combination of the homogeneous and

inhomogeneous solutions. The inhomogeneous terms all contain $b(x, t)$ or a spatial derivative of b ; therefore, they vary on a slow time scale. However, the solution to the homogeneous equation

$$\frac{1}{2\sigma_0} \frac{\partial J}{\partial t} + J = 0$$

will be an exponential term acting on a faster time scale. This implies that after a short initial period, J approaches a quasi-equilibrium. This gives the following equation:

$$J \approx \frac{1}{2\sigma_0} \left(-v^2 \frac{\partial b}{\partial x} + 2\Delta\sigma vb \right) \quad (2.5)$$

By substituting this approximation for the flux into (2.3), one can recover the Keller-Segel equation:

$$\frac{\partial b}{\partial t} \approx \frac{\partial}{\partial x} \left(\mu \frac{\partial b}{\partial x} - \chi b \right) \quad (2.6)$$

with

$$\begin{aligned} \mu &= \frac{v^2}{2\sigma_0} \\ \chi &= \frac{v\Delta\sigma}{\sigma_0} \end{aligned} \quad (2.7)$$

The advantage of this formulation over the Keller-Segel equation is clear, since (2.7) shows that the two important coefficients, the motility coefficient and the chemotactic coefficient, can be expressed in terms of empirically observable quantities, namely the cell velocity and the turning rates. It is also clear from Grünbaum's analysis that the assumption of a small spatial gradient is necessary in order to arrive at the Keller-Segel chemotaxis equation, (2.6).

In addition to the assumption of a small spatial gradient, another difficulty with this model is that an exact measure of the difference of turning frequencies, $\Delta\sigma$, is very difficult to obtain empirically, or to approximate analytically. An analytical expression for χ , the taxis coefficient, can be derived in terms of the characteristic

time scale of a run, the bacterial speed and the characteristic attractant concentration. This analytical result does not rely on having to measure the turning frequency, but is rather obtained by a perturbation method which separates time scales of the reaction. In this perturbation analysis, the characteristic run time is obtained based on the assumption that adaptation is slow. This is not a correct assumption in the aerotaxis experiments.

Another significant development in mathematical modeling of chemotaxis came in the late 1980's and early 1990's. A large effort was made to unite knowledge about receptor dynamics and signal transduction pathways (many times referred to as 'internal state dynamics') to random motility [18, 51]. In many of these models (e.g. [51]), not only bacterial chemotaxis but chemotaxis of animal cells is considered, making the internal state dynamics far more complex than in the bacterial case. There were several models, for example those by Barkai and Leibler [4] and by Tranquillo et al. [18, 51] which included very detailed models for the biochemical mechanism.

One such detailed model of chemotaxis in an animal cell is due to Tranquillo [51]. The general approach of Tranquillo and his collaborators is as follows. Identify a simplified (but still realistic) scheme to describe all possible receptor states and intracellular chemicals that govern the turning behavior. All rate constants and parameters are approximated based on empirical data. Each of the receptor states are interdependent stochastic variables, and their time evolution is calculated using a multivariate probability density function.

The jump processes between the various states can be approximated by continuous stochastic differential equations by making certain assumptions about the system. The probability function must be linearized in order to be represented by an analogous system of stochastic differential equations. However, the linearization procedure implicitly assumes small fluctuations in the stochastic variables. This, again, is an assumption that would be violated in the aerotaxis experiments.

In order to analyze the stochastic differential equations, deterministic equations are derived either using averages of the stochastic variables or transformations from the stochastic variables to new, deterministic variables. With this method, the Fokker-Planck equations are derived and used to estimate cell movement on longer time scales [51].

These models ([18, 51]) are highly sophisticated biologically and mathematically alike, although lack the satisfying simplicity of the earlier Keller-Segel equations. As mentioned above, they also assume certain features of the internal state dynamics that would be violated in steep attractant gradient; therefore, they cannot be used for our purposes.

Barkai & Leibler also create a model which is very closely built on experimentally obtained data. In “Robustness in simple biochemical networks” [4] they examine the question of receptor adaptation in bacteria, and they propose a quantitative model in which a wide range of biochemical parameters are admissible. The model Barkai & Leibler propose is a system of ordinary differential equations that is based on the accurate description of the possible receptor states. The key to the model is a small network that has two states: an active and an inactive state. In the active state the external signal leads to a fast response, whereas in the inactive state there is no response. The shift between the active and inactive states is a slower process, which corresponds to the receptor methylation. The system exhibits perfect adaptation if the active state is independent of the magnitude of the outside stimulus. A model based on the same principles is presented in the chapter on animal cell chemotaxis, Section 3.3.2. The contribution of Barkai & Leibler is significant for bacterial chemotaxis, because their work shows that fine-tuning the model parameters is unnecessary in order to achieve adaptation. However, in our model for aerotaxis there is no methylation adaptation, and we argue that if there is adaptation, it must occur on the fast time scale.

There is also some literature that focuses directly on aerotactic behavior and models for aerotaxis [30, 31]. In [31], certain bioconvection patterns are described quantitatively by developing a model of aerotaxis. Kessler's experiments described in this paper involve an initially well-stirred suspension in which cells swim upwards toward oxygen, then, after the top layer becomes sufficiently denser than the bottom layer, an instability occurs. The overturning instability evolves into the observed patterns. Some of the phenomenon is similar to the Zhulin aerotaxis experiments, namely, here bacteria consuming oxygen create the gradient while the oxygen level is fixed at the meniscus. However, in the Kessler experiments the bacterial convection stirs the solution, and the bacteria carry oxygen into deeper layers of the solution.

The mathematical model describing these experiments consists of a conservation equation for the cells and a reaction-diffusion equation for the oxygen concentration. The Navier-Stokes equations are not required, since no bulk fluid flow is assumed. The authors arrive at the same equation as the Keller-Segel equation for the bacteria. The whole system is:

$$\frac{\partial b}{\partial t} = -\nabla \cdot [b(u + v) - D \cdot \nabla b] \quad (2.8)$$

$$\frac{\partial L}{\partial t} = -\nabla \cdot (Lu - D_L \nabla L) - kb \quad (2.9)$$

In this model $L(x, y, z, t)$ is the concentration of oxygen, $b(x, y, z, t)$ is the density of bacteria, as above, u is the fluid velocity taken to be zero, $v(\Theta)$ is the average cell velocity which is a function of a dimensionless measure of L denoted Θ , D and D_L are the diffusion coefficients of the bacteria and of oxygen, respectively, and, finally, $k(\Theta)$ is the coefficient of nutrient consumption by the bacteria. The boundary conditions are applied at $z = 0$ and at $z = -h$, the bottom of the suspension. They are given

by:

$$L = L_0 \text{ at } z = 0, \quad \frac{\partial L}{\partial z} = 0 \text{ at } z = -h \quad (2.10)$$

$$v_z b - D \frac{\partial b}{\partial z} = 0 \text{ at } z = 0 \text{ and } -h \quad (2.11)$$

These boundary conditions mean that there is no flux of oxygen or bacteria at any of the boundaries. The initial condition is given for a well-stirred solution and uniform suspension:

$$L(z, 0) = L_0 \quad (2.12)$$

$$b(z, 0) = b_0 \quad (2.13)$$

By non-dimensionalizing the equations, the authors arrive at a perturbation problem whose analysis leads to a good quantitative description of the experiments. There are several reasons why this model would not be valid for the Zhulin aerotaxis experiments. First, just like the Keller-Segel equation, Hillesdon et al. make use of the small gradient assumption implicitly. Also, the Kessler experiments are examples of kinesis rather than taxis. In kinesis the movement is determined by local concentration of attractant, not by concentration gradients, as it is in taxis.

In his review article [30], Hill summarizes other models of various types of chemotaxis related to pattern formation (gyrotaxis, geotaxis, phototaxis). These equations make very similar assumptions to the models discussed above, namely, conservation equations for the bacteria involving gradients of the flux due to swimming and random motility. When, in addition, randomness in drift speed and direction of motility are introduced, the Fokker-Planck equation is used to describe tactic behavior.

In all the above mentioned models, there are two important aspect of chemotaxis that must be taken into account: the gradient of attractant concentration and the adaptation time. For small gradients and fast adaptation, it is simple to find approximations to the hyperbolic advection equations describing bacterial motion. Grünbaum also

shows that for slow adaptation in shallow gradients, one is able to simplify the equations to a parabolic system. However, if the attractant gradients are large, then these approximations do not work for slow adaptation any more. In this case, the only possible approach is to try Monte Carlo simulations. The model of aerotaxis presented in the next chapter uses the fact that while gradients are large, the adaptation time in our case is fast. This allows us to solve the original hyperbolic system.

It is also possible to give a heuristic argument for why conventional chemotaxis models that rely on slow adaptation cannot be used to model the Zhulin aerotaxis experiments. The following Monte-Carlo simulation, Figure 2.7 illustrates this reasoning.

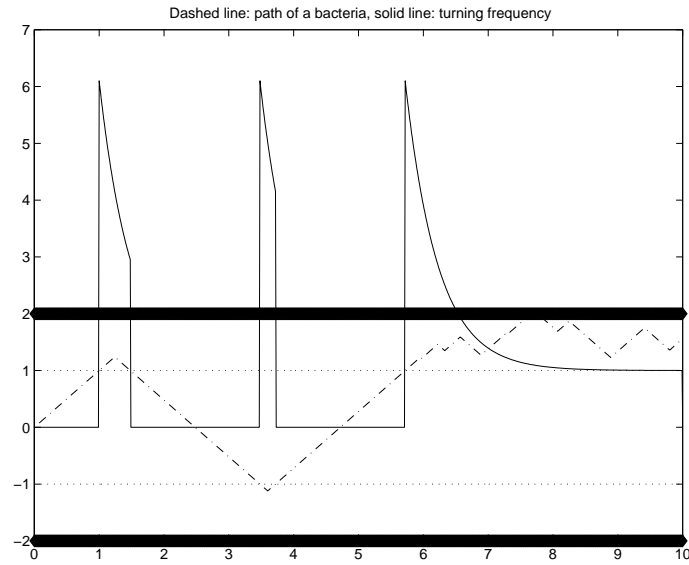


Figure 2.7: Monte-Carlo simulation.

The wide solid lines (at -2 and 2) represent the sides of the capillary tube (so the bacteria are confined to this region), and the dotted lines (at -1 and 1) represent the favorable oxygen concentrations. The following rules govern the movement of each cell:

- a cell moves straight to the left or to the right with a constant velocity, v ;
- turning frequency inside the favorable region (between -1 and 1) is $\sigma = 0$;

- the cell leaves the band at some random time, τ , and at this time the turning frequency jumps from $\sigma = 0$ to $\sigma = c$;
- characteristic time of adaptation is t_a ;
- adaptation to the baseline turning frequency of $\sigma = 0$ is exponential, and it is given by $\sigma = ce^{-\frac{t-\tau}{t_a}}$.

The adaptation in these simulations is assumed to be slow, which means that $\frac{1}{c}$, the time of a straight run, is of the same order of magnitude as t_a , the characteristic time of adaptation. Later, in our model of aerotaxis we assume that $t_a \ll \frac{1}{c}$.

In these simulations, the particle's velocity and turning frequency are given deterministically. When the cell is outside the band, the time of turning, τ , is determined based on the difference of a uniformly generated random number between 0 and 1 and the turning frequency.

In the figure, we can see a typical run of the simulation. Most of the time the bacterium stays inside the optimal oxygen concentration, because upon leaving the band, its turning frequency jumps from 0 to c , and it is likely to turn back into the band. However, outside the band the turning frequency is large for a period of time (t_a) due to slow adaptation, and it frequently causes the cell to keep tumbling and getting trapped outside the optimal environment. Running the simulation up to 10,000 times, the bacterial density inside the band was only three times the density outside the band. This is clearly very different from the 100:1 ratio observed experimentally. One must conclude that there are no existing models of bacterial chemotaxis (other than Monte Carlo simulations) that can describe the behavior in steep gradients. Most existing chemotaxis models also assume a slow adaptation of the turning rates. Exact mathematical descriptions of turning rates based on slow adaptation are very difficult to analyze, and in order to create tractable equations, one must make approximations. The approximations involve assumptions of small spatial gradients, since this allows

continuity of internal state variables. Assuming slow adaptation and a steep spatial gradient, no approximations are possible leading to simple mathematical expression. This suggests that it would be futile to attempt to model the Zhulin experiments with already existing chemotaxis equations. However, since aerotaxis is known to have fast adaptation, mathematical expression of the turning rates is much simpler; thus, we can develop a different model in which one need not rely on approximations based on shallow gradients.

2.3 Model

2.3.1 Mathematical model for aerotaxis

Now we can present the mathematical model for aerotaxis which describes the pattern formation as a result of steep concentration gradients. A brief derivation of the equations is given below. The bacteria's movement is governed by advection-reaction equations. The advection term describes the directed swimming of bacteria, while the reaction terms denote the turning of bacteria in response to the oxygen gradients. The evolution of the ligand (oxygen) concentration is given by a reaction-diffusion equation which is coupled to the advection equations through the term describing oxygen consumption by the bacteria.

We assume that bacterial movement is one-dimensional. Although some turning is possible, this assumption is based on empirical evidence of *A. brasilense* swimming. The cells are observed to swim either forward, or, upon changing their direction, backward. The hypothesis that the turning rates are dependent on oxygen concentration and the oxygen gradient is the main assumption of the model, and it is discussed at length below. The boundary conditions imposed simply mean that all left-moving cells turn to the right at the left boundary, and similarly, all right-moving cells turn to the left at the right boundary. The assumption of the conservation of the number of bacteria is used later, and it justifies the lack of birth and death terms in the equations. Since the band forms on the order of minutes, this is a reasonable omission.

$$\frac{\partial r}{\partial t} = \frac{\partial(-vr)}{\partial x} - f_{rl}r + f_{lr}l \quad (2.14)$$

$$\frac{\partial l}{\partial t} = \frac{\partial(vl)}{\partial x} + f_{rl}r - f_{lr}l \quad (2.15)$$

$$\frac{\partial L}{\partial t} = D \frac{\partial^2 L}{\partial x^2} - k(r + l) \quad (2.16)$$

$$r(0) = l(0)$$

$$r(a) = l(a)$$

$r(x, t)$ - right moving bacteria

$l(x, t)$ - left moving bacteria

$L(x, t)$ - ligand (oxygen) concentration

$f_{rl}(L)$ - rate of turning from right-moving to left-moving cell

$f_{lr}(L)$ - rate of turning from left-moving to right-moving cell

$v(L(x))$ - bacterial speed

D - diffusion coefficient for oxygen

k - rate of oxygen consumption by bacteria

a - length of the capillary

The initial condition for the left- and right-moving bacterial densities is the same constant for all positions, x , such that the sum of the two populations is the total bacterial density. The initial condition for the oxygen concentration is L_0 at the left boundary, and zero everywhere else.

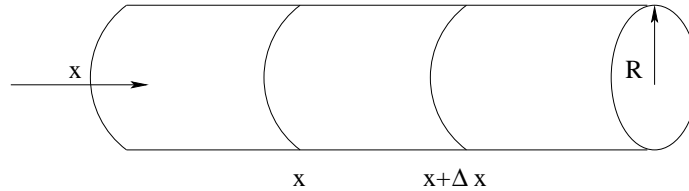


Figure 2.8: A volume element that bacteria swim through.

A brief justification (similar to the reasoning of Segel in [63]) of using the advection equation (2.14) is as follows. Consider the cells swimming in a capillary of a fixed cross-sectional area, R . Let us look at a short section of the capillary, from x to $x + \Delta x$. The density of right-moving cells in this section is given by $rR\Delta x$. Then the rate of change of the r , the right-moving bacterial density, with time respect to

time is equal to (i) change due to reversal of direction to become left-moving, and, similarly, left-moving bacteria turning to become right-moving; (ii) change due to cells swimming into and out of the slice.

The change due to turning is quite straight-forward. It is the turning rate of cells times the bacteria in the given volume, or $f_{lr}lR\Delta x - f_{rl}rR\Delta x$. The term due to cell swimming is the rate at which cells flow into the cell, and the rate at which they flow out,

$$v(x)r(x)R - v(x + \Delta x)r(x + \Delta x)R.$$

This leads to

$$\frac{\partial(rR\Delta x)}{\partial t} = f_{lr}lR\Delta x - f_{rl}rR\Delta x - R[r(x + \Delta x)v(x + \Delta x) - r(x)v(x)].$$

Dividing by $R\Delta x$ and letting Δx approach zero, we obtain

$$\frac{\partial r}{\partial t} = -\frac{\partial(vr)}{\partial x} - f_{rl}r + f_{lr}l$$

Equation (2.15) can be obtained in a similar fashion.

The most important question regarding the model is the determination of the the turning frequencies. There are two questions to be answered: what function of L are the turning frequencies? What is the biological evidence in support of this mathematical expression? Both of these questions are answered below.

2.3.2 Expression for the turning frequencies

We must consider the mathematical expression for the turning rates. It is known from the experiments that there is a range of concentrations where bacteria do not turn around. We can call this range L_{min} to L_{max} . This is the range where the proton motive force (PMF) is the highest; therefore, it is the preferred concentration range where the bacterial band develops. Outside this range, there must be some threshold values, \tilde{L}_{min} and \tilde{L}_{max} such that if a cell is between \tilde{L}_{min} and L_{min} , or between L_{max}

and \tilde{L}_{max} , it turns back inside the band. The bacterial frequencies are shown in Figure 2.9.

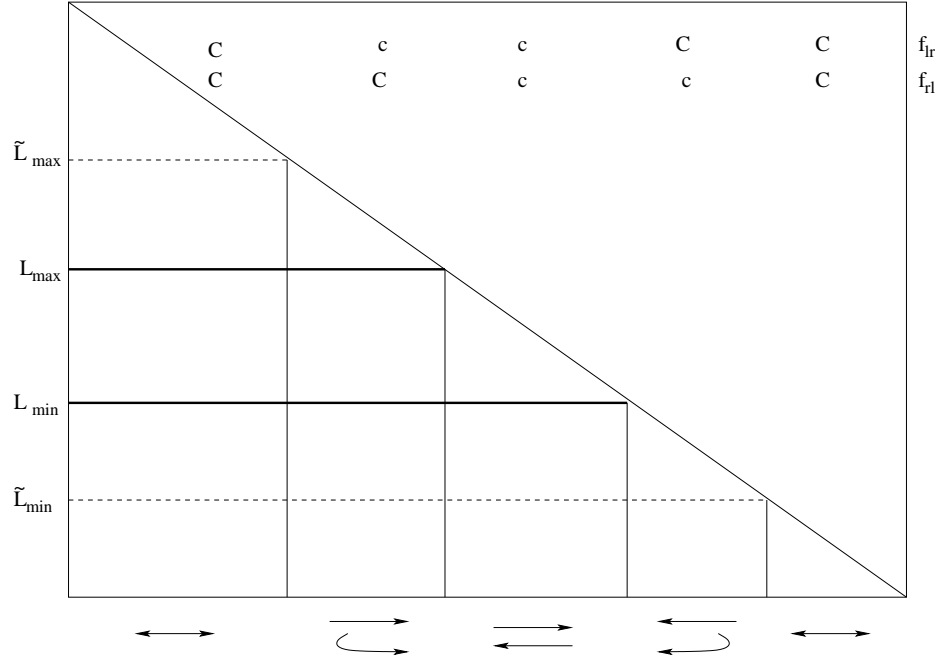


Figure 2.9: Turning rates of the bacteria.

However, the turning rates cannot depend on the values of oxygen concentration alone, since if that were the case, a cell getting to \tilde{L}_{min} from outside the band would have to turn, and would therefore never enter the favorable oxygen range. This suggests that the bacteria must be able to retain some additional information about the environment, for example the gradient of the ligand. This would allow a cell arriving to \tilde{L}_{min} to determine whether to keep on swimming (if it came from outside of the band) or to turn around (if it came from within the band).

In our hypothesis, this additional information comes from monitoring the proton motive force inside the cell. As it is shown in Figure 2.10, the PMF has its largest value, and it is a constant, when the cell is between L_{min} and L_{max} . Outside the band, the PMF has a low value, and it is also a constant. The turning signal for a cell

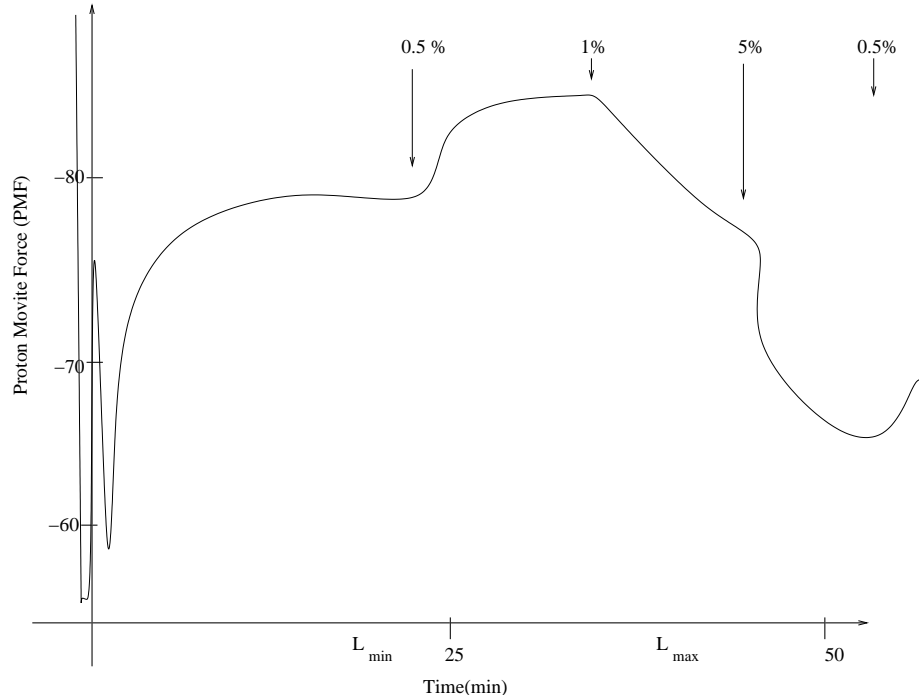


Figure 2.10: The figure shows the proton motive force (PMF) versus the oxygen concentration. The highest proton motive force is observed between L_{min} and L_{max} . PMF is increasing between \tilde{L}_{min} and L_{min} and decreases between L_{max} and \tilde{L}_{max} . (Figure based on Zhulin, [78].)

is the negative temporal gradient of the PMF. Positive temporal gradients and the high constant value of PMF suppresses tumbling. Cells are able to detect temporal gradients of PMF by swimming through a spatial gradient of oxygen (which is linearly proportional to time). The biological justification for such turning rates is given in Appendix A. Further details on a model of a receptor producing such turning rates are also included.

The easiest way to construct such turning rates is by defining piecewise linear functions as is shown in the above figure (Fig. 2.9). We express the turning rates of the left-turning bacteria and the turning rate of the right-turning bacteria separately, so now the two rates only depend explicitly on the ligand concentration, and their dependence on the oxygen gradient is implicit. (If a general turning rate was given for

all bacteria, this rate would explicitly depend on the gradient of oxygen.) This simple choice for the turning frequencies makes the system of equations almost linear, with the only non-linearity resulting from the dependence of turning rates on the ligand gradient. Now we can explicitly write down the turning rates.

$$f_{rl} = \begin{cases} C, & L < \tilde{L}_{min} \\ c, & \tilde{L}_{min} < L < L_{min} \\ c, & L_{min} < L < L_{max} \\ C, & L_{max} < L < \tilde{L}_{max} \\ C, & \tilde{L}_{max} < L \end{cases} \quad (2.17)$$

$$f_{lr} = \begin{cases} C, & L < \tilde{L}_{min} \\ C, & \tilde{L}_{min} < L < L_{min} \\ c, & L_{min} < L < L_{max} \\ c, & L_{max} < L < \tilde{L}_{max} \\ C, & \tilde{L}_{max} < L \end{cases} \quad (2.18)$$

In all the above equations C is some larger turning rate than c . The exact value of C and c will be specified later. Now with equations (2.14), (2.15), (2.16), (2.17) and (2.18), we have the complete system of equations describing bacterial swimming.

2.3.3 Non-dimensionalization and scaling

We have the full system of equations for the aerotaxis experiments including turning rates and boundary conditions.

$$\begin{aligned} \frac{\partial r}{\partial t} &= \frac{\partial(-vr)}{\partial x} - f_{rl}r + f_{lr}l \\ \frac{\partial l}{\partial t} &= \frac{\partial(vl)}{\partial x} + f_{rl}r - f_{lr}l \\ \frac{\partial L}{\partial t} &= D \frac{\partial^2 L}{\partial x^2} - k(r+l) \end{aligned}$$

$$f_{rl} = \begin{cases} C, & L < \tilde{L}_{min} \\ c, & \tilde{L}_{min} < L < L_{min} \\ c, & L_{min} < L < L_{max} \\ C, & L_{max} < L < \tilde{L}_{max} \\ C, & \tilde{L}_{max} < L \end{cases}$$

$$f_{lr} = \begin{cases} C, & L < \tilde{L}_{min} \\ C, & \tilde{L}_{min} < L < L_{min} \\ c, & L_{min} < L < L_{max} \\ c, & L_{max} < L < \tilde{L}_{max} \\ C, & \tilde{L}_{max} < L \end{cases}$$

$$r(0) = l(0)$$

$$r(a) = l(a)$$

Before the system can be analyzed, it is important to non-dimensionalize all variables.

The following parameters are important:

Size of capillary tube: 50x2x0.1 mm

Preferred $[O_2]$: 0.3-0.5 percent

Band width: 0.2 mm

Distance of band from capillary tube end: 1.6 mm

Time of band formation: 50 sec - 3 min

$[O_2]$ outside the capillary tube: 21 percent

Speed: $40 \frac{\mu m}{sec}$

Diffusion coefficient: $2 \cdot 10^{-9} \frac{m^2}{sec}$

Turning frequency: $1 sec^{-1}$

Rate of oxygen consumption: $3 \cdot 10^{-11} \frac{\mu M}{(cell)(sec)}$

The appropriate spatial scale can be found by estimating the distance which would allow the bacteria to outrun the invasion of the oxygen. The diffusion of oxygen implies that $x \sim \sqrt{Dt}$, whereas the distance for the escape of bacteria is $x \sim vt$. From these two expressions we can approximate the time for the cells to outrun diffusion, it is $t_0 \sim \frac{v}{D} \approx 5$ sec, which means that $x_0 \sim vt_0 \approx 100 \mu m$. This suggests that the time scale should be on the order of about 10 seconds (which agrees with the experiments where the band develops between 50 seconds and 3 minutes). For the spatial scale, we choose 2 mm, since this is the length of the region where the bacteria are found, but from the scaling argument it is clear that the resolution must be smaller than $100 \mu m$. Based on this we arrive at the characteristic scales summarized in Table 2.2.

Measurement	One unit
Length	2 mm
Time	10 sec
Oxygen concentration	$1 \frac{\mu M}{ml}$
Bacterial concentration	$2 \cdot 10^7 \frac{cells}{ml}$

Table 2.2: Table gives the units of measurement for length, time, oxygen concentration and bacterial concentration.

Measurement	Dimensional quantity	Non-dimensional value
Speed	$40 \frac{\mu m}{sec}$	0.2
Diffusion coefficient	$2 \cdot 10^{-9} \frac{m^2}{sec}$	0.01
Turning frequency	$1 sec^{-1}$	10
Rate of oxygen consumption	$3 \cdot 10^{-11} \frac{\mu M}{(cell)(sec)}$	$4 \cdot 10^{-3}$

Table 2.3: Non-dimensional parameter values.

These scales give us the non-dimensionalized values for our parameters, shown in Table 2.3.

Values for \tilde{L}_{min} and \tilde{L}_{max} are not readily measured experimentally, so several different

parameter values were used in the simulations. The non-dimensionalization gives the following differential equations:

$$\begin{aligned}\frac{\partial r}{\partial t} &= \frac{\partial(-r)}{\partial x} - f_{rl}r + f_{lr}l \\ \frac{\partial l}{\partial t} &= \frac{\partial(l)}{\partial x} + f_{rl}r - f_{lr}l \\ \frac{\partial L}{\partial t} &= \frac{\partial^2 L}{\partial x^2} - \kappa(r + l)\end{aligned}$$

$$f_{rl} = \begin{cases} C', & L < \tilde{L}_{min} \\ c', & \tilde{L}_{min} < L < L_{min} \\ c', & L_{min} < L < L_{max} \\ C', & L_{max} < L < \tilde{L}_{max} \\ c', & \tilde{L}_{max} < L \end{cases}$$

$$f_{lr} = \begin{cases} C', & L < \tilde{L}_{min} \\ c', & \tilde{L}_{min} < L < L_{min} \\ c', & L_{min} < L < L_{max} \\ c', & L_{max} < L < \tilde{L}_{max} \\ C', & \tilde{L}_{max} < L \end{cases}$$

$$\begin{aligned}r(0) &= l(0) \\ r(1) &= l(1)\end{aligned}$$

Here, $\kappa = \frac{kt_0b_0}{L_0}$ where k is the rate of oxygen consumption by bacteria, t_0 is the time scale, b_0 and L_0 are the scales of the original bacterial and oxygen concentrations, respectively. The non-dimensional values for the turning rates, C' and c' are given by $C' = Ct_0$, and $c' = ct_0$.

2.4 Results

2.4.1 Numerical simulations

This chapter describes the main results of the model. The most important result is the series of computer simulations showing the band development as it is observed in the actual experiments.

Analytical solutions for the steady state are possible, but numerical results are given to see the time evolution of the solutions. In order to have numerical stability, the equations describing the left-moving bacteria were solved with a forward-differencing scheme, the equations for the right-moving bacteria with a backward-differencing scheme. The diffusion equation for the oxygen was discretized with a forward-time, centered space (FTCS) scheme. The boundary condition at the right is that all right-moving bacteria become left-moving, and at the left boundary all the left-moving bacteria become right-moving. The domain was discretized by 40 grid points, representing the full length of the capillary, 2 mm. The number of grid points was chosen to be 40 so the developing aerotactic band would have sufficient resolution. The size of the time step, $\Delta t = 0.01$ was chosen such that the solution to the diffusion equation would be stable. The initial conditions in all simulations were that the bacterial density (both left- and right-moving) is a constant, scaled to 1. The initial oxygen concentration is also scaled.

2.4.2 Numerical results

In the following figures, one can follow the development of the aerotactic band.

In the figures one can follow the development of the aerotactic band. Initially, (Figure 2.11) the bacterial density is uniform everywhere. The oxygen concentration is a constant at the first grid point, and zero on all other gridpoints. The apparent gradient of oxygen is due to the software package, Matlab connecting the first and

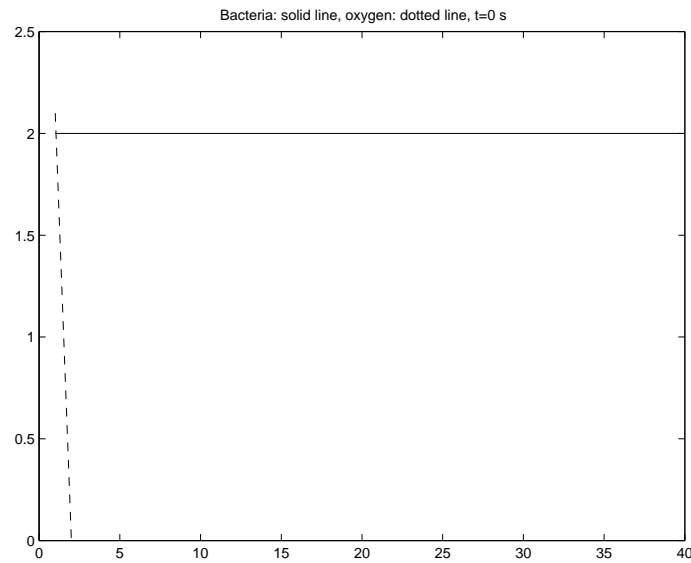


Figure 2.11: Initial condition. Before the aerotactic band forms, the bacterial density is uniform. (Bacterial density is given by solid line.) Oxygen is zero everywhere, except at the left boundary. (Oxygen concentration is given by dashed line.)

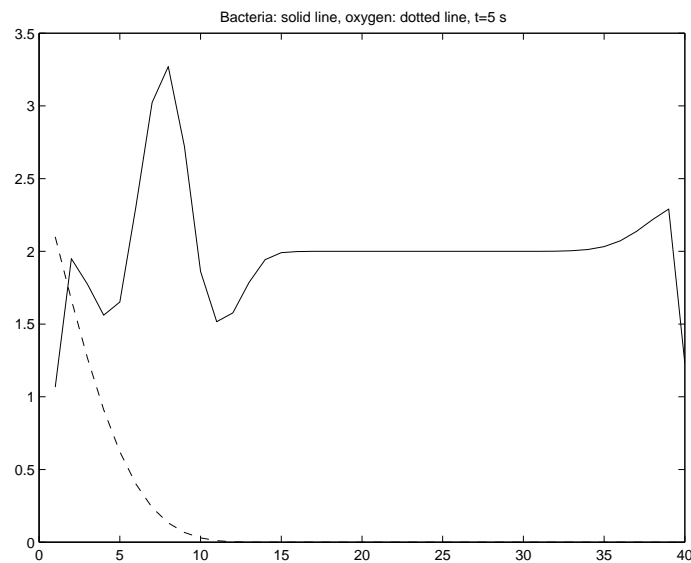


Figure 2.12: Bacteria beginning to aggregate at the favorable oxygen concentration. Sharp oxygen gradient is developing.

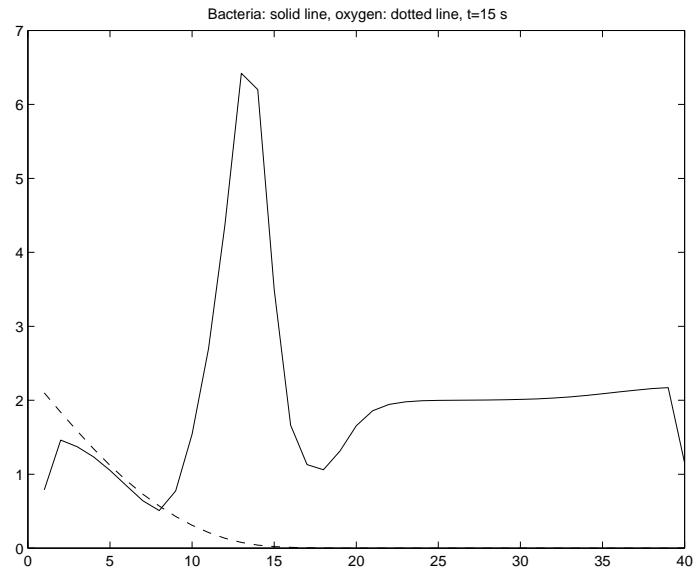


Figure 2.13: After 15 seconds the band is clearly visible. Bacterial density in front of the band still changing.

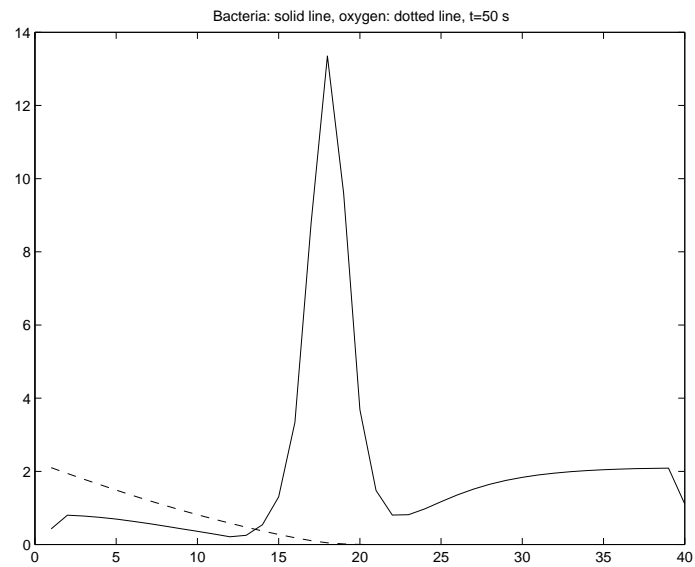


Figure 2.14: Aerotactic band after 50 seconds.

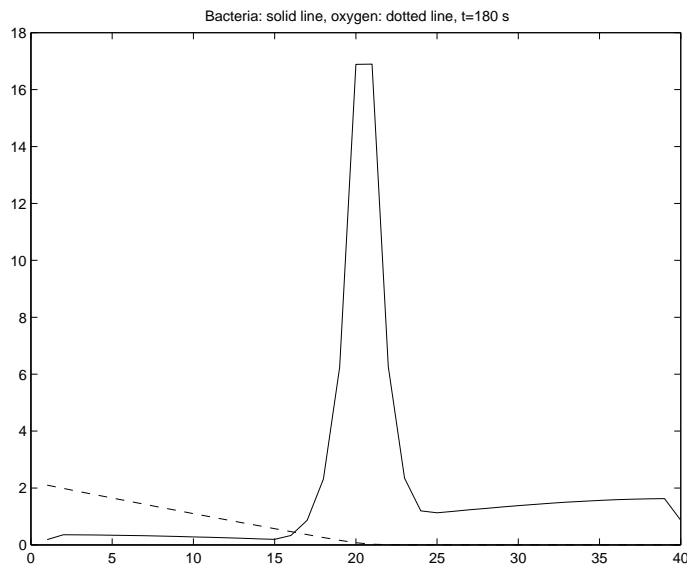


Figure 2.15: Quasi steady state of bacterial band. Ratio of bacterial densities in front of the band and inside the band agree with experimental measurements.

second gridpoints. After 5 seconds, in Figure 2.12, the cells at the open end of the capillary that are exposed to high levels of oxygen concentration start swimming toward the lower, optimal oxygen concentrations. Meanwhile, some of the bacteria at the back that are close enough to the oxygen are also able to detect the optimal oxygen range, and the aggregation begins from both sides. Oxygen also begins to diffuse through the solution, and a sharp gradient evolves.

In the figure which shows the aerotactic band after 15 seconds (Figure 2.13), it is clear that most cells from the open end of the capillary have already aggregated to the band. There is low bacterial density on either side of the band, because all cells at these positions are able to swim into the optimal range. Cells at the back of the band never sense the oxygen, and the bacterial density here remains practically unchanged. Once the band reaches its steady state (after 3 minutes), it is clear that almost all bacteria from the front have aggregated to the band, (Figure 2.15). The ratio of the cell density inside the band to the front of the band is more than a 100, and the

density inside the band to behind the band is about 10. Both of these values agree with the experimental data. The time scale of the band formation, the width of the band and the distance of the band from the meniscus also give good agreement with the experimental measurements. The total bacterial density is conserved in all the simulations. $\tilde{L}_{min} = 0.2$ and $\tilde{L}_{max} = 0.7$ were used in the numerical computations.

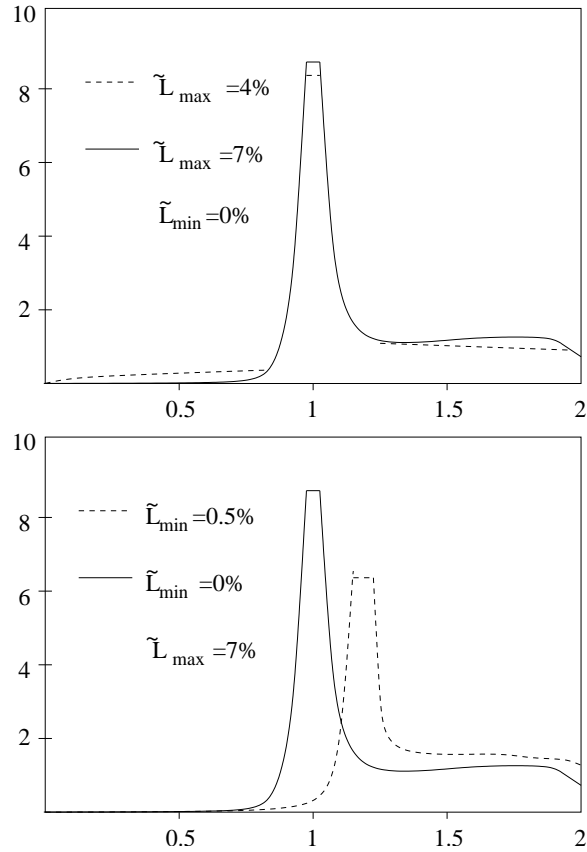


Figure 2.16: The top figure shows how the final bacterial band changes as \tilde{L}_{max} is changed. The bottom figure shows the numerical simulations with \tilde{L}_{max} fixed, and \tilde{L}_{min} changing.

The simulations can also help to determine the optimal values of \tilde{L}_{max} and \tilde{L}_{min} . (Figure 2.16) This is useful, because these parameters are difficult to measure experimentally. By increasing the value of \tilde{L}_{max} , the bacterial density inside the band increases too, and the aggregation from the front of the band is more complete. This happens because a larger \tilde{L}_{max} effectively increases the region in which cells are

in favorable conditions. The cells do not have to swim very far from the meniscus to be able to sense the favorable oxygen concentration, thus more of them get trapped in the optimal zone.

Lowering the value of \tilde{L}_{min} has a similar effect. The bacterial density is higher for low values of \tilde{L}_{min} , and the aggregation from the back of the band is more complete in this case. As before, this happens because cells now get inside the band by detecting lower oxygen concentrations. For a higher value of \tilde{L}_{min} , sensing the same oxygen concentration would act as a repellent, where in this case (for the low value) it becomes an attractant. This change in \tilde{L}_{min} also results in the main bacterial density shifting toward lower oxygen concentration.

2.4.3 Analytical results

Here we obtain analytically explicit expressions for asymptotically stable stationary distributions of bacteria and oxygen. These distributions are possible to find because the nonlinear equations (2.14, 2.15, 2.16, 2.17, 2.18) of the energy taxis model are piece-wise linear. In the steady state, the system of differential equations can be solved on intervals and replaced with algebraic equations. We solve the equations in two different cases.

In the first case, we look at the fully developed band, after all the bacteria have aggregated here. (An estimate below shows approximately how much time must pass for this case to be valid.) In this case we can look at three regions, and solve the system of ordinary differential equations in these regions, using continuity and conservation arguments to match the solutions at the boundaries. In the general case, we assume that $L_{max} < L_0$ for the outside oxygen concentration, L_0 , and $L_{min} = 0$. In the next section, (“Special steady state solutions”) we discuss situations in which the above conditions do not hold. We provide solutions for $L_{min} < L_0 < L_{max}$ and $L_{min} < L_0$.

In the second case, we look at what happens if we only wait 3 minutes (in other words, wait just enough time for the bacteria to develop the band.) In this case, it is possible to show that the bacteria behind the band have not had sufficient time to feel the effect of the oxygen gradient; therefore, we can assume that the bacterial concentration there does not change at all. This allows us to solve the equations in two regions only, because the region behind the band does not need to be considered. The second case is discussed in the section “Quasi steady state solutions”.

Steady state solutions

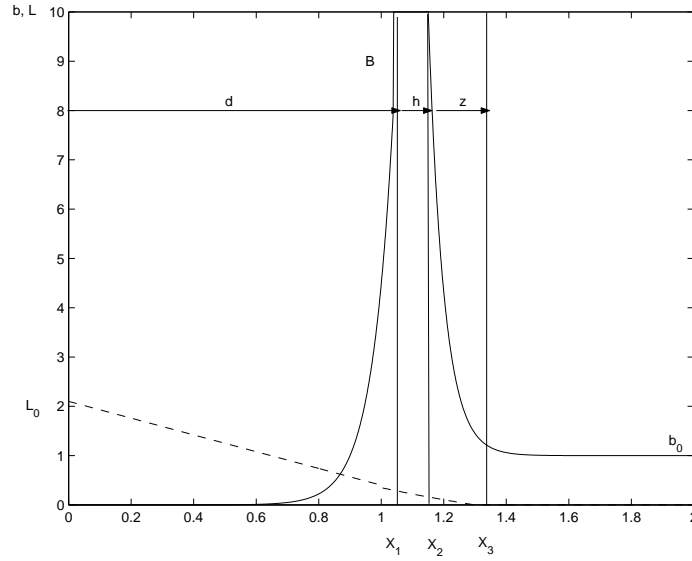


Figure 2.17: Steady state distribution of the oxygen concentration and the bacterial density for the case when $L_0 > L_{max} > L_{min}$.

Let us now first consider the steady state solution when $L_{max} < L_0$ and $L_{min} = 0$. There are three regions in this case: region I, in front of the band, from $x_0 = 0$ to $x_1 = d$; region II, inside the band, from $x_1 = d$ to $x_2 = d + h$; and region III, behind the band, from $x_2 = d + h$ to $x_3 = d + h + z$. Figure 2.17 illustrates this scenario.

Let $b(x)$ and $L(x)$ be stationary linear densities of cells and oxygen, respectively,

where the x -axis has its origin at the meniscus and is directed inside the capillary. Let the oxygen concentration reach values L_{min} and L_{max} at distances x_1 and x_2 from the meniscus, respectively. Let $s = v/(f_{rl} - f_{lr}) \simeq 100\mu m$, $k = \kappa/D$. We use s as our length scale.

In region I the bacterial density does not change with respect to time and is therefore given by:

$$-vr' - f_{rl}r + f_{lr}l = 0, \quad vl' + f_{rl}r - f_{lr}l = 0.$$

By noting that the steady state densities of left- and right-moving bacteria are the same and adding the two equations, we obtain:

$$r = l \sim e^{x/s}.$$

Let B be the density of bacteria inside the band and d be the distance of the band from the open end of the capillary. Then,

$$b = Be^{(x-d)/s}$$

The equation for oxygen in this region is:

$$L'' = kb = kB e^{(x-d)/s}$$

Here we can use the fact that the oxygen concentration outside the capillary is L_0 , we integrate to find the oxygen concentration in this region, L_I :

$$L_I(x) = L_0 - c_1x + kB s^2 [e^{(x-d)/s} - e^{-d/s}].$$

In region II we can write the same expression for the bacterial density as the expression in region I:

$$-vr' - f_{rl}r + f_{lr}l = 0, \quad vl' + f_{rl}r - f_{lr}l = 0.$$

We note that the bacterial density in this region is a constant; therefore, we have:

$$r = l = B/2; \quad b = B.$$

The equation for oxygen in this region is given by:

$$L'' = kB$$

We integrate this expression and use the information that at one edge of the band the oxygen concentration is L_{max} and the fact that the band is d distance away from the meniscus to find:

$$L_{II}(x) = L_{max} - c_2(x - d) + \frac{1}{2}kB(x - d)^2.$$

In region III:

$$-vr' - f_{rl}r + f_{lr}l = 0, \quad vl' + f_{rl}r - f_{lr}l = 0; \quad r = l \sim e^{-x/s}.$$

Then, we use the continuity of the bacterial density at the boundary of the band, x_2 to write down the equation for the density in this region:

$$b = Be^{(x_2-x)/s}.$$

For oxygen we substitute this expression into the bacterial density:

$$L'' = kb = kB e^{(x_2-x)/s}$$

To find the equation for oxygen we integrate, and use the fact that the oxygen concentration at $x_2 = d + h$ is L_{min} :

$$L_{III}(x) = L_{min} - c_3(x - d - h) + kB s^2 [e^{(d+h-x)/s} - 1].$$

Here we have 7 unknown parameters: $B, c_1, c_2, c_3, d, h, z$. To find them we use the following boundary conditions:

- 1) Continuity of bacterial density at $x = x_3$: $Be^{((d+h)-(d+h+z))/s} = e^{(-z/s)} = b_0$.
- 2) No oxygen behind $x = x_3$ (which provides constant bacterial density there): $L(d + h + z) = 0$.

3) No flux of oxygen to $x > x_3$: $L'(x_3) = 0$.

4-5) Continuity of oxygen at the boundaries between the zones: $L_I(x_1) = L_{max}$ and $L_{II}(x_2) = L_{min}$.

6-7) Continuity of flux of oxygen at the boundaries between the zones: $L'_I(x_1) = L'_{II}(x_1)$ and $L'_{II}(x_2) = L'_{III}(x_2)$.

These conditions lead to the following system of algebraic equations using the notation $\lambda = e^{z/s}$: (Note: Throughout the following calculations, we will use $k = 0.003$, $b_0 = 2$, $L_{min} = 0.003$, $L_{max} = 0.005$, $s = 1$.)

$$B = b_0\lambda \quad (2.19)$$

$$L_{min} - c_3z + kB s^2[\lambda^{-1} - 1] = 0 \quad (2.20)$$

$$-c_3 + kB s \lambda^{-1} = 0 \quad (2.21)$$

$$L_0 - c_1d + kB s^2[1 - e^{-d/s}] = L_{max} \quad (2.22)$$

$$L_{max} - c_2h + \frac{1}{2}kB h^2 = L_{min} \quad (2.23)$$

$$-c_1 + kB s = -c_2 \quad (2.24)$$

$$-c_2 + kB h = -c_3 + kB s \quad (2.25)$$

From (2.21) and using (2.19): $c_3 = kb_0s$. From (2.24, 2.25):

$$c_1 = kb_0(s + h\lambda), \quad c_2 = kb_0(s + h\lambda - s\lambda).$$

We can find analytic approximations for z , d and h . We start by approximating z . Substituting c_1, c_2, c_3 as functions of z, h into (2.20), we find:

$$z/s = (L_{min} + kb_0s^2(1 - e^{z/s})) / (kb_0s^2)$$

Let $\alpha = \frac{L_{min}}{kb_0s^2} + 1$, and $\zeta = z/s$. Then we can rewrite the expression for z/s as follows:

$$\alpha - \zeta = e^{-\zeta}$$

Approximating this expression we find that

$$z \simeq \alpha s$$

(The approximation can be obtained as follows: We assume that $e^{-\zeta} \ll 1$. Then we can express ζ in the form $\zeta = \alpha - \epsilon$, where ϵ is a small parameter. This parameter can be found from: $\epsilon = e^{-\alpha+\epsilon}$. In the zeroth approximation $\epsilon \simeq e^{-\alpha}$. Thus, $z \simeq \alpha s$.) Numerically, $z \simeq 1.5$ and $e^{-\zeta} \simeq 0.2231$ which verifies the original assumption of $e^{-\zeta} \ll 1$.

Next, to find h we use (2.23) to obtain the expression:

$$(h/s)^2 - 2\frac{\lambda-1}{\lambda}(h/s) - \frac{2(L_{max}-L_{min})}{kb_0s^2\lambda} = 0$$

From above, $\lambda = e^{z/s} \simeq 4.4817$, so we have $\frac{\lambda-1}{\lambda} \sim 1$. Let $y = (h/s)$, $u = \frac{2(L_{max}-L_{min})}{kb_0s^2\lambda} \simeq 0.1488$. Then, from the equation

$$y^2 - 2y - u = 0$$

using the smallness of u in comparison with 1 we arrive at two roots, $y_1 \simeq \frac{u}{2}$, $y_2 \simeq 2 - \frac{u}{2}$. Only the second root corresponds to a biologically meaningful situation, since the width of the bacterial band must be of the same order as the length of the straight runs. Choosing the first solution would predict the band width to be much narrower; therefore, the bacteria would always have to swim across the band without turning. If we substitute y_2 into the expression for h , then we get, in terms of the original variables, $h = s(2 - \frac{(L_{max}-L_{min})}{kb_0s^2\lambda}) \simeq 1.8512$

Finally, we approximate d/s . From (2.22):

$$e^{-d/s} + (d/s)\frac{c_1}{kb_0\lambda s} = \frac{L_0 - L_{max}}{kb_0\lambda s^2} + 1$$

Since the value of d is expected to be large in comparison with s , we can approximate the above expression by letting $e^{-d/s} \simeq 0$. We obtain:

$$d/s = \frac{\frac{L_0 - L_{max}}{kb_0s^2} + \lambda}{1 + \lambda h/s} \simeq \frac{\frac{L_0}{kb_0s^2} + \lambda}{\lambda h/s} = \frac{\frac{L_0}{kb_0s^2\lambda} + 1}{h/s}$$

We have $\frac{L_0}{kb_0s^2\lambda} + 1 \simeq 8.4377 \gg 1$ Then, using $h \simeq 2s, d = 4.2188$. This also verifies the assumption that $e^{-d/s} \simeq 0$.

In summary, we get the following values:

- $h \simeq 2s \simeq 185\mu m$
- $z \simeq (1 + \frac{L_{min}}{kb_0s^2})s \simeq 150\mu m$
- $d \simeq \frac{L_0}{2kb_0s\lambda}s \simeq 370-1860\mu m$ using the values $L_0 = 0.2$ and $L_0 = 1.00$, respectively

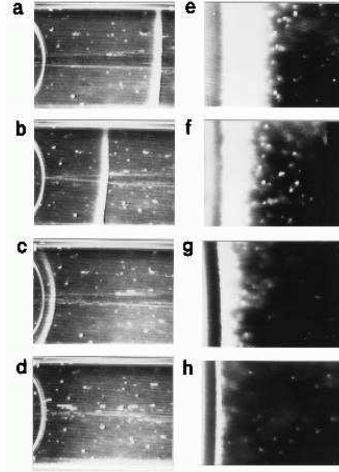


Figure 2.18: Spatial assays for different oxygen concentrations. A, 100 percent. B, 21 percent. The width of the band is independent of L_0 . The distance between the meniscus and the band increases with increasing L_0 . (Figure from Zhulin, [78])

Conclusion:

- (1) Because of the absence of detailed measurements of bacterial density profile, we do not have data on z .
- (2) The band's width, h , is close to $200\mu m$, exactly as predicted by our theory if the favorable value for velocity is chosen.
- (3) The band was observed to form 400 to $900\mu m$ from the meniscus corresponding to 20 percent to 100 percent oxygen concentrations, which is in agreement with our

rough estimate of 370 to 1860 μm

(4) According to the estimate, d is proportional to L_0 . In the experiment, d was observed to grow at greater values of L_0 . Thus, we capture the qualitative dependence of d on L_0 .

(5) h does not depend on L_0 .

Both conclusions (4) and (5) are in agreement with Figure 2.18 from Zhulins's paper, [78].

Special steady state solutions

As discussed above, in this section we look at special cases of the steady state solution where the assumption that $L_0 > L_{max} > L_{min}$ no longer holds. This section extends the analytical results to two other cases, namely to the case where $L_{min} < L_0 < L_{max}$ and when $L_0 < L_{min}$.

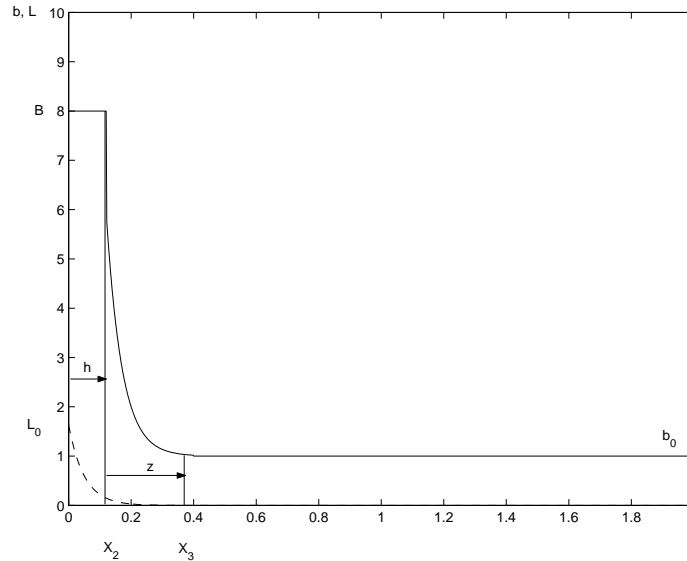


Figure 2.19: Special steady state distribution of the oxygen concentration and the bacterial density for the case when $L_0 < L_{max}$.

First case: L_0 falls between L_{min} and L_{max} , as shown in Figure 2.19. In this case we

expect to find two regions only. In region I, the band is from $x_1 = 0$ to $x_2 = h$, and region II, from $x_2 = h$ to $x_3 = h + z$, is behind the band.

In region I the equation for the bacterial density is a constant; therefore, it is given by:

$$-vr' - f_{rl}r + f_{lr}l = 0, \quad vl' + f_{rl}r - f_{lr}l = 0; \quad r = l = B/2$$

Here B is density of bacteria inside the band. The equation for oxygen in this region, using $L(0) = L_0$, and substituting the above expression for the bacterial density:

$$L'' = kb = kB/2, \quad L_I(x) = L_0 + c_1x + 1/2kBx^2$$

The other boundary condition, $L(h) = L_{min}$ helps to determine c_1 :

$$L_I = L_0 + \left(\frac{L_{min} - L_0}{h} - \frac{1}{2}kBh\right)x + \frac{1}{2}kBx^2$$

In region II we have the following equations. For the bacterial density we have exponential decay:

$$-vr' - f_{rl}r + f_{lr}l = 0, \quad vl' + f_{rl}r - f_{lr}l = 0; \quad r = l \sim e^{-x/s}.$$

Then, using the continuity of the bacterial density at $x_2 = h$ we get:

$$b = Be^{(h-x)/s}$$

For oxygen we have the following equations:

$$L'' = kb = kB e^{(h-x)/s}.$$

By integrating the equation twice, we have:

$$L_{II}(x) = kB s^2 e^{(h-x)/s} + c_2(x - h) + c_3$$

Using $L(h) = L_{min}$, $L(h + z) = 0$ we get

$$L_{II}(x) = kB s^2 [e^{(h-x)/s} + \frac{kBs^2(1 - e^{-z/s}) - L_{min}}{z}(x - h) + L_{min} - kB s^2]$$

To find B, h, z we need the following conditions:

(1) Continuity of bacterial density at $x = x_3$.

(2-3) Continuity of flux at the boundaries of the regions.

$$L'_I(x_2) = L'_{II}(x_2), L'_{II}(x_3) = 0$$

$$B = b_0 e^{z/s} \quad (2.26)$$

$$\frac{L_{min} - L_0}{h} + \frac{1}{2}kBh = -kBs + \frac{kBs^2(1 - e^{-z/s}) - L_{min}}{z} \quad (2.27)$$

$$-ksBe^{-z/s} + \frac{kBs^2(1 - e^{-z/s}) - L_{min}}{z} = 0 \quad (2.28)$$

Substituting the expression for B into (2.28) we get:

$$-kb_0s + \frac{kb_0s^2e^{z/s} - kb_0s^2 - L_{min}}{z} = 0$$

Simplifying this equation we arrive at:

$$e^{z/s} - \frac{z}{s} - 1 - \frac{L_{min}}{kb_0s^2} = 0$$

Recalling that $\alpha = 1 + \frac{L_{min}}{kb_0s^2}$ and $\zeta = z/s$ we can simplify the above expression to:

$$e^\zeta - \zeta - \alpha = 0$$

An analytical approximation of ζ is difficult to achieve, since all the terms of the equation are expected to be of the same order of magnitude. Based on a numerical estimate, $\zeta = 0.85$. This, indeed, verifies that all terms of the above equation are of order 1. In terms of the original variables we get $z \simeq 0.85s \simeq 85\mu m$

We can also substitute the expression for B into (2.27), and we get:

$$\frac{L_{min} - L_0}{h} + \frac{1}{2}kb_0e^{z/s}h = -kb_0e^{z/s}s + \frac{kb_0s^2e^{z/s} - kb_0s^2 - L_{min}}{z}$$

This gives us a quadratic equation in h which can be written in a simplified form by introducing $\beta = kb_0e^{z/s}$.

$$h^2 + 2\left(s + \frac{L_{min} + kb_0}{z\beta} - \frac{s^2}{z}\right)h + \frac{L_{min} - L_0}{\beta} = 0$$

We know the numerical values of all terms in the equation, so we can estimate h .

Conclusions:

- (1) As before, experimental data does not exist for z .
- (2) Values of h can be estimated for various values of L_0 . (For example, for $L_0 = 0.35$ percent, $h \approx 35\mu m$.) In our estimates there is a dependence of h on $L_{min} - L_0$ which could be tested by running experiments with various species that have different preferences for L_{min} , the minimum tolerable oxygen concentration.

Second case: L_0 falls under L_{min} . We expect that there is no bacterial band developing in this scenario since the outside oxygen concentration, L_0 , is below the minimum preferred concentration. There is only one region in this case, region I, from $x = 0$ to $x = z$.

In region I the equation for the bacterial density is:

$$-vr' - f_{rl}r + f_{lr}l = 0, \quad vl' + f_{rl}r - f_{lr}l = 0; \quad r = l \sim e^{-x/s}$$

B is density of bacteria at the boundary. $b = Be^{-x/s}$. The equation for oxygen is given by:

$$L'' = kb = kB e^{-x/s} \quad L_I(x) = kB s^2 e^{-x/s} + c_1 x + c_2$$

We use that the oxygen concentration outside the capillary is L_0 : $L(0) = L_0$.

$$L_I(x) = kB s^2 e^{-x/s} + c_1 x + L_0 - kB s^2$$

To find B , c_1 and z we need the following conditions:

- (1) Continuity of bacterial density at z : $Be^{-z/s} = b_0$

(2) Continuity of flux of oxygen at $x = z$:

$$kBs e^{-z/s} + (kBs^2)/z(e^{-z/s} - 1) + L_0/z = 0$$

(3) Boundary condition at $x = z$: $L_I(z) = 0$

By making the appropriate substitutions we arrive at:

$$kb_0sz + kb_0s^2(1 - e^{z/s}) = L_0$$

Again, recalling $\zeta = z/s$, a simple form of the expression is

$$e^\zeta - \zeta = 1 - \frac{L_0}{kb_0s^2}$$

Here we must use a numerical estimate as well, since we again expect the terms to be the same order of magnitude.

Conclusion:

(1) A numerical estimate for z is possible, but, as mentioned above, it cannot be compared to experimental values.

This concludes the steady state solutions. Now we can examine how the solution behaves on the time scale over which the band develops.

Quasi steady state solutions

In the previous section we provided an analytical solution for the steady state in three different regions: in front of, inside, and behind the band. In this section we obtain an analytical solution for the time interval 50 seconds to 3 minutes, during which the bacterial band forms, shown on Figure 2.20. We cannot obtain transient solutions for our system, but we know that the steady state solutions will be valid only after a very long time period (hours). On the other hand, the experimental observations are for a much shorter time scale, on the order of minutes, so we would like to find the quasi steady state solutions for this time period. We will show below that during

this time period only the bacteria in front of the band have time to move inside the band, so in fact, we only have two regions: one in front of the band and one inside the band. We check our heuristic analytical results against the experimental findings.

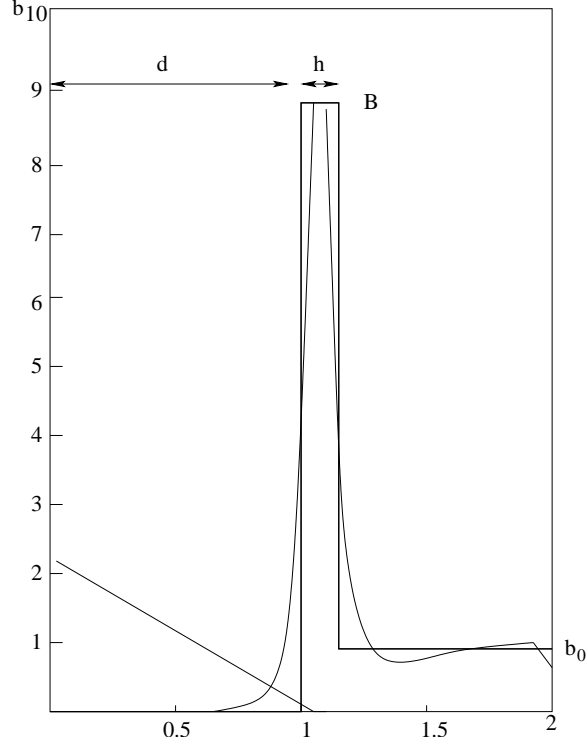


Figure 2.20: Quasi steady state solution of the bacterial density.

In order to demonstrate that only the bacteria in front of the band are involved in the band formation, we must estimate the time for the cells from behind the band to move into the band by pure diffusion in the absence of oxygen. The diffusion coefficient is given by: $D \sim \frac{v^2}{f} \simeq \frac{(20\mu\text{m})^2}{0.5\text{s}^{-1}} \simeq 8 \cdot 10^2 \frac{\mu\text{m}^2}{\text{s}} \simeq 8 \cdot 10^{-4} \frac{\text{mm}^2}{\text{s}}$. Now we can estimate the time of diffusion, $t \sim \frac{L^2}{D} \simeq \frac{(1.5\text{mm})^2}{8 \cdot 10^{-4} \text{mm}^2/\text{s}} \simeq 2.8 \cdot 10^3 \text{s} \simeq 47 \text{min}$. This confirms that if we only want to look at the time interval up to 3 minutes, we only need to consider two regions, region I, from $x_0 = 0$ to $x_1 = d$, which is in front of the band, and region II, from $x_1 = d$ to $x_2 = d + h$, inside the band.

Region I:

The equation for oxygen in this region is:

$$D \frac{d^2 L}{dx^2} = 0$$

with boundary conditions:

$$L(0) = L_0 \tag{2.29}$$

$$L(d) = L_{max} \tag{2.30}$$

Using (2.29) we arrive at the equation for the oxygen in region I:

$$L(x) = L_0 - c_1 x$$

We assume that there are no bacteria in this region because they have all aggregated to the band.

Region II:

The equation for oxygen in this region is:

$$D \frac{d^2 L}{dx^2} = \chi B$$

With boundary conditions:

$$L(d) = L_{max} \tag{2.31}$$

$$L(d + h) = 0 \tag{2.32}$$

Using (2.31) the equation for oxygen in this region is

$$L = L_{max} - c_1(x - d) + \frac{\chi B}{2D}(x - d)^2$$

The number of bacteria in the band is constant, $b = B$.

We are trying to find four parameters, c_1 , d , h and B .

$$c_1 = \frac{L_0 - L_{max}}{d} \quad (2.33)$$

$$L_{max} - c_1 h + \frac{\chi B}{2D} h^2 = 0 \quad (2.34)$$

$$L'_I(d) = L'_{II}(d) \quad (2.35)$$

$$L'_{II}(d+h) = 0 \quad (2.36)$$

$$Bh = b_0(d+h) \quad (2.37)$$

We obtained (2.33) using (2.30), and (2.34) from (2.32). In (2.35) the conservation of flux at the left edge of the band is a redundant condition, $-c_1 = -c_1 + (d-d)$. The expression (2.36) gives $-c_1 + \frac{\chi B}{2D} h = 0$. Equation (2.37) follows from the conservation of bacteria. Solving (2.33) and (2.36) for c_1 and setting them equal gives $\frac{L_0 - L_{max}}{d} = \frac{\chi B}{2D} h$. We can solve this for d ,

$$d = \frac{D(L_0 - L_{max})}{\chi B h}$$

From (2.34), again using (2.36) we arrive at $L_{max} - \frac{\chi B}{2D} h^2 = 0$ which we can use to obtain

$$h = \sqrt{\frac{2DL_{max}}{\chi B}}$$

From (2.37) we obtain $B = b_0 \frac{d+h}{h}$.

Now we introduce a new variable, $k = \frac{\chi}{D}$. Using the new notation we can rewrite as $d = \frac{(L_0 - L_{max})}{k B h} \simeq \frac{L_0}{k b_0 (d+h)}$. We impose the condition that d , the distance in front of the band must be much larger than the width of the band, $d \gg h$ which implies that $d \simeq \frac{L_0}{k b_0 d}$. This gives

$$d \simeq \sqrt{\frac{L_0}{k b_0}} \simeq 8$$

if $L_0 = 0.2$. If $L_0 = 1$, then $d \simeq 17$.

The expression $d \simeq \frac{L_0}{k b_0 d}$ also can be obtained in a more intuitive way. According to our assumption, the oxygen flux is equal to the oxygen consumed, or: $D \frac{L_0}{d} = \chi B h$.

This implies $\frac{L_0}{d} = \frac{\chi B}{D} h = kBh = kb_0 \frac{d}{h} h$ (by using the expression for the conservation of bacterial cells). From this we arrive at $d \simeq \sqrt{\frac{L_0}{kb_0}}$

Our assumption on d allows us to rewrite $B \simeq b_0 \frac{d}{h}$. Then we can substitute this expression for B into the expression for h we had earlier, $h \simeq \sqrt{\frac{2DL_{max}}{\chi B}} \simeq \sqrt{\frac{2L_{max}}{kb_0 d/h}}$.

Solving this quadratic expression for h we obtain $h \simeq \frac{2DL_{max}}{\chi b_0 d} \simeq \frac{2L_{max}}{kb_0 d} = \frac{2L_{max}}{kb_0} \sqrt{\frac{kb_0}{L_0}}$.

For $L_0 = 0.2$ this gives $h = 0.4$, and for $L_0 = 1$, $h = 0.2$.

Since we have an expression for both d and h in terms of the original variables, we can find c_1 from (2.33) and B from $B \simeq b_0 \frac{d}{h}$

Conclusions:

(1) The distance of the band from the meniscus, d , is given as a function of the outside oxygen concentration, L_0 :

$$d \simeq \frac{L_0}{kb_0 d}$$

This formula provides estimates $d \simeq 0.8$ mm for $L_0 = 0.2$ and $d \simeq 1.7$ mm for $L_0 = 1$.

These values are in agreement with the figures from the Zhulin experiment. (See Figure 2.17)

(2) The band width, h is given as a function of L_0 and L_{max} . More experimental data would be necessary to determine whether the dependence of h on L_{max} is correct.

The two values for the band width, $h = 0.4$ mm and $h = 0.2$ mm for $L_0 = 0.2$ and $L_0 = 1$, respectively, are also in agreement with empirical findings.

2.5 Conclusions

Our main accomplishment is the development of a mathematical model for aerotaxis in a steep attractant gradient for fast-adapting bacterial turning frequencies. As discussed in Section 2.2.4, most of the literature is focused on shallow attractant gradients because this allows approximations and the use of the Keller-Segel-type chemotaxis equations (2.1). As we note, the only possible approach to steep gradients and slow adaptation is Monte-Carlo simulations.

The significance of our model for biologists is its prediction of the appropriate pattern formation by assuming novel receptor mechanics and fast adaptation, while the same patterns are impossible to obtain by models of conventional chemotaxis. This indicates that aerotaxis (and probably other forms of energy taxis) uses a distinct biochemical mechanism to achieve motility. The separation of biochemical pathways supports the notion [73] that energy taxis is a “flight response” which can overrule chemotactic behavior thus giving organisms with aerotaxis a selective advantage over purely chemotactic bacteria.

An immediate benefit of our model are its estimates for the maximal and minimal tolerable oxygen concentrations, \tilde{L}_{max} and \tilde{L}_{min} , respectively. The analytical solutions also show dependence of the band width and the distance of the band from the meniscus on other parameters which makes our predictions experimentally testable. A possible limitation of the model is the assumption that adaptation has to be faster than the length of the run. A further question to investigate is the dynamic of the model if the run length and adaptation occur on the same time scale. The option that adaptation is longer than the time scale of the run is ruled out by our Monte-Carlo simulations. Determining whether there is an optimal characteristic adaptation time for given attractant gradients would also be scientifically valuable.

Chapter 3

Growth cone guidance

3.1 Introduction

Sensory input from the environment and responses to such inputs are characteristic of all animal cells. Chemotaxis, the movement along effector gradients toward sources of attractants (e.g. nutrients or certain guidance molecules) or away from chemical repellents, provides an example of such a process. In fact, even bacterial cells are capable of chemotaxis (see Chapter 2), although the mechanism underlying chemotaxis of eukaryotic cells and of bacteria are very different. Bacterial cells, because of their extremely small size, are unable to detect concentration differences across their body. They swim through gradients, and compare concentration differences in time. Animal cells, on the other hand, are thought to genuinely measure concentration differences at different parts of the cell body. Yet another difference is that the signal transduction pathways involved in bacterial chemotaxis of some species (e.g. *E. coli*) are very well known, and accurate mathematical models of bacterial chemotaxis exist as well [4]. Signal transduction pathways involved in chemotaxis of animal cells have not been so completely uncovered, and it is possible that there are significant differences between the pathways as well as in the mechanisms of gradient sensing

between neutrophils, growth cones or slime molds (*Dictyostelium discoideum*).

Understanding gradient sensing is an interesting theoretical question in its own right, even without considering potential biological applications of successful theoretical models. Many different hypotheses can be formulated regarding how concentration differences are compared in a cell. Dallon & Othmer [15] discuss several distinct mechanisms, such as comparing receptor occupancy at different sides of the cell or setting up an internal gradient in response to external gradients. Theoretical models help to distinguish between these, and other possibilities. Many authors [48, 54, 56] also believe that the amplification of the external signal is of key importance in understanding chemotaxis. It is not well understood how a 2-3 % concentration change over its body in a noisy background is sufficient to unambiguously orient a cell in a gradient. While adaptation is known to be an important feature of bacterial chemotaxis, it is unclear whether adaptation occurs in all animal cells.

This work focuses on chemotaxis of growth cones, partially because of the biological significance of the question, and partially because of exciting experimental findings in growth cone chemotaxis discussed in Section 3.2.1. Growth cones are the highly sensitive and extremely dynamic tip of axons. They are finger-like protrusions that are able to detect ligand gradients, and initiate the axon movement in them. Growth cone guidance is most important during development when axons can cover enormous distances to their final place in the nervous system, and also during axon regeneration following injuries. A successful theoretical description of growth cone chemotaxis could lead to very important medical applications. Growth cones are also unique among animal cells, because they can respond to gradients of the same chemical differently, depending on the receptors expressed in the cell, and also, depending on the internal chemical state of the cell. How the internal chemical state might influence growth cone guidance is explained in the experiments with *Xenopus* spinal neurons, described below.

The next section provides the necessary biological background, and explains experimental data relevant to the models formulated later. The second part of the Background, Section 3.2.2 describes previous theoretical models of chemotaxis of eukaryotic cells. Two papers, one by Meinhardt [48], and the other one by Levchenko & Iglesias are in the focus. Next, we formulate two mathematical models of chemotaxis, and provide analysis and numerical results of the models. The results are interpreted, and the we discuss the merits and shortcomings of both models. New experimental data on adaptation of growth cones [66] and the limitations of the two models suggests some directions for further work in this area.

3.2 Background

3.2.1 Biological background

Our project aims to create a mathematical model of early events in growth cone response to extracellular effectors, because these events have a clear significance in axon guidance. During development, axons must find their appropriate targets in the nervous system, and they accomplish this with the help of their growth cones. Growth cones are able to detect spatial ligand gradients, and turn toward the source of the attractant. The axon body follows the guidance of growth cones in this direction. How growth cones are able to 'measure' gradients, even in cases where the concentration differences are very small, is not well understood, and is currently an important research topic.

In spite of extensive research, there are many obstacles in understanding chemotaxis. Gradient sensing involves an enormous number of signaling pathways, and some of the pathways are unique to certain organisms. Many years of research has been devoted to studying *Dictyostelium* cells, for example, while growth cone signaling pathways are a relatively new topic of investigation. The hope is that the underlying principles are the same in all eukaryotic cells, however, important exceptions exist. It is generally accepted [56] that chemotactic cells adapt to persistent stimulus, i.e. certain signaling events occur transiently shortly after the stimulus is changed. This appears necessary in order to explain how cells can orient in a wide range of external stimulus. However, it is not clear whether adaptation occurs in growth cones, as *in vivo* they navigate in attractant concentration gradients that may not span many orders of magnitude. Although this question is not resolved, experts in the field believe growth cones adapt too (Mu-ming Poo, personal communications).

We will focus our attention on growth cone responses in netrin-1 gradients, because netrin-1 is the best characterized molecule which has proven to exert a tropic effect

in vivo. Part of the problem of gradient detection is the determination of the signal transduction events immediately following ligand binding, and the reconstruction of the signal transduction pathway. We focus on the early events, because it is well established that in animal cell chemotaxis sensing and motility are independent processes [56], and we make the assumption that the decision to turn toward or away from a substance is made at an early stage of the pathway. There is also strong evidence suggesting that the decision is made by the time a common second messenger, cAMP is produced. We do not consider events happening downstream from this point, although we recognize that many other downstream events must take place for the actual turning response to be executed.

Song and Poo [66, 67] note that there are two categories of guidance cues, type I and type II. Members of the first group are characterized by the termination of the turning response when extracellular Ca^{2+} is depleted, and by the co-activation of two pathways: the PI-3 kinase and PLC- γ pathways. Whether the turning response is attractive or repulsive, depends on the level of cAMP activity. In contrast, type II. guidance cues are independent of extracellular calcium and PI-3 kinase. The level of cAMP activity does not alter the turning response in guidance molecules of this group. The experiments of the Song, Poo, and Tessier-Lavigne labs [48, 64, 67, 65], demonstrate that turning response of growth cones toward a netrin-1 source strongly depends on internal cAMP levels. Several results [32, 77] indicate the dependence of the turning response on internal calcium dynamics as well, therefore netrin-1 is a type I guidance molecule. Whether the turning response to netrin-1 is attractive or repulsive also depends on the receptor expressed in the cell. DCC is a receptor that leads to attractive turning while UNC-5 leads to repulsion. However, in the same cell the turning response can be altered by changing the cytosolic cAMP concentration. For example, in a neuron expressing DCC receptors attractive turning can be changed to repulsion by lowering cAMP amounts. Some of the experiments

investigating the calcium and cAMP dependence of the response are described in further detail, because we hypothesize that understanding calcium and cAMP dynamics leads to understanding how attractive or repulsive turning decision is made in growth cones. Additional information is provided about signal transduction components, in particular, about the interaction of the calcium and cAMP pathways.

A number of experiments were performed whose results provide constraints for a model of how ligand binding leads to a turning response. The basic idea, that high concentrations of cytosolic cAMP correspond to attractive turning, and low concentrations to repulsive turning, has been widely accepted, and is reviewed by Song and Poo, [67]. This relationship is clearly demonstrated by the experiments of Ming et al. on *Xenopus* spinal neurons [48] which show that attraction to a netrin-1 gradient can be abolished by bath addition of Rp-cAMP, an antagonist of cAMP which causes lowered cAMP levels in the cell. Figure 3.1. provides information on the relevant parts of the signal transduction pathway.

Song and Poo also note [67] that for each guidance cue, there is a characteristic range of cAMP which determines whether attractive or repulsive turning is exhibited. When cAMP activity falls below the critical range, repulsive turning is observed and when cAMP activity is above the critical range, attractive turning is induced. The critical range of cAMP must be low for guidance cues that induce attraction, but further reduction of the cAMP converts attractive to repulsive turning.

The justification to talk about a "critical range" or "threshold" comes from experiments done on *Xenopus* spinal neurons by Ming et al. [48]. They want to determine whether the cAMP concentration changes turning behavior gradually, or if at a certain concentration attractive response changes to repulsive response (and vice versa). They test this by administering an increasing amount of Rp-cAMP to the bath in addition to the same netrin-1 gradient. What they find is that there is a clear transition from attraction to repulsion consistent with the idea of the "switch". On the

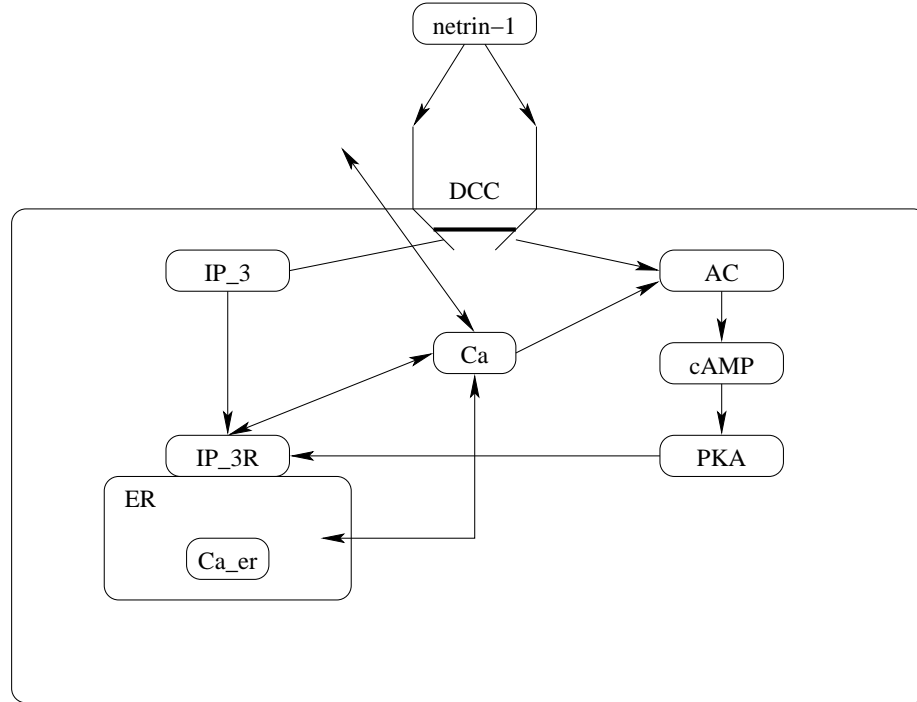


Figure 3.1: Part of the signal transduction pathway in growth cones. Abbreviations: **AC**: adenylate cyclase, **Ca**: cytosolic calcium ion, Ca^{2+} , Ca_{er} : calcium ion in the endoplasmic reticulum, **cAMP**: cyclic AMP, **DCC**: Deleted in Colorectal Cancer, **ER**: endoplasmic reticulum, IP_3 : inositol 1,4,5 triphosphate, **L**: ligand, netrin-1, **PKA**: protein kinase A. References: [2, 5, 8, 32, 48, 49, 64, 65]

other hand, enhancing the effectiveness of cAMP by adding Sp-cAMP to the bath (a chemical which enhances the effect of cAMP) has no effect on the angle of turning. The turning angle is statistically the same during attractive and repulsive turning [48, 65].

Ming et al. also examine the effects of low netrin-1 concentrations, and they find that for sufficiently low concentrations there is no turning response. These experiments give us the following important pieces of information regarding growth cone turning in a netrin-1 gradient: (Note: a concentration of 5-10 $\frac{\mu g}{mL}$ at the pipette which results in about a thousand times the concentration at the cell leads to clear turning response while 0.5 and 1.5 $\frac{\mu g}{mL}$ at the pipette leads to no response.)

- There is a certain low concentration of netrin-1 which is insufficient to elicit any sort of response from the growth cone.
- Under normal circumstances, netrin-1 binding to the receptors induces turning toward the higher netrin-1 concentration, but lowering cytosolic cAMP levels can change the attractive response to repulsive turning.
- Experiments with other molecules (rMAG) which induce repulsion, show that this turning response can also be reversed and changed into attractive turning by increasing the cytosolic cAMP levels.
- The turning response is a 'switch-like' behavior as demonstrated by the fact that the angle of turning cannot increase by increasing the internal cAMP levels, and cannot be decreased by decreasing the cAMP levels, rather, decreasing cAMP levels changes attractive turning into repulsive turning abruptly.

The abrupt, switch-like change in the turning response suggests that the internal cAMP levels must reach a value that we can call the 'threshold', above which level the growth cone is able to turn into the gradient, and below which the gradient is repulsive. There is no empirical evidence on how cAMP is distributed inside the cell during attraction or repulsion. The reversal of behavior is achieved by bath additions of substances which are known to lower or increase cAMP levels. If we assume that cAMP levels are uniform in the cell, and the attraction or repulsion is only dependent on whether the cAMP levels are above or below threshold, then quite clearly, we need another mechanism to provide the spatial information about which direction the growth cone must turn. On the other hand, if we assume that cAMP is elevated to different levels in the cell, and this is the only mechanism that drives the turning, we arrive at a contradiction again, because raising the internal cAMP levels by bath addition of Sp-cAMP should (depending on the amount of Sp-cAMP) increase the cAMP level everywhere in the cell above the threshold level which would terminate

any type of response. Based on this heuristic argument, it is unlikely that cAMP activation alone could be responsible for the observed behavior. Let us examine what is known about the Ca^{2+} pathway.

First of all, many experimentalists note that depleting the external calcium completely, any sort of turning response is abolished [32, 64]. Hong et al. [32] examine how different calcium levels regulate the turning response in *Xenopus* neurons, by blocking plasma membrane channels, channels of the internal storage, and by triggering calcium efflux from the internal storage by bath addition of ryanodine. They observe that high level internal Ca^{2+} signals (resulting from normal extracellular calcium concentrations) in a netrin-1 gradient lead to attractive turning, while low level Ca^{2+} signals (resulting from a depleted extracellular calcium level) lead to repulsive turning. In these experiments the authors cannot indicate whether the Ca^{2+} level elevation is local in all growth cones, although in the larger ones they are able to observe a transient calcium gradient on the side facing netrin-1.

A natural question, given the role of calcium as an intracellular messenger, is the spatial distribution of calcium during growth cone turning. Both Hong et al. [32] and Zheng [77] conduct experiments on *Xenopus* neurons to show that spatially restricted calcium elevation on one side of the growth cone is sufficient to trigger a turning response. Zheng is able to quantify the amount of calcium present by his technique of releasing caged calcium with a laser beam, and he is able to calculate the amount of caged calcium by controlling the frequency of the laser. He shows that the base level of cytosolic calcium plays an important role, because the same amount of increase induces attraction in a cell which has 'normal' cytosolic calcium levels, and repulsive turning in a cell which has lowered cytosolic calcium levels. Hong et al. manipulate calcium induced calcium release (CICR) by creating a ryanodine gradient across the growth cones. Ryanodine is known to activate the receptors of the internal calcium storage, the endoplasmic reticulum, ER. The calcium release from the stores is auto-

catalytic. Hong et al. do not quantify the amount of released calcium, only note that repulsive turning corresponds to shallower gradients and a lowered cytosolic calcium level.

The interaction between the cAMP and calcium pathways is examined by Hong et al. They induce attractive turning by bath addition of ryanodine, which leads to increased calcium release, and subsequently override the attractive response by blocking a downstream component, PKA, of the cAMP pathway. Similarly, they can overturn a calcium induced repulsion by bath addition of Sp-cAMP.

There is also a steady calcium elevation in some growth cones 10 -15 minutes after the netrin-1 gradient is set up, which only terminates when the netrin-1 gradient is no longer present. This was not observed in all growth cones, and it is possible that this is a result of other processes (for example actin dynamics) that are unrelated to the initial decision making regarding the direction of turning [32].

We can summarize the relevant facts about the calcium pathway as follows:

- Influx from the extracellular medium is important, because depleting the calcium here abolishes the turning response.
- Local elevation of calcium mediates a response, but whether it is attractive or repulsive, depends on the absolute amount of calcium, not just the gradient of calcium across the growth cone. High levels of calcium lead to attractive turning in the side of the cell where calcium levels are elevated, but elevation of calcium to a only a low level leads to repulsive turning from the side with the elevated calcium.
- cAMP can change the turning response initiated by a calcium gradient. If the growth cone is responding by repulsion, elevating the cAMP levels will change the response to attraction, and vice versa, attraction induced by high calcium levels on one side can turn into repulsion, if cAMP is lowered.

Calcium and cAMP are common second messengers and are known to interact with each other several ways. cAMP is produced by adenylylate cyclase, and different adenylylate cyclase isoforms can be activated or inhibited by calcium. Adenylylate cyclase in *Xenopus* spinal neurons is calcium-activated (Y. Gorbunova, personal communication). Calcium activates three types of AC, namely AC1, AC8 and AC3, but currently it is not known which of these AC isoforms is found in *Xenopus* spinal neurons. Each of these isoforms responds to different calcium levels. AC3 only appears activated by un-physiologically high concentrations of calcium. AC8 also responds to calcium in concentrations 5 to 10 times higher than the concentration necessary to activate AC1, and is considered a "pure calcium detector" [16]. AC1, on the other hand responds to simultaneous activation by G-proteins and calcium concentrations in the physiological 0.1-1 μM range [53], and is considered "a coincidence detector". This is consistent with experimental data on *Xenopus* neurons, therefore we consider interactions of AC1 and calcium in our model. Also in favor of AC1 is the fact that this particular isoform is abundant in the central nervous system, mainly in the brain, particularly during development when growth cone guidance is especially relevant [16].

Another known effect connecting the two pathways is the phosphorylation of IP₃ receptors by protein kinase A or PKA (downstream product of cAMP) which leads to changes in calcium flux from the endoplasmic reticulum, ER into the cytosol. In some systems it increases calcium flux, in some others the phosphorylation leads to a decrease. We hypothesize that in our case the flux increases, and also, that phosphorylation due to PKA to be proportional to adenylylate cycles. This concludes all the biological information necessary to understand the development of our theoretical model of axon guidance.

3.2.2 Theoretical models of gradient sensing

Theoretical descriptions of how cells can detect sometimes only a few percent change over their body and orient themselves toward attractants have a long history. Previous models (Moghe & Tranquillo [50], Tranquillo & Lauffenburger [75]) focus on a phenomenological description of chemotactic movement. Although these models do include one intracellular messenger, their goal is not the accurate description of the signal transduction underlying gradient sensing, rather, they attempt a complete description of leukocyte chemotaxis from sensing to directional movement. Although these models made important contributions to the understanding of chemotactic movement, their approach to model chemotaxis is significantly different from later models which separate sensing from motility, and build on detailed information about signal transduction events. Since these models, separation of sensing and motility has emerged as an important principle in understanding chemotaxis [56], discussed below. Although we do not describe the Moghe & Tranquillo and Tranquillo & Lauffenburger models in detail, they are similar to models discussed in Section 2.2.4. Recently, several sophisticated types of theoretical models of the signal transduction events underlying bacterial and leukocyte chemotaxis have been developed [4, 15, 41, 44]. However, chemotaxis in eukaryotic cells is still not well characterized for a number of reasons. One problem is the sheer number of connections and pathways that exist in these organisms, which makes the design of a tractable model of all signaling molecules involved in gradient detection and motility impossible with traditional methods. Another problem is the difficulty in deciding which experimental data is widely applicable to all chemotactic cells, which data may be true for *Dictyostelium*, for instance, but not growth cones. An example of such a case is the question whether growth cones adapt. Developing and maintaining polarity may not be important for growth cone chemotaxis either. Difficulty can also arise from the correct interpreta-

tion of the experiments. For example, Meinhardt [44] bases his model partially on observations about the dynamic nature of the membrane protrusions of *Dictyostelium*, however, later these protrusions were proved to be unnecessary for sensing.

So far no theoretical model of chemotaxis in growth cones has been developed, in spite of the intriguing recent data on the signal transduction mechanism presented by Ming et al. [48] and Song & Poo [67], among others.

Parent & Devreotes [56] established a widely accepted characterization of chemotaxis. Their work provides important criteria for every model of chemotactic sensing and movement must meet.

- Extreme sensitivity and the ability to detect a concentration difference of as little as 2 % between front and back of the cell in a range of absolute concentrations;
- Polarity: when the cell is exposed for a period of time to the same gradient the rear becomes less sensitive;
- Directional sensing is not essential for movement;
- Movement is not necessary for sensing (i.e. it is not like bacterial chemotaxis)
- Adaptation: transient response is observed in response to uniform changes in the attractant concentration, while responses at the leading edge are persistent; eventhough uniform changes lead to transient response, immobile cells are still able to sense an unchanging gradient.

Although Parent and Devreotes do not emphasize this, the amplification of the signal (which is necessary to explain the enormous sensitivity) is also a common goal of theoretical descriptions of chemotaxis.

We review two fundamentally different theoretical models of growth cone sensing, one by Meinhardt [44], and the other one by Levchenko & Iglesias [41]. We discuss how these models address the criteria set by Parent & Devreotes, and some implica-

tions and limitations of these models. Three other models exploring some aspect of chemotactic sensing are also mentioned.

Perhaps one of the most widely quoted and most widely criticized model of recent years is Meinhardt's chemotaxis model [44], which attempts to give a general framework of chemotactic sensing. His model is based on two main observations. Firstly, that chemotactic cells are extremely sensitive and are able to detect only a few percent change in the attractant concentration over the cell body, regardless of the absolute concentration of attractants. Secondly, that sensing is a dynamic process involving quickly changing protrusions of the cell membrane, called pseudopods. Even when no external stimulus is present, pseudopods of *Dictyostelium* can travel around the cell circumference or, in other cases, happen in synchrony on opposite sides of the cell. Meinhardt's model seeks to reproduce these characteristic patterns of pseudopod extension. Meinhardt, echoing Parent & Devreotes, assumes that sensing and motility are independent processes. Based on the observations, he sets four criteria for the model: high sensitivity; sensitivity in a wide range of attractant concentrations; polarization of the cell adapts to changes in the orientation of the external signal; intracellular pattern formation continues even in the absence of an external signal. Meinhardt's model describes what he calls an abstract "intrinsic pattern forming system" that is responsible for orienting the cell. Meinhardt first addresses the question of sensitivity. He proposes a Turing-like mechanism, in which a global inhibitor and a local activator amplify a small change in the attractant concentration. The activator enhances its own production as well as the production of the inhibitor. Although the mathematical details are not given, one can assume that this is a standard reaction-diffusion model, in which the inhibitor diffuses faster than the activator, therefore the range of inhibitor is larger than that of the activator. Such mechanisms produce a stable pattern which does not respond to later fluctuations in the attractant concentration. The size of the response is independent of the initial attractant gradient. The

model, therefore, explains how sensitivity can be independent of the absolute ligand concentration. However, an important shortcoming of this mechanism is that once the cell orients itself, it is unable to respond to new stimulus, because of the stable pattern of the internal signaling system. Meinhardt explores several ways a stable pattern can be re-set, and checks the predictions of each method against experimental findings.

First, if the half life of the inhibitor is longer than that of the activator, oscillations occur. First, the activator level peaks, subsequently the inhibitor accumulates and ends the activation, and this gives one full cycle of oscillation. This model implies that sensing is not continuous, rather, it is possible in certain time intervals corresponding to the phase when the activator levels are low. However, there is experimental evidence to the contrary at least in *Dictyostelium*. Another way to destabilize a pattern is by reducing the range of the inhibitor to a region smaller than the whole cell surface. This allows more protrusions to appear, but often this orients the cell in the wrong direction.

Patterns produced by reaction-diffusion systems are also adjustable when an upper bound is imposed on the production rate of the activator. If, in addition, the activator is slowly diffusing, then the activated region can move around the cell surface, but it also becomes broad, unlike the appearance of the protrusions observed. If the activator is almost non-diffusible, then the protrusions have some very desirable characteristics. Namely, a steeper attractant gradient leads to more preferential protrusions in the cell, and without the external gradient protrusions appear randomly distributed over the cell surface. However, in this case the appearing peaks cannot be shifted. In order to explain the random appearance of pseudopods over the cell surface in the absence of attractants, Meinhardt keeps the assumption that the production of the activator has an upper bound and that the activator diffuses very slowly. This model still does not adjust to new attractant gradients, however. To achieve this,

Meinhardt assumes the existence of a second inhibitor that diffuses slowly and that acts on a slow time scale. The second inhibitor accumulates over time where the peak of the activator is located, and it destroys the activator peak. This process readjusts the cell, and it allows the formation of new protrusions.

The model is analyzed exclusively numerically. The equations given by Meinhardt are ordinary differential equations describing the evolution of the activator and two inhibitors at the surface of the cell broken into n sections. a is the activator, b is the global inhibitor with fast diffusion and c is the local inhibitor that acts on a slow time scale. The constants of the equation are: s - ligand concentration; several different functions are used here to reflect random fluctuations or external asymmetry in different sections of the cell surface; b_a - basic production rate of the activator; s_c - Michaelis-Menten constant for the local inhibitor; s_a - saturation constant of the activator; r_a - decay rate of the activator; r_b - decay rate of the global inhibitor; b_c - production rate of the local inhibitor; r_c - decay rate of the local inhibitor.

$$\begin{aligned}\frac{da_i}{dt} &= \frac{s_i(a_i^2/b + b_a)}{(s_c + c_i)(1 + s_a a_i^2)} - r_a a_i \\ \frac{db}{dt} &= r_b \sum_{i=1}^n a_i/n - r_b b \\ \frac{dc}{dt} &= b_c a_i - r_c c_i\end{aligned}\tag{3.1}$$

These equations contain the implicit assumption that the activator, a and the local inhibitor, c do not diffuse while the global inhibitor, b diffuses so rapidly that it is given by the same function in each part of the cell membrane. The term

$$\frac{s_i(a_i^2/b + b_a)}{(s_c + c_i)(1 + s_a a_i^2)} = \frac{a_i^2 + b_a b}{b(1 + s_a a_i^2)} \frac{s_i}{s_c + c_i}$$

shows that a_i , the activator is autocatalytic, and as its level increases, it saturates. Both b and c inhibit the production of a . The activator decays at the rate r_a . a promotes the production of both b and c . The production of b depends on the average level of the activator in the cell, while the production of the local activator only

depends on the local activator level, a_i . The mathematical treatment of the model in this paper is superficial, as the author draws on his extensive experience of reaction-diffusion systems.

Several aspects of the model have been attacked. It is unclear what biochemical mechanism the proposed pattern forming system [44] represents, and which components of the signal transduction mechanism play the role of the activator and the inhibitors. Meinhardt does suggest a molecular interpretation, but he calls it "tentative" as well. Levchenko & Iglesias note that although the existence of a second inhibitor is a theoretical solution, it makes the model less likely to be biologically accurate [41]. Another problem is that with the Meinhardt model persistent activation at a given small region of the cell membrane is impossible. Instead, activated regions move around the circumference of the cell. This is consistent with the dynamic fluctuations of the pseudopods that are at the basis of the Meinhardt model, however, these fluctuations have since been shown to be unnecessary both for the adaptability and persistence of signaling in *Dictyostelium* cells [41]. In spite of these and other criticism, the model is widely known, because it does provide an appealing framework for the processes that results in chemotactic sensing. Specifically, the model provides a mechanism for amplification and the readjustment of the signaling pathways, so the cell can reorient itself in a changing external stimulus. Meinhardt's model is also attractive, because it is minimal, in the sense that it explains chemotactic sensing with assuming the fewest possible signaling components. This makes the model easy to grasp and test against experimental data. There have been few theoretical alternatives proposed which can so consistently and clearly explain the most important features of chemotactic orientation.

Such a theoretical alternative is offered by Levchenko & Iglesias [41]. Their interpretation of the experimental data, therefore, their modeling goals, are different from those of Meinhardt. They believe that chemotactic signaling pathways must be able

to adapt to spatially uniform increases in the external attractant concentration and they must also be able to signal persistently when graded stimulus is presented to the cell. The hypothesis that chemotactic cells adapt to uniform increases in the stimulus directly contradicts Meinhardt's basic assumption regarding the necessity of dynamic pseudopods for successful sensing. This hypothesis is based on experiments with *Dictyostelium* and neutrophils where certain signaling components called phosphoinositides are shown to adapt perfectly. There are no differences in the other theoretical goals. Levchenko and Iglesias also want to account for the huge internal amplification of the external signal, the reorientation of cells when a different stimulus is presented, sensitivity in a wide range of concentrations, and the independence of motility and sensing.

Levchenko and Iglesias believe that the most important feature of chemotactic sensing is adaptation to uniform changes in the stimulus, because this is what allows cells to orient in a wide range of external attractant concentrations. Thus, they begin by building a model for adaptation. The pathway they assume is shown in figure 3.2. Both the activator, A and the inhibitor, I are activated by the signal, S .

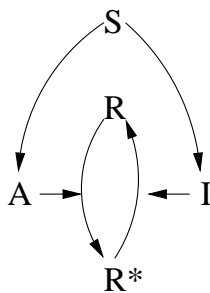


Figure 3.2: Illustration of the mechanism proposed by Levchenko and Iglesias. This is the mechanism for perfect adaptation. The signal, S activates both the activator, A and the inhibitor, I . The output is the activated form of the response element, R^* .

Based on this signaling scheme, one can write down the following equations.

$$\begin{aligned}
\frac{dR^*}{dt} &= -k_{-r}IR^* + k_rAR \\
\frac{dA}{dt} &= -k_{-a}A + k'_a S(A_{tot} - A) \\
\frac{dI}{dt} &= -k_{-i}I + k'_i S(I_{tot} - I)
\end{aligned} \tag{3.2}$$

The quantities, A_{tot} and I_{tot} refer to the total amount of activator and inhibitor available. Activation of A and I depend on the signal, while the inactivation is constitutive. R could be found by the conservation $R_{tot} = R + R^*$. By assuming that the available substrate for S is always much larger than A and I , i.e, that $A_{tot} \gg A$ and $I_{tot} \gg I$, and by non-dimensionalizing the equations, Levchenko and Iglesias arrive at the equations

$$\begin{aligned}
\frac{dr}{dt} &= -\beta ir + a(1 - r) \\
\frac{dA}{dt} &= -(a - s) \\
\frac{dI}{dt} &= -\alpha(i - s)
\end{aligned} \tag{3.3}$$

The two new constants are given as follows.

$$\alpha = k_{-i}/k_{-a}$$

and

$$\beta = \frac{(k_{-r}/k_r)(k_{-a}/k_a)}{k_{-i}/k_i}$$

It is easy to see that the steady state of the active response element, r_{ss} is given by the ratio of the activator and inhibitor concentration, and it is independent of the signal:

$$r_{ss} = \frac{a/i}{a/i + \beta}$$

The authors show numerical simulations for the adaptation of the response element. Next, the authors consider amplification of the signal. This is illustrated in Figure 3.3. The goal is to amplify the production of the output, $R1^*$, They note that there

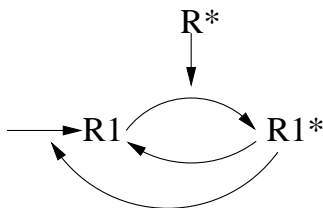


Figure 3.3: Illustration of the mechanism proposed by Levchenko and Iglesias. This is the mechanism for amplification. R^* promotes the production of $R1^*$, the signaling component which is amplified in this scheme. $R1^*$ is autocatalytic, because it controls the substrate for its own precursor, $R1$.

are several ways to achieve signal amplification: for example, increasing the amount of enzyme or the substrate. Increasing the enzyme concentration would correspond to increasing the concentration of R^* , while increasing the substrate concentration corresponds to increasing the amount of $R1$. The figure shows that the authors choose amplification by increasing the substrate. By letting $R1^*$ control the production of $R1$, they create what they call "substrate-supply positive feedback". The significance of this mechanism is that amplification only occurs when R^* is turned on. The implication of this is better understood when the entire signal transduction pathway is considered.

Adaptation and amplification occur at different levels of this signal transduction pathway. Let us examine how the level of $R1^*$ changes according to this scheme. As we have seen in the first scheme, R^* can only be activated when a signal is present, and R^* can adapt, or return to a base level. Only when there is a signal, S , can there be an amplified response, $R1^*$. Therefore, the autocatalytic activation is dependent on the existence external signal, and it cannot grow unboundedly. More importantly, there is no need for an inhibitor to end the signal and force the signaling pathways to be readjustable, like in Meinhardt's model.

By assuming Michaelis-Menten kinetics for the production of $R1^*$, and assuming that the production of $R1$ is mediated by another enzyme, E , the authors give the following

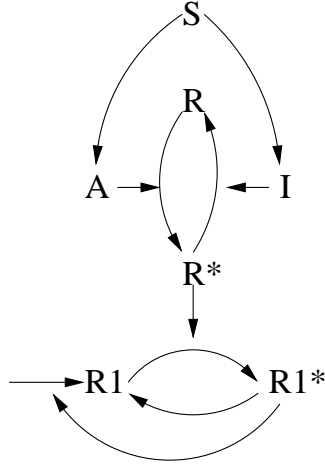


Figure 3.4: Illustration of the mechanism proposed by Levchenko and Iglesias. This is the mechanism for perfect adaptation. This figure shows the whole signaling pathway. Signaling is possible only when S is present. R^* adapts to persisting stimulus, and $R1^*$ is the final, amplified output.

equations for $R1^*$, $R1$ and E .

$$\begin{aligned}
 \frac{dR1^*}{dt} &= -k_{-2}R1 + \frac{k_2R1R^*}{k_M + R1} \\
 \frac{dR1}{dt} &= -k_{-1}R1 + (k_1 + k_2E)R1^* \\
 \frac{dE}{dt} &= -k_{-e}E + k_e(E_{tot} - E)R1^*
 \end{aligned} \tag{3.4}$$

However, so far the model only describes temporal dynamics, and does not show how an internal spatial gradient of might develop. If signaling takes place entirely locally, then adaptation means that all components of the signaling pathway return to the same base level everywhere, and no internal gradient develops. To answer this question, the authors assume that all reactions described in equations 3.2 and 3.4 (with the appropriate initial conditions) happen in n separate compartments along the cell membrane and, in addition, the inhibitor is allowed to diffuse. They add the appropriate terms, $k_D(I_{j+1} + I_{j-1} - 2I_j)$ to the equation describing the evolution of the inhibitor in the j th compartment. (They also assume that there is not flux at the two endpoints.) Now, because the greatest level of inhibitor is produced where

the external signal is the strongest, each compartment experiences a slightly different ratio a/i , so the steady state of the activated response element will be different in each compartment. This allows the development of a gradient in the internal signaling system. Numerical simulations illustrate how the model works, and verify that both perfect adaptation and an amplified graded response are possible. The authors also enter a lengthy discussion of how this theoretical scheme is mapped onto the actual biochemical pathways of amoebae and neutrophils. At the heart of their argument are G-protein activated phosphoinositide kinases and phosphatases.

The Levchenko & Iglesias model shares a lot in common with Meinhardt's model. They both use an activator-inhibitor system where the activator is assumed non-diffusive and the inhibitor diffuses quickly. However, in Levchenko & Iglesias the production of the inhibitor is linked to the signal rather than the activator, and in this model the amplification is a "substrate-supply feedback" mechanism that is switched on only in the presence of the external signal as well. Another significant difference between the models is that in Levchenko & Iglesias adaptation and amplification happen at separate levels of signal transduction. These features solve some problems of the Meinhardt model. Levchenko and Iglesias offer a plausible theoretical framework for the understanding of chemotaxis, and the authors make some experimentally verifiable predictions regarding the nature of the inhibitor and activator.

The two mathematical models discussed so far offer the two most comprehensive conceptual approaches to chemotactic sensing. Some other models must also be mentioned because their results illuminate particular aspects of chemotaxis.

Dallon and Othmer [15] developed a mathematical model which carefully analyzes chemotactic signals between *Dictyostelium discoideum* (slime mold) cells. Their novel approach focuses on the signal characteristics at the boundary of the cells. The authors use these characteristics to make predictions regarding which, out of four potential mechanisms, is the most feasible to act as a signal to initiate chemotactic

orientation. The four mechanisms to orient cells in a ligand gradient which had been proposed in the literature are as follows. Spatial sensing: the cell measures the concentration difference or the difference in the number of occupied receptors in the front and the back of the cell. Differential force mechanism: the cell adhesion to the substratum and to other cells depends on the level of chemoattractant. Pseudo-spatial mechanism: the cell extends pseudopods to convert the spatial gradient in the attractant into a temporal gradient. Spatio-temporal sensing: the external attractant gradient sets up an intracellular gradient. Adaptation is possible with this mechanism, by allowing the internal gradient to decay if the external gradient is unchanging. [15] Dallon and Othmer focus on distinguishing between the spatial, pseudo-spatial and spatio-temporal mechanisms.

When *Dictyostelium* cells are starved, they start secreting cAMP which acts as a chemotactic signal to initiate aggregation of cells. cAMP diffuses, and it is broken down by two chemicals: mPDE inside the cell and ePDE outside the cell. Externally, these are the only reactions included in the model. The signal transduction inside the cell is based on a previous model which postulates two pathways: an excitable one and an inhibitory one. These two pathways regulate the production of cAMP by the cell. The model assumes two cylindrical cells which are homogeneous in the vertical direction, so the problem can be solved in the plane. After non-dimensionalization and the use of the conservation for mPDE and ePDE, the model consists of the following equations. Outside the cells cAMP diffuses and it is degraded by ePDE. At the external boundary of the cells, the outward flux of cAMP is equal to the degradation due to mPDE and secretion. Inside the cell there is another reaction-diffusion equation for cAMP accounting for the cAMP diffusion and its degradation due to mPDE. At the internal boundary, the inward flux for cAMP is equal to the basal production, stimulated production minus the secretion. The relevant components of the signal transduction mechanism are membrane-bound, and their evolution is given

by three ordinary differential equations.

A first set of numerical simulations examines the early phase, when only one cell is signaling and the receiver cell is inactive. The difference in the cAMP concentrations at the front and back of the receiving cell are shown for various distances between the cells, and for various activity levels of mPDE. Increasing the activity of mPDE, which corresponds to an increase in the attractant levels everywhere, results in a decreased difference between the front and back cAMP concentrations. This implies that basing the orientation on the difference in attractant concentrations at the front and back of the cell is not advantageous, so spatial sensing is unlikely. In order to use the pseudo-spatial mechanism the cell must detect the time rate of change in the cAMP concentration. However, the front-to-back ratio of this is essentially a constant during the early phase of the signaling, and it only peaks when the rates of change in cAMP are negative both in the front and the back. This suggests that pseudo-spatial sensing would also work poorly. However, the front-to-back ratio of cAMP increases with increasing activity levels of mPDE, and this aspect of the signal is also not hampered by cAMP levels increasing everywhere around the receiving cell. Based on the signal characteristics of the first set of simulations, spatio-temporal sensing is the most feasible alternative.

Next, the authors also include the internal signal transduction. During the initial time frame when cells must orient, the qualitative cAMP profiles are the same, although the peaks shift. The overall time evolution of cAMP also changes. A second peak of cAMP appears that corresponds to the production of cAMP by the receiving cell. Similarly to the first set of simulations, spatial sensing still does not work well, because the difference between the front and back concentrations is too small. However, under certain assumptions regarding the effectiveness of mPDE, the pseudo-spatial mechanism might be useful. In general, the front-to-back difference in the time derivatives is too small to orient cells, but the ratio of the rates does have a peak at

a later time which might be a signal to initiate cell movement. The authors conclude that a pseudo-spatial mechanism cannot be excluded, but it may control initiation of movement rather than orientation. As before, the front-to-back ratio of cAMP concentrations gives a clear signal again, which further supports the notion of the spatio-temporal sensing. Although the internal cAMP gradients are weak, because cAMP diffuses quickly, a stable gradient is established which may be amplified by some other part of the signal transduction mechanism.

The most significant argument of the article is that purely spatial mechanism is ineffective for organisms which must orient in a wide range of concentrations, and this would restrict cells to navigate only in specific concentration ranges. However, this may be the case for nerve growth cones. It is also important to note that measuring the front-to-back ratio of the attractant concentrations is an effective sensing mechanism regardless of the absolute concentration. Many aspects of the problem are particular to chemotactic sensing in *Dictyostelium*: the degradation of the external cAMP gradient, and the fact that cells themselves can change the cAMP profile by secreting cAMP. Although the particular mechanism might be very different for growth cones, it is likely that here also a spatio-temporal sensing based on a steady internal gradient is at work.

Finally, two articles ought to be mentioned that were published very recently, in 2001. They reflect the renewed interest in describing chemotactic sensing. Narang et al. [54] attempt to formulate a model of chemotactic sensing based on an accurate description of what they believe to be the most relevant part of the signal transduction pathway. The model addresses two questions, namely, the sensitivity of the chemotactic cells, and why the cellular response is only dependent on the attractant gradient while it is independent of the absolute concentration of the attractant. The biochemical mechanism the authors focus on is similar to the one examined by Levchenko & Iglesias. Unlike Meinhardt or Levchenko & Iglesias who create a theoretical model

first, Narang et al. focus on identifying the part of the signal transduction pathway responsible for a polarized response in an attractant gradient. They pinpoint certain membrane phosphoinositides that respond to uniform attractant changes transiently and spatially uniformly inside the cell, while they maintain a polarized distribution in a gradient.

The model has four variables: active receptors, R_{10} ; membrane phosphoinositides, P ; cytosolic inositides and phosphates, I ; and stored phosphoinositides, P_s . All four species are allowed to diffuse. The cell is assumed to be two dimensional and disk shaped, but the diffusion inside the cytosol is assumed to be fast, so radial gradients are ignored. This simplifies the model to one spatial variable, θ , the angle between the leading edge and a given point of the membrane. At the heart of the model is a Meinhardt-type activator-inhibitor system in which membrane phosphoinositides play the role of activators, and the cytosolic inositides are the inhibitors. As in Meinhardt's model, the activator is autocatalytic and it diffuses slower than the inhibitor. The receptor dynamics are assumed to follow perfect adaptation, based on the work of Barkai & Leibler [4]. This assumption has been disproved by recent data showing that perfect adaptation of receptors is not characteristic of eukaryotic cells. The stored phosphoinositides do not play a crucial role in the dynamics of the model.

Numerical simulations show that the pathway responds to spatially uniform increases transiently. This is a result of the assumed perfect adaptation of the receptors. Simulations in a graded stimulus demonstrate a stable and amplified response of P , the membrane inositides. This response is also consistent with the behavior of chemotactic cells, as it is expected based on Meinhardt's analysis of activator-inhibitor systems. Further numerical experiments also verify that size of the response, i.e the size of the membrane inositide peak, is independent of the mean external gradient concentration. The authors of the article do obtain amplification of the signal; chemotactic response in a wide range of external attractant concentration; and adaptation to spa-

tially uniform stimulus. Narang et al., however, do not resolve the question of how this amplified response can be readjusted. The article proposes that a calcium surge could result in a destruction of the phosphoinositide peak, and the authors mention that they have obtained promising preliminary data supporting this hypothesis. Although it is impossible to decide based on the brief description of it in the article, the calcium surge may correspond to the action of the second inhibitor Meinhardt proposes.

Postma and Van Haastert [58] investigate the limitations on the localization and amplification of intracellular responses by analyzing the diffusion of second messenger molecules. During chemotactic sensing, second messengers must transmit signals from the cell membrane to the cytoskeleton and various locations inside the cytosol. The speed of the signal transmission depends on the diffusion speed of the second messenger, however, fast diffusion leads to the loss of spatial information. This is the first dilemma addressed in the paper. A related question is the amplification of the signal. Linear signal transduction always produces shallower second messenger gradients than the original stimulus, therefore a strong local amplification is needed. Postma and Van Haastert propose a mechanism that enhances second messenger gradients.

They consider two models for second messenger production. In the first scheme the cell is considered to be cylindrical, and second messengers are produced at one end of the cylinder. The molecules are allowed to diffuse and decay. In the second scheme, a spherical cell is considered in a linear gradient of the external chemoattractant. Production, diffusion and degradation of the second messenger occur at the cell membrane. The authors find that the dispersion range of the second messenger is given by the expression $\lambda = \sqrt{D_m/k_{-1}}$ where D_m is the diffusion coefficient of the molecule and k_{-1} is the rate of its degradation. This expression implies that fast diffusing second messengers are only able to localize if their half life is short.

Next, Postma and Van Haastert propose a model for signal amplification. They introduce nonlinearity by assuming that a component of the signal transduction pathway translocates between the cytosol and the membrane. The active receptors stimulate the already membrane-bound effector molecules which begin the production of second messengers. Then, as the second messenger concentration increases locally, more effector molecules are recruited from the cytosol to the membrane, resulting in the amplification of the original signal. The effector translocation can be considered a positive feedback, or local activation. By depleting the cytosol of effector molecules global inhibition is introduced, therefore the system is another example of an activator-inhibitor model. The authors do not model adaptation of the pathway and the readjustment of the cell. Numerical simulations demonstrate that the diffusion-translocation model is able to amplify an external gradient about tenfold. However, this amplification is smaller than experimentally observed values. The magnitude of amplification of the model also depends on the gradient in receptor activity, as stronger external gradients are enhanced more. In shallow attractant gradients the model needs to be improved, and in these situations the authors assume an additional mechanism: translocation of another molecule from the cytosol to the membrane which activates the production of second messengers. The model offers two important new concepts: the analysis of the dispersion characteristics of second messengers, and that translocation of certain components of the signal transduction pathway can also act as a positive feedback mechanism.

3.3 Mathematical models and results

Two mathematical models are presented in this section. Each model has focused on a different aspect of chemotactic sensing, and both have limitations in explaining growth cone guidance. The goals and shortcomings of each model are discussed in two separate subsections. Numerical and analytical results are presented.

3.3.1 cAMP-adenylate cyclase switch

Based on the experimental findings, the biochemically accurate description of the cAMP switch seemed like the most important goal because of its key role in determining the turning response. The main feature of the model must be the switch-like, "all or none" response. As the turning angle remains the same regardless of the external netrin-1 concentration, we concluded that the size of the cAMP response should be independent of the size of the external stimulus.

Experimental evidence [48, 64, 65] also suggests that in growth cones, similarly to other animals cells, we can decouple the cytoskeletal reorganization and other downstream parts of the signal transduction pathway from chemotactic sensing. Turning occurs over the period of minutes whereas the local elevation of calcium and the increase in cAMP in response to stimulus happen much quicker, on the order of seconds. This allows us to consider the simplified pathway as shown in Figure 3.1.

We also believed that because growth cones only encounter effector concentrations over one order of magnitude, they would only need to sense a gradient within a given range of concentrations. This implied that adaptation to a wide range of attractant concentrations would not need to be considered.

Related to size of the cAMP response is the question of how a possibly very small spatial gradient of an attractant (or repellent) in the extracellular medium is amplified into a large internal gradient. The amplification must exist, because decisive response

can only be expected if the internal signal is clear. This implies that even if the receptor occupancy on different sides of the growth cones is similar, there must be large enough differences in downstream parts of the signal transduction pathway for the growth cone to turn in the appropriate direction. We assumed that the amplification occurs at the level of cAMP, if it is the unambiguous biochemical signal for turning. There are several questions related to gradient amplification, such as the ability to clearly distinguish noise from signal, and physical limitations on receptor activation in very low and very high ligand concentrations, but we did not plan to address these questions.

This model is based on the dynamics of cAMP and Ca^{2+} . Namely, high levels of cAMP correspond to attractive turning for some guidance molecules, and for these substances, lowering the cAMP concentration means switching to repulsive turning; a gradient of cytosolic calcium leads to attraction, while the same internal calcium gradient at a lower overall calcium level induces repulsion. We want to give a plausible explanation of how cAMP concentrations are lowered and increased in a growth cone, and include realistic cAMP and Ca^{2+} interactions.

To summarize, we wanted the model in which

- sensing is modeled independently of motility
- the size of cAMP response is independent of the stimulus
- there is large internal amplification of the external stimulus
- there is no adaptation
- cAMP and Ca^{2+} dynamics are realistic.

A direct approach would be including the spatial and temporal dynamics of all parts of the signal transduction pathway represented in Figure 3.1. This signal transduction pathway could be described by a system of partial differential equations with the

appropriate rate constants and diffusion coefficients. These constants, in general, are difficult to find in the literature, and such a system would have a very large number of unknowns. Therefore, the first step in our work is the reduction of the system.

We want to find the simplest mechanism that can account for a sharp switch in cAMP levels. The idea of a smooth external gradient of netrin-1 inducing a sharp, discontinuous response in the internal cAMP concentration is very closely related to the idea of a smooth gradient giving rise to thresholds during development, as discussed by Lewis, Slack and Wolpert [42].

In order to model this mechanism, we made further reductions in the pathway to be considered, and only focused on the interaction between cytosolic calcium and adenylate cyclase (AC), the enzyme that produces cAMP. There is ample evidence [14, 16, 52] of a wide range of such interactions. By focusing on these, we hypothesize that these are the most important nonlinear interactions contributing to the switch. Such a simplification is based on all other processes happening on a faster time scale. This assertion should be checked again if other signaling molecules would be added to the model.

As discussed in the “Biological background” section, we assume that the adenylate cyclase isoform found in growth cones is calcium-activated, and it can simultaneously be activated by the receptor, via G-proteins. We also consider a positive feedback loop on AC by assuming that the protein produced by cAMP, called PKA enhances the calcium flux from the cytosolic calcium stores. This assumption is based on phosphorylation of the receptors on the calcium stores by PKA, also mentioned in the “Biological background”. We assume that the increase in the calcium flux is proportional to the concentration of AC. This implies that there is only amplification between AC and PKA, and also, that production of cAMP, then production of PKA happens on a faster time scale than the calcium-AC or calcium-PKA interactions. We

formulate the model for calcium and adenylate cyclase, so it is important to comment on how the AC level is related to the internal cAMP concentration. A large amount of cAMP is produced by active adenylate cyclase, and consequently cAMP is degraded. No other processes regulate cAMP, therefore, the concentration of cyclic AMP is proportional to the concentration of active AC. The amplification of cAMP due to its production makes the actual switch mechanism is even more dramatic than the results of our model show. Our system of differential equations for calcium, denoted by C and the activated form of AC, denoted by A is:

$$\begin{aligned} \frac{dC}{dt} &= \overbrace{k_0 \frac{L}{k_{n1} + L}}^1 - \overbrace{k_1 \frac{C^2}{K_p^2 + C^2}}^2 + \overbrace{k_2(C_b - C)}^3 \\ &\quad + \overbrace{(k_f + k_3A) \cdot \frac{LC(C_{er} - C)}{C + k_aL}}^4 \\ \frac{dA}{dt} &= \underbrace{k_4 \frac{L}{k_{n2} + L}}_5 \cdot \underbrace{\frac{C_m C^4}{K_r^5 + C_m C^4}}_6 \cdot \underbrace{(A_t - A)}_7 - \underbrace{k_5 A}_8 \\ &\quad C(0) = C_b \\ &\quad A(0) = 0 \end{aligned} \tag{3.5}$$

The equation for calcium dynamics draws heavily on previous models of calcium dynamics [21, 37, 47, 70]. The first equation describes the time evolution of cytosolic calcium concentration, $[Ca^{2+}]$. As ligand binds, there is a calcium flux from outside the cell which saturates with increasing ligand concentrations (1). The cytosolic calcium is continuously pumped into the endoplasmic reticulum (ER), as shown in (2). The pump is believed to transport two calcium ions per cycle, hence the second order form [21, 37, 47]. There are a number of mechanisms that maintain the cytosolic calcium level near the resting value, C_{a_b} . These include passive leak between the cytosol and ER, the cytosol and the extracellular medium and calcium buffering. These mechanisms are summarized in (3).

The last term, (4) describes the calcium flux from the ER into the cytosol due to the activation of the IP_3 channels. This term is similar to the analogous term in Tang et al [70] who show that flux from the internal storage, the endoplasmic reticulum (ER) in all models based receptor-kinetics can be written in the same form. It is experimentally shown that calcium has a dual role in the dynamics of the IP_3 receptors: the initial fast increase of calcium leads to the opening of the channels, but consequently calcium also contributes to the slow closing of the channel. In our model there is a flux purely due to the direct activation of the IP_3 channels which is proportional to the calcium concentration difference between the ER and the cytosol, $C_{er} - C$. This flux reaches maximal value at a calcium concentration dependent on the ER calcium level and k_a , and is small for both low and high calcium concentrations. IP_3 is taken to be proportional to the ligand concentration. We also include additional calcium flux from the ER due to the phosphorylation IP_3 channels by PKA. PKA is assumed to be proportional to the activated form of adenylate cycles.

The total amount of adenylate cyclase in the cell is fixed on a short time scale. The inactivated part of the total given in term (7) becomes activated if simultaneously stimulated by netrin-1 and calcium. Activation by the ligand is assumed to have first-order kinetics (5). The calcium activation is mediated by calmodulin, and (8) is fitted to experimental data [14]. Its fourth-order form is likely to reflect that four calcium ions are necessary to form Ca_4CaM , the calcium-calmodulin complex which is responsible for the activation of AC. Activated adenylate cyclase, AC decays linearly with rate k_5 (8).

The parameter values are shown in Table 3.1. Wherever it was possible, we used values that have been established in the literature, with the exception of the total adenylate cyclase concentration, A_t . The value for K_r was obtained by fitting experimental data in [14]. We tried several values, ranging over two orders of magnitude, for the parameters which we could not obtain from the literature. In all cases, the

Constant	Value	Value in lit.	Reference
k_0	$7 \frac{1}{s}$	$6.61 \frac{1}{s}$	[47]
k_{n1}	$1 \mu M$	$0.1 \mu M$	[47]
k_1	$5 \frac{\mu M}{s}$	$5 \frac{\mu M}{s}$	[47]
K_p	$0.15 \mu M$	$0.15 \mu M$	[47]
k_2	$10 \frac{1}{2}$	$2 \frac{1}{2}$	[33]
C_b	$0.1 \mu M$	$0.08 \mu M$	[9]
k_f	$10 \frac{1}{\mu M s}$		
k_3	$1 \frac{1}{\mu M s}$		
C_{ER}	$7 \mu M$	$6.3 \mu M$	[9]
k_a	1	1	
k_4	$2 \frac{1}{s}$		
k_{n2}	$1 \mu M$		
C_m	$20 \mu M$	$20 \mu M$	[9]
K_r	$1 \mu M$		used [14]
A_t	$20 \mu M$	$0.02 \mu M$	[9]
k_5	$1 \frac{1}{s}$		

Table 3.1: Parameter values for the calcium-adenylate cyclase switch model

qualitative behavior of the system remained the same. The equations 3.5 were not non-dimensionalized. Comments on the parameter value for A_t and the reason for leaving the model in its dimensional form are given at the end of the section.

It is important to mention how the model might change, if other isoforms turn out more important in growth cone guidance. Because AC3 responds to very high calcium levels, it is unlikely to play any role, however, it is possible that AC8 is present. AC8 can also be activated by G-proteins as well as somewhat higher calcium concentration than what is required for AC1. This would change the activation term in the differential equation for adenylyl cyclase, for example to term (5) + term (6) (instead of the current activation term which is (5)(6)), but based on numerical experiments it

is still possible to find a parameter range for which we see a similar behavior as the one in our current model. This implies that the main mechanism of the cAMP switch does not crucially depend on our current hypothesis about the AC isoform in growth cones.

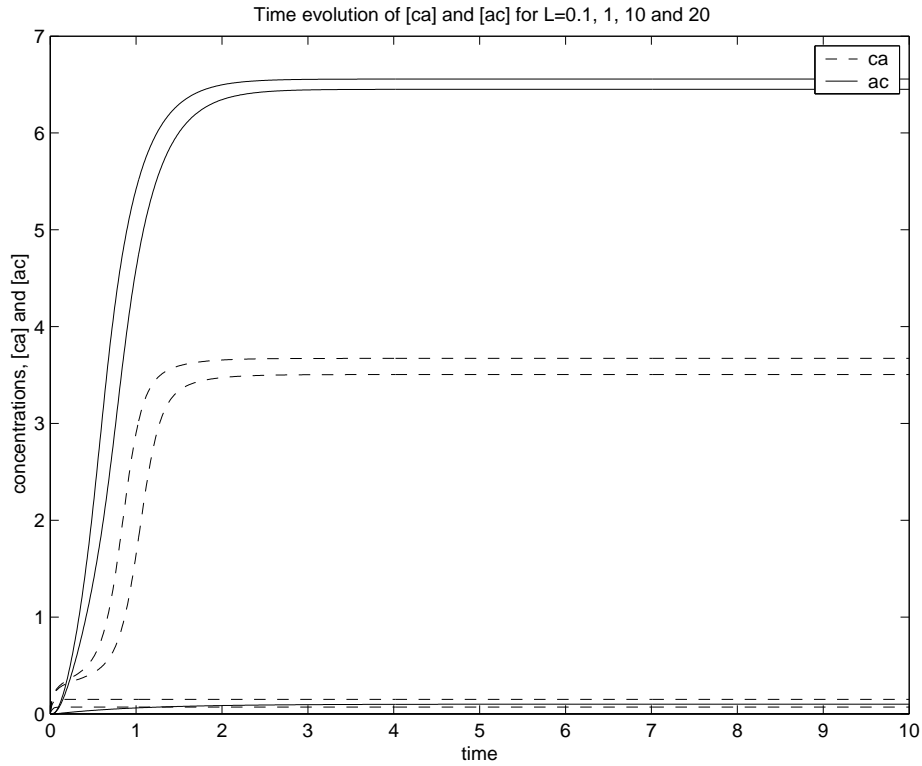


Figure 3.5: Time evolution of calcium and adenylate cyclase for four different netrin-1 concentrations.

Time units: seconds

We solved the equations numerically using Matlab. The system is in dimensional form, and we used the parameter values as they are given in table 3.1 without their units. The numerical simulation is run for 10 seconds. Solutions for various ligand concentrations are shown in Figure 3.5. As some parameter values are disputable, the following discussion on the behavior of the model is limited to the qualitative behavior. Numerical values are included in the discussion of the results only in order to make the discussion easier, but these values are not claimed to provide realistic in-

formation. Increasing ligand concentrations corresponds to increases in the cytosolic concentration of calcium and adenylate cyclase. It is clear that changing the ligand concentration from $0.1 \mu M$ to $1 \mu M$ does not change the steady state value of adenylate cyclase and Ca^{2+} significantly, just as changing the ligand concentration from $10 \mu M$ to $20 \mu M$ does not. However, there is a significant jump between the steady state values as the ligand concentration increases from 1 to $10 \mu M$. This suggests that the ligand concentration is the bifurcation parameter in the differential equations for adenylate cyclase and Ca^{2+} .

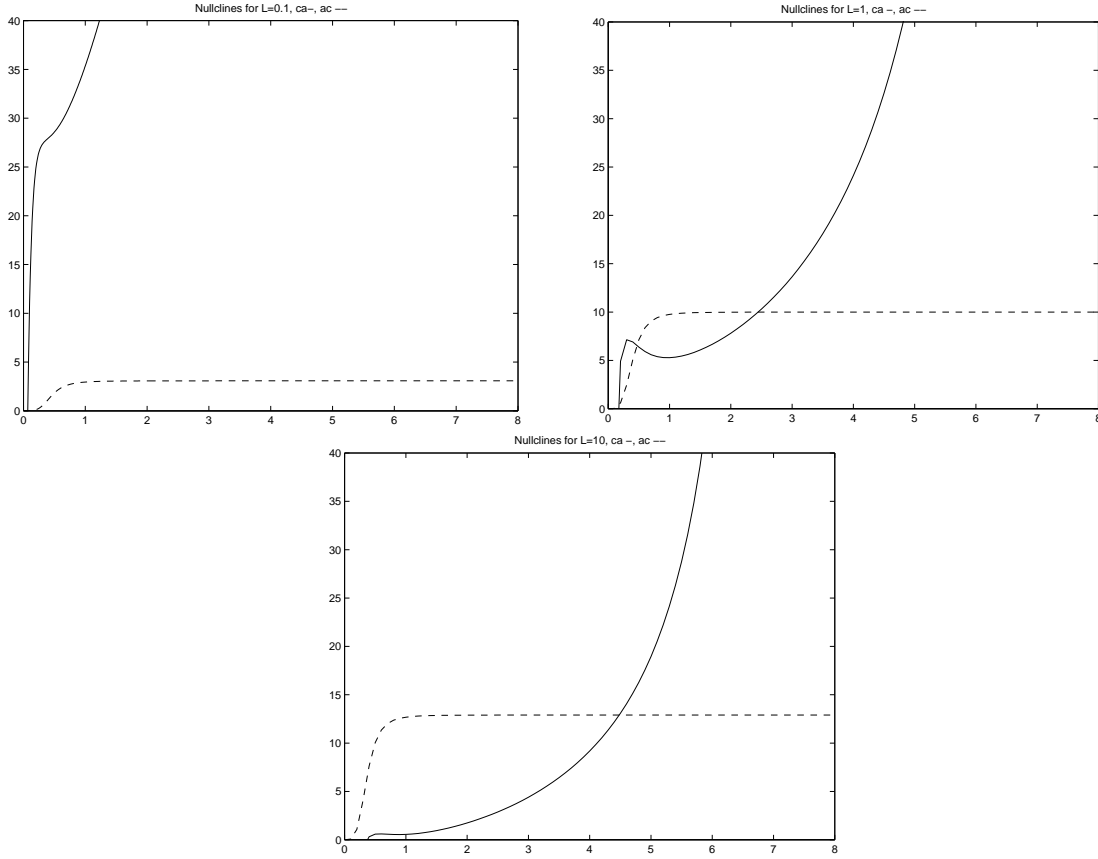


Figure 3.6: Nullclines for values of the netrin-1 concentration, $L=0.1, 1$ and 10 from left to right. The solid curve gives the nullcline for calcium and the dashed curve is the nullcline for adenylate cyclase.

This is verified when the nullclines of the system are plotted in Figure 3.6. For small values, there is only one small stable steady state. Regardless of the initial conditions, the cytosolic AC (and calcium) concentration will approach the same small value. For intermediate values, we see two stable steady states, and an unstable steady state separating them. If we start with low cytosolic calcium and low AC levels, the solution converges to the same steady state as before. However, by raising the level of L , only the high steady state remains. Changing the concentration of the ligand even very slightly changes the steady state level of AC (and calcium) drastically. This provides the mechanism of the cAMP switch.

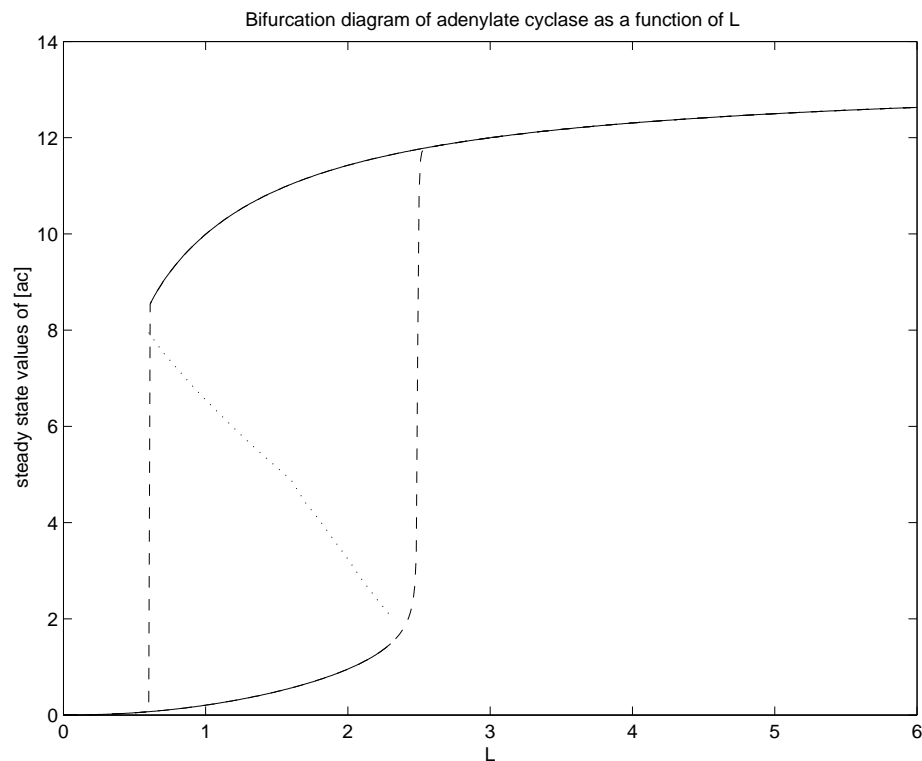


Figure 3.7: Bifurcation diagram of adenylate cyclase as a function of L

The bifurcations are further illustrated by Figure 3.7, showing the steady state of AC as a function of netrin-1 and Figure 3.8 with the calcium steady state as a function of netrin-1. In Figure 3.7 we see that increasing ligand concentrations slowly increases

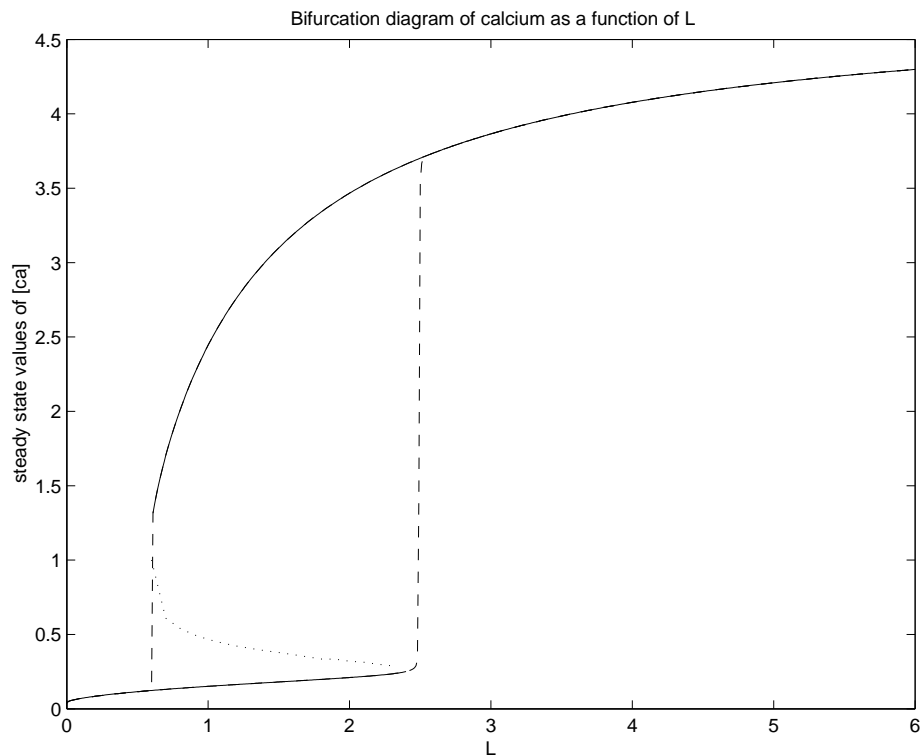


Figure 3.8: Bifurcation diagram of calcium as a function of L

the low steady state value of AC. This continues until netrin-1 reaches the threshold value of $L=2.3$, at which point the lower stable steady state disappears and only the higher steady state value remains. This results in a sudden drastic change in the steady state AC concentration which jumps from the lower steady state value of approximately $1.7 \mu M$ to the higher steady state value of approximately $12 \mu M$. This process corresponds to following the solid line representing the small steady state values for AC, then making the jump through the dashed line to the upper solid line which represents the high AC steady state values. In fact, there is a hysteresis here, because now decreasing the ligand value below 2.3 (moving to the left along the upper solid line) will not change the steady state value of AC dramatically. The high steady state value decreases gradually until the ligand concentration reaches about 0.6. At this point we drop from the high steady state value to the low one instantaneously.

Similar behavior is shown for calcium.

In terms of the chemotactic sensing, we have modeled a cAMP switch that signals unambiguously in certain ligand gradients. We can consider a cell divided into two internal compartment, both of which contain the same signal transduction pathways. We also note that the concentration of cAMP is proportional to the concentration of adenylate cyclase. In some ligand gradients that contain the threshold value of $2.3 \mu M$, a small steady state value of AC is obtained at one side of the cell where the ligand concentration remains below $2.3 \mu M$, and there is a sharp jump in the steady state of the cytosolic AC concentration at the part of the cell membrane where the ligand concentration exceeds the threshold. If the ligand concentration obtains the threshold value, the model does satisfy the goals as follows. The size of the cAMP response is nearly independent of the stimulus, as the steady state value does not change much with the netrin-1 concentration. This is shown in Figure 3.9 where ligand concentrations are changed over five orders of magnitude. The only significant increase in the steady state values is where the system goes through a bifurcation. Because of the bifurcation of the AC concentration, even a very small change in netrin-1 can produce a very large change in the concentration of AC. The model does not assume adaptation, and it is built on realistic calcium-adenylate cyclase dynamics. It is also clear from the above discussion that the model has serious limitations. Even if we continue to assume that growth cones do not adapt (although recent experiments by Poo suggest that they do), the model fails in ligand gradients that does not contain the threshold value. Clearly, this is the most important shortcoming of the model, because this implies that chemotactic sensing in growth cones is dependent on the absolute concentration of the ligand, and sensing is only able to occur under special circumstances. This is clearly not true.

There are a few other problems as well. First of all, as it became clear that the model did not properly explain chemotactic sensing, efforts to calibrate the parameter val-

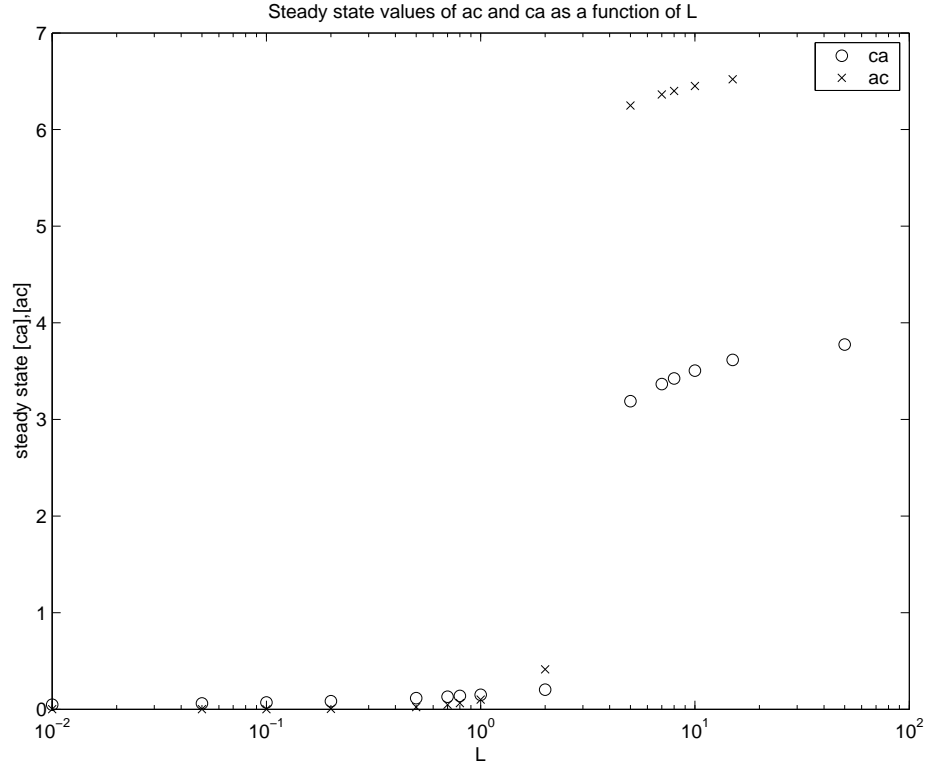


Figure 3.9: Steady state values of calcium and adenylate cyclase as a function of the netrin-1 concentration. Initial conditions for all simulations are given by $Ca(0)=Ca_b$; $AC(0)=0$.

ues and to non-dimensionalize the model were abandoned. Therefore, the numerical value for the bifurcation parameter, and the steady state values of Ca^{2+} and AC are meaningless. We assume the appropriate ligand gradient necessary to orient the cell is presented. In this case, the cell is locked onto this direction, and it will be unable to re-orient itself, unless the ligand concentrations fall below the value of $0.6 \mu M$ again. During all the previous discussion only the temporal dynamics of calcium and adenylate cyclase are considered, and the spatial behavior was greatly simplified by the two-compartment model in which the signaling components of the two compartments do not interact. Diffusion of the second messengers always occurs. Even considering that the fast half-life of cAMP would limit the range of diffusion, there must be diffusion between the two compartments, leading to a diminished difference

between the cAMP concentration of the two compartments. Finally, this model also fails to explain the experimental observation that lowering the cytosolic calcium level changes attractive turning to repulsive turning.

3.3.2 Adaptation and diffusion model

The model for the Ca^{2+} -AC switch does not account adaptation, i.e. for transient signaling in uniform changes of the attractant concentration, and for a cell's ability to choose new orientation in a changed attractant gradient. It also predicts that gradient sensing can only occur in certain ligand concentrations. In this section we provide a model which corrects these problems. The model is fundamentally similar to the Levchenko & Iglesias model which allowed for both adaptation to uniform increases and persistent signaling in attractant gradients. The basic concept, based on the Levchenko & Iglesias model is summarized below. We include this heuristic explanation in order to give a general idea of the approach, and the details are made more concrete in this section.

Adaptation and persistent signaling are achieved by allowing the temporal adaptation of some response element to any given ligand concentration. This is similar to the Barkai-Leibler bacterial chemotaxis model [4] where the receptors are known to adapt. Then, by letting other components (in Levchenko & Iglesias, the inhibitor) diffuse, the response element is forced to adapt to slightly different levels throughout the cell whenever a gradient of the "inhibitor" are produced. In these cases the process leads to an internal spatial gradient of the response element. Thus, uniform changes in the attractant concentration lead to spatially uniform, transient changes inside the cell, whereas an attractant gradient leads to a spatial gradient of the response element. The conditions under which such a mechanism can function are discussed in this section. Our model does not consider the amplification of the graded response, because we assume that once an internal spatial gradient exists, its amplification can

be achieved in several ways downstream from sensing, and this is briefly discussed in 3.3.2. Although our approach is very similar to that of Levchenko & Iglesias, we create a minimal model in which it is sufficient to consider two components of the signaling pathway, and we also offer a more detailed mathematical treatment of the model than the original paper.

In summary, the goals of the model are adaptation to uniform attractant increments; persistent signaling in gradients; and the ability to reorient the cell when new stimulus is presented. A model with such features must be able to sense gradients in a wide range of attractant concentrations. We assume motility and sensing are independent, and focus on the description of sensing only.

Perfect adaptation

Let us consider the chemical pathway represented in Figure 3.10. We can describe the pathway by the following system of equations with the appropriate initial conditions that we impose later.

$$\begin{aligned}\frac{dM}{dt} &= m + \lambda(-k_a(l)M + k_dA) \\ \frac{dA}{dt} &= -rA + \lambda(k_a(l)M - k_dA)\end{aligned}\tag{3.6}$$

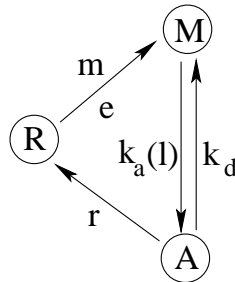


Figure 3.10: Hypothetical signal transduction pathway. R: stored, or "recycled" substance; A: "activated substance" which adapts; M: "modified substance", part of the signaling pathway that mediates adaptation.

The variables are $A(t)$, the activated substance and $M(t)$, the modified substance. (In the original bacterial chemotaxis model, R , A and M are the number of receptors in the "refractory", "activated" and "modified" state, respectively.) The rate k_a depends on the ligand concentration, l and λ is a large nondimensional ratio of the time scales of the slow and fast reactions. In bacterial chemotaxis the fast and slow reactions correspond to phosphorylation and methylation, respectively. In animal cell chemotaxis there is no reason to assume a priori that similarly, a quick biochemical response is followed by slow adaptation, therefore our analysis also considers the case when $\lambda \approx O(1)$. The equations assume that the production of M does not depend on the concentration of R , the stored substance. This is true when the concentration of R is very large compared to concentration of the enzymes mediating the transition from R to M . Another assumption is that only the activated substance, A is able to become "recycled", or R , and the modified substance is not. Furthermore, we assume that downstream effects, such as turning, depend on the concentration of the active substance.

The steady state of the system is given by

$$A_s = \frac{m}{r}$$

and

$$M_s = \frac{m(r + \lambda k_d)}{k_a(l)\lambda r} \simeq \frac{k_d m}{k_a(l)r}$$

so the steady state of A , the activated substance does not depend on the ligand concentration. M_s assumes that $\lambda \gg 1$. The steady state of A implies that regardless of the ligand concentration, l , the concentration of the activated substance will always adapt, i.e. return to the same value which is intrinsic to this system, as it depends on two fixed rates, m and r . In the simplest case $k_a(l) = kl$. Let us assume that the ligand concentration l_0 jumps to l_1 at time $t = 0$, and we start from the steady state of the system at the ligand concentration l_0 , so $A(0) = A_s = \frac{m}{r}$ and $M(0) = M_s = \frac{m k_d}{r k l_0}$.

The analytical solution of the system of equations is given by (see Appendix B.1 for details):

$$\begin{aligned} M(t) &\simeq M_2 + (M_0 - M_1)e^{-r_f t} + (M_1 - M_2)e^{-r_s t} \\ A(t) &\simeq A_s + (A_1 - A_s)(e^{-r_s t} - e^{-r_f t}) \end{aligned} \quad (3.7)$$

where we have defined

$$\begin{aligned} r_f &\simeq \lambda(k_d + kl_1) & r_s &\simeq r \frac{kl_1}{k_d + kl_1}, \\ A_s &= \frac{m}{r}, & A_1 &= \frac{m}{r} \frac{1 + (k_d/kl_0)}{1 + (k_d/kl_1)}, \\ M_0 &= \frac{m}{r} \frac{k_d}{kl_0}, & M_1 &= \frac{m}{r} \frac{k_d}{kl_1} \frac{1 + (k_d/kl_0)}{1 + (k_d/kl_1)}, & M_2 &= \frac{m}{r} \frac{k_d}{kl_1}. \end{aligned} \quad (3.8)$$

When the ligand concentration increases, then the concentration of A grows from the base line A_s to $A_1 > A_s$ on the fast time scale $T_f \sim 1/r_f$. Meanwhile, M , concentration of the modified substance drops from M_0 to M_1 . On the fast time scale, the levels of modified and activated substances change, but their sum is not altered. On the slow time scale $T_s \sim 1/r_s$, the concentration of activated substance returns to the base line A_s from A_1 , while the concentration of the modified substance changes from M_0 to $M_2 \neq M_0$. Now we have a set of equations (eqn. 3.6) that describes the perfect adaptation of a system to a given ligand concentration.

Figure 3.11 illustrates how the model works. This system of differential equations and all the following ones, are solved with the Euler method. The simulation is run for 800 seconds, and it shows that after a transient drop in the concentration of the active substance it returns to the baseline level. The time step is chosen to be $h = 0.1$. As it is clear from the analytical solution, the adaptation is slower when the ligand concentration is small. The parameter values in the simulations are $m = 0.1$, $\lambda = 5$, $k = 0.2$, $k_d = 0.2$ and $r = 1$. $k_a(l) = k \cdot l$ in these and all the following simulations. The same parameter values are used for m , λ , k , k_d and r in all of the following simulations, unless otherwise stated.

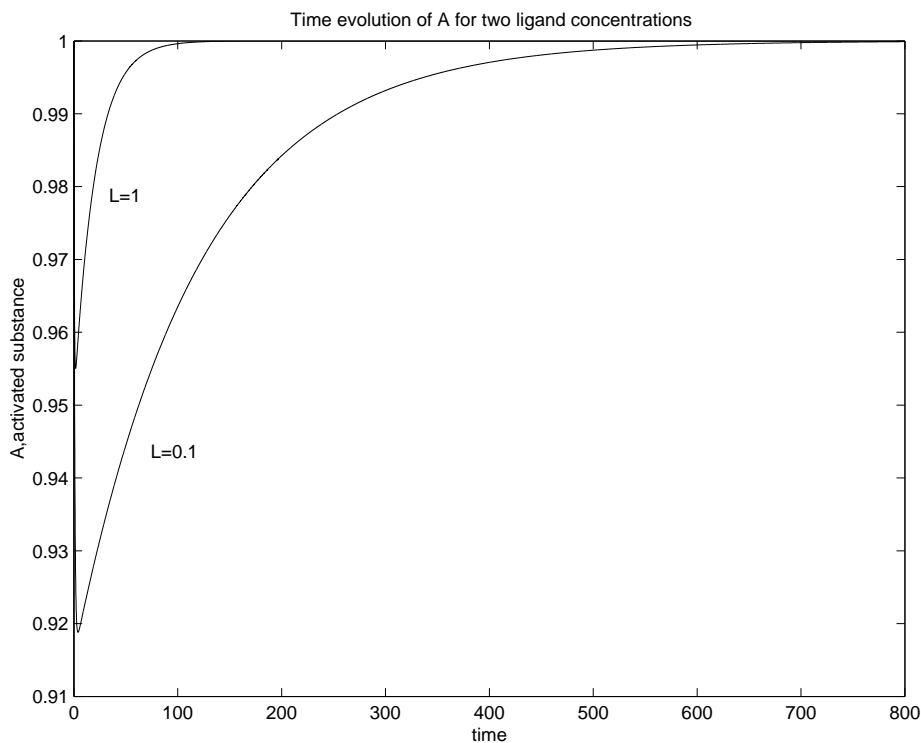


Figure 3.11: Time evolution of the active substance, A for two different ligand concentrations, $l=0.1$ and $l=1$. The concentration of the active substance returns to the baseline in each case.

Spatial models

We are interested in spatial gradient sensing, so we must look at what happens when both A and M are functions of time and space. In order to gain some insight on the behavior of the system, let us first consider an axon consisting of two compartments. We want to investigate how a spatial gradient of A can develop in this model. In each compartment the same set of reactions happens, and in addition, there is a flux between the compartments. We consider the case when the ligand concentration jumps from l_0 to l_1 in the first compartment and to l_2 in the second compartment.

The equations in the two compartment model are:

$$\begin{aligned}\frac{dM_1}{dt} &= m + \lambda(-k_a(l_1)M_1 + k_dA_1) + k_1(M_2 - M_1) \\ \frac{dA_1}{dt} &= -rA_1 + \lambda(k_a(l_1)M_1 - k_dA_1) + k_2(A_2 - A_1) \\ \frac{dM_2}{dt} &= m + \lambda(-k_a(l_2)M_2 + k_dA_2) - k_1(M_2 - M_1) \\ \frac{dA_2}{dt} &= -rA_2 + \lambda(k_a(l_2)M_2 - k_dA_2) - k_2(A_2 - A_1) \\ M_1(0) = M_2(0) &= \frac{m}{r} \frac{k_d}{k(l_0)} \quad A_1(0) = A_2(0) = \frac{m}{r}\end{aligned}$$

The steady state solutions are given by

$$\begin{aligned}A_{1s} &= \frac{m}{r} \cdot \left[1 + \frac{r_1 k_1 k}{\lambda r_2 k_p + k_1 k_s (r_2 + \lambda k_d)} \right] \\ A_{2s} &= \frac{m}{r} \cdot \left[1 + \frac{-r_1 k_1 k}{\lambda r_2 k_p + k_1 k_s (r_2 + \lambda k_d)} \right] \\ M_{1s} &= \frac{m r_1}{\lambda r} \cdot \left[\frac{r_2 (\lambda k_a(l_2) + 2k_1) + 2\lambda k_d k_1}{r_2 [\lambda k_p + k_1 k_s] + \lambda k_d k_1 k_s} \right] \\ M_{2s} &= \frac{m r_1}{\lambda r} \cdot \left[\frac{r_2 (\lambda k_a(l_1) + 2k_1) + 2\lambda k_d k_1}{r_2 [\lambda k_p + k_1 k_s] + \lambda k_d k_1 k_s} \right]\end{aligned}$$

where we have defined

$$\begin{aligned}r_1 &= r + \lambda k_d, \quad r_2 = r + 2k_2 \\ k &= k_a(l_1) - k_a(l_2), \quad k_s = k_a(l_1) + k_a(l_2) \\ k_p &= k_a(l_1)k_a(l_2)\end{aligned}$$

The calculations are shown in Appendix B.2. If $l_1 = l_2 = \bar{l}$, or the ligand concentration on the two sides of the growth cone are the same, then

$$\begin{aligned}A_{1s} = A_{2s} &= \frac{m}{r}. \\ M_{1s} = M_{2s} &= \frac{m}{r} \frac{r + \lambda k_d}{\lambda k_a(\bar{l})}\end{aligned}$$

and if we let

$$\lim_{\lambda \rightarrow \infty} M_{1s} = \lim_{\lambda \rightarrow \infty} M_{2s} = \frac{m}{r} \frac{k_d}{k_a(\bar{l})}$$

so we have recovered the steady state solution to equations 3.6. This means that a spatially uniform increment in the ligand concentration still results in adaptation in the system, and no spatial gradient of the activated substance develops. These calculations are also included in Appendix B.2.

Now let us investigate how the flux of the modified substance, k_1 and the flux of the activated substance, k_2 will influence the steady state of the system. It is important to note that the results of the following calculations and the qualitative behavior of the system remains the same under the assumption that $\lambda \gg 1$. See Appendix B.2 for details.

First, assume that M is non-diffusible, so $k_1 = 0$. Then

$$\begin{aligned} A_{1s} &= A_{2s} = \frac{m}{r} \\ M_{1s} &= \frac{mr_1}{\lambda r} \cdot \frac{\lambda k_a(l_2)r_2}{\lambda k_p r_2} = \frac{m(r + \lambda k_d)}{r \lambda k_a(l_1)} \simeq \frac{m k_d}{r k_a(l_1)} \\ M_{2s} &\simeq \frac{m k_d}{r k_a(l_2)} \end{aligned}$$

The steady state of the system reveals that if the modified substance does not diffuse between the two compartments, then it is as if the two compartment were entirely separated. A and M settle into the same steady state values that they would have if the two compartments were not connected at all.

We do not gain additional information from assuming that $k_2 = 0$, because the qualitative behavior of the system remains the same in this case. (See Appendix B.2.) However, assuming that $k_2 \gg 1$ changes the qualitative behavior.

$$\begin{aligned} \lim_{k_2 \rightarrow \infty} A_{1s} &= \lim_{k_2 \rightarrow \infty} \frac{m}{r} \left[1 + \frac{r_1 k_1 k}{\lambda(r + 2k_2)k_p + k_1 k_s(r_1 + 2k_2)} \right] = \frac{m}{r} \\ \lim_{k_2 \rightarrow \infty} A_{2s} &= \frac{m}{r} \\ \lim_{k_2 \rightarrow \infty} M_{1s} &= \frac{mr_1}{\lambda r} \cdot \left[\frac{\lambda k_a(l_2) + 2k_1}{k_a(l_1)(\lambda k_a(l_2) + 2k_1) - k_1 k} \right] \\ \lim_{k_2 \rightarrow \infty} M_{2s} &= \frac{mr_1}{\lambda r} \cdot \left[\frac{\lambda k_a(l_1) + 2k_1}{k_a(l_2)(\lambda k_a(l_1) + 2k_1) + k_1 k} \right] \end{aligned}$$

These calculations show that the steady state of the active substance will be independent of the external ligand concentrations in the limit as $k_2 \rightarrow \infty$. Therefore $k_2 \gg 1$ leads to a diminished ability of the system to respond to stimulus. The steady state of the modified substance still depends on the external stimulus for $\lambda \approx O(1)$. However, if $\lambda \gg 1$, then $M_{1s} = \frac{mk_d}{rk_a(l_1)}$, and similarly, $M_{2s} = \frac{mk_d}{rk_a(l_2)}$, so in the limit as $\lambda \rightarrow \infty$, our system again responds to stimulus as two unconnected compartments would.

These simple calculations above suggest that the flux of M , the modified substance must be larger than the flux of the activated substance, A , or $k_1 \gg k_2$. A heuristic explanation of this is as follows. If $k_2 > k_1$, i.e. if A were allowed to diffuse faster than M , then regardless of the external ligand concentration the amount of activated substance in the two compartments becomes the same. In this case the steady state of M still depends on the ligand concentration, unless the reactions between M and A are much faster than all other rates, i.e. if $\lambda \gg 1$. If λ is large, then M and A are allowed to exchange quickly, and the concentration of the modified substance will depend mainly on $k_a(l)$ and k_d , therefore M_{1s} and M_{2s} return to the values they would have in case of two unconnected compartments.

Now let us consider the case that A is non-diffusive, but M is. Let us assume that the ligand concentration at the first compartment is larger than in the second compartment, i.e. $l_1 > l_2$. As we had seen from eqn. 3.6, the steady state of M is inversely proportional to $k_a(l)$ which we are taking to be proportional to the ligand concentration, i.e. the steady state of M is inversely proportional to the ligand concentration. This implies that M_1 , the concentration of the modified substance in the first compartment is smaller than M_2 . The flux between the two compartments will increase the value of M_1 (and decrease M_2), therefore more A_1 is produced in compartment one than A_2 in compartment two. Because the flux, k_2 between A_1 and A_2 is negligible compared to k_1 , the difference $A_1 - A_2$ is maintained. Figure 3.12 illustrates this mechanism.

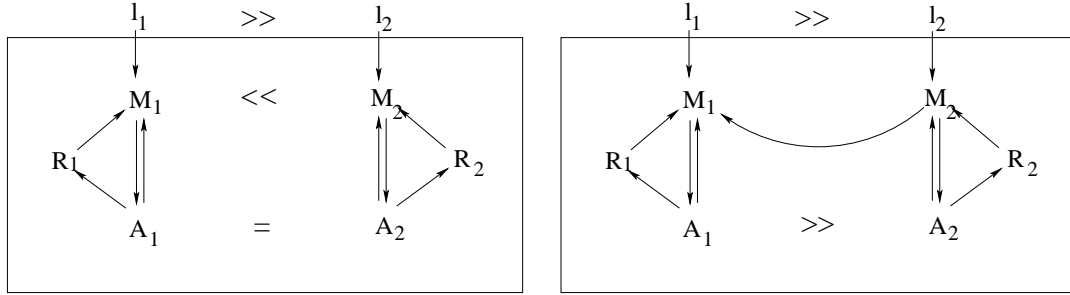


Figure 3.12: Illustration of the two compartment model when $k_1 \gg k_2$. The first figure shows the two compartments without any connection. In the second figure we assume that M is allowed to diffuse between the compartments. This results in the creation of a spatial gradient of A .

We are also interested in how the difference between the levels the activated substance in the two compartments, $A_1 - A_2$ changes with the ligand concentration. Based on our previous calculations, we assume that $k_2 \approx 0$. Furthermore, we assume that $k_a(l)$ is a monotonically increasing function of l , and that $k_a(l) > 0$ for all l . When two different ligand concentrations are presented for compartments one and two, we see a difference in the rates $k_a(l_1)$ and $k_a(l_2)$, thus a spatial gradient in the ligand produces the spatial gradient of A . We notice that $|A_{1s} - A_{2s}| = 0$ if $k_a(l_2) = k_a(l_1)$, and this is the minimum value $|A_{1s} - A_{2s}|$ can obtain.

$$0 < |A_{1s} - A_{2s}| = \left| \frac{2m}{r} \cdot \frac{k_1 r_1 k}{\lambda r k_p + k_1 k_s r_1} \right| < \frac{2m}{r} \left| \frac{k_1 r_1 k}{k_1 r_1 k_s} \right| < \frac{2m}{r}$$

The absolute difference, $|A_{1s} - A_{2s}|$ is bounded below by 0, and above by $\frac{2m}{r}$. It is also easy to show that for arbitrarily large differences in the ligand concentrations the difference between A_1 and A_2 approaches $\frac{2m}{r}$. (We show this by taking $\lim_{k_a(l_1) \rightarrow \infty}$ and $\lim_{k_a(l_2) \rightarrow 0}$. Because of the symmetry of the expression, $\lim_{k_a(l_2) \rightarrow \infty}$ and $\lim_{k_a(l_1) \rightarrow 0}$ leads to the same result.)

We want to know how $|A_{1s} - A_{2s}|$ depends on the difference in ligand concentrations, k and on absolute size of the ligand concentrations, k_s . We introduce new constants:

$a_1 = \frac{2m}{r}$, $a_2 = k_1(r + \lambda k_d)$ and $a_3 = \lambda r$.

$$A_{1s} - A_{2s} = f(k, k_s) = a_1 \frac{a_2 k}{a_2 k_s + \frac{a_3}{4}(k_s^2 - k^2)}.$$

We are interested in $\frac{\partial f}{\partial k}$, how the absolute value of the difference in steady state of A in our two compartment depends on the ligand difference, and $\frac{\partial f}{\partial k_s}$, how the difference depends on the size of the ligand concentrations.

$$\frac{\partial f}{\partial k} = a_1 a_2 \frac{a_2 k_s + \frac{a_3}{4}(k_s^2 + k^2)}{[a_2 k_s + \frac{a_3}{4}(k_s^2 - k^2)]^2} > 0 \quad \forall k, k_s$$

The difference, $A_{1s} - A_{2s}$ always increases with the increasing difference in the ligand concentration. (This is clear from the formula $A_{1s} - A_{2s}$ as well.) Now we look at how the absolute concentration level of the ligand changes $A_{1s} - A_{2s}$:

$$\begin{aligned} \frac{\partial f}{\partial k_s} &= a_1 \frac{-a_2 + \frac{a_3}{2} k_s}{[a_2 k_s + \frac{a_3}{4}(k_s^2 - k^2)]^2} \\ \frac{\partial f}{\partial k_s} &< 0 \quad \text{if} \quad a_2 > \frac{a_3}{2k_s} \end{aligned}$$

In our original notation this expression means that $|A_{1s} - A_{2s}|$ is a decreasing function of the sum of the ligand concentrations if

$$k_1(r + \lambda k_d) > \frac{\lambda r}{k_a(l_1) + k_a(l_2)}$$

or $k_1(r + \lambda k_d)(k_a(l_1) + k_a(l_2)) > \lambda r$. This relationship shows that (depending on the explicit form of $k_a(l)$), there is an absolute ligand concentration at which the difference between the activated substance in the two compartments will be the largest. Let us assume that we fix the difference in the ligand concentrations $k_a(l_1) - k_a(l_2)$, and only change their sum. Increasing the absolute concentration of the ligand beyond the point where

$$k_a(l_1) + k_a(l_2) = \frac{\lambda r}{k_1(r + \lambda k_d)}$$

will result in decreased sensitivity in sensing, and similarly, smaller ligand concentrations also result in a loss of sensitivity. The existence of a range of ligand concentrations in which sensing is optimal corresponds to experimental observations. If the

ligand concentrations are too low, then the noise in the receptor occupancy leads to errors in gradient sensing. If the ligand concentrations are too high, then receptors are saturated, and the cell's ability to to detect gradients is compromised again.

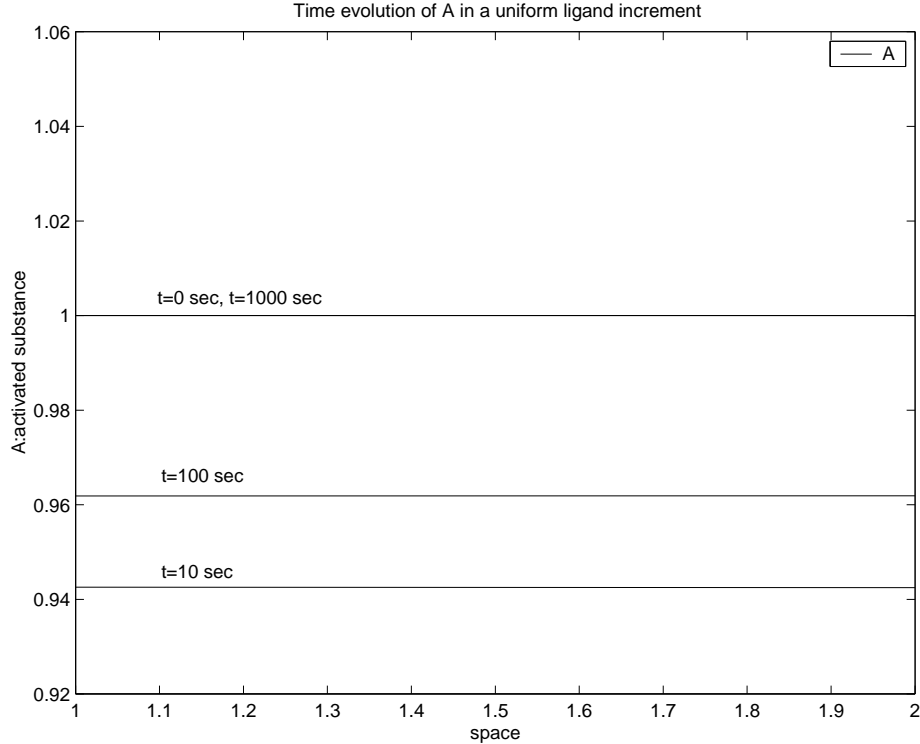


Figure 3.13: Time evolution of the active substance, A in a ligand increment.

The following numerical simulations confirm the behavior of the system. The first figure, 3.13 shows the response of the activated substance, A in a spatially uniform change of the ligand concentration. The initial condition of A is $A(0) = \frac{m}{r}$ which is independent of the ligand concentration. We start with our two compartment model adapted to a spatially uniform ligand concentration, $l_0 = 0.1$. Figure 3.13 shows the temporal dynamics of the system in a spatially uniform ligand step to $l_1 = 1$. There is a quick drop in the concentration of A , then a slow adaptation to the steady state level, $A_{ss} = \frac{m}{r}$.

We see similar behavior if we start with our system adapted to a ligand gradient

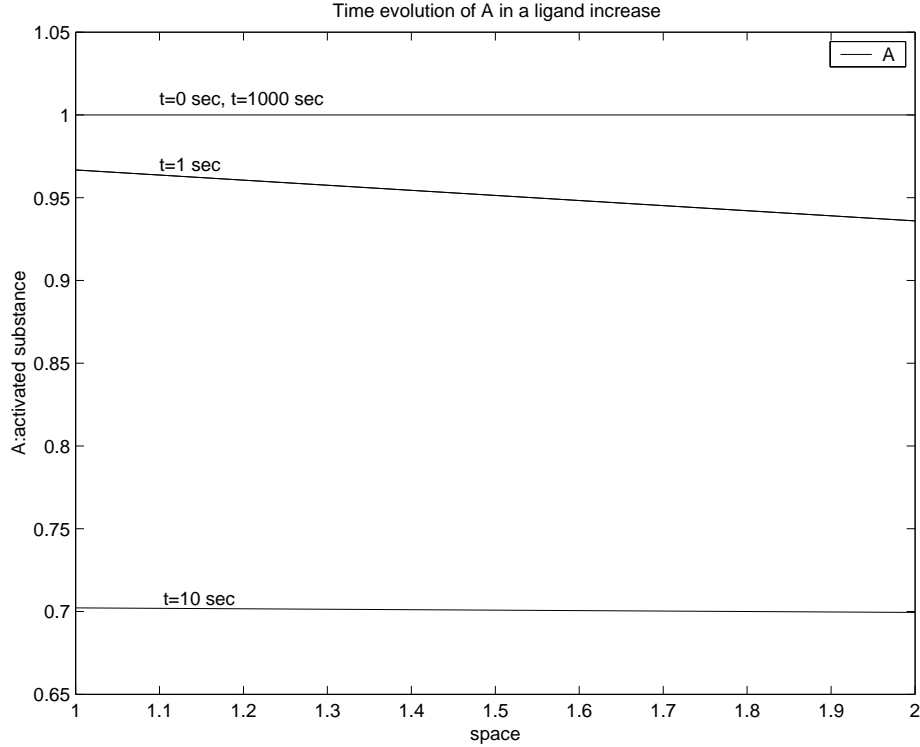


Figure 3.14: Initial condition: A is adapted to a ligand gradient. Temporal dynamics of A when the two compartments are exposed to the same ligand concentration.

(which does not reflect in the initial conditions for A), and then let the ligand concentration jump to the same uniform level inside both compartments. In compartment one the initial ligand concentration is 0.1, and in compartment two the ligand concentration is 0.5, and the ligand concentration jumps to $l = 1$ in both compartments. Although the transient levels of A are not the same in the two compartments, the steady state levels are. Figure 3.14 shows these simulations. The values for k_1 and k_2 are 1 and 0.1, respectively. The qualitative behavior of the system remains the same if $k_2 = 0$ is used. In these figures the active substance in compartment one, A_1 is always given by $A(1)$, and A_2 by $A(2)$. Matlab, instead of plotting the value A_1 from 1 to 1.5 and A_2 from 1.5 to 2 connects A_1 and A_2 . These numerical simulations illustrate that our two compartment system responds transiently to changes in the

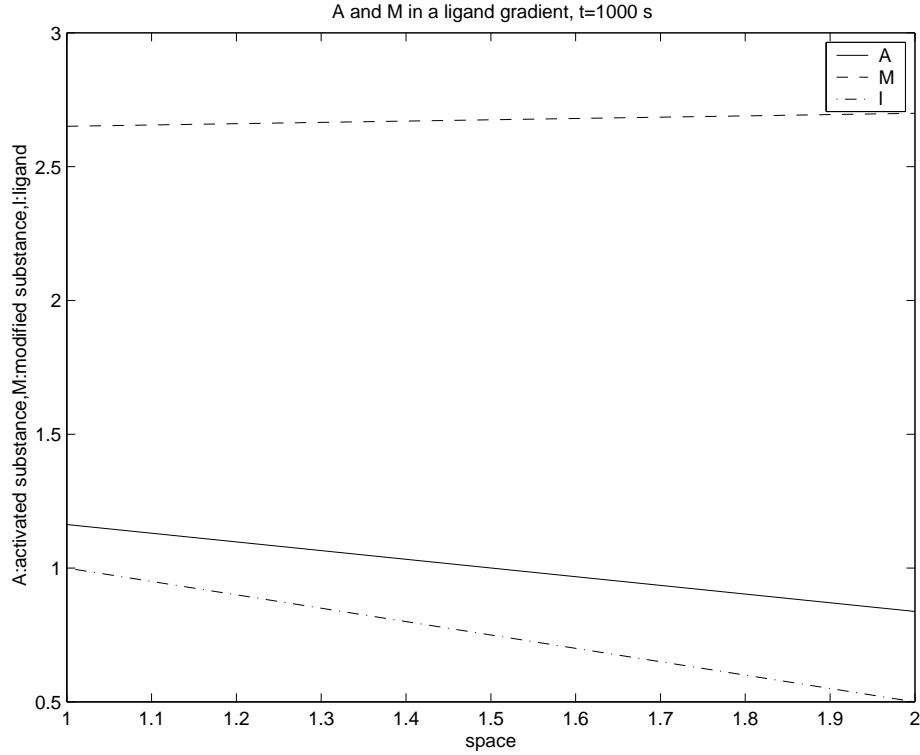


Figure 3.15: Steady state of the two compartment system in a ligand gradient.

ligand concentration, and it settles into a ligand-independent steady state in uniform ligand concentrations.

Now we must examine the other main claim of our model, namely, that it sets up an internal gradient of the active substance when presented with a spatial attractant gradient. The numerical simulation for this is shown in Figure 3.15. This figure depicts the steady state of the modified and the active substance when the ligand concentration in the first compartment is $l_1 = 1$, and in second compartment $l_2 = 0.5$. The simulation is run for $t=1000$ seconds. $k_1 = 1$ and $k_2 = 0.1$, and again, $k_2 = 0$ does not change the qualitative behavior. The spatial gradient of the activated substance is maintained while the ligand gradient remains unchanged. This results in the persistent signaling of the system in ligand gradients.

Appendix B.3 contains notes and comments on the analytical solution of the two

compartment model, as well as approximate solutions to the problem if $\lambda \gg 1$.

In a general case we can assume that both A and M are functions of time and space, and they are both allowed to diffuse. We obtain the following equations:

$$\begin{aligned}\frac{\partial M}{\partial t} &= m + \lambda(-k_a(l)M + k_dA) + D_1 \frac{\partial^2 M}{\partial x^2} \\ \frac{\partial A}{\partial t} &= -rA + \lambda(k_a(l)M - k_dA) + D_2 \frac{\partial^2 A}{\partial x^2} \\ A(x, 0) &= \frac{m}{r} \quad M(x, 0) = \frac{m}{r} \frac{k_d}{k_a(l)} \\ \frac{\partial A}{\partial x} \Big|_{x=0} &= \frac{\partial A}{\partial x} \Big|_{x=L} = 0 \\ \frac{\partial M}{\partial x} \Big|_{x=0} &= \frac{\partial M}{\partial x} \Big|_{x=L} = 0\end{aligned}$$

We provide numerical solutions to this system on the interval $(0, L) = (0, 10)$ in Figures 3.17 and 3.18. Based on our analysis of the two compartment model, we assume $D_1 \gg D_2$ and $\lambda \gg 1$. The diffusion coefficient of A , D_2 is chosen to be zero, but as before, $D_2 \ll 1$ would also provide qualitative similar results. The initial conditions are chosen to be the same as in the differential equation with $\lambda \gg 1$. The equations are solved with a FTCS (forward time center space) method. The time step is chosen to be $\Delta t = 0.01$, and the grid size is $\Delta x = \frac{1}{9} = 0.11$. We show three sets of simulations verifying that in uniform ligand concentrations there is a transient response, and that ligand gradients elicit a persistent graded response.

In figure 3.16 we examine the behavior of the system which has adapted to a ligand gradient, but at time $t=0$ we present to the cell a spatially uniform ligand concentration, $l = 1$. The middle panel shows that the cell responds very quickly, and in one second the both A and M are almost uniform. (The ligand concentration is equal to one everywhere which is difficult to see in the figures.) Finally, the panel on the right shows the steady state of the system at $t=1000$ seconds. A returns to the baseline value of one, and M also becomes a constant in space.

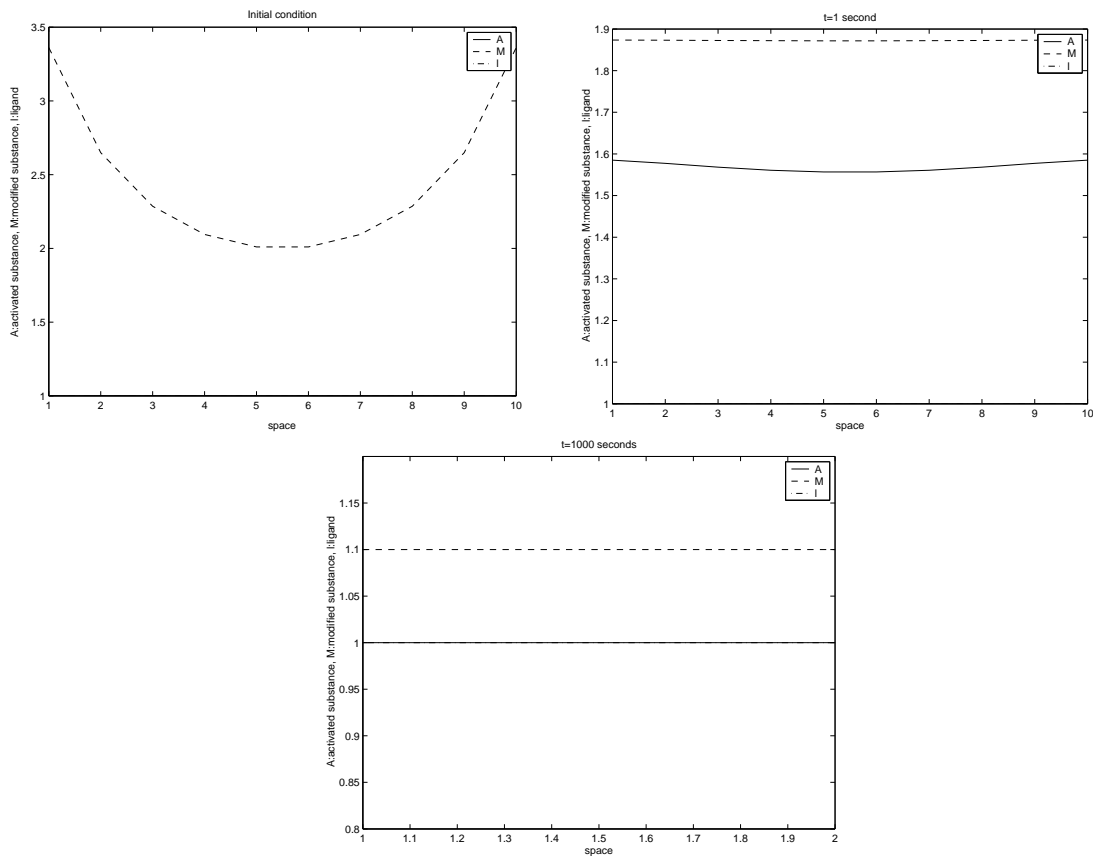


Figure 3.16: The figures show the temporal dynamics of the reaction-diffusion system in a uniform attractant concentration. The first figure shows the initial condition, the second one the system at $t=1$ second, and the third one shows the steady state of the system at $t=1000$ seconds.

The following two figures show the response of a cell to an attractant gradient. In the first one, in Figure 3.17 the attractant concentration, l is linear, as before, and in the second one, in Figure 3.18, l is quadratic.

As before, the active substance, A is spatially uniform initially, while the modified substance, M is inversely proportional to the ligand concentration. The system is shown at $t=1$ second on the second figure, at $t=100$ seconds in the third figure and at the steady state, in the last figure. As in the two compartment model with a ligand gradient, in the steady state the concentration of A is proportional to the ligand concentration, and the concentration of M is inversely proportional to it. This

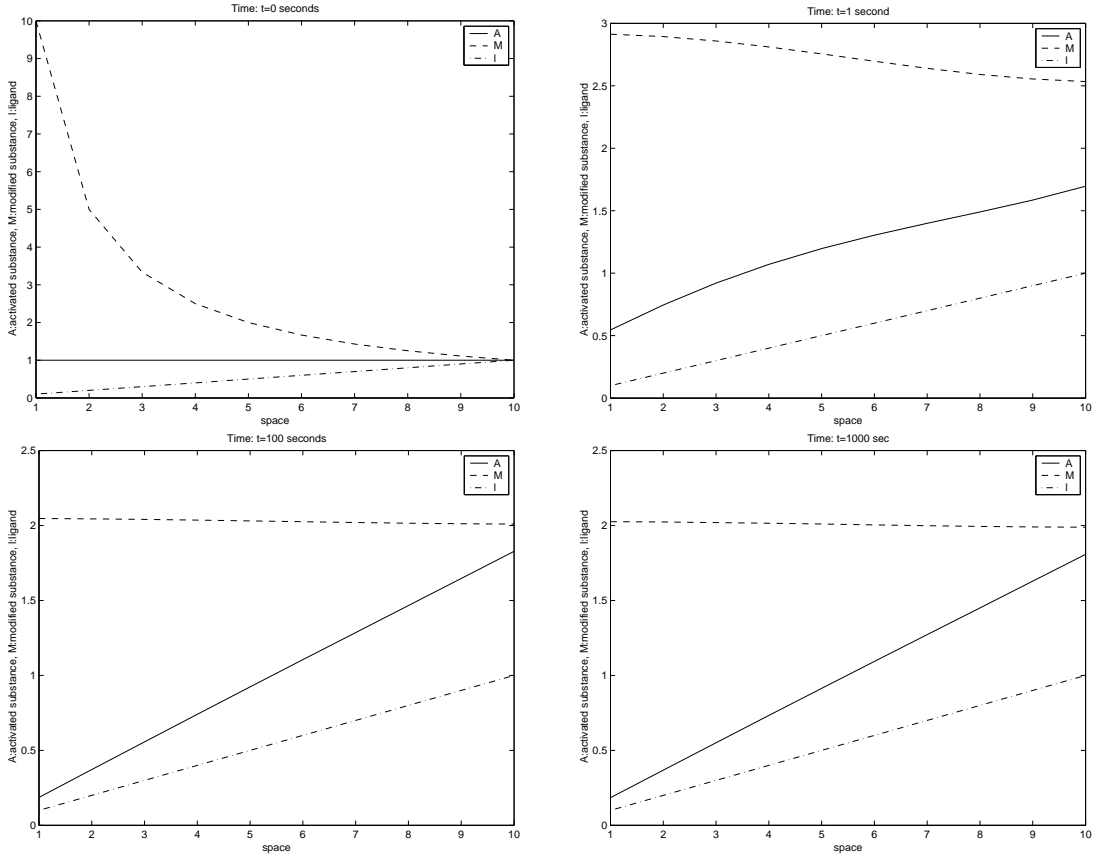


Figure 3.17: The figures show the temporal dynamics of the reaction-diffusion system in a linear attractant gradient. The first figure shows the initial condition, the second one the system at $t=10$ seconds, and the third one shows the steady state of the system at $t=100$ seconds, and the fourth one at $t=1000$ seconds.

spatial profile persists, representing the persistent signaling of the system in a spatial gradient.

Figure 3.18 shows dynamics in a nonlinear ligand gradient. Similarly to Figure 3.17, initial conditions of A are spatially uniform, and those of M are inversely proportional to the ligand concentration. The second subfigure shows the system after $t=10$ seconds, and finally, the third subfigures shows the steady state after $t=1000$ seconds. At the steady state the modified and the activated substances are quadratic. As expected, the highest value of M corresponds to the lowest value of the ligand, and the

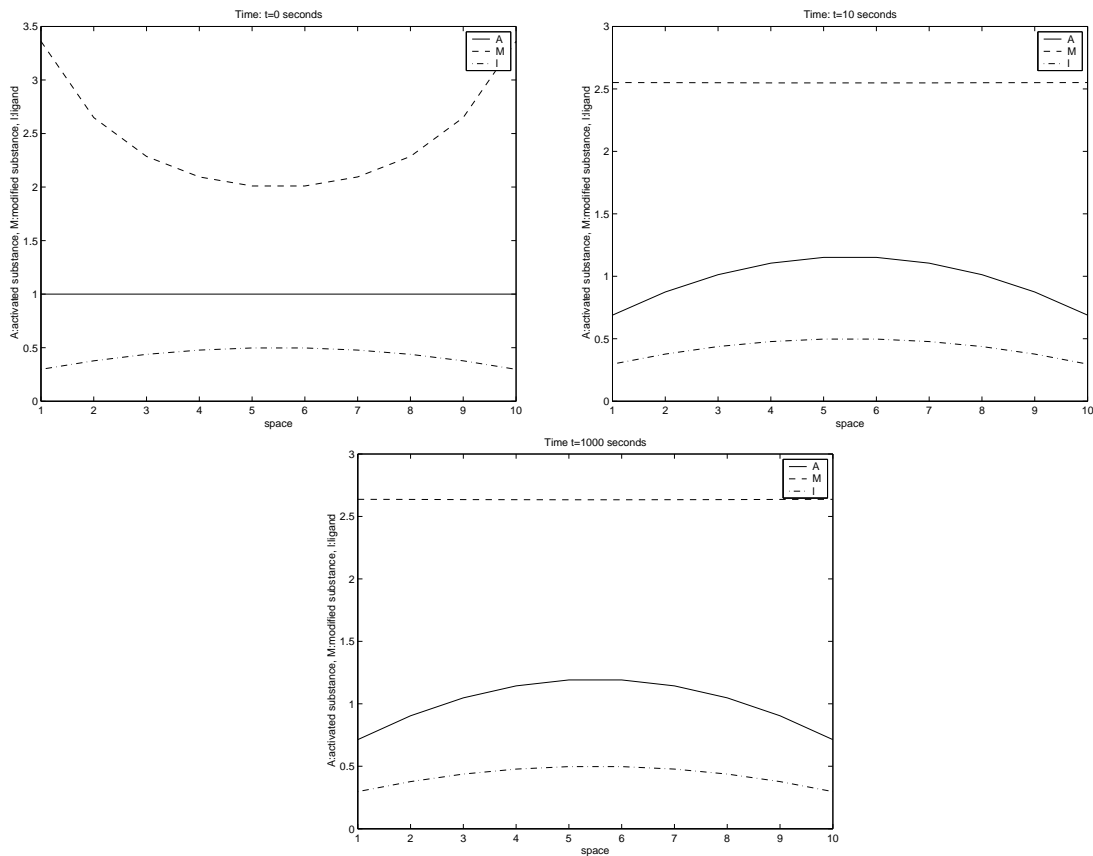


Figure 3.18: The figures show the temporal dynamics of the reaction-diffusion system in a quadratic attractant gradient. The first figure shows the initial condition, the second one the system at $t=10$ seconds, and the third one shows the steady state of the system at $t=1000$ seconds.

highest value of A corresponds to the highest value of the ligand. Persistent signaling is predicted again.

Discussion

Our model aimed at recreating a few key features of chemotactic sensing. First, we wanted the cell model to respond with transient signaling to a spatially uniform ligand concentration and with a persistent signal in a spatial ligand gradient. The numerical simulations for both the two compartment model (which can be considered

a discretized version of the reaction diffusion equations) and the reaction diffusion equations show, in Figures 3.13,3.14 and 3.16 that a spatially uniform ligand concentration elicits a transient response from the system, but the steady state of the active substance is spatially uniform. Persistent signaling is also achieved in ligand gradients, illustrated by Figures 3.15, 3.17 and 3.18. Both transient and persistent signaling can also be deduced from the steady state analysis of the two compartment model where the steady state of the active substance depends on the difference of ligand concentrations.

Secondly, the model must allow the cell to choose new orientation in a changed attractant gradient. This is clearly the case, as both the active and the modified substance depend on the ligand concentration through $k_a(l)$, the rate of production of A from M .

Finally, this model does not have the limitation of the calcium-cAMP model, as it allows sensing in all ligand concentrations. The adaptation-diffusion model predicts that there is an optimal range of ligand concentrations when $k_a(l_1) + k_a(l_2) = \frac{\lambda r}{k_1(r + \lambda k_d)}$. A fixed ligand difference will result in the largest signal when this condition is satisfied. The model also predicts that increasing the ligand difference results in an increase in the signal.

We can also improve the model by showing the simple modifications can result in the amplification of the signal. In all previous simulations parameters were chosen so that the ligand concentration is amplified moderately by the concentration of the active substance, however, this need not be the case for our current system with other parameter values. It is also important to note that huge amplification of the external signal is characteristic of chemotaxis, and such amplification is impossible to produce with our current model. As in the Levchenko & Iglesias model, we assume that amplification takes place downstream from A , because this assumption guarantees that when the external signal, l is terminated, the internal signal stops as well. The na-

ture of this amplification could be similar to what Levchenko & Iglesias has assumed, shown in Figure 3.3 where A would play the role of the activated response element, R^* .

Another possibility for amplification is based on Goldbeter & Koshland [22] who show that amplification can result not only from nonlinear interactions, but also from covalent modifications under certain conditions. Figure 3.19 shows a reaction in which A is the enzyme in the production of an active response element, $R1^*$. Based on Goldbeter & Koshland, there can be a drastic amplification in the amount of $R1^*$ produced when the enzymes A and E are saturated, so the total amount of free A and E are negligible when compared with their concentrations in the complexes produced with $R1$ and $R1^*$. This is one possible mechanism for amplification of A .

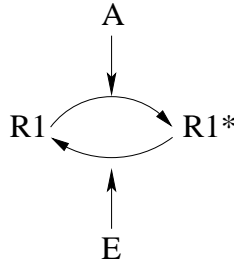


Figure 3.19: A as an enzyme in the production of an activated response element, $R1^*$.

It is clear both from the analytical solution to the perfect adaptation model 3.7 and the analysis of the steady state solution of the two compartment model that the size of λ is very important. In the original equations 3.6 λ is the non-dimensional ratio of the fast and slow time scales which means that λ determines how fast the initial transient response is in comparison to the adaptation. In animal cell chemotaxis the time scales for a transient response and for adaptation to a signal are not well known. We have run the numerical simulations for the two-compartment model and the reaction-diffusion model for several values of λ . The only observation that can be made based on these simulations is that for small values of λ the initial transient of

A is longer in comparison with the time it takes for A to return to its baseline value. Changing λ by three orders of magnitude did not appear to alter the qualitative behavior of the system. Further analytical treatment of the problem is necessary to understand the role of and the constraints on the size of λ .

Finally, we must discuss the limitations of the adaptation-diffusion model. So far we have not linked the activated or the modified substance of the model to any particular components of the biochemical pathway, because there are no clear candidates for such connections. It is possible that one might find chemical species that adapt to a certain ligand concentration, but based on the current experimental data one cannot say with certainty what it might be. Related to this, our original aim was to explain the results of the calcium and cAMP experiments on *Xenopus* neurons in the framework of chemotactic sensing. We have not addressed this, although in Appendix B.4 we propose an extension of the current model that accounts for how changing the absolute calcium concentration changes turning behavior in growth cones.

3.4 Conclusions and further direction

We presented two mathematical models that attempted to describe chemotactic movement of growth cones in response to a netrin-1 gradient. In our first model we assumed that the signal transduction pathways would not be able to adapt to a constant signal. In addition, we aimed at basing our model on experimentally observed phenomena, in particular, the way turning response is determined by cytosolic cAMP and Ca^{2+} concentrations. This model described a cAMP switch which is very sensitive at a certain threshold concentration of netrin-1. Mathematically, the threshold value is a bifurcation parameter. The system goes through a bifurcation as the two stable steady states separated by an unstable steady state change to one stable steady state. This model did not successfully explain how gradient sensing is possible in concentration ranges that do not include the threshold concentration. This is a severe limitation of the model, because, a growth cones moving past the threshold level concentration would permanently lock onto the same direction, even if the ligand gradient changed. In addition, it is possible that the assumption of no adaptation is also flawed.

The second model attempts to satisfy most of the criteria set for chemotactic sensing, except internal signal amplification. This model demonstrably explains how a graded internal response develops in ligand gradients, and how a uniform increase in the ligand concentration leads to a transient internal response. Although the model is theoretically more sound than the first one, it is equally limited to that, because its lack of connection to experimentally observable signaling pathways. The variables of the model may represent particular chemicals, or they might represent many components of the signal transduction pathway which acts as a unit on a time scale faster than what is considered in the model.

Much of the model builds on the understanding how perfect adaptation occurs in bacterial chemotaxis. However, there are important differences between bacterial

and growth cone chemotaxis which might influence the mathematical analysis of the problem. One such example is the known separation of time scales between phosphorylation and methylation in bacterial chemotaxis which allows simplifications in the mathematical treatment of the problem. The same simplifications may be incorrect in the description of growth cone chemotaxis.

Clearly, this topic is open for further theoretical and experimental research. Experimental observations of Song & Poo [66] on adaptation might be a promising starting point for further work. Song & Poo believe that growth cones periodically lose and regain their sensitivity to gradients. Such adaptation (which is different from the adaptation assumed in our second model) appears similar to an idea proposed by Meinhardt [44]. He states that in a reaction-diffusion system, if the half-life of the inhibitor is shorter than that of the activator, then oscillations occur. The accumulation of the activator is overtaken by the inhibitor, and for the period of time that only the inhibitor is present, the cell is unable to respond to new gradients. However, in order to pursue a mathematical model based on this idea, more biological data is necessary to formulate a hypothesis.

Chapter 4

Endothelial cell deformation

4.1 Introduction

The present chapter concerns a topic very distinct from gradient sensing, the subject of the previous sections. In the model developed in this section, we investigate the mechanical effects of blood flow on endothelial cells. As opposed to previous models in which we aimed to understand biochemical signal transduction pathways, here we investigate a mechano-transduction pathway, i.e. a pathway which transmits physical signals such as forces and deformations.

Endothelial cells form a monolayer inside blood vessels, acting as a boundary between the blood flow and the vessel walls. The endothelial layer is exposed to various mechanical stresses, such as pressure, circumferential stretch, and tangential shearing forces due to blood flow. Endothelial cells respond in a wide variety of ways to these forces, and their response is thought to protect the arterial system from potential damages. Evidence supporting this hypothesis is offered by experiments which have demonstrated that the development of certain vascular diseases, such as atherosclerosis, coincides with the failure of the proper responses of the endothelium to flow.

There is an array of events that takes place in endothelial cells exposed to flow, some

of which are immediate upon the application of shear stresses, and some, which occur on the time scale of many hours. Among the fast responses are activations of flow-sensitive ion channels and activation of G-proteins. Changes in gene expression are also observed, although on these events happen on a slower time scale, and finally, cells go through morphological changes after they have been exposed to shear stress approximately a day. In steady and in pulsatile flow (a superposition of oscillatory and steady flow) endothelial cells tend to elongate and align with the direction of the flow. Such enormous changes require cells to extensively rearrange their cytoskeletal structure. Although the cytoskeletal reorganization in response to flow induced shear stress has been studied, it is still an open area of research.

The morphological changes in the cytoskeleton are well documented ([3] original source: [29, 55]), but it is unknown how the cells are able to sense shear stress, and once it is detected, how shear stress is transmitted from the cell membrane to the cytoskeleton. There have been quite a lot of previous theoretical and numerical investigations of the cytoskeletal changes produced by shearing forces. Our aim is to incorporate the effects of flow on the cytoskeleton, but in addition, we want to examine the viscoelastic behavior of other structures, such as the nucleus, cell-cell adhesions, and focal adhesion sites. However, as the cytoskeleton is thought to be the main force-bearing structure of endothelial cells, much of the deformation and mechanical response must come from it. For this reason, we summarize some previous results regarding the reorganization of cytoskeleton without attempting to provide an exhaustive review of theoretical work in this area.

Theoretical models focusing on how shear stress is transmitted often make one of two assumptions. They either propose that stress is transmitted by producing deformations in filaments, or, that there exists an internal mechanical tension inside cells independently of the external shearing forces, and that instead of significant deformations, there is simply a rotation or change in spacing in order to respond to

stress. The first assumption is consistent with a model by Satcher & Dewey, called an "open-cell foam" model, the second assumption is used by Wang & Ingber ([69], original source: [76]), and by Stamenovic et al. [69] in so called "tensegrity" models as well as "cable net" models.

Satcher & Dewey [62] investigate how shearing forces distort the polymers of the cytoskeleton: F-actin, intermediate filaments and microtubules. The thesis of their work is that F-actin stabilizes cells by decreasing deformability. The role of stress fibers, which are microfilaments connected into bundles, is also considered. Satcher & Dewey model the F-actin filaments as open lattices. (The structure of the actin filaments is similar to other material, such as glass foams, etc, hence the name "open-cell foam model".) The advantage of such a model formulation is that the Young's modulus, the measure of the material's ability to resist distortion, can be expressed in terms of filament properties, instead of having to find the density and moment of inertia for the entire F-actin cytoskeleton. With the open-lattice model properties of the cytoskeleton (shear modulus, which is the coefficient of the rigidity of a material, and the modulus of elastic deformation) are computed. The obtained values are the same order of magnitude as experimental data. The article also shows that although stress fibers increase the rigidity of the actin network, their elastic deformation is too small to effect the network, therefore their role is unclear based on the model.

Stamenovic & Coughlin [68] compare predictions of three different types of models of the cytoskeleton. The first type is the "open-cell foam" model, the second is the "cable net" model, and the third is the "tensegrity" model. The latter two share the assumption that pre-existing tensions are present in the cytoskeleton even in absence of external stress. In the cable net model the actin filaments are represented by elastic cables that are pulled tight by various forces generated inside the cell. The tensegrity model is similar: it assumes cables connected to rigid beams or "struts", and the network of struts and cables represents the cytoskeleton. The basis of comparison of the

three models is the model's estimate of Young's modulus for the cytoskeleton. This question is further complicated by the large range ($10^0 - 10^5 Pa$) given for the Young's modulus attained by different experimental techniques, such as magnetic bead microrheometry, magnetic twisting cytometry, micropipette aspiration and atomic force microscopy. The paper discusses possible ways experimental procedures might bias the obtained values.

The Young's modulus predicted by the open-cell foam model were much higher ($10^3 - 10^4 Pa$) than the Young's modulus predicted by the cable net and tensegrity models ($10 - 10^2 Pa$). The article concludes that different models may be appropriate for modeling cytoskeletal changes under different conditions. For example, the cable net and tensegrity models may be applicable in low stress whereas under large stress the cytoskeletal filaments bend, and the open-cell foam model provides a better description. The models compared by Stamenovic & Coughlin describe only the elastic properties of the cytoskeleton. However, Satcher & Dewey in [62] note that the open-cell foam model lends itself easily to the description of viscoelastic properties, if the open space between the lattices is assumed to be filled with a liquid.

Now we return to the larger goal of understanding how shear stress sensing and transduction occur in endothelial cells. One hypothesis is that shear stress deforms flow-sensitive parts of the membrane, such as certain ion-channels or receptors. The deformation of these structures could then be immediately transmitted to cytoskeletal elements connected to them. Such a mechano-transduction pathway may complement other, biochemical signaling pathways. A realistic model of the mechanical signaling pathway would allow quantitative tests of whether deformations and stresses generated in the cell would provide a sufficient signal. A previous model by Barakat [3] shows that flow sensors, modeled by a viscoelastic body, respond differently in oscillatory, pulsatile and steady flows, and the differences in the response could provide the necessary signal for downstream components of the pathway.

Our current work extends this model, and we represent other parts of the endothelial cell, namely actin filaments, the nucleus, and transmembrane proteins as viscoelastic Kelvin bodies as well. The final goal of this line of investigation is the development of a complex network of viscoelastic bodies where each body is described by experimentally obtained parameters. This dissertation is only concerned with two small networks, one consisting four, and the other one of seven viscoelastic bodies. Our work derives the equations for single bodies in series and in parallel, however, further work is necessary to describe more complicated connections (for example, n bodies connected in series which are connected to in parallel to n bodies in series again). Numerical simulations of the model are generated to test the model's dependence on parameter values, and numerical solutions of the deformation due to shear stress of the two simple model networks are also given. We discuss the implications of our results regarding endothelial cell behavior.

4.2 Mathematical Model

In this section, first we derive the equations describing the deformations of coupled Kelvin bodies and discuss solutions to the equations. Next, we describe the networks we use to model endothelial cells, and finally we discuss how the parameter values were obtained for parts of the network.

4.2.1 Kelvin bodies in series

Our goal is to develop a mathematical framework to describe the deformations of the cell surface and intracellular structure within endothelial cells with respect to steady and oscillatory flow. Kelvin bodies are the most general models for viscoelastic materials, and they have frequently been used to model how the deformation of cell tissues depends on the forcing [3], [20]. In addition, experimental data is also available which describes the viscoelastic properties of the cell nucleus [24], cytoskeletal structures [61] and transmembrane proteins [6] in terms of the parameters of a Kelvin body. This makes the Kelvin body a very effective tool for theoretical modeling of endothelial cell deformations.

First, we give the equation relating the deformation and the force exerted by the flow for one Kelvin body as derived by Fung [20]. (The derivation is very similar to the case where two Kelvin bodies are connected in parallel which is shown in detail below.)

The deformation $u(t)$ of one Kelvin body as a function of a given forcing, $F(t)$, is obtained by solving a first order linear equation (Fung, [20]):

$$F + \frac{\eta_1}{\mu_{11}} \dot{F} = \mu_{01}u + \eta_1 \left(1 + \frac{\mu_{01}}{\mu_{11}}\right) \dot{u} \quad (4.1)$$

$$u(0) = \frac{F(0)}{\mu_{01} + \mu_{11}} \quad (4.2)$$

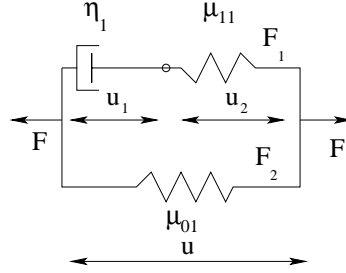


Figure 4.1: Diagram to illustrate one Kelvin body. The parameters to characterize the body are as follows. Dashpot viscosity: η_1 , spring constant in upper branch: μ_{11} , spring constant in lower branch: μ_{01} .

The solution in steady flow, $F = F_0$ is (Barakat, [3]):

$$u(t) = \frac{F_0}{\mu_0} \left[1 - \left(1 - \frac{\tau_\epsilon}{\tau_\sigma} \right) \exp \left(\frac{-t}{\tau_\sigma} \right) \right] \quad (4.3)$$

where

$$\tau_\sigma = \frac{\eta_1}{\mu_{01}} \left(1 + \frac{\mu_{01}}{\mu_{11}} \right)$$

and

$$\tau_\epsilon = \frac{\eta_1}{\mu_{11}}.$$

τ_ϵ is the relaxation time for a Kelvin body under constant strain (i.e. the stretch per unit length), and τ_σ represents the relaxation time for constant stress (i.e. the force per unit area). The deformation of the two springs in the Kelvin body is instantaneous, as it is seen from the initial condition for the deformation, 4.2 while the dashpot slowly creeps to the steady state of its deformation. Examining the expression for the deformation in steady flow (Eqn. 4.3), it is clear that large coefficients of viscosity lead to longer relaxation times under constant stress while large spring coefficients result in decreasing relaxation time. The deformation in oscillatory and pulsatile flow is also given by Barakat, [3].

When Kelvin bodies are coupled in series, the deformation for each body can be found individually, so in essence it is exactly like the one-body case. The force acting on

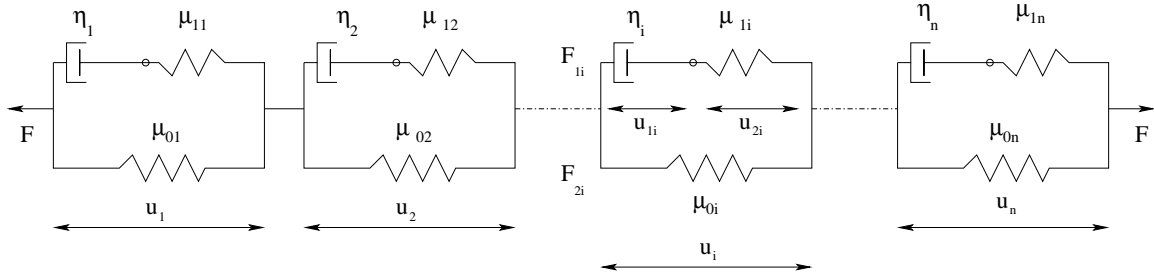


Figure 4.2: Diagram to illustrate n Kelvin bodies in series. The parameters to characterize the i th body are as follows. Dashpot viscosity: η_i , spring constant in upper branch: μ_{1i} , spring constant in lower branch: μ_{0i} .

each Kelvin body is the same, so the overall deformation can be calculated as the sum of deformations, u_i for $i=1, \dots, n$ where each deformation is the function of the same forcing function, F :

$$F + \frac{\eta_i}{\mu_{1i}} \dot{F} = \mu_{0i} u + \eta_i \left(1 + \frac{\mu_{0i}}{\mu_{1i}}\right) \dot{u}_i$$

$$u_i(0) = \frac{F(0)}{\mu_{0i} + \mu_{1i}}$$

$$u(t) = \sum_{i=1}^n u_i(t)$$

4.2.2 Kelvin bodies in parallel

We want to find the deformation for Kelvin bodies in more complicated networks. We begin by taking two Kelvin bodies coupled in parallel. Each of the Kelvin bodies is described by three parameters: the viscosity of the dashpot, and the two spring constants, as Figure 4.3 shows below.

In both the upper and the lower Kelvin body there are some relationships that must hold, namely, the total deformation, u must be a sum of the deformations of the dashpot and the spring in the upper branch, and this deformation is the same as the deformation of the spring in the lower branch. We must also note that the deformation of the upper body and the deformation of the lower body must be identical. These

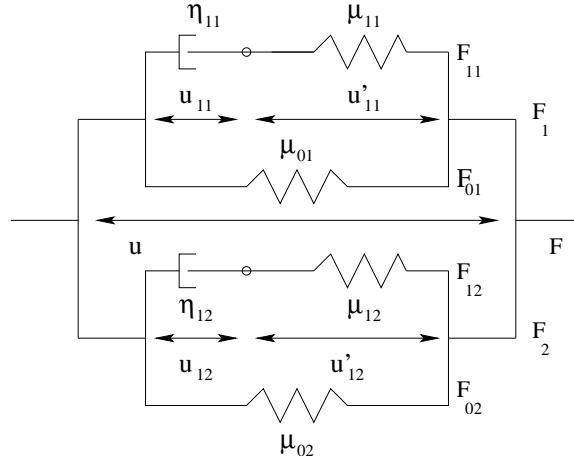


Figure 4.3: Diagram to illustrate two Kelvin bodies in parallel. The parameters to characterize the bodies are as follows. Upper Kelvin body: dashpot viscosity: η_{11} , spring constant in upper branch: μ_{11} , spring constant in lower branch: μ_{01} . Lower Kelvin body: dashpot viscosity: η_{12} , spring constant in upper branch: μ_{12} , spring constant in lower branch: μ_{02} .

relationships give us the following equations.

$$u_{11} + u'_{11} = u$$

$$u_{12} + u'_{12} = u$$

Another observation is that the total force, F of the two bodies splits into the force in the upper body, F_1 and the force in the lower body, F_2 . The total force in the upper body is also given as a sum of the force in the upper branch and the lower branch, and similarly for the lower body. This is described by the equations:

$$F_1 + F_2 = F$$

$$F_{01} + F_{11} = F_1$$

$$F_{02} + F_{12} = F_2$$

Now let us consider the upper body only. The same force in the upper branch, F_{11} is transmitted from the dashpot to the spring. The force acting on the spring is

proportional to the deformation it produces, and the force acting on the dashpot is proportional to the velocity of the dashpot. Using the variables of the diagram we can write this as:

$$F_{11} = \eta_{11}\dot{u}_{11} = \mu_{11}u'_{11}.$$

Here \dot{u}_{11} denotes the derivative of u_{11} , the deformation of the dashpot, and u'_{11} is the deformation of the spring. The force in the lower branch of this body acts entirely on the dashpot, and here the deformation is going to be the sum of the deformation due to the dashpot plus the deformation due to the spring in the upper branch, therefore

$$F_{01} = \mu_{01}(u_{11} + u'_{11}).$$

Similarly, we can write down the corresponding equations for the lower body as well.

$$F_{12} = \eta_{12}\dot{u}_{12} = \mu_{12}u'_{12}$$

$$F_{02} = \mu_{02}(u_{12} + u'_{12})$$

Using the nine equations above, one can derive two differential equations that describe the the deformation of the two coupled Kelvin bodies as a function of time and the force acting on the bodies, with the appropriate boundary conditions. The derivation is similar to Fung's [20]. In the equations below we assume that $F(t)$ is given, therefore we can also find $\dot{F}(t)$. For the particular forcing functions we are interested in, the derivative always exists, and it is continuous.

$$\begin{aligned} F_1 + \frac{\eta_{11}}{\mu_{11}}\dot{F}_1 &= \mu_{01}u + \eta_{11}\left(1 + \frac{\mu_{01}}{\mu_{11}}\right)\dot{u} \\ u(0) &= \frac{F_1(0)}{\mu_{01} + \mu_{11}} \end{aligned} \tag{4.4}$$

$$\begin{aligned} F_2 + \frac{\eta_{12}}{\mu_{12}}\dot{F}_2 &= \mu_{02}u + \eta_{12}\left(1 + \frac{\mu_{02}}{\mu_{12}}\right)\dot{u} \\ u(0) &= \frac{F_2(0)}{\mu_{02} + \mu_{12}} \end{aligned} \tag{4.5}$$

Now we can use the fact that F_1 and F_2 sum to F to substitute $a(t)F(t) = F_1(t)$ and $1 - a(t)F(t) = F_2(t)$. $a(t)$ is the coefficient of force splitting, and it is an unknown function of time.

$$aF + \frac{\eta_{11}}{\mu_{11}}(a\dot{F}) = \mu_{01}u + \eta_{11}\left(1 + \frac{\mu_{01}}{\mu_{11}}\right)\dot{u}$$

$$u(0) = \frac{a(0)F(0)}{\mu_{01} + \mu_{11}} \quad (4.6)$$

$$(1 - a)F + \frac{\eta_{12}}{\mu_{12}}((1 - a)\dot{F}) = \mu_{02}u + \eta_{12}\left(1 + \frac{\mu_{02}}{\mu_{12}}\right)\dot{u}$$

$$u(0) = \frac{(1 - a(0))F(0)}{\mu_{02} + \mu_{12}} \quad (4.7)$$

Now we have a system of two differential equations with initial conditions and two unknown functions, $u(t)$ and $F(t)a(t)$, and we would like to solve for them. Solving the equations for $u(t)$ and $a(t)$ is not practical, for two reasons. For particular choices of the flow, for example, for oscillatory flow $F(t) = F_0 \cos(\omega t)$, the matrix A , defined below, would depend on the forcing function, and A^{-1} would become singular periodically when $\cos(\omega t) = 0$. Also, matrices A and D (also defined below) would both depend on time, and this could considerably slow down the computations. In order to avoid these problems, we compute $u(t)$ and $F(t)a(t)$. $F(t)$ is a known function of time, so it is always possible to find $a(t)$, if necessary. Now rearranging equations 4.6 and 4.7 gives us the following.

$$\begin{bmatrix} \eta_{11}\left(1 + \frac{\mu_{01}}{\mu_{11}}\right) & -\frac{\eta_{11}}{\mu_{11}} \\ \eta_{12}\left(1 + \frac{\mu_{02}}{\mu_{12}}\right) & \frac{\eta_{12}}{\mu_{12}} \end{bmatrix} \begin{bmatrix} \dot{u} \\ (a\dot{F}) \end{bmatrix} = \begin{bmatrix} -\mu_{01} & 1 \\ -\mu_{02} & -1 \end{bmatrix} \begin{bmatrix} u \\ (aF) \end{bmatrix}$$

$$+ \begin{bmatrix} 0 \\ F + \frac{\eta_{12}}{\mu_{12}}\dot{F} \end{bmatrix}$$

$$\begin{bmatrix} u(0) \\ a(0)F(0) \end{bmatrix} = \begin{bmatrix} \frac{F(0)}{\mu_{01} + \mu_{11} + \mu_{02} + \mu_{12}} \\ \frac{F(0)(\mu_{01} + \mu_{11})}{\mu_{01} + \mu_{11} + \mu_{02} + \mu_{12}} \end{bmatrix} \quad (4.8)$$

We can let

$$A = \begin{bmatrix} \eta_{11}(1 + \frac{\mu_{01}}{\mu_{11}}) & -\frac{\eta_{11}}{\mu_{11}} \\ \eta_{12}(1 + \frac{\mu_{02}}{\mu_{12}}) & \frac{\eta_{12}}{\mu_{12}} \end{bmatrix}$$

$$D = \begin{bmatrix} -\mu_{01} & 1 \\ -\mu_{02} & -1 \end{bmatrix}$$

$$\vec{c} = \begin{bmatrix} 0 \\ F + \frac{\eta_{12}}{\mu_{12}} \dot{F} \end{bmatrix}$$

$$\vec{u} = \begin{bmatrix} u(t) \\ a(t)F(t) \end{bmatrix}$$

Now we can write the system of equations as

$$A \frac{d\vec{u}}{dt} = D\vec{u} + \vec{c}.$$

In order to compute the solution for \vec{u} , we can express the system of differential equations in the form

$$\frac{d\vec{u}}{dt} = A^{-1}D\vec{u} + A^{-1}\vec{c} \quad (4.9)$$

$$\vec{u}(0) = \vec{u}_0 \quad (4.10)$$

This is the equation with the appropriate initial conditions that describes the dynamics of two Kelvin bodies coupled in parallel.

Now we can look at a generalization of the two body problem to deriving the differential equations governing n Kelvin bodies coupled in parallel. Let us start again with the diagram of the bodies with their appropriate parameters, shown in Figure 4.4. As before, the sum of the forces in the branches has to be the total force, F .

$$\sum_{i=1}^n F_i = F$$

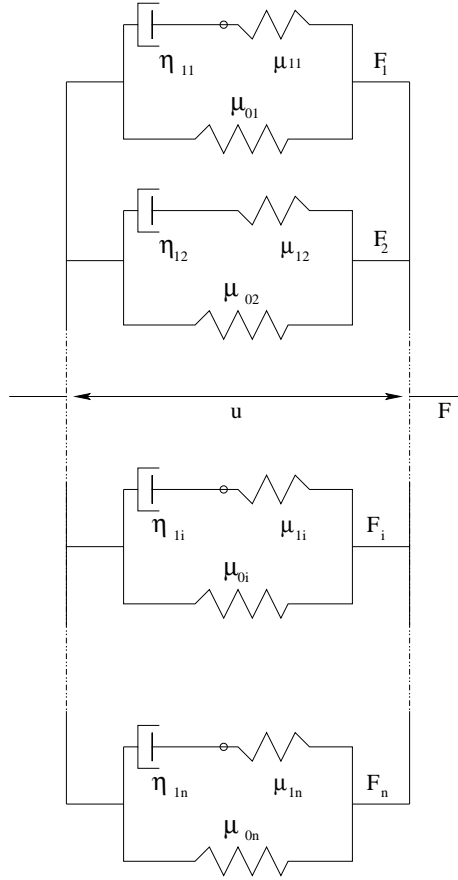


Figure 4.4: Diagram to illustrate n Kelvin bodies in parallel. The parameters to characterize the bodies are as follows. i th body (for $i=1, \dots, n$): dashpot viscosity: η_{1i} , spring constant in upper branch: μ_{1i} , spring constant in lower branch: μ_{0i} .

In general, we do not know how the forces split into these branches because this depends on the particular parameter values of the Kelvin bodies. Therefore we can call the force splitting coefficient for the i th branch to be $a_i(t)$, and the force in this branch $a_i(t)F(t)$. Using the above relationship we get the following:

$$\left(1 - \sum_{i=1}^{n-1} a_i\right)F = F_n$$

The equation for the the i th body for $i = 1, \dots, n - 1$ is:

$$a_i F + \frac{\eta_{1i}}{\mu_{1i}}(a_i \dot{F}) = \mu_{0i} u + \eta_{1i} \left(1 + \frac{\mu_{0i}}{\mu_{1i}}\right) \dot{u}$$

$$u(0) = \frac{a_i(0)F(0)}{\mu_{0i} + \mu_{1i}} \quad (4.11)$$

And for the n th body we have a similar expression:

$$\left(1 - \sum_{i=1}^{n-1} a_i\right) F + \frac{\eta_{1n}}{\mu_{1n}} \cdot \frac{d}{dt} \left(\left(1 - \sum_{i=1}^{n-1} a_i\right) F \right) = \mu_{0n} u + \eta_{1n} \left(1 + \frac{\mu_{0n}}{\mu_{1n}}\right) \dot{u}$$

$$u(0) = \frac{\left(1 - \sum_{i=1}^{n-1} a_i(0)\right) F(0)}{\mu_{0n} + \mu_{1n}} \quad (4.12)$$

Now we must rearrange the equations so we are solving for $u(t)$ and $a_i(t)F(t)$ again.

When we rearrange differential equations we get for $i = 1, \dots, (n - 1)$:

$$\eta_{1i} \left(1 + \frac{\mu_{0i}}{\mu_{1i}}\right) \dot{u} - \frac{\eta_{1i}}{\mu_{1i}}(a_i \dot{F}) = -\mu_{0i} u + a_i F$$

for n :

$$\eta_{1n} \left(1 + \frac{\mu_{0n}}{\mu_{1n}}\right) \dot{u} + \frac{\eta_{1n}}{\mu_{1n}} \sum_{i=1}^{n-1} (a_i \dot{F}) = -\mu_{0n} u - \sum_{i=1}^{n-1} a_i F + F + \frac{\eta_{1n}}{\mu_{1n}} \dot{F}$$

We also need to find the appropriate expression for the initial conditions. We have, first for $i = 1, \dots, (n - 1)$:

$$u(0)(\mu_{0i} + \mu_{1i}) = a_i(0)F(0) \quad (4.13)$$

and for $i=n$:

$$u(0) = \frac{F(0) - F(0) \sum_{i=1}^{n-1} a_i(0)}{\mu_{0n} + \mu_{1n}} \quad (4.14)$$

$u(0)$, the initial deformation of all of the bodies is the same, so we get n equations and n unknowns: $u(0)$ and $a_i(0)$ for $i=1, \dots, n-1$. The force splitting coefficient of the n th body is already determined from this to be $a_n(0) = 1 - \sum_{i=1}^{n-1} a_i(0)$. We must rearrange the equations 4.13 and 4.14 to solve for $u(0)$ and $a_i(0)$.

$$u(0)(\mu_{0n} + \mu_{1n}) = F(0) - \sum_{i=1}^{n-1} a_i(0)F(0)$$

$$u(0)(\mu_{0n} + \mu_{1n}) = F(0) - \sum_{i=1}^{n-1} u(0)(\mu_{0i} + \mu_{1i})$$

$$u(0) \sum_{i=1}^n (\mu_{0i} + \mu_{1i}) = F(0)$$

Therefore the initial conditions are:

$$u(0) = \frac{F(0)}{\sum_{i=1}^n (\mu_{0i} + \mu_{1i})}$$

$$a_i(0) = \frac{F(0)(\mu_{0i} + \mu_{1i})}{\sum_{i=1}^n (\mu_{0i} + \mu_{1i})}$$

Now we can look at the equations in matrix form:

$$A = \begin{bmatrix} \eta_{11}(1 + \frac{\mu_{01}}{\mu_{11}}) & -\frac{\eta_{11}}{\mu_{11}} & 0 & \cdots & \cdots & \cdots & 0 \\ \eta_{12}(1 + \frac{\mu_{02}}{\mu_{12}}) & 0 & -\frac{\eta_{12}}{\mu_{12}} & 0 & \cdots & \cdots & 0 \\ \vdots & \vdots & & \ddots & & & \vdots \\ \eta_{1i}(1 + \frac{\mu_{0i}}{\mu_{1i}}) & 0 & & & -\frac{\eta_{1i}}{\mu_{1i}} & & 0 \\ \vdots & \vdots & & & & \ddots & \vdots \\ \eta_{1(n-1)}(1 + \frac{\mu_{0(n-1)}}{\mu_{1(n-01)}}) & 0 & \cdots & \cdots & \cdots & 0 & -\frac{\eta_{1(n-1)}}{\mu_{1(n-1)}} \\ \eta_{1n}(1 + \frac{\mu_{0n}}{\mu_{1n}}) & \frac{\eta_{1n}}{\mu_{1n}} & \cdots & \cdots & \cdots & \cdots & \frac{\eta_{1n}}{\mu_{1n}} \end{bmatrix}$$

$$D = \begin{bmatrix} -\mu_{01} & 1 & 0 & \cdots & \cdots & \cdots & 0 \\ -\mu_{02} & 0 & 1 & 0 & \cdots & \cdots & 0 \\ \vdots & \vdots & & \ddots & & & \vdots \\ -\mu_{0i} & 0 & & & 1 & & 0 \\ \vdots & \vdots & & & & \ddots & \vdots \\ -\mu_{0(n-1)} & 0 & \cdots & \cdots & \cdots & \cdots & 1 \\ -\mu_{0n} & -1 & \cdots & \cdots & \cdots & \cdots & -1 \end{bmatrix}$$

$$c = \begin{bmatrix} 0 \\ \vdots \\ 0 \\ F + \frac{\eta_{12}}{\mu_{12}} \dot{F} \end{bmatrix}$$

Just like before, we have the differential equation for $\vec{u}(t)$, an $n \times 1$ vector whose entries are $u(t)$ and $a_i(t)F(t)$ for $i = 1, \dots, (n - 1)$ with the appropriate initial conditions:

$$\begin{aligned} \frac{d\vec{u}(t)}{dt} &= A^{-1}D\vec{u} + A^{-1}c \\ \vec{u}(0) &= \vec{u}_0 \end{aligned}$$

This is the same linear equation as 4.9 and 4.10 with the matrix $A^{-1}D$ and vector $A^{-1}c$ defined appropriately, and its solution is given by

$$\vec{u} = (\vec{u}_0 + D^{-1}c)e^{\Lambda t} - A^{-1}c \tag{4.15}$$

where Λ is a diagonal matrix whose eigenvalues are the same as the eigenvalues of the matrix $M = A^{-1}D$. (Obtaining the solution to equations 4.9 and 4.10 is similar to the derivation shown in Appendix B.3.) Let us first discuss how to find $D^{-1}c$ and $A^{-1}c$, then turn to finding Λ . If $D^{-1}c = y$, then $c = Dy$, in other words,

$$\begin{bmatrix} 0 \\ \vdots \\ \vdots \\ 0 \\ F + \frac{\eta_{1n}}{\mu_{1n}} \dot{F} \end{bmatrix} = \begin{bmatrix} -\mu_{01} & 1 & 0 & \cdots & 0 \\ -\mu_{02} & 0 & 1 & & 0 \\ \vdots & \vdots & & \ddots & \vdots \\ -\mu_{0(n-1)} & 0 & \cdots & \cdots & 1 \\ -\mu_{0n} & -1 & \cdots & \cdots & -1 \end{bmatrix} \begin{bmatrix} y_1 \\ y_2 \\ \vdots \\ y_{n-1} \\ y_n \end{bmatrix}$$

In the i th row we have $-\mu_{0i}y_1 + y_{i+1} = 0$, and this implies that for $i=1, \dots, n-1$

$$y_{i+1} = y_1 \mu_{0i}.$$

In the n th row we get $-\mu_{0n}y_1 - \sum_{i=2}^n y_i = F + \frac{\eta_{1n}}{\mu_{1n}} \dot{F}$. By substituting the expression for y_{i+1} in terms of y_1 into this

$$y_1(-\mu_{0n} - \sum_{i=2}^n \mu_{0i-1}) = F + \frac{\eta_{1n}}{\mu_{1n}} \dot{F}.$$

$$y_1 = \frac{F + \frac{\eta_{1n}}{\mu_{1n}} \dot{F}}{-\mu_{0n} - \sum_{i=2}^n \mu_{0i-1}}$$

This gives an explicit formula for y_1 and based on our expression for y_i in terms of y_1 we can find all the other components of y .

We can use a similar argument to find $x = A^{-1}c$. If we let $h_i = \eta_{1i}(1 + \frac{\mu_{0i}}{\mu_{1i}})$ and $d_i = -\frac{\eta_{1i}}{\mu_{1i}}$ then we get that

$$x_1 = \frac{F + \frac{\eta_{1n}}{\mu_{1n}} \dot{F}}{h_n - d_n \sum_{i=1}^{n-1} \frac{h_i}{d_i}}$$

$$x_{i+1} = \frac{h_i x_1}{d_i}.$$

Now let us return to the matrix of eigenvalues, Λ . We are looking for the diagonal matrix whose entries $\lambda_1, \dots, \lambda_n$ satisfy the equation $A^{-1}Dx = \lambda_i x$ for $i=1, \dots, n$ and for $x \neq 0$. This is equivalent to $(D - \lambda_i A)x = 0$ which is called the generalized eigenvalue problem. It is easy to see that the matrix $(D - \lambda_i A)$ has the same very nice and sparse structure that both A and D have, but solving the generalized eigenvalue problem leads to having to find the roots of an n th degree polynomial. In the most general case this can only be solved numerically, but some special cases of the problem can be solved analytically (for example, if all n Kelvin bodies have the same parameter values). Other methods can also be applied to solve the original system of linear differential equations, for example Laplace transform methods, but they lead to the same problem of having to find roots of an n -degree polynomial.

In this dissertation we only use networks with two Kelvin bodies in parallel, and in these cases the deformation can be found analytically as well as numerically, because it only requires finding solutions to a quadratic equation. Extensions of the model to a large number of bodies in parallel would have to be done numerically, and even

analytical solutions can only be found by numerically computing the roots of an n th-degree polynomial.

4.2.3 Model networks

The aim of our model is to gain further understanding of how flow over the surface of endothelial cells leads to regulation of the cell shape. It is known that the cytoskeletal structure is re-organized in a period of approximately a day, but there is no clear evidence to what extent biochemical events, and to what extent purely mechanical processes contribute to this. We want to examine how the flow-induced shear stress which deforms flow sensors is transmitted through the cytoskeleton to the nucleus and to other transmembrane proteins such as ion channels and attachments to the substrate. We want to use networks of coupled Kelvin bodies to model endothelial cells, and we want to investigate how deformations of the individual parts will contribute to the overall deformation of the cell.

The cytoskeleton consists of three types of polymers: actin filaments, microtubules and intermediate filaments each of which deform if shear stress is applied to the cell [62]. Qualitatively, actin filaments rupture at relatively low strain, but actin can be rapidly recycled and filaments re-formed as it is required for cell motility, among its other functions. Below a critical strain actin networks show the greatest rigidity [34]. Microtubule networks can withstand very high strain, and the greatest deformability. This is consistent with their role as structural support of the actin filaments [34]. Vimentin networks, which mostly make up the intermediate filaments, tend to be less rigid at low shear strain, but they harden at high strains. These responses make them ideal for the support of nucleus [34]. Because of this, we expect very significant differences in the responses of the actin cytoskeleton and the nucleus of the cell.

Based on the above, we choose a simple network to model an endothelial cell. This model is shown in Figure 4.5. The flow sensor, body 1, is attached to the actin

cytoskeleton which is represented by bodies 2 and 3 in parallel. The actin cytoskeleton then attaches to the nucleus, body 4 in the diagram.

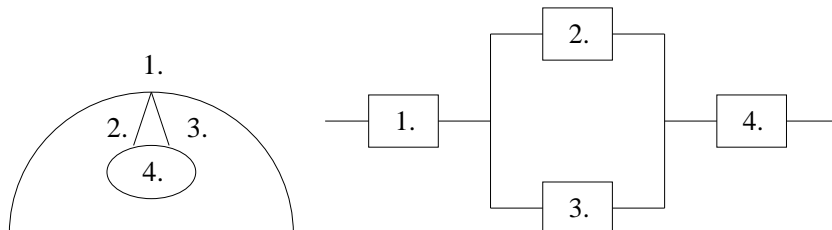


Figure 4.5: Model I. of an endothelial cell.

Next, we can elaborate on our initial diagram and add the connections between the nucleus and the attachments to the substrate. Part of this second model is the same as the first network, but now the nucleus (body 4) is further connected to actin bundles (bodies 5 and 6) that end at transmembrane proteins (body 7).

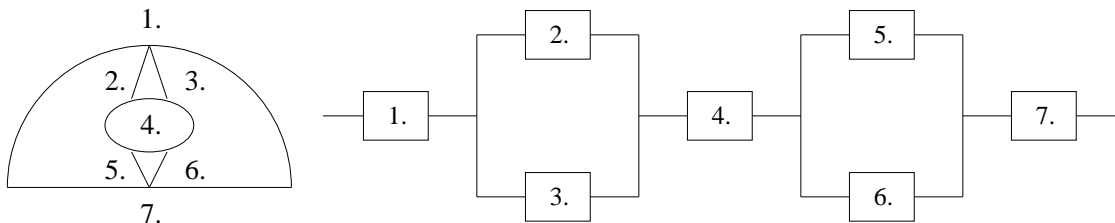


Figure 4.6: Model II. of an endothelial cell.

4.2.4 Parameter values

Appropriate parameter values must be chosen for all of the bodies. The parameter values for the actin filaments are taken from Sato et al. [61] who measure viscoelastic properties of endothelial cells with a micropipette technique. Guilak et al. give the parameter values for the nucleus based on a study also with a micropipette aspiration, and they conclude that the nucleus is about 3-4 stiffer and approximately twice as viscous as the cytoplasm [24]. Finally, the parameter values for transmembrane proteins is found by Bausch et al. [6] who use the novel technique of magnetic bead

microrheometry. All the parameter values are summarized in Table 4.1.

	η_1 (Pa s)	μ_{01} (Pa)	μ_{11} (Pa)	Ref.
Actin filaments	5000	50	100	[61]
Nucleus	10 000	200	400	[24]
Transmembrane proteins	7.5	100	200	[6]

Table 4.1: Parameter values for the endothelial cell models

The parameter values for transmembrane proteins were given in the original paper in units of Pa m for the spring constants and Pa s m for the dashpot viscosity, and had to be converted to Pa and Pa s, respectively. These calculations are given below.

Sato et al. give the formula for the deformation as

$$L(t) = \frac{2a\Delta p}{\pi\mu_{01}} \left(1 - \frac{\mu_{11}}{\mu_{01} + \mu_{11}} e^{-\frac{t}{\tau}}\right).$$

The dimensions are as follows: $[a] = \text{m}$, $[\Delta p] = \text{Pa}$ and $[\mu_{01}, \mu_{11}] = \text{Pa}$. The formula for the deformation in Bausch et al. is

$$L(t) = \frac{F}{\mu_{01}} \left(1 - \frac{\mu_{11}}{\mu_{01} + \mu_{11}} e^{-\frac{t}{\tau}}\right)$$

with dimensions $[F] = \text{N}$, $[\mu_{01}, \mu_{11}] = \text{Pa m} = \text{N/m}$. In order to compare the spring constants given in the two papers, we must have them in the same dimensions. First we will find what the applied force is in Sato et al., then we use the expression for the initial deformation and final deformation to determine the spring constants. The force is given by $F = \Delta p \pi a^2 \simeq 2500 \text{ pN}$. The initial deformation,

$$L_0(t) = \frac{F}{\mu_{01}} \left(1 - \frac{\mu_{11}}{\mu_{01} + \mu_{11}}\right) = \frac{F}{\mu_{01} + \mu_{11}}$$

and the deformation at steady state is

$$L_s(t) = \frac{F}{\mu_{01}}.$$

Using the data in Sato et al. this gives us $\mu_{01} = 6.35 \times 10^{-4} \text{ Pa m}$ and $\mu_{11} = 9.38 \times 10^{-4} \text{ Pa m}$. The same calculations with the data in Bausch et al. leads to $\mu_{01} = 1.25 \times 10^{-3}$

Pa m and $\mu_{11} = 1.61 \times 10^{-3}$ Pa m. Finally, we must obtain the viscosity of the dashpot, η_1 .

$$\eta_1 = \frac{\tau \mu_{01} \mu_{11}}{\mu_{01} + \mu_{11}}.$$

In Sato, $\eta_1 = 4.125 \times 10^{-2}$ Pa m s and in Bausch $\eta_1 = 6.33 \times 10^{-5}$ Pa m s. Now we can compare the parameter values. μ_{01} and μ_{02} for the nucleus is approximately twice the value of μ_{01} and μ_{11} , respectively, for actin filaments, and the viscosity in the nucleus is approximately 1.5×10^{-3} the dashpot viscosity of actin filaments. Based on this we arrive at:

$$\mu_{01} = 2(50) = 100 \text{ Pa}$$

$$\mu_{11} = 2(100) = 200 \text{ Pa}$$

$$\eta_1 = (1.5 \times 10^{-3})(5000) = 7.5 \text{ Pa s}.$$

4.3 Results

This section contains two sets of numerical simulations. The first set of simulations examines the relationships between the parameters of the Kelvin bodies and the deformation, $u(t)$ and the force splitting, $a(t)F(t)$ in a the two-body problem. Both steady and oscillatory flow are considered.

The second set of simulations takes the four-body and the seven-body model networks with realistic parameter values and finds the temporal dynamics of the deformation, and the force splitting coefficients.

The differential equations are solved with a four-stage fourth-order Runge-Kutta method. The Matlab code used to solve the equations is presented in Appendix C. The time step chosen for the simulations is $h = 0.1$. This method is of order 4, so the error is $O(h^5) = 0.00001$.

4.3.1 Parameter sensitivity analysis

We investigate the behavior of two Kelvin bodies coupled in parallel. We focus on three questions:

- temporal dynamics of the system with one parameter value changed over three orders of magnitude;
- the steady state behavior of the system as a parameter value is changed over several orders of magnitude;
- the behavior of the system when all three parameters are changed over three orders of magnitude

This analysis allows us to understand how the parameter values determine the viscoelastic properties of a material which gives us intuition into the behavior of the more complicated model networks involving materials of different properties.

In all of the figures depicting the deformation $u(t)$ and the force splitting, $a(t)F(t)$, the parameters for body one are set to baseline levels, $\mu_{01} = 50$, $\mu_{11} = 100$ and $\eta_{11} = 5000$. With the exception of Figures 4.30-4.33 in which all three parameters of body 2 are changed, in all other figures of this section two parameters of body two are kept constant, and only one parameter is changed. When the steady state behavior of the two Kelvin bodies is investigated, the following values are used: $\mu_{02} = \mu_{12} = 1, 2.5, 5, 7.5, 10, 25, 50, 75, 100, 250, 500, 750$ and 1000 and $\eta_{12} = 1, 2, 5, 10, 20, 50, 100, 250, 500, 1000, 2500, 5000, 10000, 25000, 50000$ and $100\ 000$. The baseline value for η_{12} is larger than the other two constants, and this is why we consider much larger values when examining the steady state behavior. The figures show which parameter is altered, and the values used in the simulations. The time steps of the simulations are $h = 0.1$, so one second of time is depicted by ten time steps on the graphs.

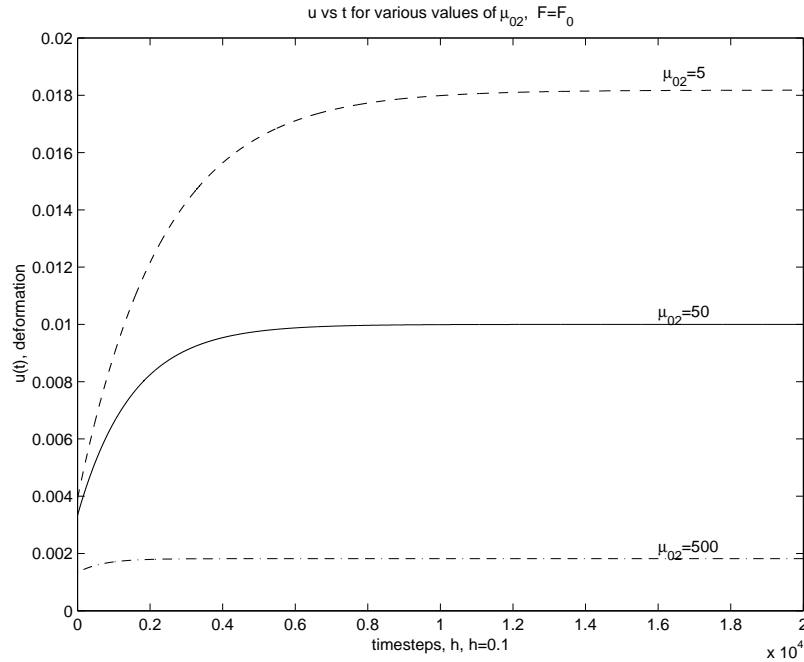


Figure 4.7: Dependence of deformation on μ_{02} . Steady flow.

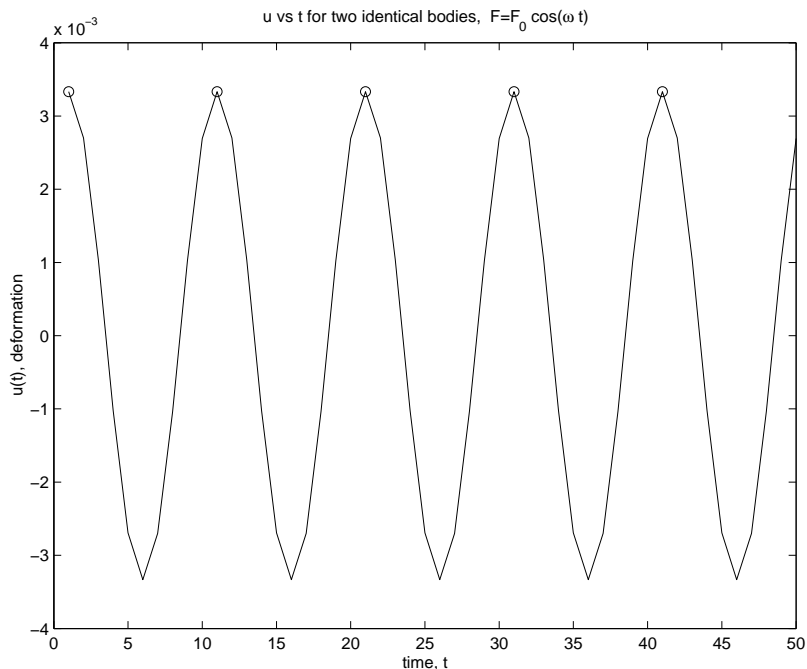


Figure 4.8: Oscillations in the deformation for a particular value of μ_{02} . The circles show the only points which are displayed in the subsequent figures displaying the dependence of deformation on parameter values. Oscillatory flow.

Figures 4.7-4.10 show the deformation of the two body model as one of the spring constants, μ_{02} changes. (μ_{02} is the constant that characterizes the isolated spring.) Figure 4.7 shows the deformation in steady flow for three values of the spring constant $\mu_{02} = 5, 50, 500$. The spring becomes stiffer as μ_{02} increases, and this results in reducing the deformation, because the spring is more difficult to stretch. The steady state is reached very quickly for μ_{02} large.

Figure 4.8 illustrates the treatment of oscillatory flow. Because the frequency of oscillations is high, we do not want to display all the oscillations, only the peak values that the deformation reaches. These values are marked with an 'o' on this figure, and in subsequent graphs of oscillatory flow only these are displayed. We also note in this figure that the steady state value in oscillatory flow is obtained within the first few

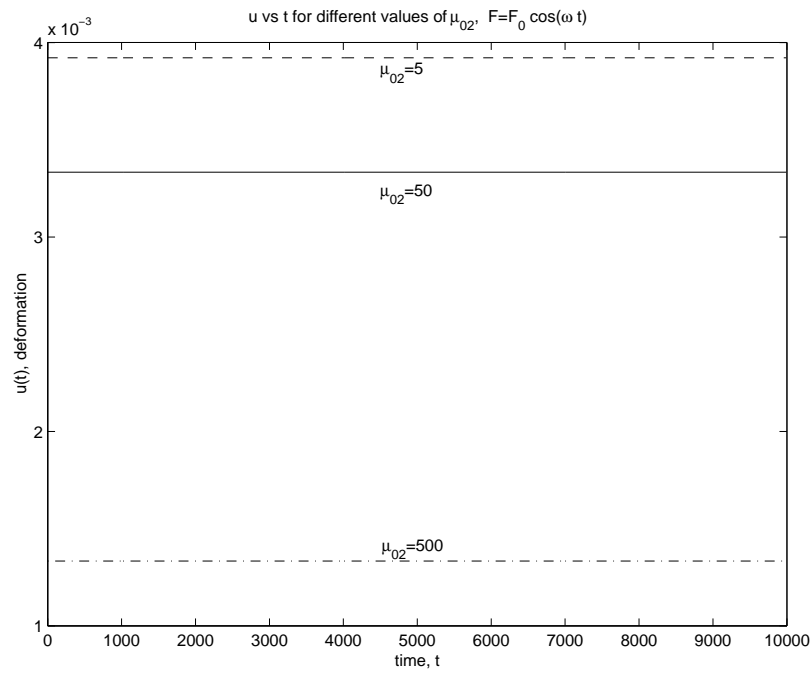


Figure 4.9: Dependence of deformation on μ_{02} . Oscillatory.

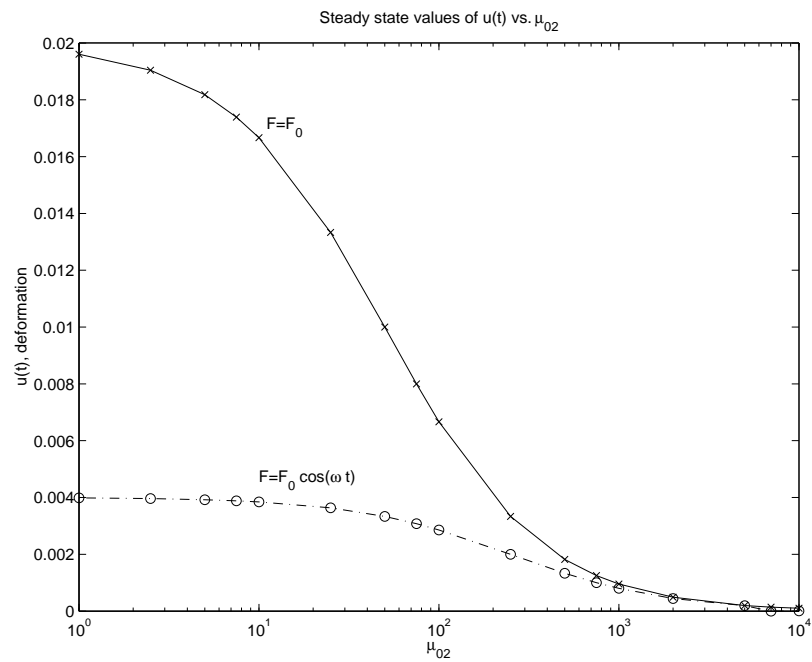


Figure 4.10: Dependence of steady state deformation on μ_{02} .

oscillations (2-3) seconds. This observation is confirmed by figure 4.9 which depicts the time evolution of the deformation for oscillatory flow as the spring constant μ_{02} is varied. The steady state of the deformation is reached almost immediately, and it is a very small value (≈ 0.004), even if the spring constant is small $\mu_{02} = 5$. Stiffer springs result in even smaller deformations, as expected.

We can compare how the steady state of deformation changes with the spring constant μ_{02} in steady flow, and the steady state of the peak deformation in oscillatory flow in Figure 4.10. Each peak value is obtained after 2×10^4 time steps, which corresponds to 2000 time units (seconds). Clearly, much larger deformation is produced in steady flow than in oscillatory flow, then, as the spring becomes increasingly stiff, the deformation tends to zero regardless of the flow.

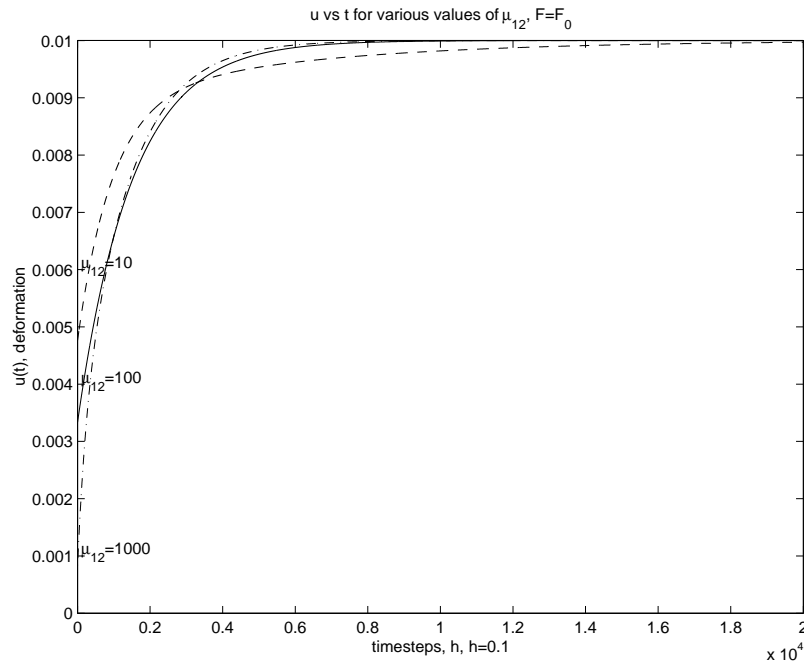


Figure 4.11: Dependence of deformation on μ_{12} . Steady flow.

The next three figures, Figures 4.11-4.13 show how the deformation of a cell changes as the other spring constant of body two, μ_{12} changes. (This spring constant charac-

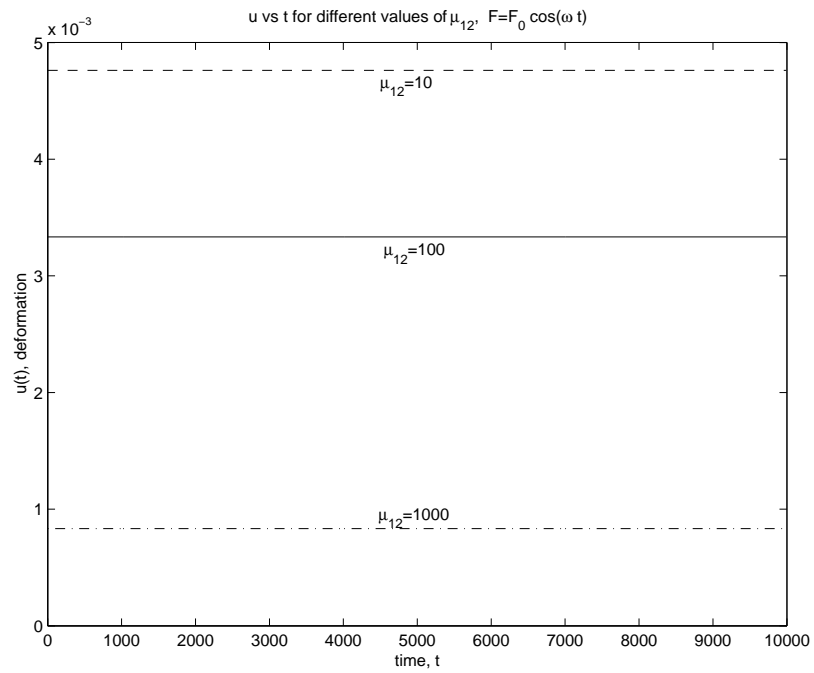


Figure 4.12: Dependence of deformation on μ_{12} . Oscillatory flow.

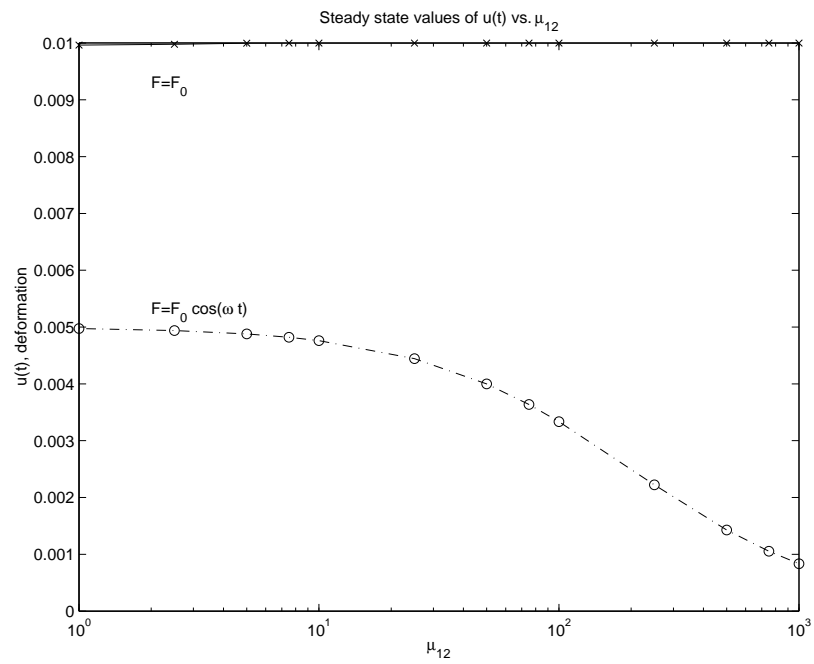


Figure 4.13: Dependence of steady state deformation on μ_{12} .

terizes the spring next to the dashpot in the second Kelvin body.) Figure 4.11 shows that although the initial deformation is different for the three values of μ_{12} (as one expects, because the initial condition depends on μ_{12}), the steady state obtained is the same for the three values. Similarly, in Figure 4.12, we see that in oscillatory flow the steady state is obtained virtually immediately again (in 2-3 seconds), and that the deformation for all three values of μ_{12} is very small, less than 0.005.

In Figure 4.13 most steady state values are obtained after 2000 seconds again. In oscillatory flow, as the spring becomes stiffer, the deformation decreases, just like it did in Figure 4.10. However, in steady flow, the deformation stays almost the same regardless of the spring constant. This is due to more of the force concentrating on the dashpot if the spring is very pliable. In this case the steady state value is obtained slower too, in (3000 seconds) which also suggests that the force is concentrated on the dashpot which creeps to the steady deformation slower. Just like before, the overall deformation is always smaller in oscillatory flow, because the oscillatory flow only produces a large force periodically and not continuously. Also, there is a force of equal magnitude but opposite direction acting on the dashpot periodically, therefore the dashpot is unable to extend fully. (This claim is verified later in simulations where the frequency of oscillations is changed, allowing the dashpot more time to deform.) When the spring next to the dashpot is very pliable, i.e for small values of μ_{12} , much of the force is allowed to act on the dashpot, therefore the overall deformation is larger when the μ_{12} is changed (Figure 4.13) than if μ_{02} is changed (Figure 4.10).

Now we turn to examining how the dashpot viscosity influences the behavior of the system. Figures 4.14 and 4.15 depict the time evolution of the deformation for $\eta_{12}=500, 5000$ and 50000 . In steady flow the steady state of the deformation is the same regardless of the value of η_{12} , but for large dashpot viscosities the steady state takes longer to obtain, approximately 5000 seconds. Figure 4.15 shows the steady state of the deformation in oscillatory flow. For the three values of η_{12} shown here,

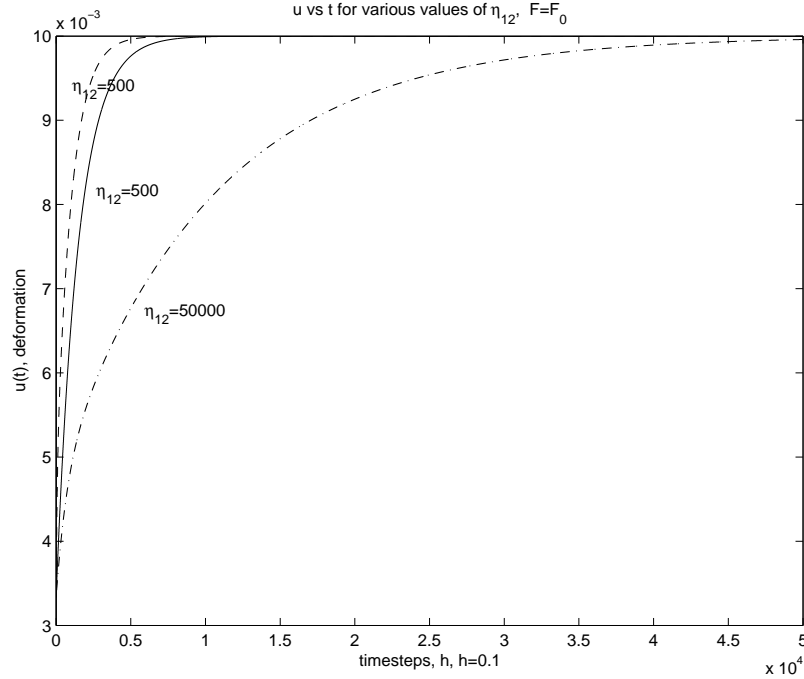


Figure 4.14: Dependence of deformation on η_{12} . Steady flow.

the difference in deformations is negligible, on the order of 10^{-6} . The largest deformation is obtained when η_{12} is the smallest, and the bodies in this case deform very quickly, within the first 100 seconds.

Figure 4.16 is created by running the simulations longer than in the previous figures, to time $t = 1.2 \times 10^4$ seconds to ensure that the deformation reaches its steady state. In oscillatory flow, the steady state of the deformation is slightly larger for small dashpot viscosities, but after about $\eta_{12} = 100$, the deformation is independent of the viscosity. The interpretation of this is that when the viscosity is sufficiently low, the force is able to deform the dashpot quickly, then, as the forcing oscillates the deformation remains the same. For larger viscosities the initial deformation of the dashpot is negligible, and the later oscillations are again unable to change the deformation of the dashpot. As noted before, the deformation in steady flow is independent of the dashpot viscosity.

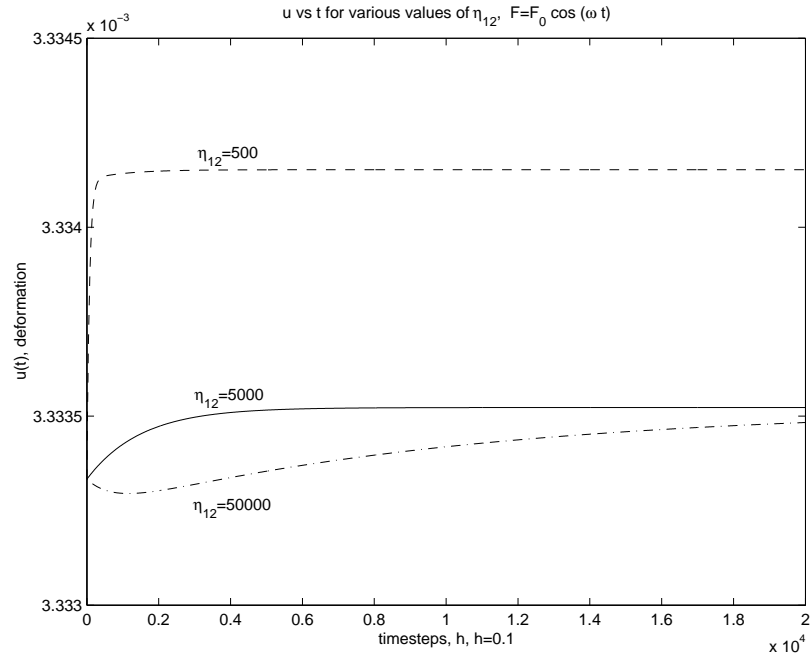


Figure 4.15: Dependence of deformation on η_{12} . Oscillatory flow.

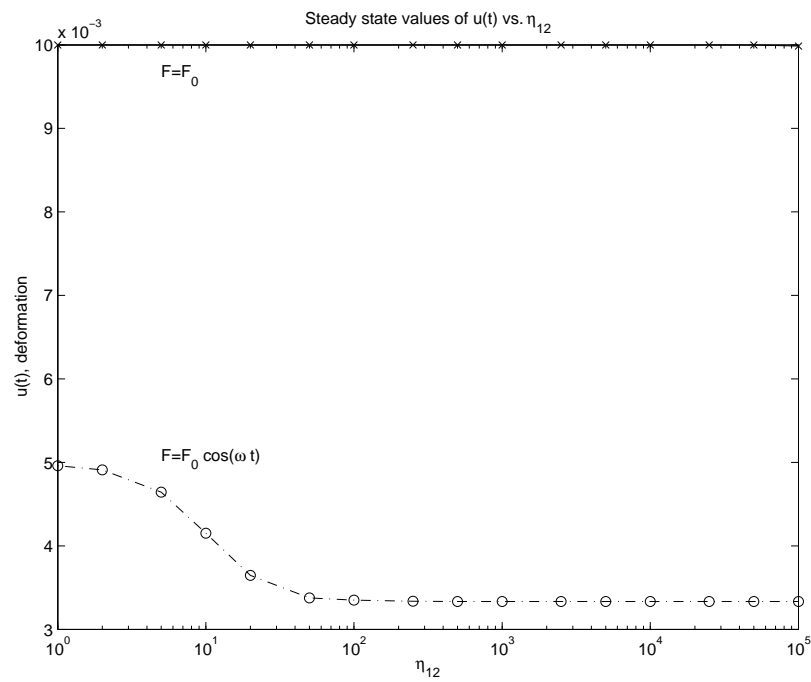


Figure 4.16: Dependence of steady state deformation on η_{12} .

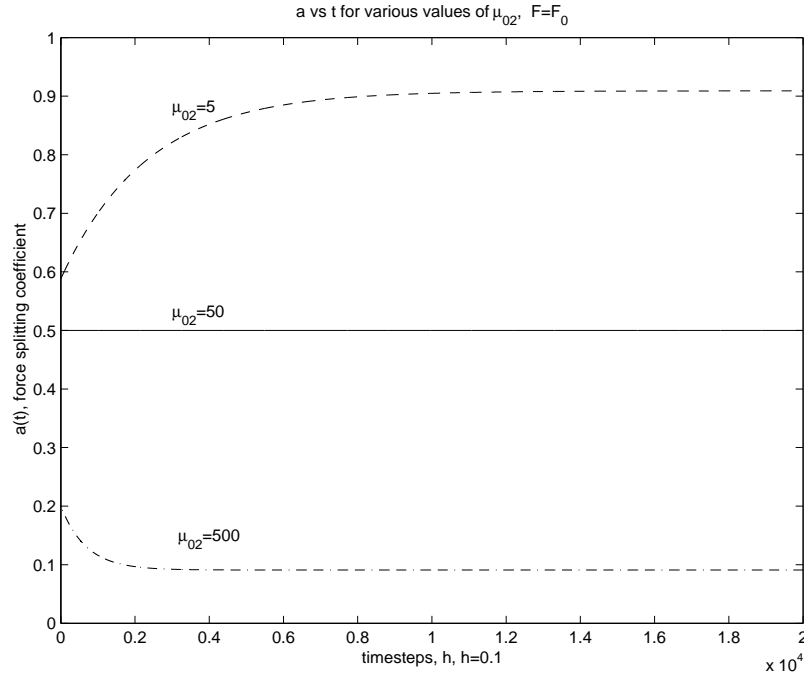


Figure 4.17: Dependence of force splitting coefficient on μ_{02} . Steady flow.

Now we can turn to investigating how the force splitting is effected by the parameter values. All the figures of the force splitting show the force acting on body one, and the force on the second body can be found from this by recalling that the sum of the two forces is one. We use the same values for μ_{02} as previously. The simulations in steady flow are shown in Figure 4.17. As expected, if the spring is very pliable in body two, then most of the force will have to focus on body one. For two identical bodies (i.e. if $\mu_{02} = 50$), the force splits equally between the two bodies. A very stiff spring in body two means that all the force has to concentrate here. In oscillatory flow we are only interested in the peak force acting on body one. Figure 4.18 shows the oscillations of the overall force, the force acting on body one, and the force splitting coefficient, a displayed on the same graph. Only the peak values of aF (which are identical to the value of a) are displayed subsequently. As before, the peak values of the force do not change with time, as shown in Figure 4.19. In the oscillatory flow, just like in steady

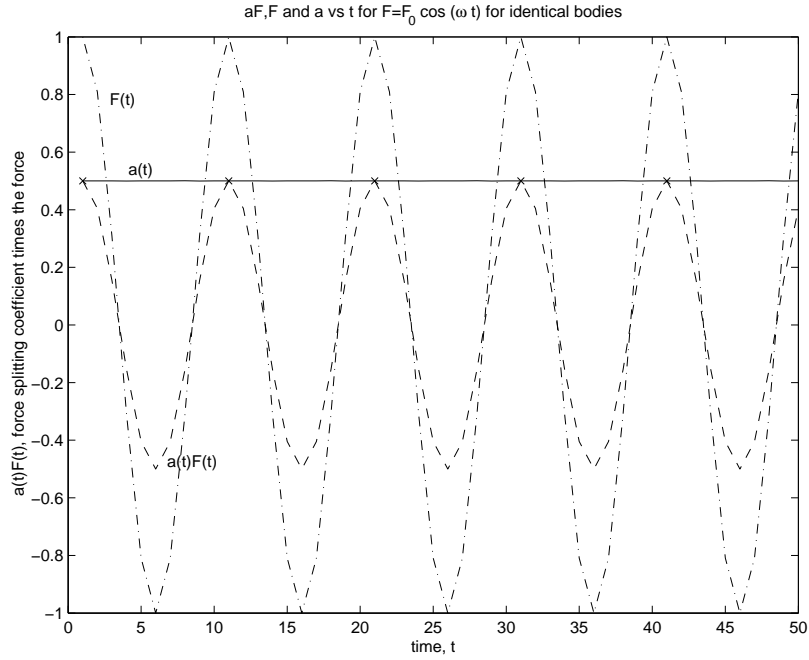


Figure 4.18: Oscillations of $a(t)F(t)$, $F(t)$ for identical bodies. $a(t)$ also displayed. 'x' marks the points which are used to display peak oscillations of $a(t)$ in the following figures. Oscillatory flow.

flow, a pliable spring in body two leads to more of the force concentrating on body one, in identical bodies the forces split evenly, and stiff springs require more force to deform.

Figure 4.20 depicts the steady state values of force splitting for a range of values of μ_{02} . The curves for steady flow and oscillatory flow intersect when $\mu_{02}=50$, because this is the baseline value at which the two bodies are identical, therefore the forces split evenly regardless of the flow. It is interesting to note that in steady flow the force splitting is more extreme than in oscillatory flow. More specifically, a small μ_{02} (pliable spring in body two) in steady flow allows much more of the force to act on body one than in oscillatory flow, but a large value of μ_{02} in steady flow leads to a smaller force on body one than in oscillatory flow. The interpretation of this is that in oscillatory flow the dashpot offers a constant resistance, thus much of the overall force is always trying to stretch the dashpot.

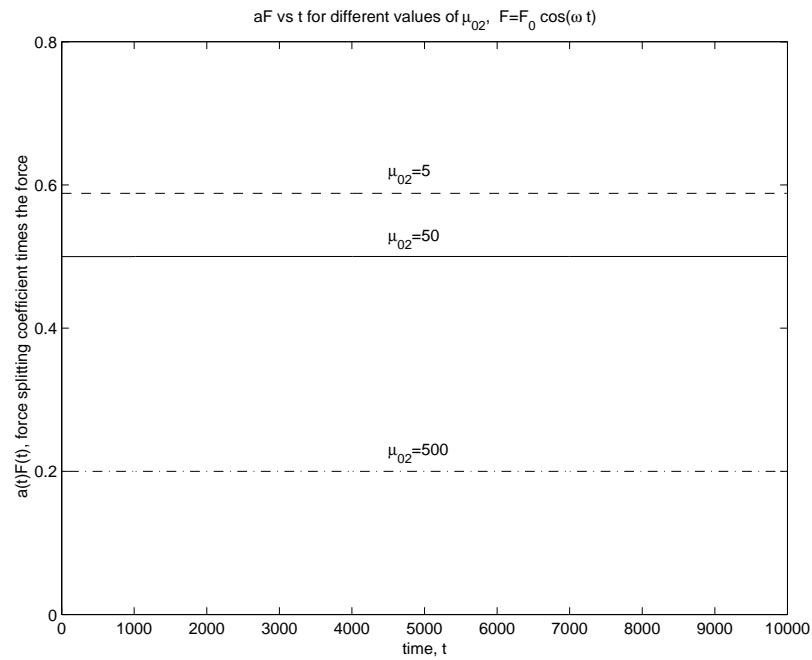


Figure 4.19: Dependence of $a(t)$ on μ_{02} . Graph shows peak values of $a(t)F(t)$. Oscillatory flow.

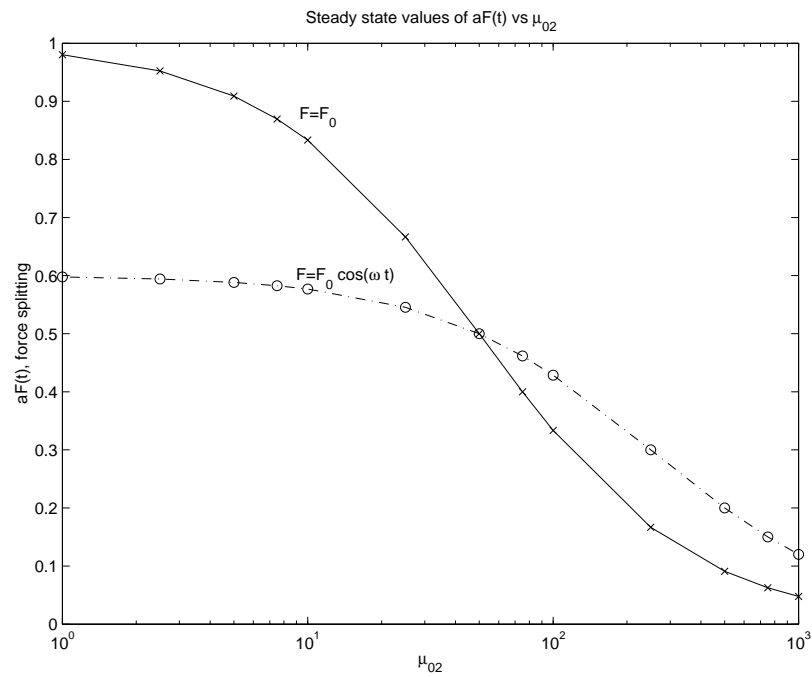


Figure 4.20: Dependence of steady state force splitting on μ_{02} .

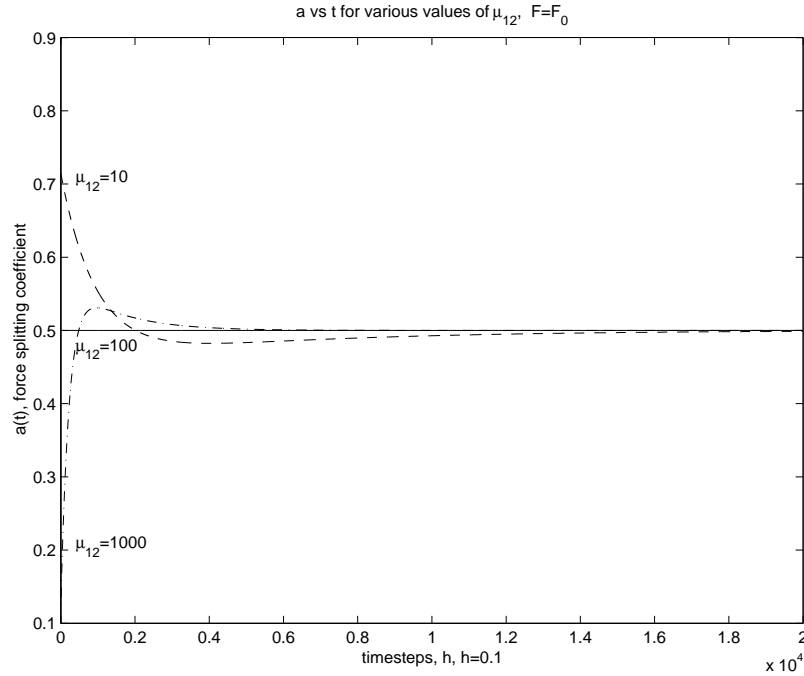


Figure 4.21: Dependence of force splitting coefficient on μ_{12} . Steady flow.

Next, we examine the dependence of the force splitting on the other spring constant, μ_{12} . Figure 4.21 shows the force splitting in steady flow. The initial condition of the force in the bodies depends on μ_{12} , but clearly, the steady state of the force tends to the same value, 0.5. Regardless of the stiffness of the spring in body two, eventually the forces acting on the two bodies become the same. When the force acts on a pliable spring, more force goes to the dashpot, and when the spring is stiff, more of the force goes to it. The mediating effects of the dashpot lead the equal force splitting between the two bodies.

In oscillatory flow, shown in Figure 4.22 the mediating effects of the dashpot are smaller, so there is a larger difference between force splitting between bodies one and two for different values of the spring constant, μ_{12} . As before, the peak force acting on body one reaches its steady state very quickly, so we see constants. For small values of μ_{12} the more of the force acts on body one, and for stiff springs more force

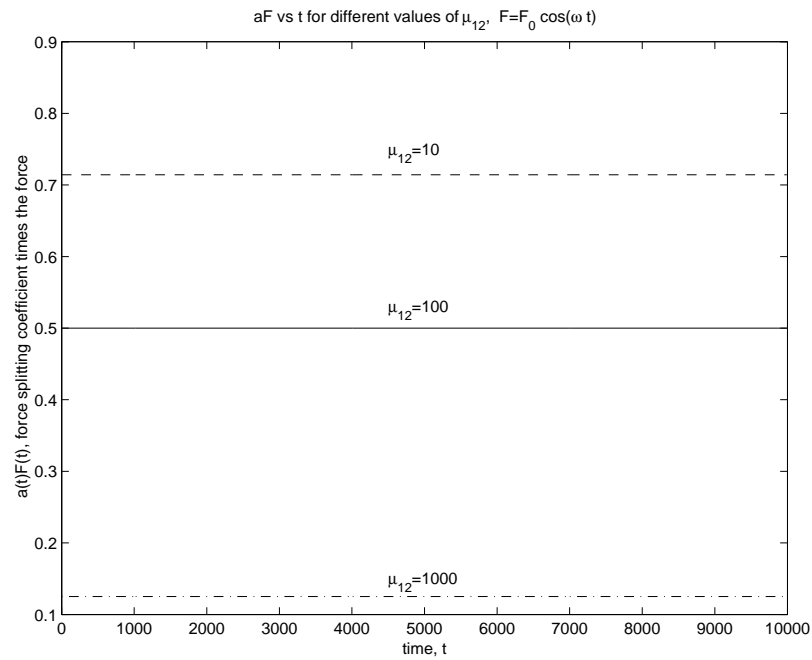


Figure 4.22: Dependence of $a(t)$ on μ_{12} . Graph on shows peak values of $a(t)F(t)$. Oscillatory flow.

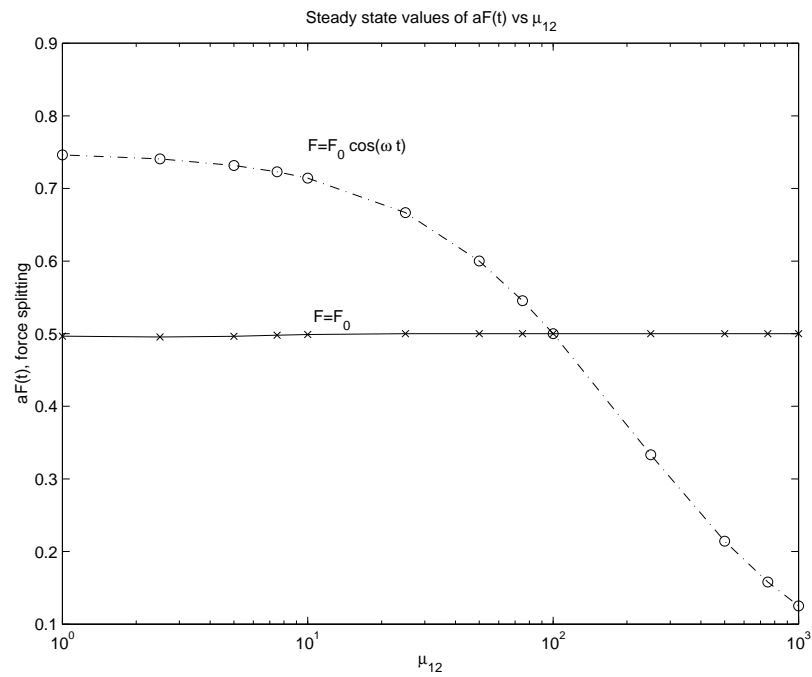


Figure 4.23: Dependence of steady state force splitting on μ_{12} .

is concentrated on body two. The comparison of steady states in oscillatory flow and steady flow, as depicted by Figure 4.23 brings no significant new information.

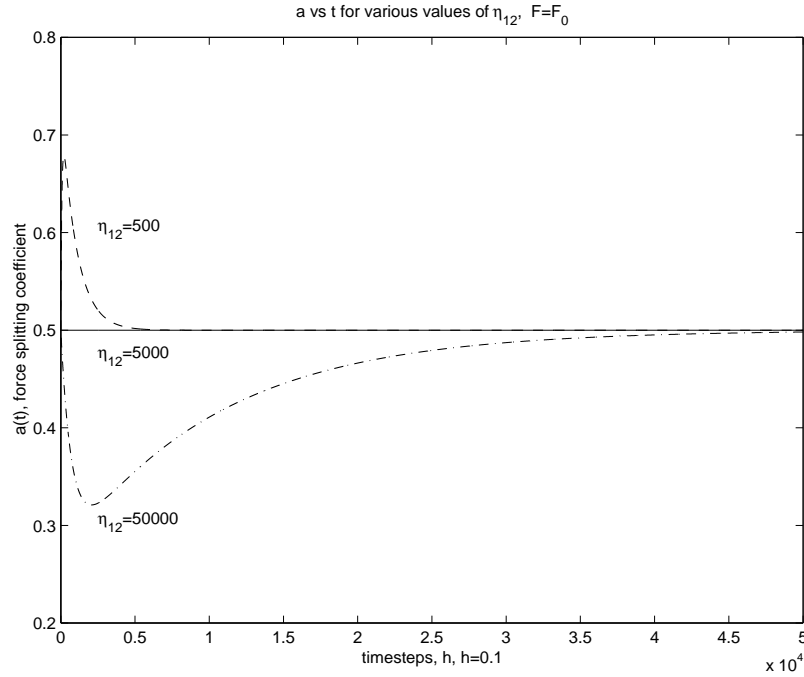


Figure 4.24: Dependence of force splitting coefficient on η_{12} . Steady flow.

Now we turn to looking at the dependence of force splitting on the dashpot viscosity. Longer simulation times are necessary again to obtain the steady state values. In steady flow, shown in Figure 4.24 small dashpot viscosity in body two leads to a transient increase of the force acting on body one, but at the steady state the force splits equally between the bodies. The transient increase is due to more force needing to deform the dashpot of body one. When the dashpot viscosity of body two is large, there is a transient decrease in the force acting on body one. The reason for this is similar to our argument above: now more force is necessary to deform the dashpot of body two. It is also clear from the figure that for large dashpot viscosities the transient time is longer. This is consistent with our previous observations on the role of the dashpot viscosity.

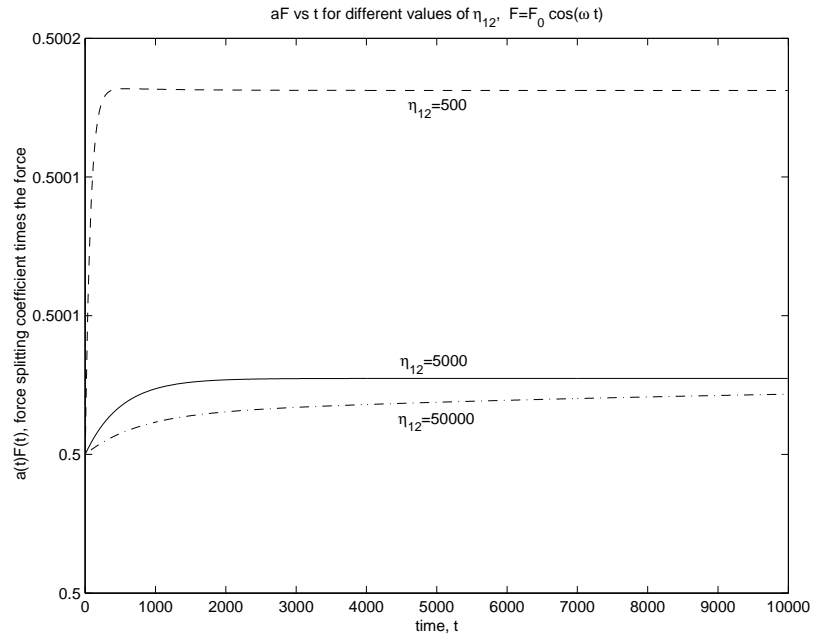


Figure 4.25: Dependence of $a(t)$ on η_{12} . Graph shows peak values of $a(t)F(t)$. Oscillatory flow.

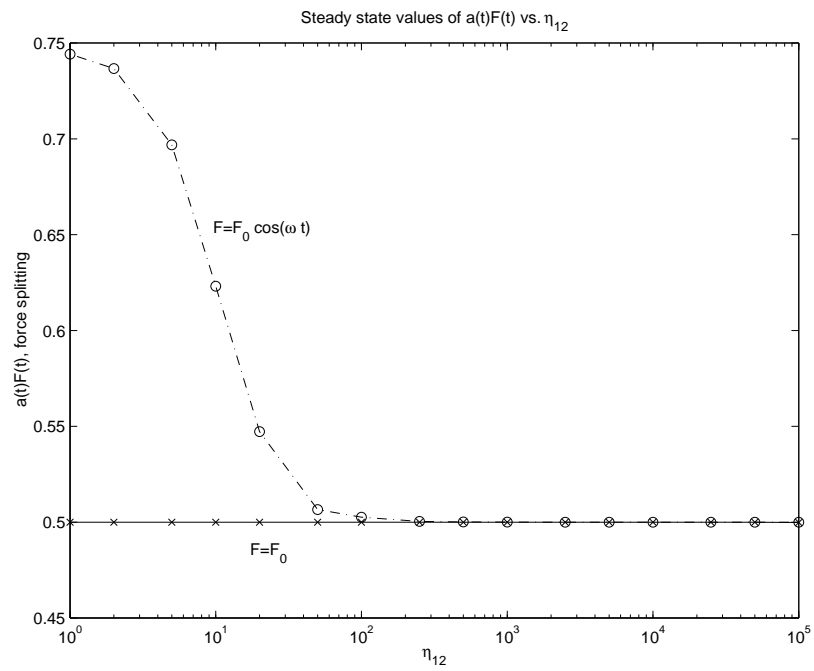


Figure 4.26: Dependence of steady state force splitting on η_{12} .

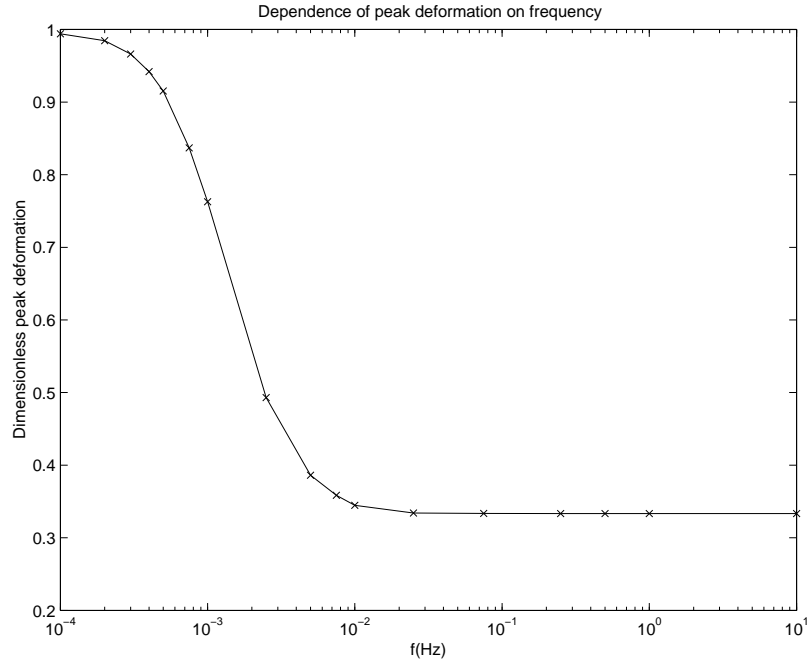


Figure 4.27: Dependence of peak steady state deformation on the frequency. Peak steady state deformation of oscillatory flow is divided by the steady state value of steady flow.

In oscillatory flow, Figure 4.25, the force split is almost exactly equal independently of the dashpot viscosity. Small viscosities lead to a quicker and slightly larger deformation. Figure 4.26 shows how the steady state values of the force in body one change with the dashpot viscosity in steady and in oscillatory flow. The most notable observation is that in oscillatory flow the forces do not split equally. This is the result of the initial quick dashpot relaxation of body two (when η_{12} is small) that leads to more force being necessary for body one. Similarly, if the dashpot viscosity of the second body is large, then the initial dashpot relaxation occurs in the first body, therefore more force will always be applied to the second body.

So far all of our numerical simulations in oscillatory flow used the frequency $f = 1\text{Hz} = 2\pi$ rad/sec. This is a physiological value which corresponds to the frequency at which the heart pumps the blood through the blood vessels, however, this frequency may change during exercise, or due to pathologies. This raises the question of how

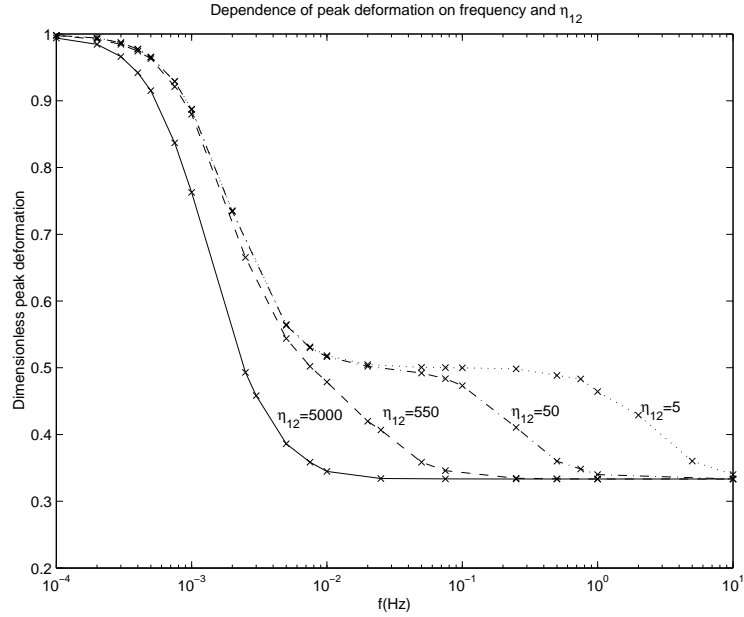


Figure 4.28: Dependence of peak steady state deformation on the frequency and η_{12} . Peak steady state deformation of oscillatory flow is divided by the steady state value of steady flow.

the frequency of oscillations may change our model, in particular how the frequency effects the deformation and force splitting of the Kelvin bodies.

Figures 4.27 - 4.29 show the results of simulations where the frequency of oscillations is altered. In these plots we used the values $f = 10^{-4}, 2 \times 10^{-3}, 3 \times 10^{-3}, 4 \times 10^{-3}, 5 \times 10^{-3}, 10^{-2}, 2 \times 10^{-2}, 5 \times 10^{-2}, 7 \times 10^{-2}, 10^{-1}, 2.5 \times 10^{-1}, 7.5 \times 10^{-1}, 1, 10$ Hz. All other parameter values for body 1 and body 2 are baseline values. The peak deformation (and the peak force splitting) for each of the simulations is divided by the deformation (and the force splitting) for steady flow.

Figure 4.27 shows that if the frequency of oscillations is very small, then the deformation in oscillatory flow is essentially the same as in steady flow. As the frequency increases, the deformation decreases, because the dashpot is unable to fully deform once the oscillations become fast enough. This is the result of the sign of the force changing quickly, therefore the force not acting for sufficiently long periods of time

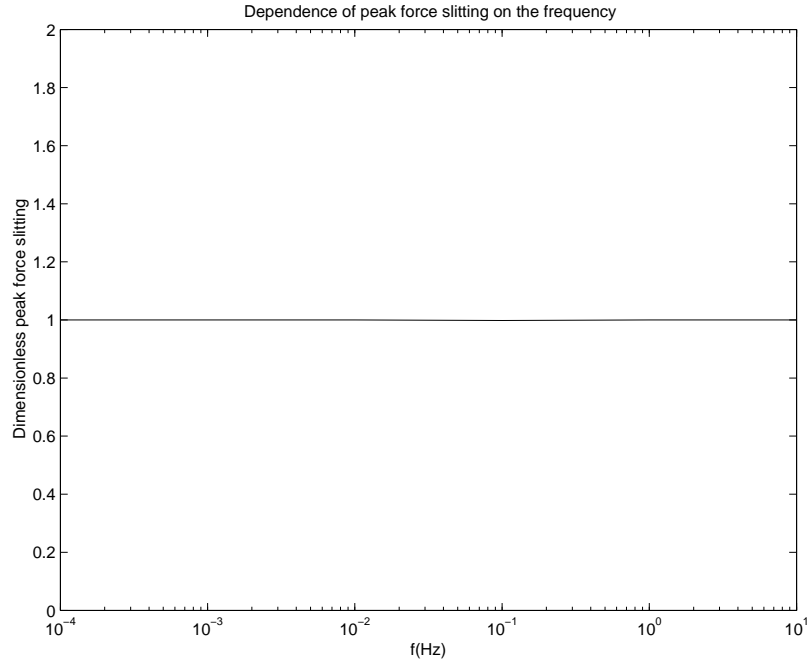


Figure 4.29: Dependence of peak steady state force splitting on the frequency. Peak steady state force splitting of oscillatory flow is divided by the steady state value of steady flow.

to fully stretch the dashpot. Once the frequency reaches a critical value, $f_{crit} \approx 10^{-2}$, the deformation is independent of the frequency of oscillations. This signals the frequency at which the deformation is entirely due to the springs. (Deformation of the springs is instantaneous when force is applied.)

Just like in the one Kelvin body case, $f_{crit} = 10^{-2}$ [3], two orders of magnitude below the physiological value. This implies that endothelial cells exposed to purely oscillatory flow will only deform to a small fraction (approximately one third) of deformation possible in steady flow. If there is a threshold value of deformation that permits cells to align and go through other significant physiological changes, it is very likely that purely oscillatory flow will not be able to reproduce these effects. Also, it is interesting to note that the deformation for frequencies $f > f_{crit}$ is the same for one Kelvin body as for two. This implies that any number of Kelvin bodies coupled in parallel will not deform more than this value, therefore a model consisting of n

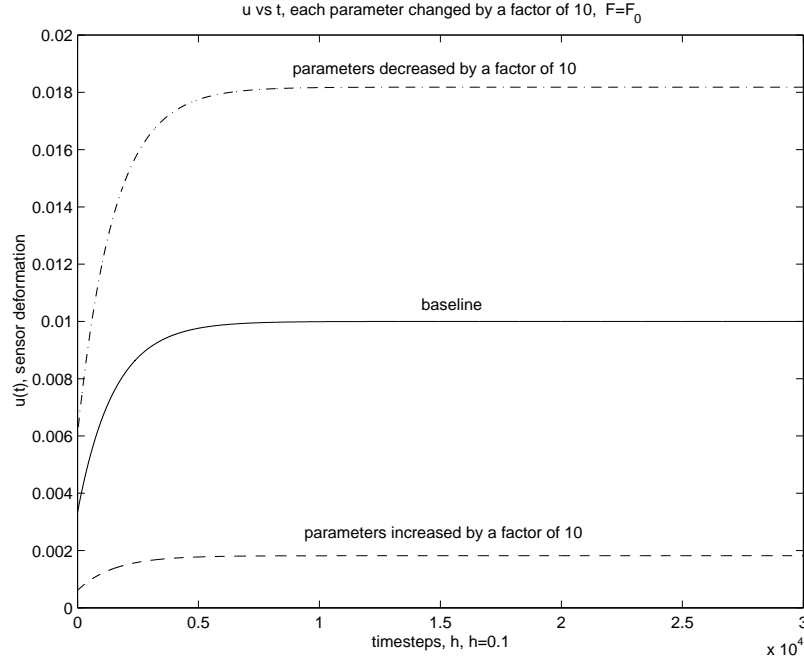


Figure 4.30: Deformation when every parameter of body 2 is changed by a factor of 10. Steady flow.

Kelvin bodies in parallel would retain the feature that f_{crit} is well below physiological values.

We have heuristically argued before that for all values of viscosity $\eta_{12} > 100$ the dashpot is not able to react in oscillatory flow, because the direction of the force changes very quickly, and there is not enough time for the dashpot to deform. This suggests that the relationship between frequency and deformation has to be examined. Figure 4.28 shows these simulations. We observed in the previous plot, (Figure 4.27) that as the frequency increases, the overall deformation decreases to a constant value. This can be explained, if very small frequency oscillations allowed sufficient amount of time for the dashpot to react, but once the frequency increased to about $f = 0.01$ Hz, the dashpot did not have time to respond at all. Beyond this frequency all the deformation is due to the springs. Our figure confirms that by making the dashpot very inviscid (decreasing η_{12} below 100) allows the dashpot to react much

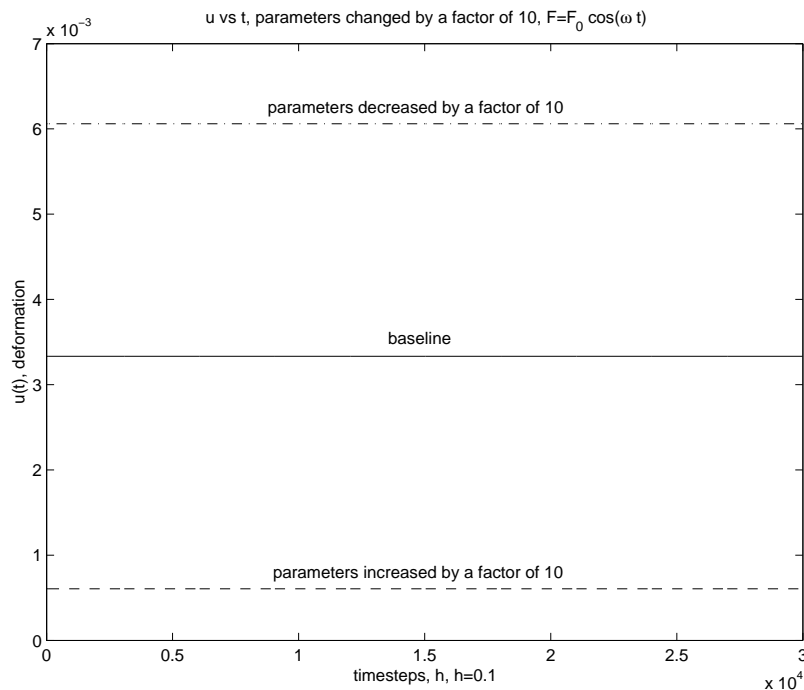


Figure 4.31: Deformation when every parameter of body 2 is changed by a factor of 10. Oscillatory flow.

more quickly, and we see larger deformations for given frequencies. When the frequency is very low, then the deformation is similar to the deformation in steady flow for any value of the viscosity, therefore the dimensionless value (peak deformation in oscillatory flow divided by the deformation in steady flow) is near 1. When the frequency is very large, then the deformation is always a constant around 0.333 independently of the frequency or the viscosity. Between these two regimes there is a range of frequencies for which increasing the frequency means decreasing the deformation. Interestingly, for small values of the dashpot viscosity the normalized peak deformation is bi-sigmoidal.

Figure 4.29 describes the dependence of the peak force splitting on the frequency of oscillations. As before, the largest amplitude at the steady state is taken for the appropriate value of the frequency, and this amplitude is divided by the steady state

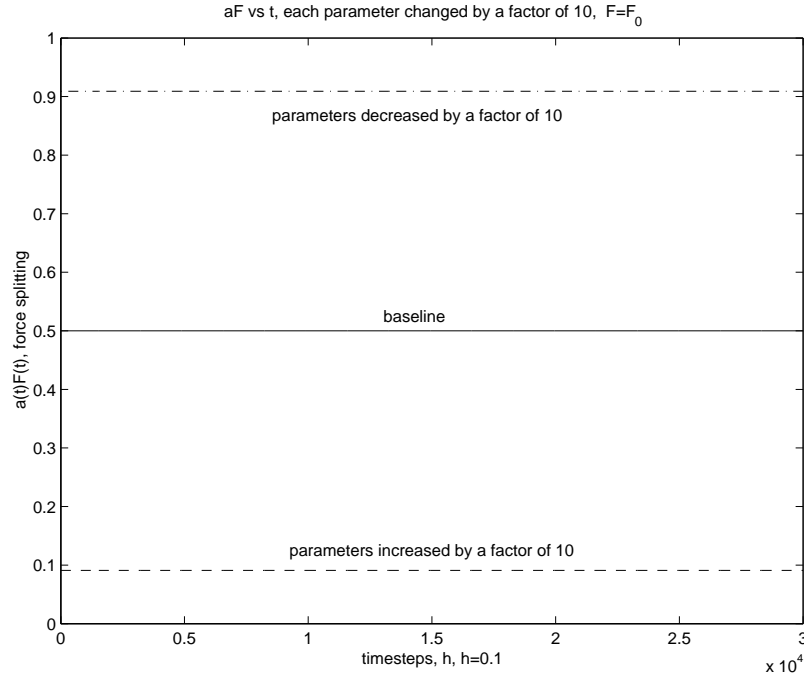


Figure 4.32: Force splitting when every parameter of body 2 is changed by a factor of 10. Steady flow.

value in oscillatory flow. As we can see, the frequency of oscillations does not change the fact that the peak force split in oscillatory flow is always the same as the steady state force split in steady flow.

We must also examine the case that all parameters in the second body are changed, because contradictory predictions could be made based on changing individual parameters only. Figures 4.30 -4.33 reveal that regardless of the type of flow, the deformation decreases if the parameters are increased, and the deformation is increased if all the parameters are decreased. Similarly, in either type of flow the force in body one decreases if the parameters are increased in body two, and the force increases in body 1, if the parameters in the other body are decreased.

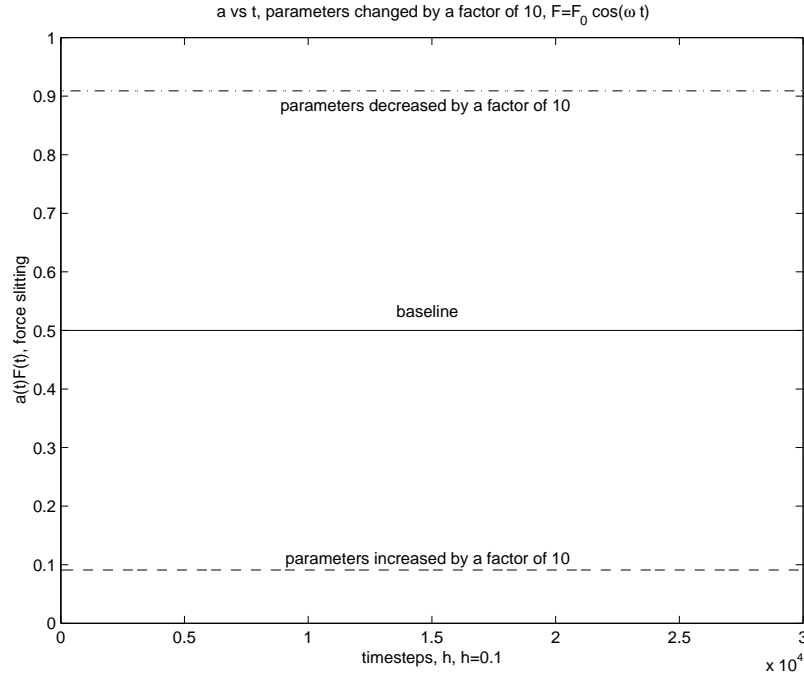


Figure 4.33: Force splitting when every parameter of body 2 is changed by a factor of 10. Oscillatory flow.

4.3.2 Network simulations

We represent endothelial cells as a network of viscoelastic bodies. Each part of the cell we model, namely, the transmembrane proteins, flow sensors, cytoskeletal elements and the nucleus are thought of as Kelvin bodies with different parameter values for the spring constant and the dashpot viscosity. The baseline values which we use for actin filaments are: $\mu_{02} = 50$ Pa, $\mu_{12} = 100$ Pa and $\eta_{12} = 5000$ Pa s. For the nucleus the spring constants are four times the baseline values and the viscosity of twice the baseline: $\mu_{02} = 200$ Pa, $\mu_{12} = 400$ Pa and $\eta_{12} = 10000$ Pa s. These estimates are based on experimental measurements by Guilak et al. [24]. The parameter values for the transmembrane proteins (flow sensors, ion channels, attachments to the substrate) based on [6] are: $\mu_{02} = 100$ Pa, $\mu_{12} = 200$ Pa and $\eta_{12} = 7.5$ Pa s. The parameter values are calculated in Section 4.2.4 and summarized in Table 4.1.

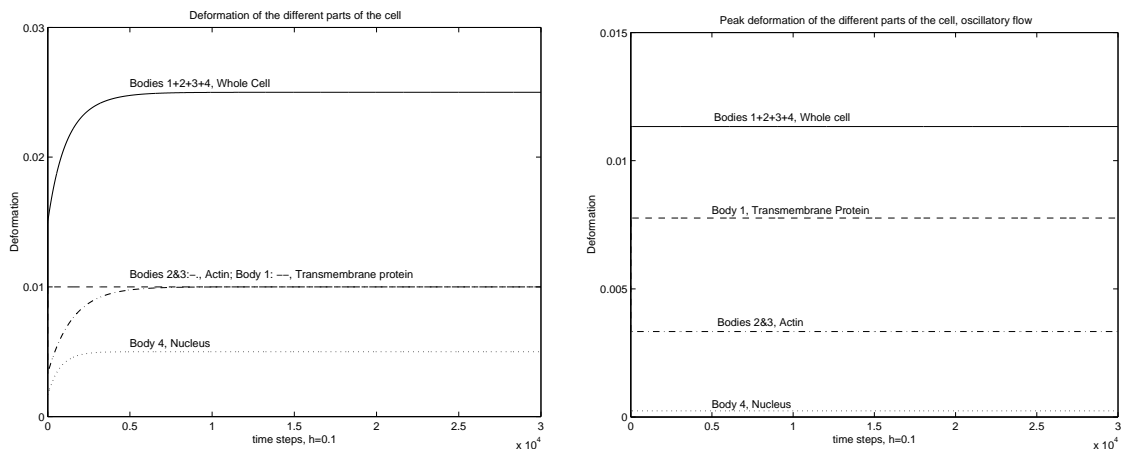


Figure 4.34: Deformation of different parts of a simple endothelial cell in steady and oscillatory.

Figure 4.34 shows numerical simulations for the simple four-body model of the endothelial cell (Figure 4.5) in steady and in oscillatory flow. In steady flow transmembrane proteins deform immediately, followed by the deformation of the nucleus, then the deformation of the actin filaments. This behavior is consistent with transmembrane proteins having the smallest, and actin filaments having the largest dashpot viscosities. Transmembrane proteins and actin filaments reach the overall deformation whereas the nucleus only deforms slightly. Because our model is linear, the overall cell deformation is the sum of the deformation of the components. The time constants are consistent with experimental data in which transmembrane proteins such as flow sensors and ion channels respond to flow very quickly, on the order of seconds, and cytoskeletal reorganization is the slowest, in fact, it happens on the time scale of many hours.

Next, we examine the same four-body model in oscillatory flow. Only peak values of the deformation are plotted, as before. The overall deformation is much smaller here than in steady flow, and the steady state of deformation is attained immediately (within 2-3 seconds). The nucleus deforms the least amount again, and here the largest deformation is that of the transmembrane protein.

Because in our four-body model the nucleus and the flow sensor are both modeled as a single Kelvin body, the force acting on each of them is a constant, $F = 1$. The same parameter values characterize the two actin filaments which are modeled as two Kelvin bodies connected in parallel, therefore the forces acting on them are also equal, $aF = (1 - aF) = 0.5$. This is true for steady as well as in oscillatory flow.

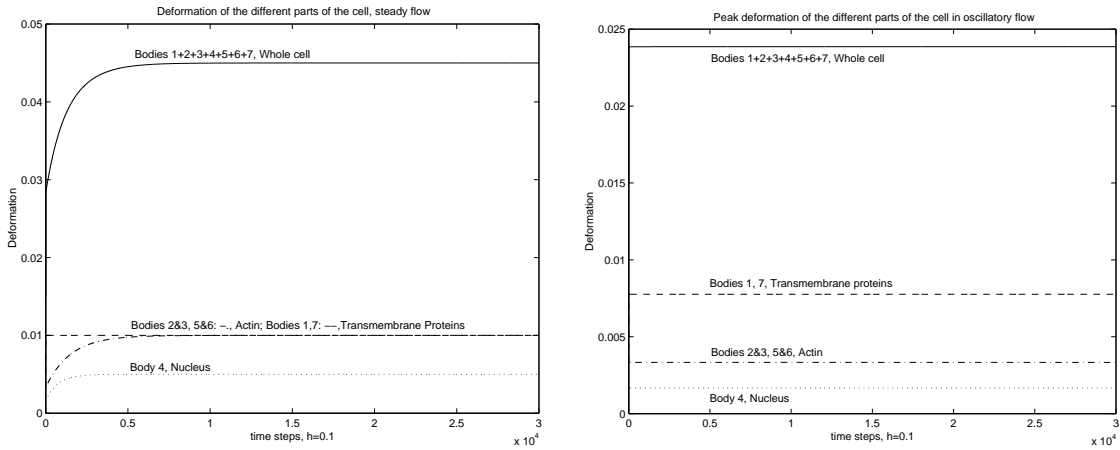


Figure 4.35: Deformation of different parts of a simple endothelial cell in steady and in oscillatory flow.

The final graph, Figure 4.35 and shows the response of the seven Kelvin-body model (depicted in Figure 4.6) in steady and oscillatory flow. The results are very similar to the simulations of the four-body model. The forces for the bodies are all constants: for the transmembrane proteins and nucleus (which are modeled as single Kelvin bodies) the force is equal to one, and for acting filaments, modeled as Kelvin bodies in parallel the force is split equally.

4.4 Discussion

Our numerical results included a parameter sensitivity analysis and simulations for two simple model networks of endothelial cells. The results of the simulations have been interpreted so far only in terms of the elements of the Kelvin body, but it has not been discussed what their implications are for endothelial cells. This section describes the conclusions we can draw regarding endothelial cell behavior from the numerical results. We also briefly mention further work that can be done to improve the current model.

The most notable difference between the effect of steady and oscillatory flow is that in oscillatory flow deformation tends to be much smaller than in steady flow for the same viscoelastic materials, as it is depicted in Figures 4.10, 4.13 and 4.16. The importance of the large deformation difference in the two types of flow is clear when we recall experimental results in which endothelial cells exhibit elongation and certain other biological responses (such as activation of flow-sensitive ion channels and mobilization of intracellular calcium) depending on the specific form of the shear stress cells are exposed to. Dewey et al. ([3], original source:[17]) demonstrate that endothelial cells exhibit some morphological responses when exposed to large shear stress, for example in steady or pulsatile flow, but not when their exposure to shear stress is below a certain level, for example, in oscillatory flow.

According to our model, the forces acting on each part of an endothelial cell, regardless of its viscoelastic properties elicits a much smaller response in oscillatory flow. This can be particularly important for a flow sensor, as discussed by Barakat [3], which in oscillatory flow may not be stimulated sufficiently to initiate a signaling cascade for downstream responses to the flow. Our model shows, that even given an signal from the flow sensor, the deformation of materials whose viscoelastic properties are consistent with those of the nucleus and cytoskeletal elements would be much smaller

in oscillatory flow.

Another observation we can make (still based Figures 4.10, 4.13 and 4.16) is that the viscoelastic materials which display the largest difference in deformation can be characterized by small spring constants but a viscosity coefficient which is at least $\eta \approx 10^2$. This characterization would allow us to estimate parameter values for microtubules and intermediate filaments for future simulations, because we have experimental observations of the relative behavior of actin filaments, microtubules and vimentin [34].

We have investigated how the frequency of oscillations effects the deformation. Our simulations show that within physiological conditions (even accounting for conditions where the frequency of the flow changes one order of magnitude) the normalized deformation is small, unless the viscosity coefficient becomes very small. This implies that materials whose viscosity is small, for example various transmembrane proteins, such as attachments to the substratum or cell-cell adhesions, are less able to differentiate between oscillatory and steady flow than the cytoskeleton or the nucleus. (As discussed above, the cytoskeleton and the nucleus respond very distinctively to steady and to oscillatory flow.)

Now let us examine the network simulations of endothelial cells. Both networks hugely oversimplify the complex connections between endothelial cells, therefore no detailed conclusions should be drawn from our results, rather we ought to make simple qualitative observations. More sophisticated networks need to be created in the future, and the main significance of our current simulations is to demonstrate the sort of models we are able to create with our elements now (namely n Kelvin bodies in parallel, coupled in series with single Kelvin bodies).

Qualitatively, the time scale of deformations as predicted by our model fits with experimental observations. Instantaneous response can be seen from transmembrane proteins (flow sensors, focal adhesions, cell-cell adhesions), followed by the deforma-

tion of the nucleus, and finally, the changes in the cytoskeleton. Flow sensor and ion channel deformation can occur within seconds whereas changes in the gene expression takes hours, and the cytoskeletal re-organization takes place over the span of about a day. These time scales do not compare well with the prediction of our model, which does predict flow sensor and ion channel deformations within seconds, but it also predicts the response of the nucleus and the actin filaments to be on the order of minutes. Clearly, our model must be modified, and in order to obtain quantitatively accurate results, the effects of the biochemical signaling pathways must be considered as well.

Our model is the first step in creating more realistic model networks of endothelial cells. The current project can be extended in a number of ways to lead to better approximations of the cellular response to flow. The extension promising the most extensive changes in the results is the assumption that the parameters describing the Kelvin bodies can alter in time too. This new assumption would turn our linear system of equations to a nonlinear system with possibly much more complicated dynamics. Other changes to incorporate in the model are: formulating the equations for new networks based on combinations of bodies which our system does not describe, assuming that the forcing function is applied gradually (there is a "ramp" for the force). Allowing the force to act gradually on the bodies could be compared to experimental results in which cell responses are altered by applying shearing forces instantaneously or gradually. Although even the understanding of viscoelastic Kelvin bodies in parallel lead to new insights on the hypothesized mechano-transduction of flow induced shear stress in endothelial cells, further improvements and extensions are necessary to clarify the role of this mechanism.

Appendix A

Receptor model

An important question is whether there is biological evidence of the signal transduction pathway allowing the existence of the proposed turning rates that depend on the oxygen concentration and the spatial gradient of oxygen. In [72], Taylor and Johnson propose a model that aims to explain experiments in which receptors are rewired to produce inverse responses. Using their model for a receptor, it is easy to explain how the turning rates of our model could be a result of a simple two-state receptor.

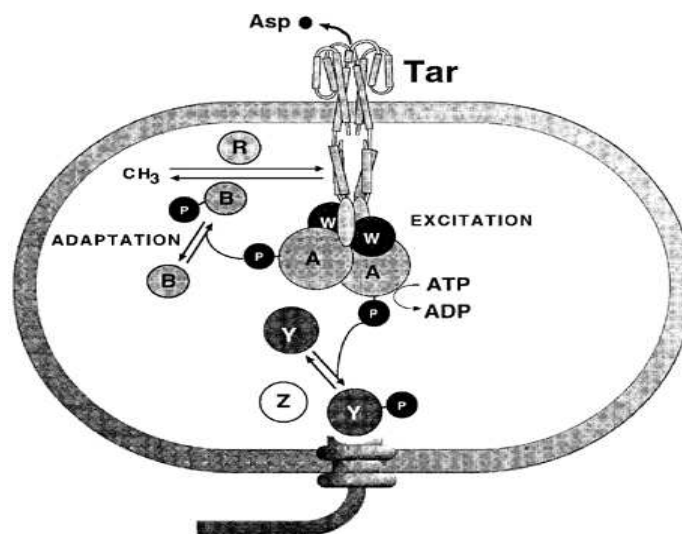


Figure A.1: The four-helix bundle of Tar receptor. (Figure from Taylor and Zhulin, [73].)

It is known that part of the Tar (and Tsr) receptors is a four-helix bundle outside the cell, and as ligands bind to the receptor, the bundle goes through a conformational change. By representing the receptor as two independently moving parts, we have a simplified model ('piston model') of the receptor. Each part of the receptor is able to move in the z direction as a function of the proton motive force, PMF. One part of the receptor is able to change its position fast in response to PMF, while the other part reacts slower. When the two parts of the receptor in the model are at the same position, they lock (representing the conformation change in the real receptor), and this initiates tumbling. When the two parts of the receptor are not in the same position, the cell swims smoothly.

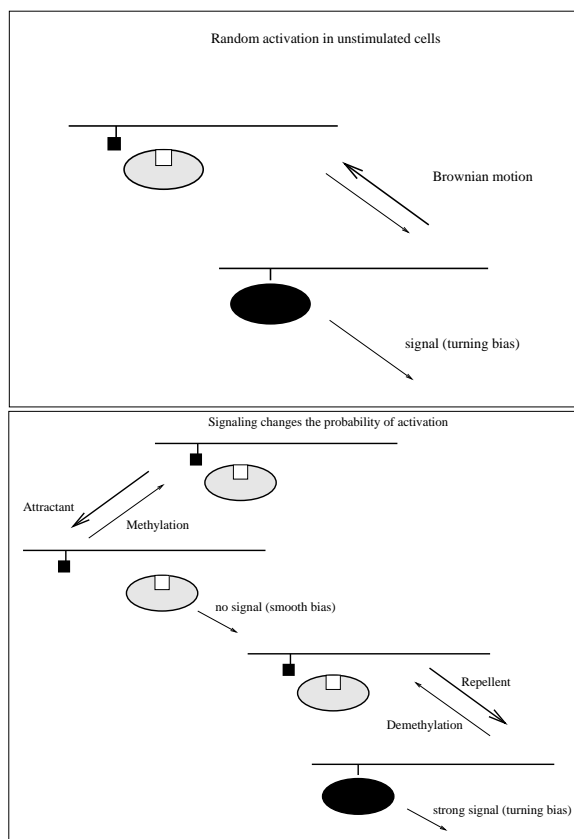


Figure A.2: Piston model of a receptor. (Figure based on Taylor and Johnson, [72].)

In ground state, the two parts are displaced from one another. Thermal energy is

able to randomly move the parts, which causes tumbling in unstimulated cells if the parts are moved together, and it promotes smooth swimming if the parts are moved further apart. Attractant binding to the receptor also moves the fast and slow parts further, which makes smooth swimming more likely. Adaptation returns the receptor to the ground state.

In our mathematical model such a receptor could be responsible for the same oxygen concentrations triggering different signals. When a bacterium is outside the optimal oxygen concentration, the cell is in ground state; therefore, it has its baseline turning frequency. As the cell enters the favorable oxygen concentration, the fast-changing part moves; thus, the two parts get further from each other, and the cell swims smoothly inside the band. By the time the cell gets across the band, the slow-changing part moves too, and the two parts lock which causes tumbling. The tumbling turns the cell back into the favorable concentration, and the fast-moving part changes position again, leading to smooth swimming.

Consider z_f : z coordinate of fast-changing part, z_s : z coordinate of slow-changing part.

$$\tilde{z}_f = z_f^{(0)} + c_1 p \quad (\text{A.1})$$

$$\tilde{z}_s = z_s^{(0)} + c_1 p = z_f^{(0)} - \Delta z + c_1 p \quad (\text{A.2})$$

In these equations \tilde{z}_f and \tilde{z}_s are the equilibrium positions of the fast-moving and slow-moving parts, respectively. In ground state, the equilibrium positions are not the same, as discussed above. $z_f^{(0)}$ and $z_s^{(0)}$ are constants. p is the proton motive force (which is proportional to the oxygen concentration).

$$p = \pm kt + c_0$$

We can assume that the PMF is a linear function of time, since the fully developed oxygen gradient is linear in space, and it is observed by the bacteria swimming through it as oxygen changing linearly in time.

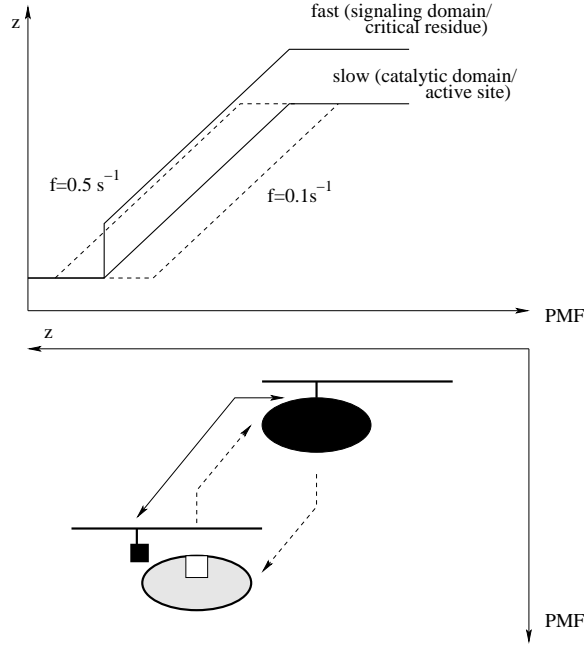


Figure A.3: Fast and slow states of a receptor. The top figure shows how the receptor switches from high turning frequency to low turning frequency and vice versa. The bottom figure shows a different representation of the same process. (Bottom portion of the figure based on Taylor and Johnson, [72].)

We can assume that the fast-moving part is just a function of the proton motive force (i.e. its position changes immediately as it detects changes in the proton motive force.) We assume that the slow-moving part changes its position after a delay. This results in the following two equations:

$$z_f \approx \tilde{z}_f(p(t)) \quad (\text{A.3})$$

$$\frac{dz_s}{dt} = \frac{1}{\tau}(\tilde{z}_s(p(t)) - z_s) \quad (\text{A.4})$$

The first equation is an algebraic equation, and we can solve it by substituting the expression for the proton motive force into (A.3). This gives the equation:

$$z_f = [z_f^{(0)} + c_0 c_1] \pm c_1 k t$$

This shows that the coordinate of the fast part will be increasing as it moves up the

concentration gradient, and it will be decreasing as the cell swims down the gradient.

Now we can solve (A.4).

$$\frac{dz_s}{dt} = \frac{-z_s}{\tau} + \frac{z_f^{(0)} - \Delta z + c_1 p}{\tau}$$

We have to solve the homogeneous equation on the left-hand side, then find the particular solution, $z_{sp} = A + Bt$, using the right-hand side of the equation:

$$\frac{dz_s}{dt} + \frac{z_s}{\tau} = \frac{z_f^{(0)} - \Delta z + c_1(\pm kt + c_0)}{\tau}$$

Solving the homogeneous equation we get: $z_{sh} = z_0 e^{-t/\tau}$. In the particular solution, we get $A = z_f^{(0)} + c_1 c_0 \mp c_1 k \tau - \Delta z$; $B = \pm c_1 k$. This gives the full particular solution, $z_{sp} = z_f^{(0)} + c_1 c_0 \mp c_1 k \tau - \Delta z \pm c_1 k t$. By making the appropriate substitution, this results in the full solution,

$$z_s = z_f + [\mp c_1 k \tau - \Delta z] + z_0 e^{-\frac{t}{\tau}}$$

If the adaptation time, τ , is small compared to the run (which is our assumption in the model), then the last term is negligible. Now we can see how the receptor will work by examining the position of the fast- and slow-moving parts. The position of the slow-moving part, z_s is behind the position of the fast part. To see the dynamics of the two parts, the solution to z_s can also be re-written as:

$$z_s = z_f^{(0)} + c_1 c_0 - \Delta z \pm c_1 k(t - \tau) + z_0 e^{-\frac{t}{\tau}}$$

As long as the time, t is less than the adaptation time τ , the slow part will be behind the fast one, but after the time reaches τ , the sign of $c_1 k(t - \tau)$ changes, and the difference in the position of the fast and slow part decreases. This difference is maintained until the cell turns down the gradient, at which point the z-coordinate of the fast moving part will change quickly again, followed by the z-coordinate of the slow moving part.

This simple model of the receptor based on proton motive force is sufficient to explain the turning frequencies assumed in the full mathematical model of aerotaxis.

Appendix B

Analytical calculations

B.1 Asymptotic approximation

We want to solve the system of equations

$$\begin{aligned}\frac{dM}{dt} &= m + \lambda(-k_a(l_1)M + k_dA) \\ \frac{dA}{dt} &= -rA + \lambda(k_a(l_1)M - k_dA)\end{aligned}$$

with initial conditions:

$$M(0) = \frac{mk_d}{rk_a(l_0)}, \quad A(0) = \frac{m}{r}$$

On the fast time scale, i.e. when $\tau = \lambda t$,

$$\frac{dM}{d\tau} + \frac{dA}{d\tau} = 0$$

which implies $A + M = C$ for some constant, C . We substitute this expression into the original system of equations to get:

$$\begin{aligned}\frac{dM}{d\tau} &= -k_a(l_1)M + k_d(C - M) \\ \frac{dA}{d\tau} &= k_a(l_1)(C - A) - k_dA\end{aligned}$$

The initial conditions on the fast time scale are the same as the initial conditions of the original equations,

$$M_0 = M(\tau = 0) = \frac{mk_d}{rk_a(l_0)}$$

$$A_s = A(\tau = 0) = \frac{m}{r}$$

The solution to these equations is given by:

$$A(\tau) = \left(A_s - \frac{k_a(l_1)C}{r_f}\right)e^{-r_f\tau} + \frac{k_a(l_1)C}{r_f}$$

$$M(\tau) = \left(M_0 - \frac{k_dC}{r_f}\right)e^{-r_f\tau} + \frac{k_dC}{r_f}$$

Where we defined the fast time scale to be

$$r_f = k_a(l_1) + k_d.$$

Now we use the fact that the sum of A and M is always a constant, in particular, $A(0) + M(0) = C$.

$$\left(A_s - \frac{k_a(l_1)C}{r_f}\right) + \frac{k_a(l_1)C}{r_f} + \left(M_0 - \frac{k_dC}{r_f}\right) + \frac{k_dC}{r_f} = C$$

$$C = \frac{m}{r} \left(1 + \frac{k_d}{k_a(l_0)}\right)$$

Two new constants are useful:

$$A_1 = \frac{k_a(l_1)C}{r_f} = \frac{m}{r} \frac{1 + (k_d/k_a(l_0))}{1 + (k_d/k_a(l_1))}$$

$$M_1 = \frac{k_dC}{r_f} = \frac{m}{r} \frac{k_d}{k_a(l_1)} \frac{1 + (k_d/k_a(l_0))}{1 + (k_d/k_a(l_1))}$$

Substituting the expressions for A_1 and M_1 into eqn. B.1 and B.1 we have obtain A and M on the fast time scale:

$$A(\tau) = (A_s - A_1)e^{-r_f\tau} + A_1 \tag{B.1}$$

$$M(\tau) = (M_0 - M_1)e^{-r_f\tau} + M_1 \tag{B.2}$$

We turn to the slow time scale, and we note that now $A = \frac{k_a(l_1)}{k_d}M$. Substituting this expression into the original equations gives us:

$$\frac{dM}{dt} = m \quad (\text{B.3})$$

$$\frac{k_a(l_1)}{k_d} \frac{dM}{dt} = -r \frac{k_a(l_1)}{k_d} M \quad (\text{B.4})$$

By adding equations B.3 and B.4 we get:

$$\begin{aligned} \frac{dM}{dt} &= \frac{mk_d}{k_a(l_1) + k_d} - \frac{rk_a(l_1)}{k_d + k_a(l_1)} M \\ M(t) &= \bar{c}e^{(-r_s t)} + \frac{mk_d}{(k_a(l_1) + k_d)r_s} \\ M(t) &= \bar{c}e^{(-r_s t)} + M_2 \end{aligned} \quad (\text{B.5})$$

We have defined

$$r_s = r \frac{k_a(l_1)}{k_d + k_a(l_1)}$$

and

$$M_2 = \frac{mk_d}{rk_a(l_1)}.$$

Similarly, we have an equation for A :

$$A(t) = \frac{k_a(l_1)}{k_d} \bar{c}e^{(-r_s t)} + \frac{m}{r} \quad (\text{B.6})$$

The solutions on the fast and slow times scale must match, so the limit of eqn B.1 as $\tau \rightarrow \infty$ must be equal to eqn B.6 at zero. Similarly, $\lim_{\tau \rightarrow \infty} M_f = M_s(t = 0)$. Matching the solutions allows us to find the expression for \bar{c} .

$$\frac{k_a(l_1)\bar{c}}{k_d} + A_s = A_1 \quad (\text{B.7})$$

$$\bar{c} = \frac{m}{r} \left[\frac{k_d}{r_f} \left(1 + \frac{k_d}{k_a(l_0)} \right) - \frac{k_d}{k_a(l_0)} \right] = M_1 - M_0 \quad (\text{B.8})$$

The full solution is the sum of the fast and slow terms with the common limit (A_1 and M_1) subtracted.

$$A(t) = A_s + (A_s - A_1)e^{-r_f \lambda t} + (A_1 - A_s)e^{-r_s t} \quad (\text{B.9})$$

$$M(t) = M_2 + (M_0 - M_1)e^{-r_f \lambda t} + (M_1 - M_2)e^{-r_s t} \quad (\text{B.10})$$

B.2 Steady state solution

We start with the four equations describing the two compartment model of the signal transduction system again.

$$\frac{dM_1}{dt} = m + \lambda(-k_a(l_1)M_1 + k_dA_1) + k_1(M_2 - M_1) \quad (\text{B.11})$$

$$\frac{dA_1}{dt} = -rA_1 + \lambda(k_a(l_1)M_1 - k_dA_1) + k_2(A_2 - A_1) \quad (\text{B.12})$$

$$\frac{dM_2}{dt} = m + \lambda(-k_a(l_2)M_2 + k_dA_2) - k_1(M_2 - M_1) \quad (\text{B.13})$$

$$\frac{dA_2}{dt} = -rA_2 + \lambda(k_a(l_2)M_2 - k_dA_2) - k_2(A_2 - A_1) \quad (\text{B.14})$$

$$M_1(0) = M_2(0) = \frac{m}{r} \frac{k_d}{k(l_0)} \quad A_1(0) = A_2(0) = \frac{m}{r} \quad (\text{B.15})$$

At the steady state the left hand side of these equations is zero. We start finding the expressions for the steady state by adding equations B.11 and B.13. In the following calculations we write A_1 , A_2 , M_1 and M_2 instead of A_{1s} , A_{2s} , M_{1s} and M_{2s} .

$$2m - \lambda k_a(l_1)M_1 - \lambda k_a(l_2)M_2 + \lambda k_d(A_1 + A_2) = 0 \quad (\text{B.16})$$

$$k_a(l_1)M_1 + k_a(l_2)M_2 = \frac{2m}{\lambda} + k_d(A_1 + A_2) \quad (\text{B.17})$$

Next we add equations B.12 and B.14.

$$-r(A_1 + A_2) + \lambda(k_a(l_1)M_1 + k_a(l_2)M_2) - \lambda k_d(A_1 + A_2) = 0 \quad (\text{B.18})$$

$$(A_1 + A_2)(\lambda k_d + r) = \lambda(k_a(l_1)M_1 + k_a(l_2)M_2) \quad (\text{B.19})$$

We substitute the expression for $k_a(l_1)M_1 + k_a(l_2)M_2$ from B.17:

$$\begin{aligned} A_1 + A_2 &= \frac{\lambda}{r + \lambda k_d} \left(\frac{2m}{\lambda} + k_d(A_1 + A_2) \right) \\ A_1 + A_2 &= \frac{2m}{r + \lambda k_d} + \frac{\lambda k_d}{r + \lambda k_d} (A_1 + A_2) \end{aligned} \quad (\text{B.20})$$

Solving the equation for $A_1 + A_2$ we obtain

$$A_1 + A_2 = \frac{2m}{r} \quad (\text{B.21})$$

This allows us to express $A_2(A_1) = \frac{2m}{r} - A_1$.

Now we return to B.17 to find an expression for $k_a(l_1)M_1 + k_a(l_2)M_2$ explicitly.

$$k_a(l_1)M_1 + k_a(l_2)M_2 = \frac{2m}{\lambda} + k_d \frac{2m}{r} \quad (\text{B.22})$$

$$M_2 = \frac{2m}{k_a(l_2)} \left(\frac{r + \lambda k_d}{\lambda r} \right) - \frac{k_a(l_1)}{k_a(l_2)} M_1 \quad (\text{B.23})$$

Now we add equations B.11 and B.12, and similarly, add B.13 and B.14.

$$m - rA_1 + k_1(M_2 - M_1) + k_2(A_2 - A_1) = 0 \quad (\text{B.24})$$

$$m - rA_2 - k_1(M_2 - M_1) - k_2(A_2 - A_1) = 0 \quad (\text{B.25})$$

By subtracting B.25 from B.24 we arrive at

$$A_1 - A_2 = \frac{2k_1}{r + 2k_2} (M_2 - M_1) \quad (\text{B.26})$$

We want to express A_1 as function M_1 , and this will allow us to find $A_2(M_1)$. In order to do this, we add B.21 and B.26.

$$A_1 = \frac{m}{r} + \frac{k_1}{r + 2k_2} (M_2 - M_1)$$

Now we use B.23 to find both A_1 and A_2 as a function of M_1 , so we have $A_1(M_1)$, $A_2(M_1)$ and $M_2(M_1)$.

$$A_1 = \frac{m}{r} + \frac{k_1}{r + 2k_2} \left(\frac{2m(r + \lambda k_d)}{k_a(l_2)\lambda r} - \frac{k_a(l_1)}{k_a(l_2)} M_1 - M_1 \right) \quad (\text{B.27})$$

$$A_2 = \frac{m}{r} - \frac{k_1}{r + 2k_2} \left(\frac{2m(r + \lambda k_d)}{k_a(l_2)\lambda r} - \frac{k_a(l_1)}{k_a(l_2)} M_1 - M_1 \right) \quad (\text{B.28})$$

We return to the equation B.11 with its right hand side set to zero, and substitute $A_1(M_1)$, $A_2(M_1)$ and $M_2(M_1)$ from the equations B.27, B.28 and B.23, respectively, and solve the equation for M_1 .

$$m + \lambda \left[-k_a(l_1)M_1 + k_d \left(\frac{m}{r} + \frac{k_1}{r + 2k_2} \left[\frac{2m(r + \lambda k_d)}{k_a(l_2)\lambda r} - \frac{k_a(l_1)}{k_a(l_2)} M_1 - M_1 \right] \right) - \frac{k_a(l_1) + k_a(l_2)}{k_a(l_2)} M_1 \right] + k_1 \left(\frac{2m(r + \lambda k_d)}{k_a(l_2)\lambda r} - \frac{k_a(l_1) + k_a(l_2)}{k_a(l_2)} M_1 \right) = 0$$

$$\begin{aligned}
& m + \frac{m\lambda k_d}{r} + k_1 \frac{2m(r + \lambda k_d)}{k_a(l_2)\lambda r} \cdot \left(\frac{\lambda k_d}{r + 2k_2} + 1 \right) \\
&= \left[\lambda k_a(l_1) + k_1 \cdot \frac{k_a(l_1) + k_a(l_2)}{k_a(l_2)} \left(\frac{\lambda k_d}{r + 2k_2} + 1 \right) \right] M_1
\end{aligned}$$

If we simplify this expression, and substitute it back into B.27, B.28 and B.23 we arrive at the steady state solution:

$$A_1 = \frac{m}{r} \cdot \left[1 + \frac{r_1 k_1 k}{\lambda r_2 k_p + k_1 k_s (r_2 + \lambda k_d)} \right] \quad (\text{B.29})$$

$$A_2 = \frac{m}{r} \cdot \left[1 + \frac{-r_1 k_1 k}{\lambda r_2 k_p + k_1 k_s (r_2 + \lambda k_d)} \right] \quad (\text{B.30})$$

$$M_1 = \frac{mr_1}{\lambda r} \cdot \left[\frac{r_2(\lambda k_a(l_2) + 2k_1) + 2\lambda k_d k_1}{r_2[\lambda k_p + k_1 k_s] + \lambda k_d k_1 k_s} \right] \quad (\text{B.31})$$

$$M_2 = \frac{mr_1}{\lambda r} \cdot \left[\frac{r_2(\lambda k_a(l_1) + 2k_1) + 2\lambda k_d k_1}{r_2[\lambda k_p + k_1 k_s] + \lambda k_d k_1 k_s} \right] \quad (\text{B.32})$$

where we have defined:

$$r_1 = r + \lambda k_d, \quad r_2 = r + 2k_2$$

$$k = k_a(l_1) - k_a(l_2), \quad k_s = k_a(l_1) + k_a(l_2)$$

$$k_p = k_a(l_1)k_a(l_2)$$

We want to verify that for $k_a(l_1) = k_a(l_2) = k_a$ we obtain the original steady state. This is clear for A_1 and A_2 by inspection, but we need to simplify M_1 and M_2 . We show the calculations for M_1 .

$$\begin{aligned}
M_1 &= \frac{mr_1}{k_a \lambda r} \cdot \left[\frac{r_2(\lambda k_a + 2k_1) + 2\lambda k_d k_1}{r_2[\lambda k_a + 2k_1] + 2\lambda k_d k_1} \right] \\
&= \frac{m(r + \lambda k_d)}{\lambda r k_a} \\
\lim_{\lambda \rightarrow \infty} M_1 &= \frac{m k_d}{r k a}
\end{aligned}$$

Previously we have shown that if $k_1 = 0$ then the two compartments respond to stimulus as if they were not connected. In the main text we also mention that no important qualitative changes occur when $k_2 = 0$. In this case our system of equations

becomes:

$$\begin{aligned}
 A_1 &= \frac{m}{r} \left[1 + \frac{r_1 k_1 k}{\lambda r k_p + k_1 k_s r_1} \right] \\
 A_2 &= \frac{m}{r} \left[1 - \frac{r_1 k_1 k}{\lambda r k_p + k_1 k_s r_1} \right] \\
 M_1 &= \frac{m r_1}{\lambda r} \cdot \left[\frac{r(\lambda k_a(l_2) + 2k_1) + 2\lambda k_d k_1}{r[\lambda k_p + k_1 k_s] + \lambda k_d k_1 k_s} \right] \\
 M_2 &= \frac{m r_1}{\lambda r} \cdot \left[\frac{r(\lambda k_a(l_1) + 2k_1) + 2\lambda k_d k_1}{r[\lambda k_p + k_1 k_s] + \lambda k_d k_1 k_s} \right]
 \end{aligned}$$

It is clear from the above equations that A_1 and A_2 depend on the ligand difference, so the system will respond to ligand gradients. The main text shows that the assumption $k_2 \gg 1$, on the other hand, results in cells where $A_1 = A_2$, so the cell cannot maintain an internal ligand gradient.

We also want to find the steady state of the system for $\lambda \gg 1$, and show that the qualitative behavior remains the same as in the $\lambda \approx O(1)$ case. We rearrange M_1 and A_1 to show decreasing powers of λ , and note that similar rearrangements can be made for M_2 and A_2 .

$$\begin{aligned}
 M_1 &= \frac{m}{r} \frac{\lambda^2 a + \lambda b + c}{\lambda^2 d + \delta e} \\
 a &= k_a(l_2) k_d (r + 2k_2) + 2k_1 k_d^2 \\
 d &= (r + 2k_2) k_a(l_1) k_a(l_2) + k_1 k_d (k_a(l_1) + k_a(l_2)) \\
 A_1 &= \frac{m}{r} + \frac{m}{r} \cdot \frac{\lambda \alpha}{\lambda \beta + \gamma} \\
 \alpha &= k_1 k_d (k_a(l_2) - k_a(l_1)) \\
 \beta &= k_d k_1 (k_a(l_2) + k_a(l_1)) + (r + 2k_2) k_a(l_1) k_a(l_2)
 \end{aligned}$$

We take the limit of these expressions as $\lambda \rightarrow \infty$:

$$\begin{aligned}
 M_1 &= \frac{m}{r} \cdot \frac{a}{d} \\
 A_1 &= \frac{m}{r} + \frac{m}{r} \cdot \frac{\alpha}{\beta}
 \end{aligned}$$

We arrive at the new steady state:

$$M_1 = \frac{mk_d}{r} \frac{2k_1k_d + k_a(l_2)r_2}{k_1k_dk_s + k_pr_2} \quad (\text{B.33})$$

$$M_2 = \frac{mk_d}{r} \frac{k_a(l_1)r_2 + 2k_dk_1}{k_dk_1k_s + k_pr_2} \quad (\text{B.34})$$

$$A_1 = \frac{m}{r} \left(1 + \frac{k_1k_dk}{k_1k_dk_s + k_pr_2} \right) \quad (\text{B.35})$$

$$A_2 = \frac{m}{r} \left(1 - \frac{k_1k_dk}{k_1k_dk_s + k_pr_2} \right) \quad (\text{B.36})$$

It is simple to verify that similarly to the original system where $\lambda \approx O(1)$, the qualitative behavior is the same with respect to k_1 and k_2 . If $k_1 = 0$, then the compartments reach the same steady state as when they were not connected.

$$\begin{aligned} M_1 &= \frac{mk_d}{r} \cdot \frac{k_a(l_2)r_2}{k_pr_2} = \frac{mk_d}{rk_a(l_1)} \\ M_2 &= \frac{mk_d}{rk_a(l_2)} \\ A_1 &= A_2 = \frac{m}{r} \end{aligned}$$

The case $k_2 \gg 1$ and $\lambda \gg 1$ is discussed in the main text. We conclude that regardless of the assumption we have made about λ , we must have $k_1 \gg k_2$ in order to have the desired dynamics.

Finally, we examine the absolute difference between $|A_1 - A_2|$. As previously, we can assume without loss of generality that $k_2 = 0$. Then $|A_1 - A_2|$ is bounded below by zero and above by $\frac{2m}{r}$.

$$A_1 - A_2 = \frac{2m}{r} \frac{k_1k_dk}{k_1k_dk_s + rk_p}$$

We consider $A_1 - A_2$ as a function of k and k_s , as before. The same analysis as in the $\lambda \approx O(1)$ case shows that for a fixed concentration difference, $k_a(l_1) - k_a(l_2)$, the optimal concentration range will be where $k_1k_d(k_a(l_1) + k_a(l_2)) = r$. We have shown that for the particular cases we have considered, our equations have the same qualitative behavior for $\lambda \approx O(1)$ and $\lambda \gg 1$. This is sufficient for our purposes, but

we note that in order to make this statement rigorous, we would have to compare the approximate solution based on the separation of time scales (i.e. on the assumption that λ is large) with the exact analytical solution.

B.3 Analytical solution and approximation

We consider the system of equations:

$$\begin{aligned}\frac{dM_1}{dt} &= m + \lambda(-k_a(l_1)M_1 + k_dA_1) + k_1(M_2 - M_1) \\ \frac{dA_1}{dt} &= -rA_1 + \lambda(k_a(l_1)M_1 - k_dA_1) \\ \frac{dM_2}{dt} &= m + \lambda(-k_a(l_2)M_2 + k_dA_2) - k_1(M_2 - M_1) \\ \frac{dA_2}{dt} &= -rA_2 + \lambda(k_a(l_2)M_2 - k_dA_2) \\ M_1(0) = M_2(0) &= \frac{m}{r} \frac{k_d}{k(l_0)} \quad A_1(0) = A_2(0) = \frac{m}{r}\end{aligned}$$

Based on our previous analysis we assumed that the flux of A was much smaller than the flux of M , k_1 , so we set the rate of flux of A to be zero. We rewrite the our equations in matrix form.

$$\begin{aligned}\frac{d\vec{y}(t)}{dt} &= D\vec{y} + h \\ \vec{y}(0) &= \vec{y}_0\end{aligned}$$

with

$$\vec{y} = \begin{bmatrix} M_1(t) \\ A_1(t) \\ M_2(t) \\ A_2(t) \end{bmatrix}$$

$$D = \begin{bmatrix} -(\lambda k_a(l_1) + k_1) & \lambda k_d & k_1 & 0 \\ \lambda k_a(l_1) & -(r + k_d) & 0 & 0 \\ k_1 & 0 & -(\lambda k_a(l_2) + k_1) & \lambda k_d \\ 0 & 0 & \lambda k_a(l_2) & -(r + k_d) \end{bmatrix}$$

$$h = \begin{bmatrix} m \\ 0 \\ m \\ 0 \end{bmatrix}$$

and

$$\vec{y}_0 = \begin{bmatrix} \frac{m}{r} \frac{k_d}{k_a(l_0)} \\ \frac{m}{r} \\ \frac{m}{r} \frac{k_d}{k_a(l_0)} \\ \frac{m}{r} \end{bmatrix}$$

We want to find X , Λ such that $D = X\Lambda X^{-1}$. Now our system becomes

$$\frac{d\vec{y}(t)}{dt} = X\Lambda X^{-1}\vec{y} + h \quad (\text{B.37})$$

$$X^{-1} \frac{d\vec{y}(t)}{dt} = \Lambda X^{-1}\vec{y} + X^{-1}h \quad (\text{B.38})$$

Define $v = X^{-1}\vec{y}$ and $\bar{h} = X^{-1}h$, so

$$\frac{dv}{dt} = \Lambda v + \bar{h}$$

$$v(0) = X^{-1}\vec{y}_0$$

By making one more substitution, and letting $w = v + \Lambda^{-1}\bar{h}$ we obtain

$$\frac{dw}{dt} = \Lambda w$$

$$w(0) = v(0) + \Lambda^{-1}\bar{h}$$

The solution to this equation is $w = w(0)e^{\Lambda t}$, and by making the appropriate substitutions again, this gives the solution to the equation B.38 to be

$$\vec{y} = (\vec{y}_0 + D^{-1}h)e^{\Lambda t} - D^{-1}h$$

In order to find the explicit formula for \vec{y} , we must find Λ , the diagonal matrix of eigenvalues of D and D^{-1} in terms of our parameters. In spite the fact that this is a problem with some symmetry, finding the eigenvalues and the inverse of the four-by-four matrix, D is difficult even with Matlab's Symbolic Math Toolbox. We leave the exact solution in this form.

It is possible to approximate the exact solution to equations B.11-B.15 in case $\lambda \gg 1$. The solution is similar to the solution of the equations for perfect adaptation in Appendix B.1.

Depending on the size of the flux k_1 between the two compartments we can consider two cases. First, we assume that the flux between the two compartments is very fast, and in fact, $k_1 = O(\lambda)$. Based on our intuition developed by the steady state solution and the approximate solutions, we expect in this case the greatest change to be that the fast time scale, r_f has to depend on both $k_a(l_1)$ and $k_a(l_2)$. If we write down the equations that apply on the fast time scale,

$$\begin{aligned} \frac{dM_1}{d\tau} &= -k_a(l_1)M_1 + k_dA_1 + k_1(M_2 - M_1) \\ \frac{dA_1}{d\tau} &= k_a(l_1)M_1 - k_dA_1 \\ \frac{dM_2}{d\tau} &= -k_a(l_2)M_2 + k_dA_2 - k_1(M_2 - M_1) \\ \frac{dA_2}{d\tau} &= k_a(l_2)M_2 - k_dA_2 \end{aligned}$$

we see that now we must sum all four components to get a constant, i.e., $M_1 + M_2 + A_1 + A_2 = C$, so the four equations are coupled. In fact, solving this system of equations is not simpler than providing the exact solution, therefore we do not pursue this line of investigation.

Now we examine the case when $k_1 \approx O(1)$, so on the fast time scale the it is still true that $A_1 + M_1 = C_1$ for a constant C_1 , and similarly, $A_2 + M_2 = C_2$. The same calculations we used in Appendix B.1 apply, and we can obtain the solution to on the fast time scale:

$$A_1(\tau) = (A_{s1} - A_{11})e^{-r_{f1}\tau} + A_{11} \quad (\text{B.39})$$

$$M_1(\tau) = (M_{01} - M_{11})e^{-r_{f1}\tau} + M_{11} \quad (\text{B.40})$$

$$A_2(\tau) = (A_{s2} - A_{12})e^{-r_{2f}\tau} + A_{12} \quad (\text{B.41})$$

$$M_2(\tau) = (M_{02} - M_{12})e^{-r_{2f}\tau} + M_{12} \quad (\text{B.42})$$

where we have defined the constants

$$\begin{aligned} r_{f1} &= k_a(l_1) + k_d, & r_{f2} &= k_a(l_2) + k_d \\ M_{01} &= M_{02} = \frac{mk_d}{rk_a(l_0)} \\ M_{11} &= \frac{m}{r} \frac{k_d}{k_a(l_1)} \frac{1 + (k_d/k_a(l_0))}{1 + (k_d/k_a(l_1))}, & M_{12} &= \frac{m}{r} \frac{k_d}{k_a(l_1)} \frac{1 + (k_d/k_a(l_0))}{1 + (k_d/k_a(l_2))} \\ A_{s1} &= A_{s2} = \frac{m}{r} \\ A_{11} &= \frac{m}{r} \frac{1 + (k_d/k_a(l_0))}{1 + (k_d/k_a(l_1))}, & A_{12} &= \frac{m}{r} \frac{1 + (k_d/k_a(l_0))}{1 + (k_d/k_a(l_2))} \end{aligned}$$

On the slow time scale it remains true that $A_1 = \frac{k_a(l_1)}{k_d}M_1$, and $A_2 = \frac{k_a(l_2)}{k_d}M_2$.

As before, substituting these expressions into equations B.11-B.15 we arrive at a new system of equations:

$$\frac{dM_1}{dt} = m + k_1(M_2 - M_1) \quad (\text{B.43})$$

$$\frac{k_a(l_1)}{k_d} \frac{dM_1}{dt} = -r \frac{k_a(l_1)}{k_d} M_1 \quad (\text{B.44})$$

$$\frac{dM_2}{dt} = m - k_1(M_2 - M_1) \quad (\text{B.45})$$

$$\frac{k_a(l_1)}{k_d} \frac{dM_1}{dt} = -r \frac{k_a(l_2)}{k_d} M_2 \quad (\text{B.46})$$

As before, we add equations B.43 and B.44, and equations B.45 and B.46. We arrive

at

$$\frac{dM_1}{dt} = \frac{mk_d}{k_d + k_a(l_1)} + \frac{k_1k_d}{k_d + k_a(l_1)}(M_2 - M_1) - r\frac{k_a(l_1)}{k_d + k_a(l_1)}M_1 \quad (\text{B.47})$$

$$\frac{dM_2}{dt} = \frac{mk_d}{k_d + k_a(l_2)} + \frac{k_1k_d}{k_d + k_a(l_2)}(M_2 - M_1) - r\frac{k_a(l_2)}{k_d + k_a(l_2)}M_2 \quad (\text{B.48})$$

The solution to eqns. B.47, B.48 is given by:

$$\bar{M}(t) = (\bar{M}(0) + D^{-1}h)e^{\Lambda t} - D^{-1}h$$

where

$$D = \begin{bmatrix} \frac{-rk_a(l_1) - k_1k_d}{k_d + k_a(l_1)} & \frac{k_1k_d}{k_d + k_a(l_1)} \\ \frac{k_1k_d}{k_d + k_a(l_1)} & \frac{-rk_a(l_2) - k_1k_d}{k_d + k_a(l_2)} \end{bmatrix}$$

$$h = \begin{bmatrix} \frac{mk_d}{k_d + k_a(l_1)} \\ \frac{mk_d}{k_d + k_a(l_2)} \end{bmatrix}$$

$$\bar{M}(0) = \begin{bmatrix} c_1 \\ c_2 \end{bmatrix}$$

We define $\beta = Tr(D)$ and $\gamma = \det(D)$. Then the eigenvalues λ_1, λ_2 of D can be found as follows:

$$\lambda_{1,2} = \frac{-\beta \pm \sqrt{\beta^2 - 4\gamma}}{2}$$

By making the appropriate substitutions and carrying out the calculations, the discriminant $\sqrt{\beta^2 - 4\gamma}$ can be reduced to:

$$\left(\frac{(k_1k_d + rk_a(l_1))}{(k_d + k_a(l_1))} - \frac{(k_1k_d + rk_a(l_2))}{(k_d + k_a(l_2))} \right)^2 - 2 \frac{(k_1k_d)^2}{(k_d + k_a(l_1))(k_d + k_a(l_2))}$$

If we assume that the second term is much smaller than the first one, then the above expression greatly simplifies. This is true if

$$(r + k_1)k_d(k_a(l_1) - k_a(l_2)) \gg k_1k_d \quad (\text{B.49})$$

Equation B.49 implies that our approximation is appropriate when the ligand concentrations in the two compartment are very different, i.e. when $k_a(l_1) - k_a(l_2) \gg 1$. Now we are able to find the two eigenvalues:

$$\lambda_{1,2} \simeq -\frac{rk_a(l_1) + k_1k_d}{k_d + k_a(l_1)}, -\frac{rk_a(l_2) + k_1k_d}{k_d + k_a(l_2)}$$

The two eigenvalues define the two slow time scales,

$$r_{s1} = -\frac{rk_a(l_1) + k_1k_d}{k_d + k_a(l_1)}$$

$$r_{s2} = -\frac{rk_a(l_2) + k_1k_d}{k_d + k_a(l_2)}$$

We notice that if the flux k_1 is small, then we have recovered the slow time scale for each compartment independently of each other. This result confirms conclusions we have drawn from our steady state analysis.

Next, we find $D^{-1}h$:

$$d_1 = D^{-1}h_1 = -\frac{m}{r} \frac{k_d(rk_a(l_2) + k_1k_d)}{rk_a(l_1)k_a(l_2) + k_1k_d(k_a(l_1) + k_a(l_2))}$$

$$d_2 = D^{-1}h_2 = -\frac{m}{r} \frac{k_dk_1(k_d + k_a(l_1))}{rk_a(l_1)k_a(l_2) + k_1k_d(k_a(l_1) + k_a(l_2))}$$

The solution to eqns. B.47 - B.48 is:

$$M_1 = (c_1 + d_1)e^{(-r_{s1}t)} - d_1 \tag{B.50}$$

$$M_2 = (c_2 + d_2)e^{(-r_{s2}t)} - d_2 \tag{B.51}$$

The equations for M_1 and M_2 also determine the expressions for A_1 and A_2 :

$$A_1 = \frac{k_a(l_1)}{k_d}(c_1 + d_1)e^{(-r_{s1}t)} - \frac{k_a(l_1)d_1}{k_d} \tag{B.52}$$

$$A_2 = \frac{k_a(l_2)}{k_d}(c_2 + d_2)e^{(-r_{s2}t)} - \frac{k_a(l_2)d_2}{k_d} \tag{B.53}$$

Now we can match the fast and slow solutions as before to determine the constants c_1 and c_2 , and to give arrive at the full approximation. Taking the limit as $\tau \rightarrow \infty$

of the equations on the fast time scale, and setting this equal to the initial condition of the equations of the slow time scale gives us:

$$\begin{aligned} c_1 + d_1 - d_1 &= M_{11} \\ c_2 + d_2 - d_2 &= M_{12} \\ \frac{k_a(l_1)}{k_d}(c_1 + d_1) - \frac{k_a(l_1)d_1}{k_d} &= A_{11} \\ \frac{k_a(l_2)}{k_d}(c_2 + d_2) - \frac{k_a(l_2)d_2}{k_d} &= A_{12} \end{aligned}$$

Thus the approximate solution to our system of equations

$$A_1 = (A_{s1} - A_{11})e^{-r_{f1}\lambda t} + \frac{k_a(l_1)}{k_d}(A_{11} + d_1)e^{(-r_{s1}t)} - \frac{k_a(l_1)d_1}{k_d} \quad (\text{B.54})$$

$$M_1 = (M_{01} - M_{11})e^{-r_{f1}\lambda t} + (M_{11} + d_1)e^{(-r_{s1}t)} - d_1 \quad (\text{B.55})$$

$$A_2 = (A_{s2} - A_{12})e^{-r_{f2}\lambda t} + \frac{k_a(l_2)}{k_d}(A_{12} + d_2)e^{(-r_{s2}t)} - \frac{k_a(l_2)d_2}{k_d} \quad (\text{B.56})$$

$$M_2 = (M_{02} - M_{12})e^{-r_{f2}\lambda t} + (M_{12} + d_2)e^{(-r_{s2}t)} - d_2 \quad (\text{B.57})$$

B.4 Calcium switch

We return to the experimental observation that the cytosolic calcium concentration can change the turning behavior of a growth cone. Let us assume that a netrin-1 gradient is set up outside the cell. Recall that in a cell with normal cytosolic calcium concentration a gradient develops with the high calcium concentrations facing the source of netrin-1, and the growth cone responds with attractive turning. However, in the same netrin-1 gradient a cell whose cytosolic calcium has been depleted before the trial responds with repulsive turning (eventhough the high calcium concentrations still face the source of netrin-1). Such a behavior is possible by making some assumptions regarding k_a , the rate at which A is produced in our model.

We assume that the production rate of A depends both on the ligand concentration and the cytosolic calcium concentration, $k_a(l, Ca)$. Further, we want k_a to be such

that for large values of calcium $\frac{\partial k_a}{\partial l} > 0$, so k_a is an increasing function of the ligand, and for small values of calcium $\frac{\partial k_a}{\partial l} < 0$. Without the constraints of experimental data, many such functions can be found. We chose $k_a = \exp\left(\frac{al(Ca - Ca_b)}{(l+b)(Ca+c)}\right)$ where a , b and c are new constants, and Ca_b is the normal cytosolic calcium concentration. k_a is illustrated in Figure B.1.

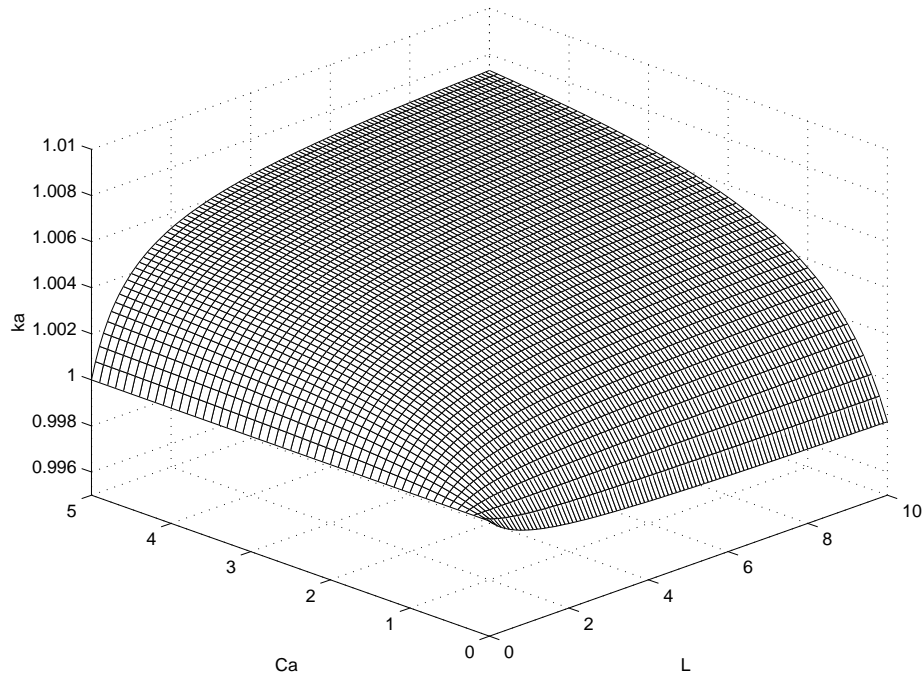


Figure B.1: $k_a(l, Ca)$, the production rate of the modified substance, A . l : ligand, netrin-1, Ca : cytosolic calcium concentration. $a = 0.01$, $b = 1$, $c = 1$, $Ca_b = 0.2$

Using this rate we can simulate what happens with our system of equations in the same ligand gradient when the calcium level is above and when the calcium level is below the baseline, Ca_b . Changing the calcium level in the simulations corresponds to changing the value of the parameter Ca in the expression for $k_a(l)$. This implicitly implies that we take the calcium level to be spatially uniform inside the cell. Figure B.2 shows that in the normal cytosolic concentration we get a gradient of the adapted substance, A when a netrin-1 gradient is presented, with the higher concentration of A

corresponding to the higher concentration of l . (As before, the "gradient" of A is based on two values only, $A_1 = A(1)$ in the left hand compartment and $A_2 = A(2)$ in the right hand compartment.) Lowering the cytosolic concentration level, and presenting the cell the same ligand gradient results in a gradient of A where now the level of A is lower in the compartment corresponding to the higher ligand concentration.

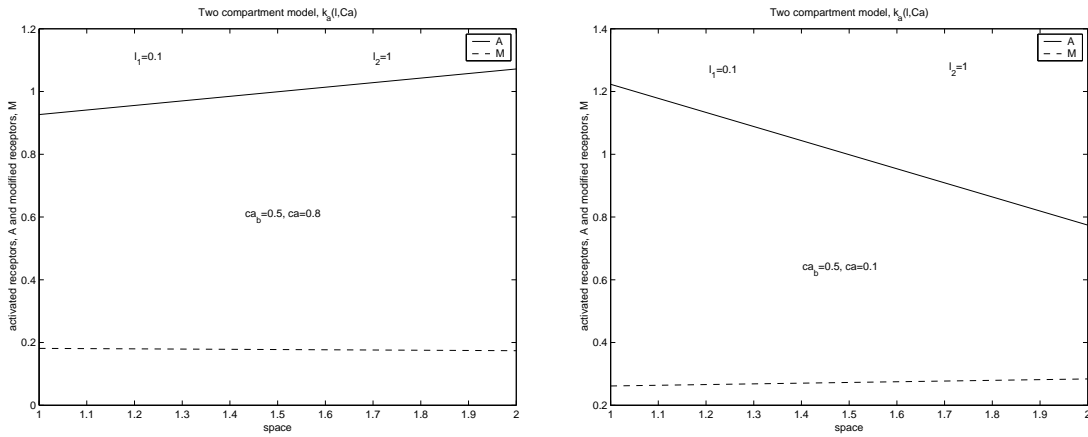


Figure B.2: Numerical simulations of the two compartment model using $k_a = \exp(\frac{al(Ca-Ca_b)}{(l+b)(Ca+c)})$. The first figure shows a cell where the cytosolic calcium level is above the baseline. The second figure shows a cell in the same ligand gradient where the calcium level is below the baseline.

Both panels of the figure are run to the same time, $t=50$ seconds. The simulations are based on the same Matlab code as the previous two compartment models, except that now $k_a(l)$ is changed.

This model presents a very simple explanation of how calcium levels influence turning behavior. Only the overall calcium concentration is considered by the simulations, the spatial and temporal gradients of calcium are not. Further investigations are necessary to create a more realistic description of the behavior.

Appendix C

Sample Matlab code

We are interested in investigating the deformations of two coupled Kelvin bodies in (i) steady flow, $F = F_0$ and (ii) oscillatory flow, $F = F_0 \cos(\omega t)$. Equations 4.9 and 4.10 were solved with a Matlab code given below. The solution presented here is for oscillatory flow.

First we can see the program `twobodies_aF.m` that asks for the input from the user and displays the results of the simulations. The user defines the coefficients for the two Kelvin bodies, and the program stores this information in the matrix `B`. In this code a function, `parallel2_aF.m` is called which actually computes the solution with a four-stage Runge-Kutta method. Then, as the output of `parallel2_aF.m`, the solution of the differential equation is returned to the matrix `u_1` in `twobodies_aF.m`, the solution (in this case $u(t)$) is plotted.

```
r=input('Two-body system with the bodies connected in parallel');
r=input('Coefficients for ith body are:
[\mu_{0i} \mu_{1i} \eta_{1i}] ');

B=zeros(2,3);

B(1,:)=input('Coefficients for Body 1:- ');
```

```

B(2,:)=input('Coefficients for Body 2:- ');

h = 0.1;                % size of the time step
N0=5;
N = N0/h;

x=[1:1:N];             % length of a, u, F

u_1=parallel2_aF(B,h,N); % function call

u1=u_1(1,1:1:N);
F=u_1(3,1:1:N);
a=u_1(2,1:1:N);
a=a./F;

plot(x,u,'r-.')
ylabel('u(t), deformation')
xlabel('time, t')
title('u vs t for different values of \eta_{12},
F=F_0 cos(\omega t)')

```

Now we can look at the code for the actual ODE solver, `parallel2_aF.m`. Here only the main loop of the program is included which contains the fourth-order four-stage Runge-Kutta method. In the actual program the matrices $M1$, $M2$, $M3$ and M are defined to be A , D , \vec{c} and $A^{-1}D$, respectively. The full code contains the initialization of all the appropriate variables. This program also calls a function, `ve2_aF.m`, given below. The input of `parallel2_aF.m` function is the matrix of coefficients of the

Kelvin bodies, denoted by B , the step size, h , and the length of the solution vector, N . The output of this function is also a matrix, called `u1_plot` whose first row is $u(t)$, second row is $a(t)F(t)$, and third row is $F(t)$. $u(t)$ and $a(t)F(t)$ are obtained as the solutions to the differential equations. $F(t)$, the third row of the matrix, is simply $F_0 \cos(\omega t)$ evaluated for each time step.

```
function f=parallel2_aF(B,h,N);

for k=1:N

    F(k+1)=F0*cos(w*(t+h));           % oscillatory

    k1=u;
    k2=u+(1/2)*h*ve2_aF(M,inM1,M3,k1,t+(h/2));
    k3=u+(1/2)*h*ve2_aF(M,inM1,M3,k2,t+(h/2));
    k4=u+h*ve2_aF(M,inM1,M3,k3,t+h);

    u_new=u+h*((1/6)*ve2_aF(M,inM1,M3,k1,t)...
    +(1/3)*ve2_aF(M,inM1,M3,k2,t+(h/2))...
    +(1/3)*ve2_aF(M,inM1,M3,k3,t+(h/2))...
    +(1/6)*ve2_aF(M,inM1,M3,k4,t+h));

    u = u_new;
    t = t+h;
    u1_plot(1:2,k+1)=u;
    u1_plot(3,k+1)=F(k+1);

end
```

```
f=u1_plot;
```

Finally, we can look at `ve2_aF.m`. The input of this function is $A^{-1}D$, denoted here by `M`; A^{-1} , denoted by `inM1`; \vec{c} , denoted by `M3`; a vector which consists of $u(t)$ and $a(t)F(t)$ at the previous time step, denoted by `u`, and finally, t , the current time step. The output of this function is the right hand side of equation 4.9 for the appropriate time step with the given type of flow. Here oscillatory flow is shown.

```
function f = ve2_aF(M,inM1,M3,u,t)
```

```
F0=1;
```

```
w=2*pi;
```

```
F=F0*cos(w*t);
```

```
dF=-F0*w*sin(w*t);
```

```
C=zeros(2,1);
```

```
C = M3*dF;
```

```
C(2,1) = F+C(2,1);
```

```
f = M*u+inM1*C;
```

Bibliography

- [1] Adler, J., *Chemoreceptors in Bacteria*, “Science”, Vol. 166:1588-1597, (1969).
- [2] Alberts, B., Bray, D., Lewis, J., Raff, M., Roberts, K., Watson, J. D., *The Cell*, Garland Publishing, New York, (1994).
- [3] Barakat, A. I., *A Model for Shear Stress-induced Deformation of a Flow Sensor on the Surface of Vascular Endothelial Cells*, “Journal of Theoretical Biology”, Vol. 210: 221-236, (2001).
- [4] Barkai, N., Leibler, S., *Robustness in simple biochemical networks*, “Nature”, Vol. 387: 913-917, (1997).
- [5] Bar-Sagi, D., Hill, A., *Ras and Rho GTPases: A Family Reunion*, “Cell”, Vol. 103: 227-238, Oct., (2000).
- [6] Bausch, A. R., Ziemann, F., Boulbitch, A. A., Jacobson, K., Sackmann, E., *Local Measurements of Viscoelastic Parameters of Adherent Cell Surfaces by Magnetic Bead Microrheometry*, “Biophysical Journal”, Vol. 75: 2038-2049, (1998).
- [7] Berg, H. C., and Turner, L., *Chemotaxis of bacteria in glass capillary arrays*, “Biophysical Journal”, Vol. 58: 919-930, (1990).
- [8] Berridge, M. J., *Neuronal Calcium Signaling*, “Neuron”, Vol. 21; 13-26, July, (1998).

- [9] Bhalla, U. S., Iyengar, R. *Emergent Properties of Networks of Biological Signaling Pathways*, "Science", Vol. 283: 381-387, January, (1999), webpage: <http://piris.pharm.mssm.edu/rilab/>.
- [10] Block, S., M., Segall, J. A. and Berg, H. C., *Adaptation Kinetics in Bacterial Chemotaxis*, "Journal of Bacteriology", Vol. 154: 312-323 (1983).
- [11] Bray, D., *Protein molecules as computational elements in living cells*, "Nature", Vol. 376: 307-312, July, (1995).
- [12] Bray, D., *Cell Movements*, Garland Publishing, Inc, New York, (1992).
- [13] Brown, D., A. and Berg H., C., *Temporal simulation of chemotaxis in Escherichia Coli*, "Proc. Nat. Acad. Sci USA", Vol. 71: 1388-1392 (1974).
- [14] Caldwell, K.K., Boyajian, C.L., Cooper, D.M.F., *The effects of Ca^{2+} and calmodulin on adenylyl cyclase activity in plasma membranes derived from neural and non-neural cells*, "Cell Calcium", Vol. 13: 107-121, (1992).
- [15] Dallon, J. C., Othmer, H. G., *A Continuum Analysis of the Chemotactic Signal Seen by Dictyostelium discoideum*, submitted to "J. Theor. Biol."
- [16] Defer, N., Best-Belpomme, M., Hanoune, J., *Tissue specificity and physiological relevance of various isoforms of adenylyl cyclase*, "Am. J. Physiol. Renal. Physiol.", Vol. 279: F400-F416, (2000).
- [17] Dewey, Jr. C. F., Bussolary, S. R., Gimborne, Jr. M. A., Davies, P. F., *The dynamic response of vascular endothelial cells to fluid shear stress*, "J. Biomed. Eng." Vol. 103: 177-188, (1981).
- [18] Dickinson, R. B., and Tranquillo, R. T., *A stochastic model for adhesion-mediated cell random motility and haptotaxis*, "J. Math. Biol.", Vol. 31:563-600, (1993).

- [19] Ford, R. M., Phillips, B. R., Quinn J. A. and Lauffenburger, D. A. *Measurement of bacterial random motility and chemotaxis coefficients: I. stopped-flow diffusion chamber assay*, "Biotechnology and Bioengineering", Vol. 37:647-660, (1991).
- [20] Fung, Y.C., *Biomechanics: Mechanical Properties of Living Tissues*, Springer-Verlag, New York, (1981).
- [21] Goldbeter, A., Dupont, G., Berridge, M. J., *Minimal model for signal-induced Ca^{2+} oscillations and for their frequency encoding through protein phosphorylation*, "Proc. Natl. Acad. Sci. USA", Vol 87:1461-1465, Feb. (1990).
- [22] Goldbeter, A., Koshland, D. E. Jr., *An amplified sensitivity arising from covalent modification in biological systems*, "Proc. Natl. Acad. Sci USA", Vol. 78: No. 11, 6840-6844, Nov. (1981).
- [23] D. Grünbaum, *Advection-diffusion equations for internal state mediated random walks*, "SIAM, J. of Applied Math.", Vol. 61: (N1), 43-73, () .
- [24] Guilak, F., Tedrow, J. R., Burgkart, R., *Viscoelastic Properties of the Cell Nucleus*, "Biochemical and Biophysical Research Communications", Vol. 269: 781-786, (2000).
- [25] Gutfreund, H., *Kinetics for the life sciences*, Cambridge University Press, Cambridge, (1995).
- [26] Hall, A., *Rho GTPases and the Actin Cytoskeleton*, "Science", Vol. 279: 509-514, January, (1998).
- [27] Harootunian, A. T., Kao, J. P. Y., Paranjape, S., Tsien, R. Y., *Generation of Calcium Oscillations in Fibroblast by Positive Feedback Between Calcium and IP_3* "Science", Vol. 251: 75-78, Jan. (1991).

- [28] Helmlinger, G., Berk, B. C., Nerem, R. M., *Calcium responses of endothelial cell monolayers subjected to pulsatile and laminar flow differ*, "Am. J. Physiol.", Vol, 269: C367-375, (1995).
- [29] Helmlinger, G., Geiger, R. V., Schreck, S., Nerem, R. M., *Effects of pulsatile flow on cultured vascular endothelial cell morphology*, "J. Biomech. Eng.", Vol. 113: 123-134, (1991).
- [30] Hill, N. A. *Ch. 15. Bioconvection*, from *In Case Studies in Mathematical Modeling: Ecology, Physiology, and Cell Biology*, editors: H. Othmer, F. Adler, M. Lewis, J. Dallon, Prentice-Hall, Englewood Cliffs
- [31] Hillesdon, A. J., Pedley T. J. and Kessler, J. O. *The development of concentration gradients in a suspension of chemotactic bacteria*, "Bulletin of Mathematical Biology", Vol. 57: No. 2, pp. 299-344, (1995).
- [32] Hong, K., Nishiyama M., Henley, J., Tessier-Lavigne, M., Poo, M., *Calcium signaling in the guidance of nerve growth by netrin-1*, Letters to Nature, "Nature", (1999).
- [33] Jafri, S. M., Keizer, J., *On the Roles of Ca^{2+} Diffusion, Ca^{2+} Buffers, and the Endoplasmic Reticulum in IP_3 -Induced Ca^{2+} Waves* "Biophysical Journal", Vol. 69: 2139-2153, Nov., (1995).
- [34] Janmey, P. A., Euteneuer, U., Traub, P., Schliwa, M., *Viscoelastic Properties of Vimentin Compared with Other Filamentous Biopolymer Networks*, "Journal of Cell Biology" Vol. 113: 155-160, (1991).
- [35] Jordan, J. D., Landau, E. M., Iyengar, R., *Signaling Networks: The Origins of Cellular Multitasking*, "Cell", Vol. 103, 193-200, Oct. (2000).

- [36] Keino-Masu K., Masu, M., Hinck, L., Leonardo, E.D., Chan, S.S.-Y., Culotti, J.G., Tessier-Lavigne, M. *Deleted in Colorectal Cancer (DCC) encodes a netrin receptor*, "Cell", Vol. 87: 175-185, (1996).
- [37] Keizer, J., De Young, G.W., *Two roles for Ca^{2+} in agonist stimulated Ca^{2+} oscillations*, "Biophys. J.", Vol. 61: 649-660, (1992).
- [38] Keller, E. and Segel, L. *Model for Chemotaxis*, "J. theor. biol.", vol. 30: 225-234, (1971).
- [39] Lauffenburger, D. A., Linderman, J.J., *Receptors: Models for Binding, Trafficking, and Signaling*, Oxford University Press, New York, (1993).
- [40] Laurent, M., Claret, M., *Signal-induced Oscillations Through the Regulation of the Inositol 1,4,5-Triphosphate-gated Ca^{2+} Channel: an Allosteric Model* " J. Theor. Biol.", Vol. 186: 307-26, (1997).
- [41] Levchenko, A., Iglesias, P., *Models of Eukaryotic Gradient Sensing: Application to Chemotaxis of Amoebae and Neutrophils*, "Biophys. J.", Vol.82(1): 50-63, (2002).
- [42] Lewis, J., Slack, J. M. W., Wolpert, L., *Thresholds in Development*, "J. theor. Biol." Vol. 65: 579-590, (1977).
- [43] Mahama, P.A., Linderman, J. J., *Simulations of membrane signal transduction events: Effects of receptor blockers on G-protein activation*. Submitted for publication. found in: Lauffenburger and Linderman, *Receptors*, Oxford University Press, New York, (1993).
- [44] Meinhardt, H., *Orientation of chemotactic cells and growth cones: models and mechanisms*, "J. of Cell Science", Vol. 112: 2867-2874, (1999).

- [45] Meyer, T., Holowka, D., Stryer, L., *Highly Cooperative Opening of Calcium Channels by Inositol 1,4,5-Triphosphate* ‘Science’, Vol. 240: 653-655, Apr., (1988).
- [46] Meyer, T., Stryer, L., *Calcium Spiking*, “Annu. Rev. Biophys. Biophys. Chem.” Vol. 20: 153-74, (1991)
- [47] Meyer, T., Stryer, L., *Molecular model for receptor-stimulated calcium spiking*, “Proc. Natl. Acad. Sci USA”, Vol: 85, 5051-5055, Jul., (1988).
- [48] Ming, G., Song, H., Berninger, B., Holt, C., Tessier-Lavigne, M., *cAMP Dependent Growth Cone Guidance by Netrin-1*, “Neuron”, Vol. 1: 1225-1235, Dec., (1997).
- [49] Ming, G., Song, H., Berninger, B., Inagaki, N., Tessier-Lavigne, M., Poo, M., *Phospholipase C-gamma and Phosphoinositide 3-Kinase Mediate Cytoplasmic Signaling in Nerve Growth Cone Guidance*, “Neuron”, Vol. 23: 139-148, (1999).
- [50] Moghe, P.V., Tranquillo, R.T., *Stochasticity in Membrane-Localized Ligand-Receptor-G Protein Binding: Consequences for Leukocyte Movement*, “Ann. Biomed. Eng.”, Vol. 23: 257-267, (1995).
- [51] Moghe P. V. and Tranquillo, R. T., *Stochastic model of chemoattractant receptor dynamics in leukocyte chemosensory movement*, “Bulletin of Mathematical Biology”, Vol. 56: No. 6, pp. 1041-1093, (1994).
- [52] Mons, N., Cooper, D.M.F., *Adenylate cyclases: critical foci in neuronal signaling*, “Trends in Neuroscience”, Vol. 18: 536-542, (1995).
- [53] Mons, N., Decorte, L., Jaffard, R., Cooper, D.M.F, *Ca²⁺-sensitive adenylyl cyclases, key integrators of cellular signaling*, “Life Sciences”, Vol. 62: Nos.17/18, 1647-1652, (1998).

- [54] Narang, A., Subramanian, K. K., Lauffenburger, D. A., *A Mathematical Model for Chemoattractant Gradient Sensing Based on Receptor-Regulated Membrane Phospholipid Signaling Dynamics*, "Annals of Biomedical Engineering", Vol. 29: 677-691, (2001)
- [55] Nerem, R. M., Levesque, M. J., Cornhill, J. F., *Vascular endothelial morphology as an indicator of the pattern of blood flow*, "J. Biochem. Eng.", Vol. 114: 274-282, (1981).
- [56] Parent, C., A., Devreotes, P., N., *A Cell's Sense of Direction*, "Science", Vol. 284: 765-769, (1999)
- [57] Parkinson J. S., *Signal Transduction Schemes of Bacteria*, "Cell", Vol. 73:857-871, (1993).
- [58] Postma, M., Van Haastert, P. J. M., *A Diffusion-Translocation Model for Gradient Sensing by Chemotactic Cells*, "Biophysical Journal", Vol. 81: 1314-1323, (2001).
- [59] Rebbapragada, Johnson, M. S., Harding, G. P., Zuccarelli, A. J., Fletcher, H. M., Zhulin, I. B., Taylor, B. L., *A novel sensor, Aer and the serine chemoreceptor, Tsr independently sense intracellular energy levels and transduce oxygen, redox, and energy signals for Escherichia coli behavior*, submitted to be published in "Biochemistry".
- [60] Rebbapragada, Johnson, M. S., Harding, G. P., Zuccarelli, A. J., Fletcher, H. M., Zhulin, I. B., Taylor, B. L., *The Aer protein and serine chemoreceptor Tsr independently sense intracellular energy levels and transduce oxygen, redox, and energy signals for Escherichia coli behavior*, "Proc. Natl. Acad. Sci. USA", Vol 94:10541-10546, (1997).

- [61] Sato, M., Ohshima, N., Nerem, R. M., *Viscoelastic Properties of Cultured Porcine Aortic Endothelial Cells Exposed to Shear Stress*, "Journal of Biomechanics", Vol. 29, No. 4: 461-467, 1996
- [62] Satcher, R. L. Jr., Dewey, C. F. Jr., *Theoretical Estimates of Mechanical Properties of the Endothelial Cell Cytoskeleton*, "Biophysical Journal", Vol. 71: 109-118, (1996).
- [63] Segel, L. E., *Incorporation of receptor kinetics into a model for bacterial chemotaxis*, "J. theor. biol.", Vol. 57: 23-42, (1976).
- [64] Song, H., Ming, G., Poo, M., *cAMP-induced switching in turning direction of nerve growth cones*, "Nature", Vol. 388: 275-279, July, (1997).
- [65] Song, H., Ming, G., Zhigang H., Lehmann M., McKerracher, L., Tessier-Lavigne, M., Poo, M., *Conversion of Neuronal Growth Cone Responses from Repulsion to Attraction by Cyclic Nucleotides*, "Science", Vol. 281: 1515-1518, Sep., (1998).
- [66] Song, H., Poo, M., *The cell biology of neuronal navigation*, "Nat. Cell Biol.", Vol. 3: E81-E88, (2001).
- [67] Song, H., Poo, M., *Signal Transduction underlying growth cone guidance by diffusible factors*, "Current Opinion in Neurobiology", Vol. 9: 355-363, (1999).
- [68] Stamenovic, D., Coughlin, M. F., *The Role of Prestress and Architecture of the Cytoskeleton and Deformability of Cytoskeletal Filaments in Mechanics of Adherent Cells: a Quantitative Analysis*, "J. Theor. Biol.", Vol. 201: 63-74, (1999).
- [69] Stamenovic, D., Fredberg, J. J., Wang, N., Butler, J. P., Ingber, D. E., *A microstructural approach to cytoskeletal mechanics based on tensegrity*, "J. Theor. Biol.", Vol. 181: 125-136, (1996).

- [70] Tang, Y., Stephenson, J.L., Othmer, H.G., *Simplification and Analysis of Models of Calcium Dynamics Based on IP_3 -Sensitive Calcium Channel Kinetics*, “Biophysical Journal”, Vol. 70: 246-263, (1996).
- [71] Taylor, B. L., *Role of proton motive force in sensory transduction in bacteria*, “Ann. Rev. of Microbiol.”, Vol. 37:551-573, (1983).
- [72] Taylor B. L., and Johnson, M. S., *Rewiring a receptor: negative output from positive input*, “Federation of European Biochemical Societies Letters”, Vol. 425: 377-381, (1998).
- [73] Taylor B. L. and Zhulin, I., *In search of higher energy: metabolism-dependent behavior in bacteria*, to be published.
- [74] Teruel, M. N., Meyer, T., *Translocation and Reversible Localization of Signaling Proteins: A Dynamic Future for Signal Transduction*, “Cell”, Vol. 103: 181-184, Oct. (2000).
- [75] Tranquillo, R. T., Lauffenburger, D.A., *Analysis of Leukocyte Chemosensory Movement*, “Adv. Biosciences”, Vol. 66: 29-38, (1987).
- [76] Wang, N., Ingber, D. E., *Control of the cytoskeletal mechanics by extracellular matrix, cell shape, and mechanical tension*, “Biophys. J.” Vol. 66: 2181-2189, (1994).
- [77] Zheng, J. Q., *Turning of growth cones induced by localized increases in intracellular calcium ions*, Letters to Nature, “Nature”, Vol. 403: 89-93, Jan., (2000).
- [78] Zhulin, I. B., Bespalov V. A., Johnson, M. S., Taylor, B. L., *Oxygen taxis and proton motive force in *Azospirillum brasilense**, “Journal of Bacteriology”, Vol. 178: No. 17, 5199-5204, (1996).